creative commons
COMMONS DEED

저작자표시-비영리-동일조건변경허락 2.0 대한민국

이용자는 아래의 조건을 따르는 경우에 한하여 자유롭게

- 이 저작물을 복제, 배포, 전송, 전시, 공연 및 방송할 수 있습니다.
- 이차적 저작물을 작성할 수 있습니다.

다음과 같은 조건을 따라야 합니다:

저작자표시. 귀하는 원저작자를 표시하여야 합니다.

비영리. 귀하는 이 저작물을 영리 목적으로 이용할 수 없습니다.

동일조건변경허락. 귀하가 이 저작물을 개작, 변형 또는 가공했을 경우에는, 이 저작물과 동일한 이용허락조건하에서만 배포할 수 있습니다.

- 귀하는, 이 저작물의 재이용이나 배포의 경우, 이 저작물에 적용된 이용허락조건을 명확하게 나타내어야 합니다.
- 저작권자로부터 별도의 허가를 받으면 이러한 조건들은 적용되지 않습니다.

저작권법에 따른 이용자의 권리는 위의 내용에 의하여 영향을 받지 않습니다.

이것은 이용허락규약(Legal Code)을 이해하기 쉽게 요약한 것입니다.

Disclaimer

dCollection

공학박사 학위논문

Electrorefining of Irradiated Spent Nuclear Fuel Zircaloy-4 Cladding in LiCl-KCl Molten Salts

LiCl-KCl 용융염 기반 사용후핵연료

방사화 지르칼로이-4 피복관 전해정련

2014년 8월

서울대학교 대학원

에너지시스템공학부

박 재 영

Electrorefining of Irradiated Spent Nuclear Fuel Zircaloy-4 Cladding in LiCl-KCl Molten Salts

지도 교수 황 일 순

이 논문을 공학박사 학위논문으로 제출함

2014 년 4 월

서울대학교 대학원

에너지시스템공학부

박 재 영

박재영의 박사 학위논문을 인준함

2014 년 7 월

위 원 장 이 경 우 (인)

부위원장 황 일 순 (인)

위 원 박 병 기 (인)

위 원 이 종 현 (인)

위 원 한 병 찬 (인)

Abstract

Electrorefining of Irradiated Spent Nuclear Fuel Zircaloy-4 Cladding in LiCl-KCl Molten Salts

Jaeyeong Park

School of Energy Systems Engineering
The Graduate School
Seoul National University

Zirconium alloys have low thermal neutron absorption cross section, high corrosion resistance and superior mechanical characteristics. These alloys have been used for structure materials in nuclear reactor systems that must maintain integrity over long period of time in harsh environment such as high temperature, high pressure and strong radiation. Nuclear power plants in the Republic of Korea utilize zirconium alloys for fuel cladding, pressure tube and calandria tube in both Pressurized Water Reactors (PWR) and CANada Deuterium Uranium reactors (CANDU). Therefore, a large amount of radioactive zirconium alloy waste is inevitably generated as results of nuclear power plant operation. Claddings of spent nuclear fuels constitute the largest portion of radioactive zirconium alloy wastes as about 16 wt. % of spent nuclear fuel assembly. In addition, the cladding separated from spent nuclear fuels is classified as an intermediate level waste in the latest radioactive waste

classification of International Atomic Energy Agency (IAEA) since non-negligible amount of long-living actinide elements and fission products could penetrate into fuel claddings during irradiation in nuclear reactor and long-living niobium-94 is produced by neutron activation (IAEA, 2009). If zirconium can be chemically separated from irradiated claddings, the final volume of radioactive waste in geological repositories can be greatly reduced and recovered zirconium can be recycled for reutilization in nuclear industry.

For this reason, limited but active investigation have been conducted in recent years to decontaminate spent nuclear fuel zirconium alloy cladding. Rudisill attempted to remove actinide elements and fission products by surface removal using hydrogen fluoride acid (Rudisill, 2009). However, since penetration depths of these elements at the concentration limit of the U.S. Class C level waste was as deep as 180 μm, the surface removal was ineffective. It is concluded that volumetric decontamination processes such as gaseous reaction methods or molten salt electrorefining techniques are required. Iodination and chlorination methods have been developed as a gaseous reaction method. While gaseous methods can separate zirconium with high purity there are some drawbacks. In iodination methods, concentration of moisture in the reaction chamber should be maintained very low since ZrI_4 is very hydroscopic. In addition, reduction of ZrI_4 into Zr metal would be very slow. In chlorination or Kroll process, large amount of Mg waste could be generated from the process to reduce $ZrCl_4$ into Zr metal.

Electrorefining in molten salts such as fluoride or chloride salt have been also developed as a volumetric decontamination process for zirconium cladding from spent nuclear fuels. Electrorefining using fluoride electrolytes such as LiF-KF has an advantage over chloride salts that dense zirconium metal with high purity could be recovered on cathode. However, the fluoride salts have high corrosivity to structural materials of electrorefiner at high (~700^{o}C) operating temperature. Chloride-fluoride mixed molten salts can

lower operating temperature to about 650°C but the corrosivity remains to be an issue. Since chloride-based molten salts has lower melting point and corrosivity, chloride based electrorefining would be preferred for commercial decontamination process with low operating temperature about 500°C. However, since redox behavior of zirconium in chloride salt is very complicated, cathode product would contain ZrCl with Zr metal in certain conditions and a disproportionate reaction producing Zr(II) from Zr(IV) and Zr metal can occur. If both ZrCl formation and disproportionate reaction of zirconium could be suppressed, chloride based electrorefining would be an attractive option for commercial spent nuclear fuel cladding decontamination processes.

It has been suggested that ZrCl formation can be retarded by introducing more stable salts such as CsCl and $SrCl_2$. Irradiated cladding contains Cs-137 and Sr-90 whose radioactivities are very high. If molten salts based on CsCl or $SrCl_2$ are used, theses radioisotopes could be diluted and this could result in volume increase of final disposed radioactive waste. Therefore, in this study, LiCl-KCl salt is selected as an electrolyte. In addition, target cladding material is selected as Zircaloy-4 cladding since Zircaloy-4 cladding is the first generation cladding used in the Republic of Korea from 1978 to 2001.

This study has been carried out in three stages. First, redox behavior of zirconium in LiCl-KCl salts has been investigated by lab-scale experiments. Second, three-dimensional computational electrochemo-hydrodynamic model has been developed to simulate actinide behavior in chloride salts and design a pilot-scale electrorefiner. Finally, based on lab-scale experiment and developed computational model, pilot-scale irradiated Zircaloy-4 eletrorefiner has been designed and performance of the electrorefiner has been verified.

In this dissertation, Zr redox behaviors in LiCl-KCl salts have been studied by cyclic voltammetries. It is identified that four oxidation peaks and

three reduction peaks would appear in cyclic voltammograms. Reduction or oxidation reactions for each peak were determined based on chemical form of cathode deposits after electrolysis and peak height changes according to scan rates and scan ranges. From cyclic voltammograms, it is shown that if cathode potential is more negative than -1.2 V (vs. Ag/AgCl), Zr(IV) ion could be reduced into ZrCl and ZrCl could be reduced again into Zr metal. If cathode potential is more negative than -1.5 V (vs. Ag/AgCl), Zr(IV) ion could be directly reduced into Zr metal. Zr(II) ion could be formed from Zr(IV) ion at near -1.0 V (vs. Ag/AgCl) but the reaction rate might be slow when the concentration of Zr(IV) ion is low. For oxidation reactions of Zr metal and ZrCl, it is identified that most of Zr metal and ZrCl would be directly oxidized into Zr(IV) without an intermediate step but if the concentration of Zr(IV) is high, Zr(II) could be produced from Zr metal and ZrCl. Since the reaction rate of ZrCl formation from Zr(IV) is dependent on Zr(IV) concentration while ZrCl reduction into Zr metal is not, net ZrCl formation rate could be reduced by lowering Zr(IV) concentration. In lab-scale experiment, redox behaviors of significant elements in irradiated Zicaloy-4 cladding (Sn, Cr, Fe and Co) were investigated in the same way of Zr and it is confirmed that these elements are much reductive than Zr and redox mechanisms are much simpler than Zr.

Lab-scale electrorefining has been conducted for unirradiated Zircaloy-4 specimen on the basis of investigated redox behaviors of Zr and other elements. Since all elements in Zircaloy-4 except Zr are more reductive than Zr, these elements could be deposited with Zr if they are dissolved from anode. To dissolve only zirconium from anode, anode potential was maintained more negative than -0.9 V (vs. Ag/AgCl). In addition, electrorefining was conducted in five different $ZrCl_4$ concentration (0.1, 0.5, 1.0, 2.0, 4.0 wt. %) and chemical form and composition of cathode deposit was investigated by X-ray diffraction (XRD) and inductively coupled plasma mass spectrometry (ICP-MS) respectively. For all cases of electrorefining,

only zirconium was detected in cathode deposits. As identified in cyclic voltammetry at low $ZrCl_4$ concentrations, 0.1 wt. % and 0.5 wt. %, respectively, Zr metal was recovered on cathode without ZrCl while ZrCl was recovered at high $ZrCl_4$ concentration, 2.0 wt. % and 4.0 wt. %, respectively.At the concentration of 1.0 wt. %, both Zr metal and ZrCl were recovered. In general, high $ZrCl_4$ concentration is preferred to secure high throughput of electrorefiner. Therefore, to recover Zr metal with high throughput, $ZrCl_4$ concentration of 0.5 wt. % would be recommendable.

A three-dimensional computational electrochemo-hydrodynamic model has been developed by combining fluid dynamic, electrostatic and electrochemical analysis based on a commercial fluid dynamic code, ANSYS-CFX©. Cathode deposition model in the developed computational model was verified by benchmarking overpotential distribution for copper deposition in rotating cylindrical Hull cell with cupric sulfate solution. Usefulness of anode dissolution model was investigated by benchmarking potential versus current data of Mark-IV electrorefiner which has been utilized for reprocessing spent fuels of Experimental Breeder Reactor-II. At the initial stage of electrorefining, computational modeling results accorded with experimental results but, as electrorefining progressed, calculated potential became very dependent on assumed effective anode surface area profiles. Therefore, the developed computational model could be utilized for modeling of cathode deposition or early stage of electrorefining.

To simulate zirconium redox behavior in chloride salts, it is required to secure material constants used for Butler-Volmer equation such as reaction rate constant and transfer coefficient because these material properties could greatly influence calculated currents and potentials. To determine proper material constants, several values were tested in conditions that are equivalent to lab-scale electrorefining experiments. In addition, multi-step electrochemical reaction model for zirconium in LiCl-KCl molten salt was

also introduced and verified by benchmarking on chemical forms of cathode deposits from lab-scale electroreifning experiments.

By applying the developed computational model benchmarked by using lab-scale experiments, a pilot-scale electrorefiner for recovery of zirconium from Zircaloy-4 cladding has been designed. In addition to three-dimensional computational modeling, one-dimensional preliminary modeling was conducted by using a one-dimensional time-dependent electrochemical reaction code, REFIN.

It is identified again that the dissolution of Sn, Cr, Fe and Co from fuel cladding can be prevented by controlling an anode potential. After electrorefining under the anodic potential, most of these elements would be remaining in the anode basket as unoxidized metals. On the other hand, actinides elements from fuel cladding will remain dissolved in the molten salts after electrorefining and they would not be deposited on the cathode and remained in the molten salts because actinide elements are more active than zirconium and other alloying elements.

The throughput of a pilot-scale electrorefiner for spent nuclear fuel Zircaloy-4 cladding designed by applying computer models is predicted to be about 0.1~0.2 ton/year at the $ZrCl_4$ concentration of 0.5 wt. %. It is expected that the throughput can be further increased by optimizing design parameters.

Keywords
Zr recycling
LiCl-KCl
Zr redox behavior
Anode potential control
3D computational model
Electrorefiner design

Student Number
2010-21032

Contents

Chapter 1 Introduction 1

1.1 Background 1

1.2 Radiological characteristics of irradiated cladding 4

1.3 Objective 13

Chapter 2 Literature Review 14

2.1 Surface decontamination process 14

2.2 Volumetric decontamination processes 18

2.2.1 Halogenation method 18

2.2.2 Electrorefining 24

Chapter 3 Research Design 43

3.1 Research questions and approaches 43

3.2 Molten salt electrochemical experiment 47

3.3 Computational electrorefining model development 49

3.4 Pilot-scale electrorefiner design 50

Chapter 4 Molten Salt Electrochemical Experiment 51

4.1 Redox behavior of Zr in LiCl-KCl 51

4.1.1 Experimental setup 51

4.1.2 Cyclic voltammetry results 59

4.1.3 Discussion 81

4.2 Redox behavior of Sn, Cr, Fe and Co in LiCl-KCl 93
4.2.1 Experimental setup 93
4.2.2 Cyclic voltammetry results 95
4.2.3 Discussion 115
4.3 Lab-scale electrorefining of unirradiated Zircaloy-4 specimen 122
4.3.1 Experimental setup 122
4.3.2 Electrorefining Results 127
4.3.3 Discussion 140
4.4 Suggestions on Zircaloy-4 electrorefining based on lab-scale experiment 145

Chapter 5 Computational Electrorefining Model Development 147

5.1 Hydrodynamic-electrochemical computational model 147
5.2 Surrogate aqueous electrodeposition system benchmark 150
5.2.1 Rotating Cylindrical Hull cell description 150
5.2.2 Mathematical model 153
5.2.3 RCH cell experiment 158
5.2.4 Results 161
5.2.5 Discussion 168
5.3 Molten salt electrorefining system benchmark 169
5.3.1 Selected experiment for simulation 169
5.3.2 Modeling strategy 174
5.3.3 Mathematical model 182
5.3.4 Results 190
5.3.5 Discussion 198
5.4 Zircaloy-4 electrorefining benchmark 204

5.4.1 Modeling strategy 204
5.4.2 Mathematical model 208
5.4.3 Results 215
5.4.4 Discussion 221

Chapter 6 Pilot-scale Electrorefiner Design 223

6.1 Preliminary Zircaloy-4 electrorefining modeling 223
6.1.1 Mathematical model 223
6.1.2 Modeling conditions and electrorefiner geometry 227
6.1.3 Results 236
6.1.4 Discussion 250
6.2 3-D Zircaloy-4 cladding electrorefiner design 255
6.2.1 Design concept and assumptions 257
6.2.2 Potential window for obtaining high purity Zr metal 259
6.2.3 Weights of molten salts 264
6.2.4 The number of anode basket 267
6.3 Verification of Zircaloy-4 cladding electrorefiner capability. 271
6.3.1 Effect of applied current and cathode rotating speed 271
6.3.2 Verified capabilities of electrorefiner 280

Chapter 7 Conclusions and Future Work.....283

7.1 Conclusions 283
7.2 Future Work 285

Bibliography.....289

초 록.....301

List of Tables

Table 1.1 Types of nuclear fuel claddings of pressurized water reactors in Republic of Korea 3

Table 1.2 Composition of Zircaloy-4 Cladding.....6

Table 1.3 Isotopic mass fraction of uranium and plutonium in PWR spent Zircaloy-4 hulls after 5 years cooling (Jung et al., 2006) 9

Table 1.4 Radioactivities of β- and γ-emitters that might exist in irradiated Zircaloy hulls after 5 years cooling (Restani et al., 1992) 10

Table 2.1 Comparison of decontamination processes for irradiated Zircaloy cladding 42

Table 4.1 Conditions and objectives of experiment sets conducted to investigate zirconium's electrochemical behavior in LiCl-KCl-$ZrCl_4$ at 500°C.....58

Table 4.2 Comparison of reaction definitions for CV peaks in LiCl-KCl-ZrCl4 in the literature. 82

Table 4.3 Comparison of diffusion coefficient of Zr(IV) in LiCl-KCl-$ZrCl_4$ at 500°C in the literature (using cyclic voltammograms for scan range from 0.0 to -1.2 and -1.6 V; see Figure 4, 6 respectively).....91

Table 4.4 Experiment sets for cyclic voltammogram of Sn, Cr, Fe and Co in LiCl-KCl salts at 500°C 94

Table 4.5 Diffusion coefficients of Sn(II), Cr(II), Fe(II) and Co(II) in LiCl-KCl at 500^{o}C 120

Table 4.6 Formal potential of Sn(II), Cr(II), Fe(II) and Co(II) in LiCl-KCl at 500^{o}C..... 121

Table 4.7 Formal reduction potentials on major reactions which could occur during Zircaloy-4 electrorefining 126

Table 4.8 Comparison of compositions of cathode deposits after Zircaloy-4 electrorefining to previous study 128

Table 5.1 Operating condition and thermodynamic data. 184

Table 5.2 Material properties used in the computational Zr multi-step reduction modeling 207

Table 5.3 Computational modeling results on weight percent of Zr metal in cathode deposits according to rate constant of Zr formation reaction..... 216

Table 6.1 Simplified weight fraction of irradiated PWR Zircaloy-4 cladding for electrochemical simulation; it is used as the composition of anode in electrorefining simulation 229

Table 6.2 Ion properties used in electrorefining simulation..... 230

Table 6.3 Molten salts composition used in spent Zircaloy-4 cladding electrorefining simulation..... 233

Table 6.4 Rotating speed of cathode equivalent to diffusion boundary layer thickness used in the simulation: Eisenberg equation is used for the relationship between diffusion boundary layer

thickness and rotating speed.....252

Table 6.5 Final design of the pilot-scale electrorefiner for irradiated spent nuclear fuel Zircaloy-4 cladding.....256

Table 6.6 Two operating conditions of the designed electrorefiner for irradiated spent nuclear fuel Zircaloy-4 cladding.....281

List of Figures

Figure 1.1 Ratio of actual radioactivity to IAEA clearance level with cooling time: PWR irradiated Zircaloy-4 cladding for 3 years (rule of sum does apply for the criteria) 7

Figure 1.2 Comparison of radioactivities of radoisotopes in irradiated Zircaloy-4 cladding to IAEA radioactive waste classification: HLW (High Level Waste), ILW (Intermediate Level Waste), LLW (Low Level Waste), VLLW (Very Low Level Waste), VSLW (Very Short-Lived Waste) and EW (Exempt Waste) ...12

Figure 2.1 Fission product concentration in Zircaloy cladding (Rudisill, 2009) 16

Figure 2.2 Transuranic elements concentration in Zircaloy cladding (Rudisill, 2009) 17

Figure 2.3 Schematic flow diagram for iodination process to decontaminate spent nuclear fuel cladding 20

Figure 2.4 Schematic flow diagram for Hydrochlorination process to decontaminate spent nuclear fuel cladding 23

Figure 2.5 Schematic diagram of the experimental apparatus for Zr scrap electrorefining in fluoride salts (Park et al., 2013) 25

Figure 2.6 X-ray diffraction patterns results for Zr deposits after electrorefining with applied currents of (a) 4, (b) 2, (c) 1 and (d) 0.5 A (Park et al., 2013).....26

Figure 2.7 Electrochemical cell for zirconium electrorefining in CsCl

based molten salts (Kipouros and Flengas, 1985) 28

Figure 2.8 Large platelike deposits after electrorefining in NaF-LiF salts (Kipouros and Flengas, 1985).....29

Figure 2.9 Schematic experimental apparatus used for electrorefining in LiCl-KCl-LiF (Fujita et al., 2005a).....31

Figure 2.10 The results of two step electrorefining in LiCl-KCl-LiF...32

Figure 2.11 Electrochemical cell for zirconium electrorefining in CsCl based molten salts (Kipouros and Flengas, 1985) 35

Figure 2.12 Cathode deposits after electrorefining in CsCl-KF-Cs_2ZrCl_6 (Kipouros and Flengas, 1985) 36

Figure 2.13 X-ray diffraction patterns of Zr compounds deposited at cathode potentials of (upper) -1.15 and (below) -1.55 V (vs. Ag/AgCl) in LiCl-KCl (Lee et al., 2012).....38

Figure 2.14 X-ray diffraction patterns of zirconium compound deposited at cathode potentials of (upper) -1.15~-1.04 and (below) -1.42~-1.35 V (vs. Ag/AgCl) (Sakamura, 2004) 40

Figure 3.1 Correlation between each section of dissertation.....46

Figure 3.2 Potential redox reactions that could occur in LiCl-KCl salts 48

Figure 4.1 Glove box for maintaining inert atmosphere during molten salt experiment.....53

Figure 4.2 Electrochemical cell for CV with LiCl-KCl salts 54

Figure 4.3 Potentiostat and PID heater controller 55

Figure 4.4 Background cyclic voltammogram on 500°C LiCl-KCl without any salts with scan rate of 300 mV/s: tungsten electrode (1Φ x 20 mm) for both working and counter electrodes, 1 wt. % Ag/AgCl for reference electrode 61

Figure 4.5 Cyclic voltammograms with the major reaction which could mainly contribute to each peak according to scan range for the scan rate of 300 mV/s in 500°C LiCl-KCl-$ZrCl_4$(1 wt. %): tungsten electrode (1Φ x 20 mm) for both working and counter electrodes, 1wt. % Ag/AgCl reference electrode.....63

Figure 4.6 Cyclic voltammograms according to scan rate for the scan range from 0 to -1.2V (vs. 1 wt. % Ag/AgCl) in 500°C LiCl-KCl-$ZrCl_4$(1 wt. %): tungsten electrode (1Φ x 20 mm) for both working and counter electrodes, 1wt. % Ag/AgCl reference electrode 65

Figure 4.7 Cyclic voltammograms according to scan rate for the scan range from 0 to -1.1V (vs. 1 wt. % Ag/AgCl) in 500oC LiCl-KCl-$ZrCl_4$(1 wt. %): tungsten electrode (1Φ x 20 mm) for both working and counter electrodes, 1wt. % Ag/AgCl reference electrode 67

Figure 4.8 Cyclic voltammograms according to scan rate for the scan range from 0 to -1.6V (vs. 1 wt. % Ag/AgCl) in 500°C LiCl-KCl-$ZrCl_4$(1 wt. %): tungsten electrode (1Φ x 20 mm) for both working and counter electrodes, 1wt. % Ag/AgCl reference electrode 69

Figure 4.9 Cyclic voltammograms according to scan range for the scan rate of 500 mV/s in 500°C LiCl-KCl-$ZrCl_4$(1 wt. %): tungsten electrode (1Φ x 20 mm) for both working and counter electrodes, 1wt. % Ag/AgCl reference electrode.....71

Figure 4.10 Cyclic voltammograms according to scan rate for the scan range from 0 to -1.3V (vs. 1 wt. % Ag/AgCl) in 500°C LiCl-KCl-$ZrCl_4$(0.5 wt. %): tungsten electrode (1Φ x 20 mm) for both working and counter electrodes, 1wt. % Ag/AgCl reference electrode.....73

Figure 4.11 Cyclic voltammograms according to scan rate for the scan range from 0 to -1.3V (vs. 1 wt. % Ag/AgCl) in 500°C LiCl-KCl-$ZrCl_4$(1.0 wt. %): tungsten electrode (1Φ x 20 mm) for both working and counter electrodes, 1wt. % Ag/AgCl reference electrode.....74

Figure 4.12 Cyclic voltammograms according to scan rate for the scan range from 0 to -1.3V (vs. 1 wt. % Ag/AgCl) in 500°C LiCl-KCl-$ZrCl_4$(2.0 wt. %): tungsten electrode (1Φ x 20 mm) for both working and counter electrodes, 1wt. % Ag/AgCl reference electrode.....75

Figure 4.13 Cyclic voltammograms according to scan rate for the scan range from 0 to -1.3V (vs. 1 wt. % Ag/AgCl) in 500°C LiCl-KCl-$ZrCl_4$(4.0 wt. %): tungsten electrode (1Φ x 20 mm) for

both working and counter electrodes, 1wt. % Ag/AgCl reference electrode 76

Figure 4.14 Cyclic voltammograms according to scan rate for the scan range from 0 to -1.3V (vs. 1 wt. % Ag/AgCl) in 500°C LiCl-KCl-$ZrCl_4$(8.0 wt. %): tungsten electrode (1Φ x 20 mm) for both working and counter electrodes, 1wt. % Ag/AgCl reference electrode 77

Figure 4.15 Cyclic voltammograms according to concentration of LiCl-KCl-$ZrCl_4$ for the scan rate of 300 mV/s: tungsten electrode (1Φ x 20 mm) for both working and counter electrodes, 1wt. % Ag/AgCl reference electrode 78

Figure 4.16 Peak potential changes according to scan rate and scan range (using cyclic voltammograms for scan range from 0.0 to -1.1, -1.2 and -1.6 V; see Figure 4.7, Figure 4.6 and Figure 4.8 respectively).....80

Figure 4.17 Cyclic voltammograms according to scan rate for the scan range from 0.5 to -1.0 V (vs. 1 wt. % Ag/AgCl) in 500°C LiCl-KCl-$SnCl_2$(0.1 wt. %): tungsten electrode (1Φ x 20 mm) for both working and counter electrodes, 1wt. % Ag/AgCl reference electrode 96

Figure 4.18 Cyclic voltammograms according to scan rate for the scan range from 0.5 to -1.0 V (vs. 1 wt. % Ag/AgCl) in 500°C LiCl-KCl-$SnCl_2$(0.2 wt. %): tungsten electrode (1Φ x 20 mm) for

both working and counter electrodes, 1 wt. % Ag/AgCl reference electrode 97

Figure 4.19 Cyclic voltammograms according to scan rate for the scan range from 0.5 to -1.0 V (vs. 1 wt. % Ag/AgCl) in 500°C LiCl-KCl-$SnCl_2$(0.5 wt. %): tungsten electrode (1Φ x 20 mm) for both working and counter electrodes, 1 wt. % Ag/AgCl reference electrode 98

Figure 4.20 Cyclic voltammograms according to scan rate for the scan range from 0.5 to -1.0 V (vs. 1 wt. % Ag/AgCl) in 500°C LiCl-KCl-$SnCl_2$(1.0 wt. %): tungsten electrode (1Φ x 20 mm) for both working and counter electrodes, 1 wt. % Ag/AgCl reference electrode 99

Figure 4.21 Cyclic voltammograms according to scan rate for the scan range from 0.6 to -1.3 V (vs. 1 wt. % Ag/AgCl) in 500°C LiCl-KCl-$CrCl_2$(0.1 wt. %): tungsten electrode (1Φ x 20 mm) for both working and counter electrodes, 1 wt. % Ag/AgCl reference electrode 101

Figure 4.22 Cyclic voltammograms according to scan rate for the scan range from 0.6 to -1.3 V (vs. 1 wt. % Ag/AgCl) in 500°C LiCl-KCl-$CrCl_2$(0.2 wt. %): tungsten electrode (1Φ x 20 mm) for both working and counter electrodes, 1 wt. % Ag/AgCl reference electrode 102

Figure 4.23 Cyclic voltammograms according to scan rate for the scan

range from 0.6 to -1.3 V (vs. 1 wt. % Ag/AgCl) in 500°C LiCl-KCl-$CrCl_2$(0.5 wt. %): tungsten electrode (1Φ x 20 mm) for both working and counter electrodes, 1 wt. % Ag/AgCl reference electrode 103

Figure 4.24 Cyclic voltammograms according to scan rate for the scan range from 0.6 to -1.3 V (vs. 1 wt. % Ag/AgCl) in 500°C LiCl-KCl-$CrCl_2$(1.0 wt. %): tungsten electrode (1Φ x 20 mm) for both working and counter electrodes, 1 wt. % Ag/AgCl reference electrode 104

Figure 4.25 Cyclic voltammograms according to scan rate for the scan range from 0.6 to -1.0 V (vs. 1 wt. % Ag/AgCl) in 500°C LiCl-KCl-$FeCl_2$(0.1 wt. %): tungsten electrode (1Φ x 20 mm) for both working and counter electrodes, 1 wt. % Ag/AgCl reference electrode 106

Figure 4.26 Cyclic voltammograms according to scan rate for the scan range from 0.6 to -1.0 V (vs. 1 wt. % Ag/AgCl) in 500°C LiCl-KCl-$FeCl_2$(0.2 wt. %): tungsten electrode (1Φ x 20 mm) for both working and counter electrodes, 1 wt. % Ag/AgCl reference electrode 107

Figure 4.27 Cyclic voltammograms according to scan rate for the scan range from 0.6 to -1.0 V (vs. 1 wt. % Ag/AgCl) in 500°C LiCl-KCl-$FeCl_2$(0.5 wt. %): tungsten electrode (1Φ x 20 mm) for

both working and counter electrodes, 1 wt. % Ag/AgCl reference electrode 108

Figure 4.28 Cyclic voltammograms according to scan rate for the scan range from 0.6 to -1.0 V (vs. 1 wt. % Ag/AgCl) in 500°C LiCl-KCl-$FeCl_2$(1.0 wt. %): tungsten electrode (1Φ x 20 mm) for both working and counter electrodes, 1 wt. % Ag/AgCl reference electrode 109

Figure 4.29 Cyclic voltammograms according to scan rate for the scan range from 0.5 to -0.5 V (vs. 1 wt. % Ag/AgCl) in 500°C LiCl-KCl-$CoCl_2$(0.1 wt. %): tungsten electrode (1Φ x 20 mm) for both working and counter electrodes, 1 wt. % Ag/AgCl reference electrode 111

Figure 4.30 Cyclic voltammograms according to scan rate for the scan range from 0.5 to -0.5 V (vs. 1 wt. % Ag/AgCl) in 500°C LiCl-KCl-$CoCl_2$(0.5 wt. %): tungsten electrode (1Φ x 20 mm) for both working and counter electrodes, 1 wt. % Ag/AgCl reference electrode 112

Figure 4.31 Cyclic voltammograms according to scan rate for the scan range from 0.5 to -0.5 V (vs. 1 wt. % Ag/AgCl) in 500°C LiCl-KCl-$CoCl_2$(1.0 wt%): tungsten electrode (1Φ x 20 mm) for both working and counter electrodes, 1 wt. % Ag/AgCl reference electrode 113

Figure 4.32 Cyclic voltammograms according to scan rate for the scan

range from 0.5 to -0.5 V (vs. 1 wt. % Ag/AgCl) in 500°C LiCl-KCl-$CoCl_2$(2.0 wt. %): tungsten electrode (1Φ x 20 mm) for both working and counter electrodes, 1 wt. % Ag/AgCl reference electrode 114

Figure 4.33 Configuration of lab-scale Zircaloy-4 electrorefining cell 123

Figure 4.34 Zircaloy-4 cuts for lab-scale electrorefining experiment 124

Figure 4.35 Picture (left) and XRD results (right) of cathode deposits after electrorefining in LiCl-KCl-$ZrCl_4$(0.1 wt. %): unnamed XRD peaks are resulting from LiCl-KCl-$ZrCl_4$..... 130

Figure 4.36 Picture (left) and XRD results (right) of cathode deposits after electrorefining in LiCl-KCl-$ZrCl_4$(0.5 wt. %): unnamed XRD peaks are resulting from LiCl-KCl-$ZrCl_4$..... 131

Figure 4.37 Picture (left) and XRD results (right) of cathode deposits after electrorefining in LiCl-KCl-$ZrCl_4$(1.0 wt. %): unnamed XRD peaks are resulting from LiCl-KCl-$ZrCl_4$..... 132

Figure 4.38 Picture (left) and XRD results (right) of cathode deposits after electrorefining in LiCl-KCl-$ZrCl_4$(2.0 wt. %): unnamed XRD peaks are resulting from LiCl-KCl-$ZrCl_4$..... 133

Figure 4.39 Picture (left) and XRD results (right) of cathode deposits after electrorefining in LiCl-KCl-$ZrCl_4$(4.0 wt. %): unnamed XRD peaks are resulting from LiCl-KCl-$ZrCl_4$..... 134

Figure.4.40 Picture (left) and XRD results (right) of molten salts after

electrorefining in LiCl-KCl-$ZrCl_4$(0.1 wt. %): XRD was conducted for the bottom of molten salts including black powders and unnamed XRD peaks are resulting from LiCl-KCl-$ZrCl_4$ 136

Figure 4.41 Picture (left) and XRD results (right) of molten salts after electrorefining in LiCl-KCl-$ZrCl_4$(0.1 wt. %): XRD was conducted for the bottom of molten salts including black powders and unnamed XRD peaks are resulting from LiCl-KCl-$ZrCl_4$ 137

Figure 4.42 Picture (left) and XRD results (right) of molten salts after electrorefining in LiCl-KCl-$ZrCl_4$(0.1 wt. %): XRD was conducted for the bottom of molten salts including black powders and unnamed XRD peaks are resulting from LiCl-KCl-$ZrCl_4$ 138

Figure 4.43 Pictures of molten salts after electrorefining in (left) LiCl-KCl-$ZrCl_4$(2.0 wt. %) and (right) LiCl-KCl-ZrCl4 (1.0 wt. %) 139

Figure 5.1 Flow chart of Hydrodynamic-electrochemical simulation algorithm 149

Figure 5.2 Sectional view of the rotating cylinder Hull cell design ... 152

Figure 5.3 Unstructured mesh configurations 157

Figure 5.4 The RotaHull® cell (left) and the modified RCH cell used in the experimental work (right) 160

Figure 5.5 Comparison of calculated primary current distributions

along the working electrode among the 3D computational model, Madore's empirical equation and a Modified Madore empirical equation.....164

Figure 5.6 Comparison of calculated primary current distributions along the working electrode between experiment and computational model.....166

Figure 5.7 Experimentally measured potential at x=3.5 cm with applied current density of 100 A/m^2.....167

Figure 5.8 Schematic view of the Mark-IV electrorefiner (two anodes were used for this study). 170

Figure 5.9 Applied current and transferred charges during 80 hours electrorefining with cathode change after 39 hours operation 173

Figure 5.10 Five anode surface area cases and cathode surface area for comparative modeling of the Mark-IV electrorefiner.....176

Figure 5.11 Current density variation of five anode surface area cases and cathode for comparative modeling of the Mark-IV electrorefiner. 181

Figure 5.12 Calculated anodic current density in proportional to material dissolution from fuel segments into molten salt electrolyte during 80 hours electrorefining (at the initial stage, Na was dissolved from and uranium was deposited to anode thermodynamically) 192

Figure 5.13 Early stage distribution of uranium concentration along

with straight line from anode to cathode at middle height. ...194

Figure 5.14 Comparison of cell potential between the experimental result and the calculated potentials based on five anode area cases 196

Figure 5.15 Root mean square deviation for 3-D analysis results from experimental molten-salt electrorefining data 197

Figure 5.16 Current densities resulting from Zr metal and ZrCl formation according to applied potential with arbitrary diffusion boundary layer 212

Figure 5.17 Lab-scale Zircaloy-4 electrorefining cell (left) geometry and (right) mesh grid generated for Zr multi-step reaction modeling 214

Figure 5.18 Computational results on mass production rate of (left) ZrCl and (middle) Zr on the cathode in LiCl-KCl-$ZrCl_4$ (0.5 wt. %) and (right) XRD patterns of cathode deposits after electrorefining in the same salts 218

Figure 5.19 Computational results on mass production rate of (left) ZrCl and (middle) Zr on the cathode in LiCl-KCl-$ZrCl_4$ (1.0 wt. %) and (right) XRD patterns of cathode deposits after electrorefining in the same salts 219

Figure 5.20 Computational results on mass production rate of (left) ZrCl and (middle) Zr on the cathode in LiCl-KCl-$ZrCl_4$ (2.0 wt. %) and (right) XRD patterns of cathode deposits after electrorefining in the same salts 220

Figure 6.1 Schematic geometry utilized for the zirconium electrorefining simulation: the anode has 1 cm diameter and 4 cm height and the cathode has 0.5 cm diameter and 4 cm height.....235

Figure 6.2 Deposition behavior on cathode during electrorefining of irradiated PWR Zircaloy-4 cladding: diffusion boundary layer thickness of 0.1 cm and impurity fraction of 1 $x10^{-4}$ in molten salt.....238

Figure 6.3 Ion concentration change in molten salt during electrorefining of irradiated PWR Zircaloy-4 cladding: diffusion boundary layer thickness of 0.1 cm and impurity fraction of 1 $x10^{-4}$ in molten salt.....239

Figure 6.4 Dissolution behavior on anode during electrorefining of irradiated PWR Zircaloy-4 cladding: diffusion boundary layer thickness of 0.1 cm and impurity fraction of 1 $x10^{-4}$ in molten salt.....240

Figure 6.5 Anode potential behavior at the end stage of electrorefining of irradiated PWR Zircaloy-4 cladding: diffusion boundary layer thickness of 0.1 cm and impurity fraction of 1 $x10^{-4}$ in molten salt.....243

Figure 6.6 Decontamination factors for Co according to diffusion boundary layer thickness and initial contamination in molten salt; the electrorefining is terminated at -2.1 V (vs. Cl_2/Cl^-) of anode potential.....246

Figure 6.7 Decontamination factors for Co according to diffusion boundary layer thickness and initial contamination in molten salt; the electrorefining is terminated at -1.8 V (vs. Cl_2/Cl^-) of anode potential. 247

Figure 6.8 Decontamination factors for Co according to diffusion boundary layer thickness and initial contamination in molten salt; the electrorefining is terminated at -1.5 V (vs. Cl_2/Cl^-) of anode potential. 248

Figure 6.9 Comparison of decontamination factors according to electrorefining termination condition; the diffusion boundary layer thickness is 0.01 cm.....249

Figure 6.10 Mass production rates of Zr metal, ZrCl and U according to applied potential at an arbitrary diffusion boundary layer thickness 263

Figure 6.11 Changes of potential range to recover Zr metal without U according to weight of LiCl-KCl molten salts and diffusion boundary layer thickness 266

Figure 6.12 Local cathode potential distributions in the circumferential direction at the mid height of the cathode according to the number of anode baskets; applied current of 50 A and rotating speed of cathode of 100 rpm 268

Figure 6.13 Local mass production rate distributions over cathode of Zr for cases of (a) one anode basket and (b) three anode baskets and those of U for cases of (c) one anode basket and (d) three

anode baskets; applied current of 52 A and rotating speed of cathode of 100 rpm 270

Figure 6.14 Mass production rate of ZrCl, Zr and U according to applied current: rotating speed of cathode is 100 rpm 273

Figure 6.15 Mass production rate of ZrCl, Zr and U according to applied current: rotating speed of cathode is 75 rpm 274

Figure 6.16 Mass production rate of ZrCl, Zr and U according to applied current: rotating speed of cathode is 50 rpm 275

Figure 6.17 Mass production rate of ZrCl, Zr and U according to applied current: rotating speed of cathode is 25 rpm 276

Figure 6.18 Local mass production rate distributions of ZrCl, Zr and U according to applied current density at cathode rotating speed of 100 rpm 279

Chapter 1 Introduction

1.1 Background[1]

Zirconium has very low thermal neutron absorption cross section of thermal neutrons, high hardness, acceptable ductility, and excellent corrosion resistance. In addition, its mechanical integrity and corrosion resistance could be further improved by Sn, Nb, Fe, Cr, Ni and other alloying elements (Sabol and Moan, 2000). For this reason, zirconium alloys have been used for structure materials in nuclear reactors having harsh environment such as high temperature, high pressure and strong radiation. Most of fuel cladding for thermal neutron nuclear reactors including pressurized water reactor (PWR), CANada Deuterium Uranium reactor (CANDU) and boiling water reactor (BWR). In addition, zirconium alloys have been used for pressure tubes and calandria tubes for CANDU reactors and channel boxes for BWRs (Vesterlund et al., 1980; Ibrahim and Cheadle, 1985). Therefore, generation of large amount of radioactive zirconium alloy waste is inevitable during nuclear power plant operation. Even in future nuclear reactor system, radioactive zirconium waste would not be unavoidable because zirconium would be utilized as a fuel constituent of metallic fuel for fast reactor (Pahl et

[1] This section has been written based on the following journal paper: Jaeyeong Park et. al., "Effect of operating conditions on molten-salt electrorefining for zirconium re covery from irradiated Zircaloy-4 cladding of pressurized water reactor," Nuclear Enginee ring and Design 275, 44-52, 2014.

al., 1990; Hofman et al., 1997; Kim et al., 2006). Among zirconium alloys in the current nuclear reactor system, Zircaloy spent nuclear fuel cladding makes up the greatest part of radioactive waste and its radioactivity would be the highest because of transuranic elements and fission products penetrating into fuel cladding during irradiation in nuclear reactor.

In the Republic of Korea (ROK), spent nuclear fuel of 750 metric tons are generated in every year and Zircaloy cladding makes up 25 weight percent and 40 volume percent of spent nuclear fuel (Collins et al., 2012). Because of extremely high population density in the ROK and public opposition to direct disposal of high level waste, the ROK would be likely to select a policy recycling spent nuclear fuel. If the policy is adopted, a lot of disintegrated fuel claddings would be generated. When it is assumed that 99.9% uranium in spent nuclear fuel is recovered, the remains of about 86 volume percent would be Zircaloy. If zirconium could be recovered from the remains, final waste would be greatly diminished.

Two types of zirconium alloy cladding have been utilized and several types of claddings are being developed in the ROK as represented in Table 1.1 (Jeong et al., 2006; Song et al., 2008). Since Zircaloy-4 cladding which is the first generation cladding would be firstly generated from spent nuclear fuel recycling process, this dissertation focuses on decontaminating Zircaloy-4 cladding.

Table 1.1 Types of nuclear fuel claddings of pressurized water reactors in Republic of Korea

		Zircaloy-4	Zirlo	HANA4	HANA6
Commercial adoption time		1978~	2001~	Under performance test	
Composition of major elements [wt. %]	Zr	Balanced			
	Sn	1.5	1.0	0.4	-
	Cr	0.1	-	-	-
	Fe	0.2	0.1	0.2	-
	Nb	-	1.0	1.5	1
	Cu	-	-	0.1	0.05
	Mn	-	-	-	-

1.2 Radiological characteristics of irradiated cladding[2]

In irradiated spent nuclear fuel Zircaloy-4 claddings, there could be a lot of radioisotopes and they could be classified into three types: activation products, actinides and fission products. Activation products are radioisotopes produced by neutron absorption of Zircaloy-4 constituent elements. Zr-93 which could be generated by neutron absorption of Zr-92 is an example of activation products in irradiated Zircaloy-4 cladding. Actinides such as U and Pu and fission products such as Sr and Cs could exist in irradiated cladding by penetrating into the cladding with high kinetic energy produced by a nuclear fission reaction during reactor operation.

To investigate radioactivity from activation products in irradiated Zircaloy-4 cladding, a one-group point depletion code, ORIGEN-2, was utilized. It was assumed that fresh Zircaloy-4 tubes were irradiated in the average neutron flux (4.5×10^{13} n/cm^2/s) of typical PWRs for 3 years (Sabol and Bradley, 1996).

As shown in Table 1.2, Zircaloy-4 cladding consists of major elements including Zr, Sn, Fe, and Cr as well as several impurities such as Co, Mn, and Ni. A number of activation products are produced during in-core neutron irradiation. In ORIGEN-2 calculations, it is assumed that zirconium cladding is irradiated for 3 years with average neutron flux in

[2] This section has been written based on the following journal paper: Jaeyeong Park et. al., "Effect of operating conditions on molten-salt electrorefining for zirconium re covery from irradiated Zircaloy-4 cladding of pressurized water reactor," Nuclear Enginee ring and Design 275, 44-52, 2014.

PWRs, 4.5×10^{13} n/cm^2/s. Figure 1.1 shows how radioactivity of each isotope in irradiated Zircaloy-4 cladding varies after it is discharged from PWRs. The radioactivity of many activations products exceeds International Atomic Energy Agency (IAEA) clearance level (IAEA, 1996). Co-60, Sb-125, Zr-93 and Nb-93M are elements that result in this difference. Zr-93 decayed to Nb-93M by emitting beta ray; Co impurities in Zr cladding generate Co-60.

Table 1.2 Composition of Zircaloy-4 Cladding

Elements[a]	Weight fraction
Zr	9.809E-01
Sn	1.500E -02
Fe	2.100E -03
Cr	1.000E -03
Al	7.500E-05
B	5.000E-06
C	2.700E-04
Co	2.000E-05
Cu	5.000E-05
Hf	2.000E-04
Mn	5.000E-05
Ni	7.000E-05
Si	1.200E-04
Ti	5.000E-05
W	1.000E-04

[a] Zr, Sn, Fe, and Cr are major elements; others are impurities. Material composition of fresh Zircaloy-4 is adopted from (Ahmad et al., 2003).

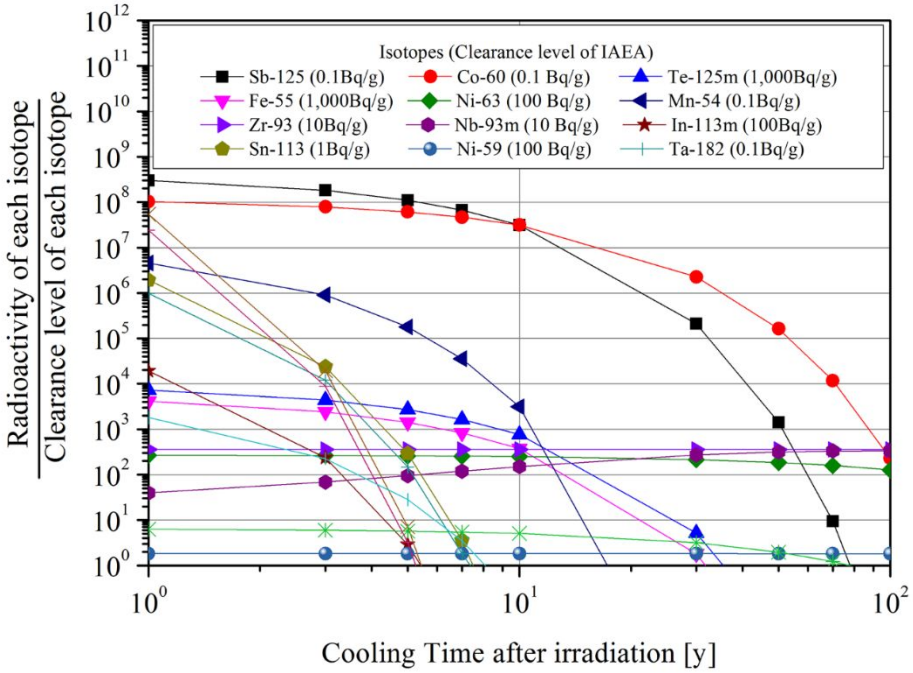

Figure 1.1 Ratio of actual radioactivity to IAEA clearance level with cooling time: PWR irradiated Zircaloy-4 cladding for 3 years (rule of sum does apply for the criteria)

In addition to activation products, irradiated Zircaloy-4 cladding contains actinides and fission products that penetrate into the zirconium oxide layer on the surface. About 99.5% of alpha-emitting actinides exist within 5 μm; the rest of actinides remain at deeper than 20 μm. There is a rapid decrease of actinide concentration between 5 and 15 μm (Restani et al., 1992). Sometimes, a very small amount of TRUs could penetrate into Zircaloy cladding even deeper than 180 μm (Rudisill, 2009). Table 1.3 shows isotope composition of uranium and plutonium in PWR spent Zircaloy-4 hulls after 5 years cooling. One kilogram of irradiated Zircaloy-4 cladding contains 1,132 mg of uranium and 13.6 mg of plutonium (Jung et al., 2006). Since fission products are much lighter than actinides, fission products could penetrate into Zircaloy-4 cladding deeper and be distributed wider (Rudisill, 2009). Restani reported that there would be some β- and γ-emitters such as Sr-90 and Cs-137 as represented in Table 1.4. I. H. Jung classified Cs-137, Ru-106, Cs-134, Ce-144 and Eu-154 as fission products (Jung et al., 2006).

Table 1.3 Isotopic mass fraction of uranium and plutonium in PWR spent Zircaloy-4 hulls after 5 years cooling (Jung et al., 2006)

U isotopes	Mass fraction	Pu isotopes	Mass fraction
U-234	0.0002	Pu-238	0.0133
U-235	0.0119	Pu-239	0.6101
U-236	0.0038	Pu-240	0.2312
U-238	0.9841	Pu-241	0.1008
		Pu-242	0.0446

Table 1.4 Radioactivities of β- and γ-emitters that might exist in irradiated Zircaloy hulls after 5 years cooling (Restani et al., 1992)

Radioisotope	Radioactivity [mCi/kg-Zry]
Mn-54	3.4
Co-60	64
Sr-90	370
Ru-106	458
Sb-125	760
Cs-134	162
Cs-137	542
Ce-144	70
Eu-154	21

Because of penetrated transuranic elements (TRU), irradiated Zircaloy-4 cladding is classified as Intermediate Level Waste (ILW) of IAEA radioactive waste classification as represented in Figure 1.2 (IAEA, 2009) . Most of fission products and activation products are classified as Low Level Waste (LLW) criteria after 5~10 years cooling but most of them could be Exempt Waste (EW) after 30~100 years cooling depending on half-life. For this reason, the first element group that should be decontaminated from irradiated Zircaloy-4 cladding might be TRU in the aspect of radioactive waste management. Fission products and activation products might be less significant than TRU for radioactive waste management but they should be removed as much as possible to recycle zirconium.

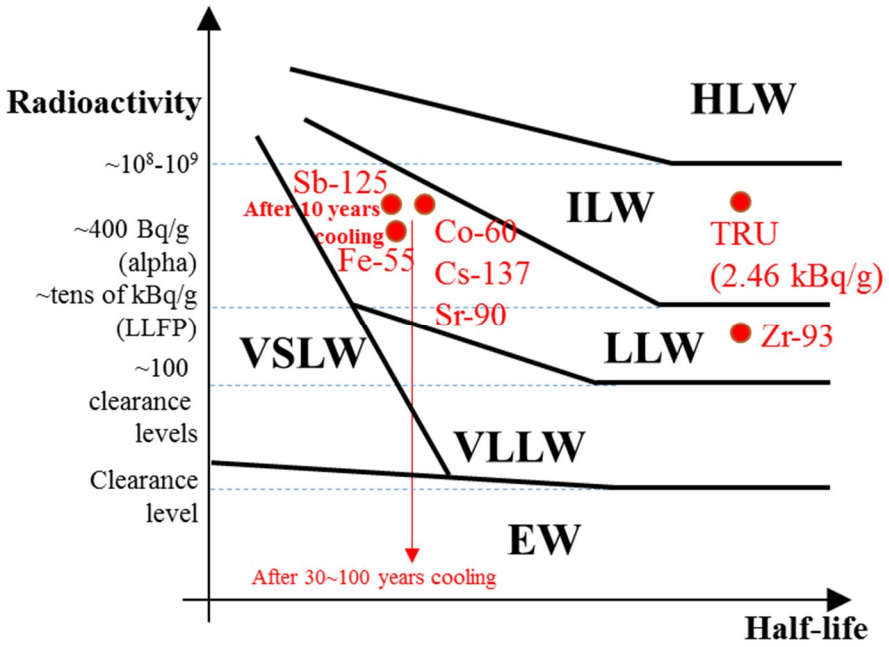

Figure 1.2 Comparison of radioactivities of radoisotopes in irradiated Zircaloy-4 cladding to IAEA radioactive waste classification: HLW (High Level Waste), ILW (Intermediate Level Waste), LLW (Low Level Waste), VLLW (Very Low Level Waste), VSLW (Very Short-Lived Waste) and EW (Exempt Waste)

1.3 Objective

The main objective of this dissertation is to develop a decontamination process for irradiated spent nuclear fuel Zircaloy-4 cladding based on electrorefiining in LiCl-KCl. To achieve the main objective, three specific objectives are established. Zirconium redox reactions among various oxidation states are very intricate and are not clarified yet. If disproportionate reaction and formation of ZrCl are not be suppressed, performance of electrorefining would be inferior. Therefore, one of specific objectives is determining Zr redox mechanism in LiCl-KCl and carrying out electrorefining based on revealed redox behavior. To investigate the feasibility of scaling up the electrorefining process verified in lab-scale experiment with less time-consuming and expensive experimental work, 3-D computational model would be utilized effectively. For this reason, another specific objective is development of 3-D computational electrorefining model that can handle both fluid dynamics and electrochemical reactions. Final specific objective is design and performance verification of pilot-scale electrorefiner for irradiated spent nuclear fuel Zicaloy-4 cladding based on lab-scale experiment and the developed computational model.

Chapter 2 Literature Review

Decontamination processes for irradiated Zirclaoy cladding has been developed in two streams: surface decontamination process and volumetric decontamination process.

2.1 Surface decontamination process

Actinides and fission products could penetrate into Zircaloy cladding during irradiation in a nuclear reactor. Since their kinetic energy obtained from nuclear fission is attenuated as penetration depth increases, it could be expected that most of penetrated actinides and fission products are located in short range near the surface of Zircaloy cladding. Paying attention to this point, T. S. Rudisill tried to decontaminate irradiated Zircaloy cladding by using concentrated hydrofluoric acid (HF) to remove cladding surface (Rudisill, 2009). He used claddings discharged from Big Rock Point nuclear reactor which was located in Michigan, U.S. Sample claddings were put into concentrated HF at 115^{o}C and radiochemical analysis were conducted to investigate concentration of actinides and fission products in the decontaminated cladding.

Radioactivity of Co-60 in Zircaloy cladding was lower than the limit of Class A LLW which is an waste classification of United States and radioactivities of Sr-90 and Cs-137 satisfied the criteria of Class C LLW. In

some experiment, radioactivities of Sr-90 and Cs-137 were met the Class B LLW critiera. However, concentrations of fission products were rarely changed even though surface removal depth was deeper than 100 μm as represented in Figure 2.1. Therefore, in the aspect of decontaminating fission products from irradiated Zircaloy cladding, surface removal might not be a proper decontamination process.

Since atomic masses of TRU elements are much larger than those of fission products, penetration depths would be much shorter. For this reason, sum of the concentration of Pu-238, Pu-239, Pu-240 and Am-241 was diminished dramatically as surface removal depth increased. However, the concentration was still higher than the limit of TRU Class C level waste after surface removal of 180 μm as represented in Figure 2.2. Therefore, surface removal might not be a proper process for TRU elements decontamination likewise with fission product decontamination.

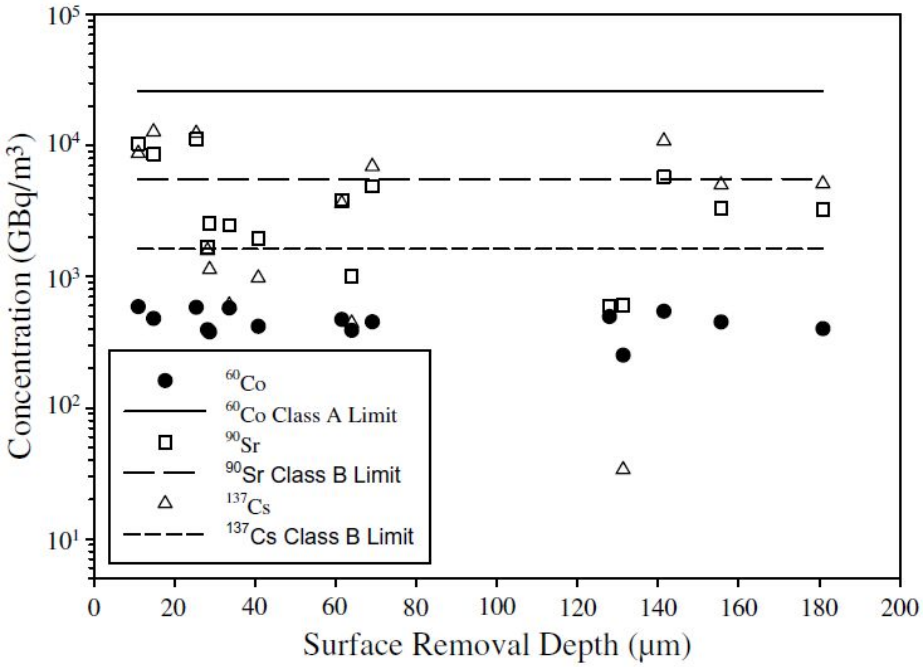

Figure 2.1 Fission product concentration in Zircaloy cladding (Rudisill, 2009)

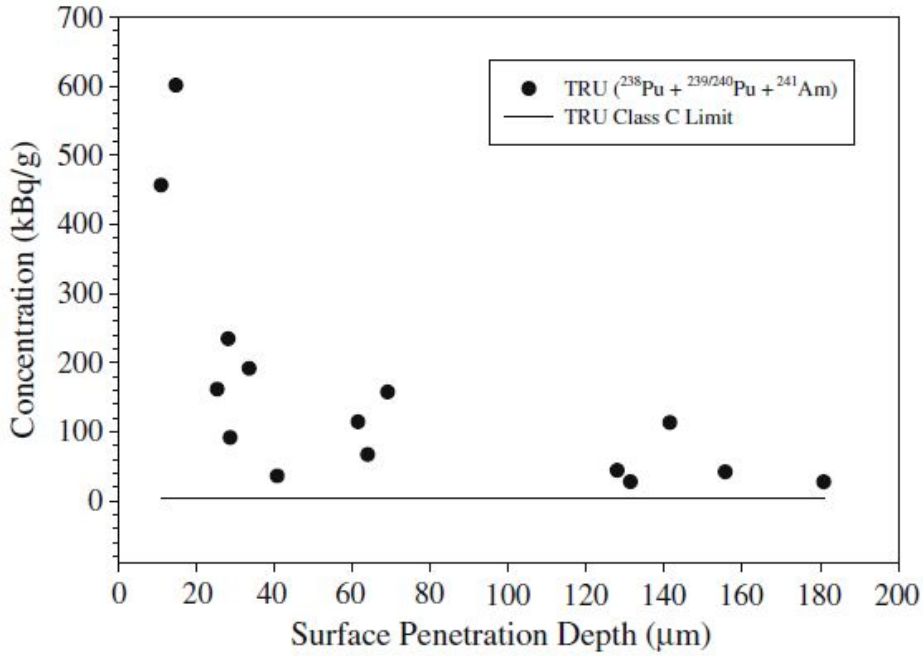

Figure 2.2 Transuranic elements concentration in Zircaloy cladding (Rudisill, 2009)

2.2 Volumetric decontamination processes

Volumetric decontamination processes for Zircaloy cladding has developed in two steams: Halogenation method and electrorefining in molten salts.

2.2.1 Halogenation method

Iodination and chlorination processes have been developed as halogenation method to recover zirconium from irradiated Zircaloy cladding. Iodination process using iodine gas is carried out in two stages as represented in Figure 2.3 (Del Cul et al., 2004; Collins et al., 2011; Del Cul et al., 2011; Collins et al., 2012). First stage is a process to make volatile ZrI_4 from irradiated Zircaloy cladding by reacting zirconium with iodine gas at 300-500^{o}C.

$$Zr + 2I_2 \rightarrow ZrI_4 \text{ at } 300\text{-}500^{o}\text{C}$$

During this process, nonvolatile elements such as U, TRU and fission products are remained at ZrI_4 formation reactor. Some of major elements of Zircaloy cladding such as Sn, Nb, and Fe could react with iodine gas but all of these iodide except SnI_2 are decomposed into metal at temperature over 300^{o}C. SnI_2 could evaporate with ZrI_4 but the vapor pressure is much smaller than ZrI_4. Produced volatile ZrI_4 is transferred to the second stage for producing Zr metal foil product. In the second stage, ZrI_4 is decomposed into Zr metal and

I_2 at over 1,100°C.

$$ZrI_4 \rightarrow Zr + 2I_2 \text{ at } >1{,}000^{\circ}\text{C}$$

E. D. Collins conducted experiments for the iodination process to recover zirconium from various unirradiated Zircaloy samples (Collins et al., 2011). In these experiments, he identified that zirconium could be recovered from Zircaloy with high purity.

However, iodination process has several points to be careful. Since ZrI_4 could react with H_2O and be decomposed, iodine gas and Zircaloy cladding should be thoroughly dried before making the reaction forming ZrI_4 and produced ZrI_4 should be handled in the environment without moisture. The reaction chamber should be also maintained without O_2, N_2 and hydrocarbons since these chemicals could react with ZrI_4. During ZrI_4 decomposition process, decomposed iodine gas should be isolated from decomposed Zr. ZrI_4 would be formed again and process efficiency might be lowered unless iodine are separated from Zr. In addition, because ZrI_4 decomposition process requires long reaction, throughput might be a problem in commercial scale decontamination process.

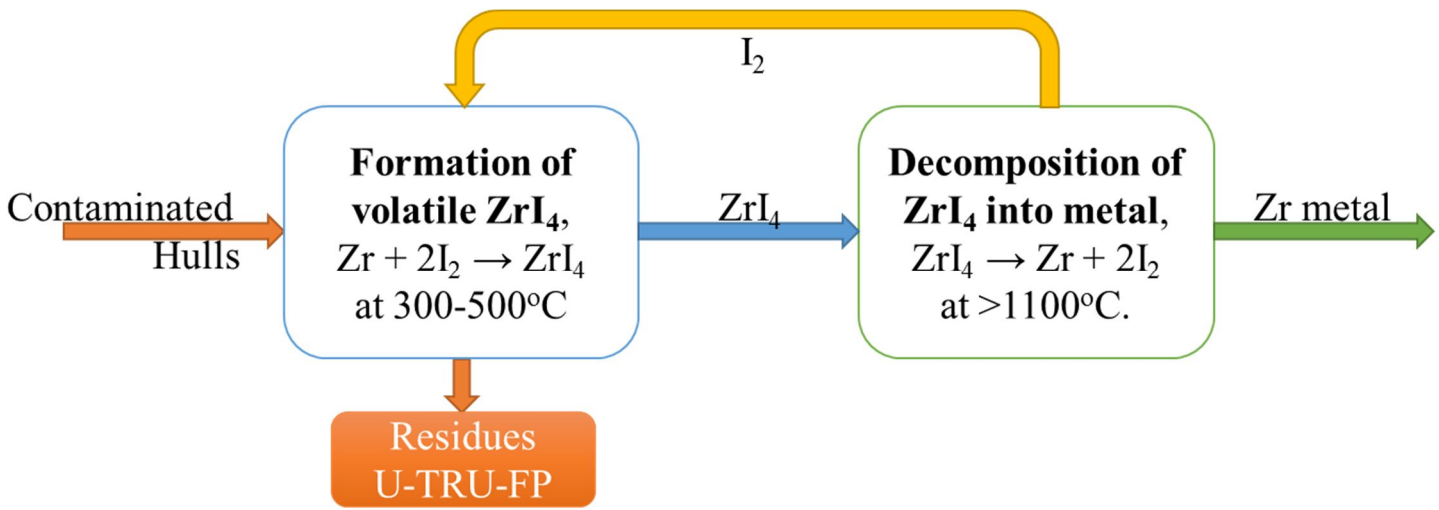

Figure 2.3 Schematic flow diagram for iodination process to decontaminate spent nuclear fuel cladding

Chlorination process also consists of two stages as represented in Figure 2.4 (Collins et al., 2012). First stage is to make $ZrCl_4$ from Zircaloy cladding. Hydrogen chloride (HCl) and chlorine gas are utilized to chlorinate zirconium:

$$Zr + 4HCl \rightarrow ZrCl_4 + 2H_2 \text{ at } 350^{\circ}\text{C} \quad \text{or}$$

$$Zr + 2Cl_2 \rightarrow ZrCl_4 \text{ at } 350^{\circ}\text{C} .$$

Chlorination process using HCl could recover $ZrCl_4$ with very small amount of $NbCl_3$ or $NbCl_4$. $SnCl_2$ could evaporate with $ZrCl_4$ but it could be separated by operating chlorination chamber below 200°C. However, since H_2 gas is generated during chlorination process using HCl, chlorination using Cl_2 gas could be an alternative method.

Recovered $ZrCl_4$ is reduced into Zr and Cl_2 in the second stage. There could be two method to reduce $ZrCl_4$. Kroll process using a strong reductant such as Mg is a method to prepare Zr (Kroll, 1937; Kroll et al., 1946; Kroll et al., 1947):

$$ZrCl_4 + 2Mg \rightarrow Zr + 2MgCl_2$$

This process has been commercialized to produce Zr metal from Zircon sand. However, since the objective of this study is to decontaminate irradiated

Zircaloy-4 cladding including radioactive elements, $MgCl_2$ which is a by-product of $ZrCl_4$ reduction could be mingled with radioactive chlorides and large amount of radioactive waste could be generated in this process.

Another method to reduce $ZrCl_4$ into Zr metal is electrolysis in chloride molten salts. By applying electric current in molten salts containing $ZrCl_4$, Zr metal would be prepared by capturing 4 electrons on the cathode:

$$ZrCl_4 + 4e^- \rightarrow Zr + 4Cl^- \text{ on the cathode and}$$

$$2Cl^- \rightarrow Cl_2 + 2e^- \text{ on the anode}$$

These reactions are very similar to reactions of electrorefining in chloride molten salts:

$$ZrCl_4 + 4e^- \rightarrow Zr + 4Cl^- \text{ on the cathode}$$

$$Zr + 4Cl^- \rightarrow ZrCl_4 + 4e^- \text{ on the anode}$$

Therefore, it might be more effective way to conduct electrorefining of irradiated Zircaloy cladding without a chlorination process.

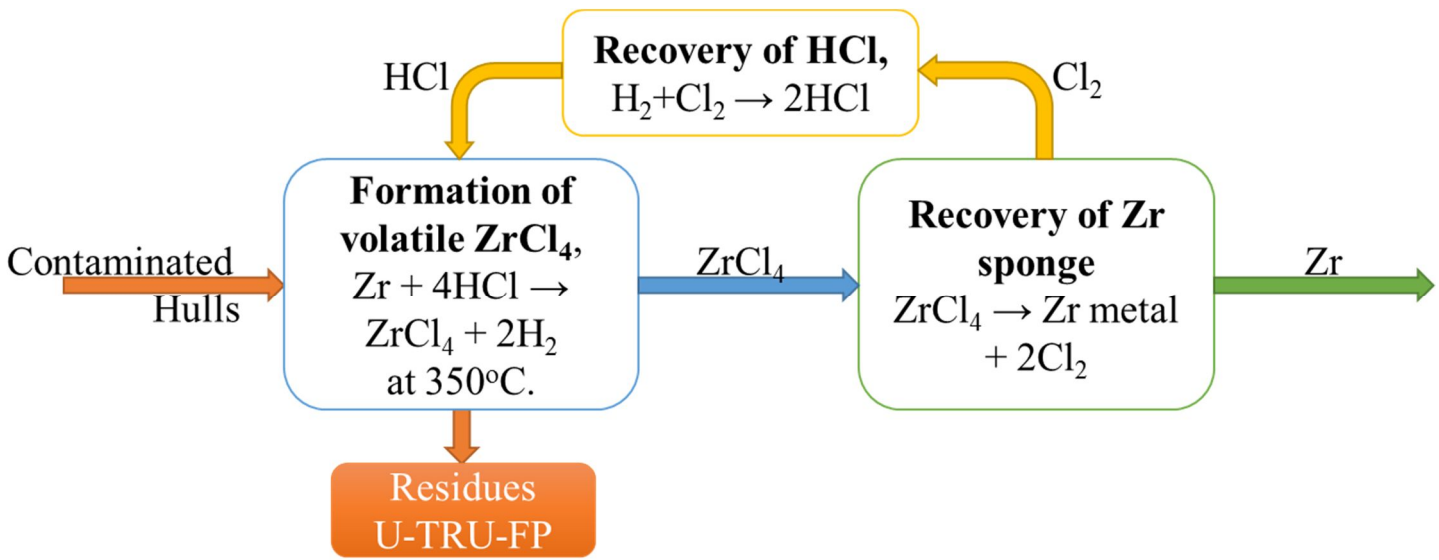

Figure 2.4 Schematic flow diagram for Hydrochlorination process to decontaminate spent nuclear fuel cladding

2.2.2 Electrorefining

Electrorefining might be preferred to decontaminate irradiated Zircaloy cladding because the process is much simpler than halogenation and reaction chamber might be more compact (Park et al., 2013). There would be a lot of electrorefining methods depending on the type of molten salts such as chloride and fluoride. Electrorefining has been developed in various molten salts because zirconium redox behavior is very complicated in molten salts. Various oxidation states such as Zr(IV), Zr(III) and Zr(II) could exist depending on molten salts. In this section, Zr and Zr alloy electrorefining experiments using LiF-KF, LiCl-KCl-LiF(10 wt. %), CsCl-KF and LiCl-KCl are reviewed.

Electrorefining expriments for Zr recovery in LiF-KF were conducted by K. T. Park to purify Zirlo scarp as the high purity dense Zr (Park, 2013; Park et al., 2013). He choose fluoride salts to obtain coarse Zr deposits and prevent disproportionate reactions such as $Zr^{4+} + Zr \rightarrow 2Zr^{2+}$. Before electroreifning experiments, cyclic voltammetry on LiF-KF-ZrF_4 was performed and it was revealed that redox reaction between Zr(IV) and Zr metal is the most major redox reaction in LiF-KF salts. Electrorefining experiments were conducted in the electrochemical cell at 700^{o}C as represented in Figure 2.5. For all experiments, Zr metal was prepared with small amount of impurities less than 700ppm and the products satisfied the ASTM B348 specifications for nuclear-grade Zr sponge as represented in Figure 2.6.

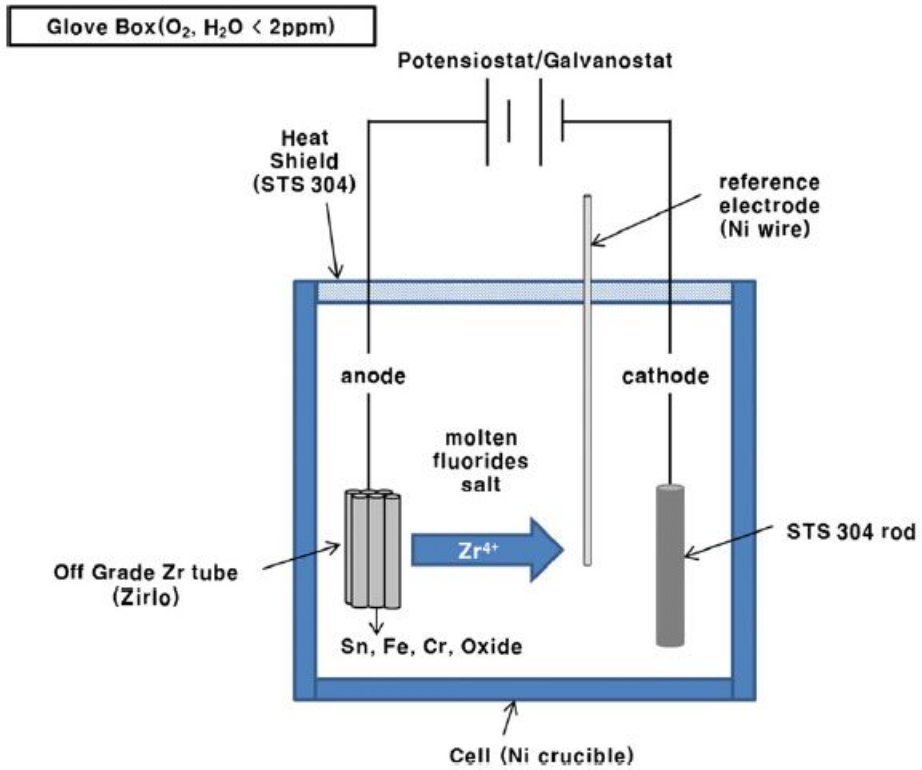

Figure 2.5 Schematic diagram of the experimental apparatus for Zr scrap electrorefining in fluoride salts (Park et al., 2013)

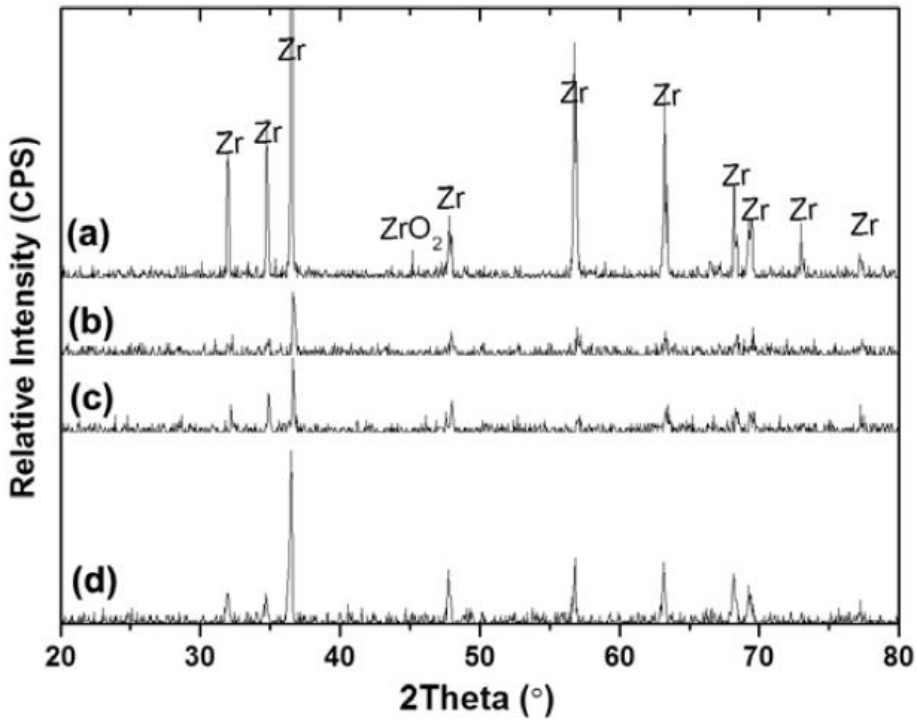

Figure 2.6 X-ray diffraction patterns results for Zr deposits after electrorefining with applied currents of (a) 4, (b) 2, (c) 1 and (d) 0.5 A (Park et al., 2013)

Even though electrorefining experiments in fluoride salts conducted successfully in lab-scale, there would be some concerns in commercial scale. Operating temperature of this process is pretty high as 700^{o}C and the molten salt is based on fluorine which is very reactive elements. Therefore, general stainless steels would be hard to be utilized as structural material because of corrosion problem caused by fluorine and operating cost would be expensive.

Different fluoride salts including NaF-LiF and KF-NaF-LiF were tested to recover coarse Zr during electrorefining by G. J. Kipouros in the cell as represented in Figure 2.7 (Kipouros and Flengas, 1985). Total 22 electrorefining experiments with various operating conditions were conducted and Zr with coarse crystalline plates was prepared in NaF-LiF salts as represented in Figure 2.8. However, this process might be hard to be commercialized because of operating temperature was very high as 750^{o}C and fluoride corrosion problem.

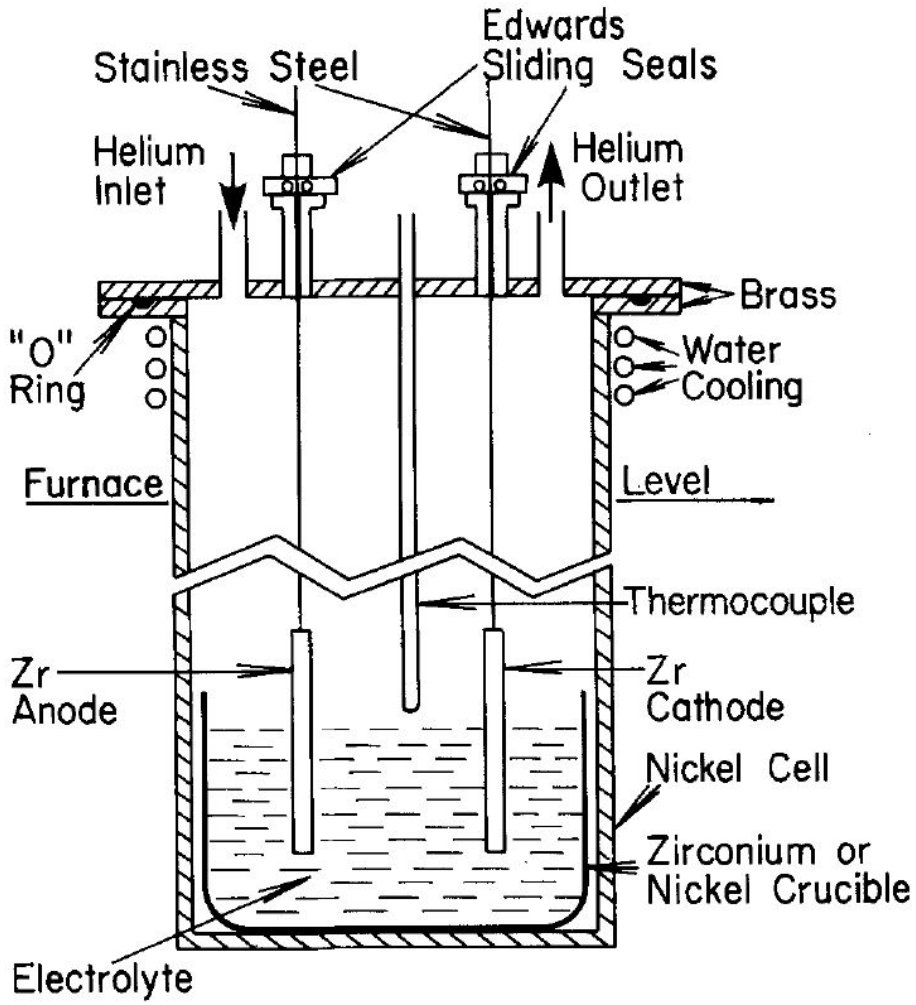

Figure 2.7 Electrochemical cell for zirconium electrorefining in CsCl based molten salts (Kipouros and Flengas, 1985)

Figure 2.8 Large platelike deposits after electrorefining in NaF-LiF salts (Kipouros and Flengas, 1985)

Chloride molten salts would be a solution for these problems because chlorine is less corrosive and melting temperature of chloride salt is lower than fluoride salt. For this reason, R. Fujita conducted electrorefining of BWR zircaloy channel box in LiCl-KCl-LiF(10 mol%) (Fujita et al., 2005a; Fujita et al., 2005b; Fujita et al., 2007). Since it has been reported that disproportionate reaction between Zr(IV) and Zr metal which could aggravate electrorefining efficiency might occur in LiCl-KCl salts, LiF of 10 mol% was added to prevent this reaction by stabilizing Zr(IV). Electrorefining using LiCl-KCl-LiF was conducted in the electrochemical cell as represented in Figure 2.9. Electrorefining was carried out in two-step. After the first electrorefining, radioactivities of Co and Sb in cathode deposits reduced into 1E+03 Bq/g from about 1E+06 Bq/g, the radioactivities of Co and Sb in the irradiated channel box, as represented in Figure 2.10. Radioactivities of Co and Sb diminished to about 1E+02 Bq/g which is lower than the limit of Very Low-Level-Waste regulation of Japan.

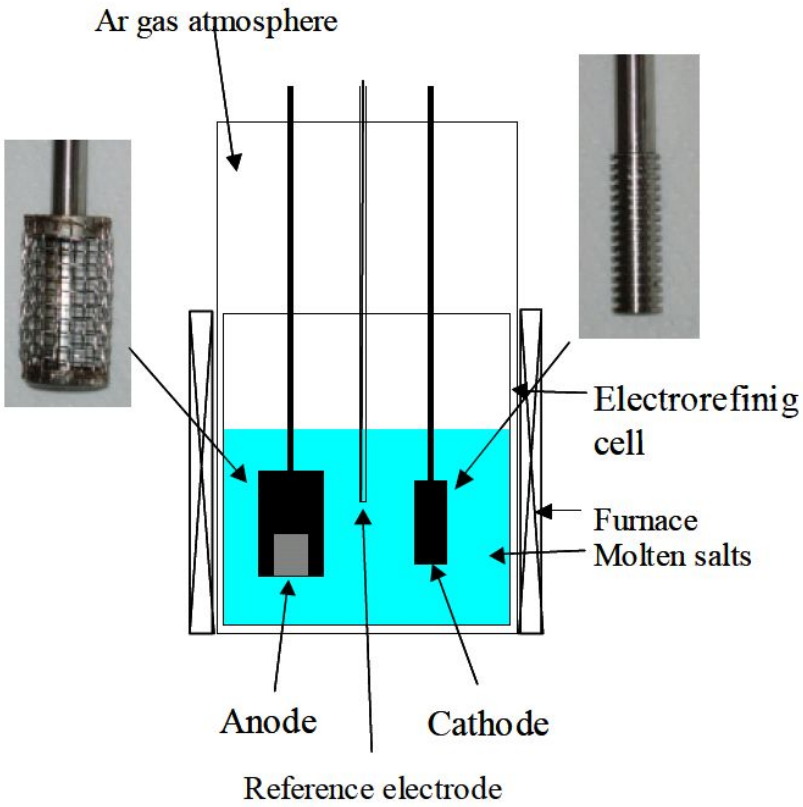

Figure 2.9 Schematic experimental apparatus used for electrorefining in LiCl-KCl-LiF (Fujita et al., 2005a)

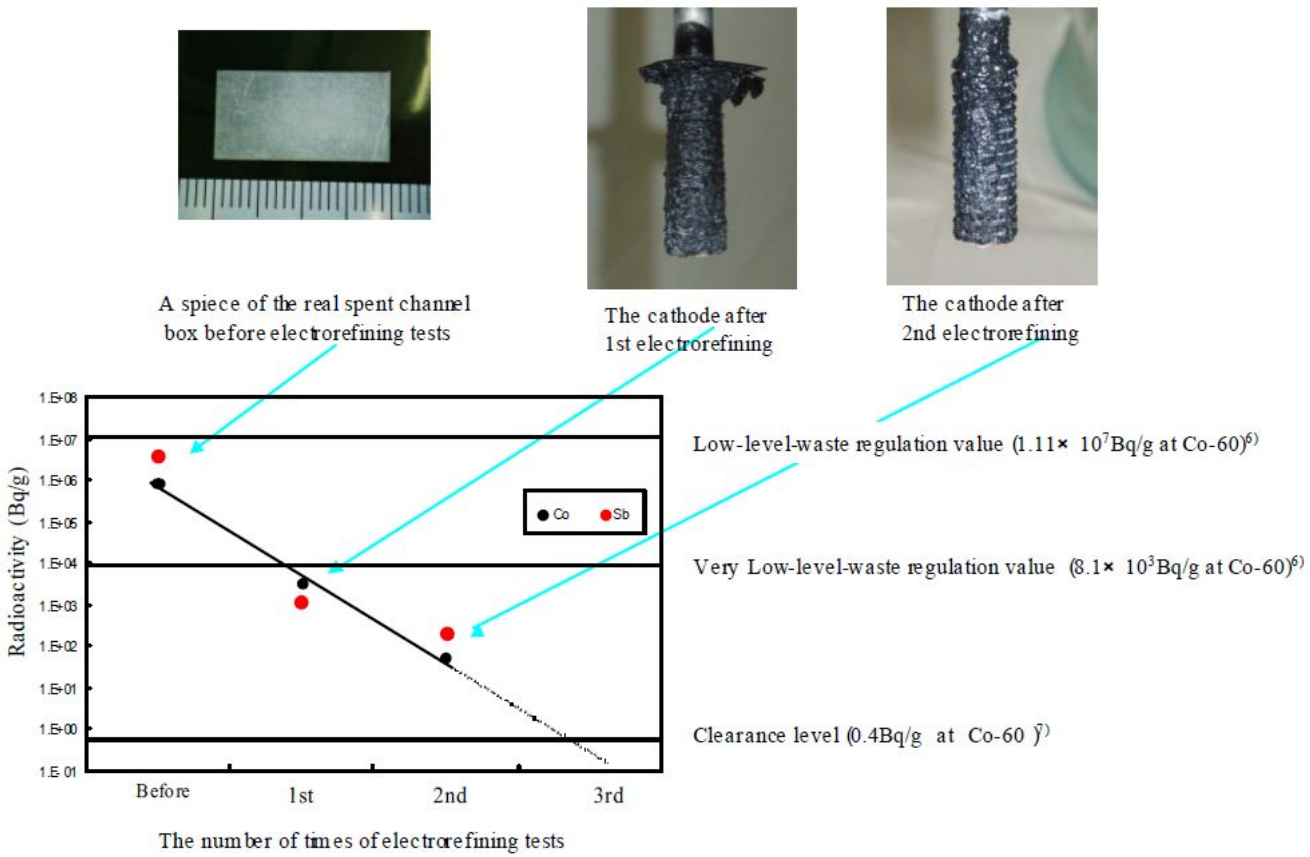

Figure 2.10 The results of two step electrorefining in LiCl-KCl-LiF

Feasibility of electrorefining of irradiated Zircaloy in LiCl-KCl-LiF was identified by decontaminating irradiated Zircaloy channel box of BWR. However, there would be still some concerns. Since this process utilizes LiF as a constituent of electrolyte, operating temperature is quite high as 650^{o}C and corrosion caused by fluorine could take place. In addition, molten salt purification after electrorefining might be complicated because the molten salts contains both chloride and fluoride.

G. J. Kipouros conducted zirconium electroreifning in CsCl-KF salts in the cell as represented in Figure 2.11 (Kipouros and Flengas, 1985). Total seven sets of experiments with different operating conditions were tested and dendritic zirconium was obtained in CsCl-KF salts at the current density of 3.0 A/dm^2 as represented in Figure 2.12. However, this process might be hard to be commercialized because of operating temperature was very high as 700^{o}C and fluoride corrosion problem. In addition, large amount of radioactive Cs waste could be generated if CsCl based salts are utilized. In irradiated Zircaloy cladding, there would be Cs-137 with radioactivity of about 2.0E+07 Bq/g after 5 years cooling (Jung et al., 2006). Since Cs is more oxidative than Zr, Cs-137 could be dissolved into molten salts during zirconium electrorefining and it could result in dilution of Cs-137. If the radioisotopes blends with radiologically stable Cs, the amount of Cs waste would increase and there would be no way to separate them without isotopes separation which requires expensive work. Therefore, CsCl based salts should not be utilized for electrorefining of irradiated Zircaloy cladding in the aspect of radioactive waste management. For similar reasons, $SrCl_2$ based

salts should not be used.

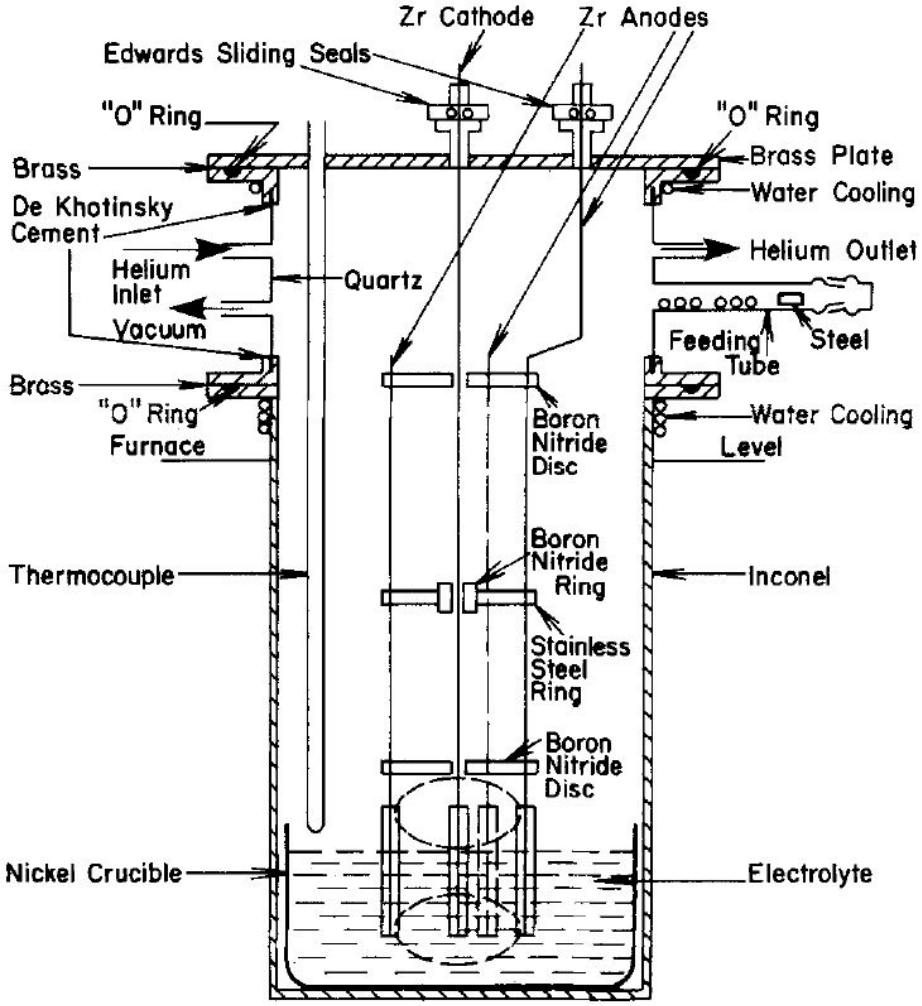

Figure 2.11 Electrochemical cell for zirconium electrorefining in CsCl based molten salts (Kipouros and Flengas, 1985)

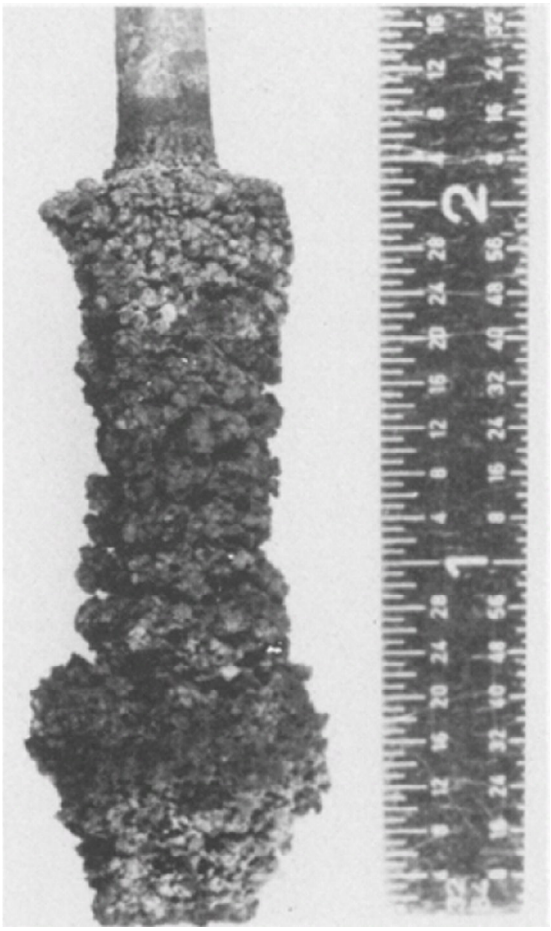

Figure 2.12 Cathode deposits after electrorefining in CsCl-KF-Cs_2ZrCl_6 (Kipouros and Flengas, 1985)

Chloride molten salts have advantatages of relatively low operating temperature and low corrosion problem. Stainless steel could be utilized for structural material and operating cost of electrorefiner might be less expensive. C. H. Lee conducted electrorefining of unirradiated Zircaloy-4 specimen in LiCl-KCl salts with 4 wt. % $ZrCl_4$ (Lee et al., 2012). He performed two electrorefining experiments by controlling cathode potential to control chemical form of cathode deposits. When cathode potential was maintained as -1.15 V (vs. Ag/AgCl), chemical form of deposited zirconium was ZrCl as represented in Figure 2.13. Small amount of Sn about 0.56 wt. % was observed in cathode deposits and other elements such as Fe and Co were not deposited. In the case that cathode potential was controlled as -1.55V (vs. Ag/AgCl), most of zirconium was deposited on the cathode as metal but small amount of ZrCl was also recovered as represented in Figure 2.13. Purity of recovered zirconium was about 98.95 wt. %. Since the Zircaloy-4 specimen contains Zr of about 98.23 wt. %, electrorefining which was conducted at -1.55 V (vs. Ag/AgCl) might be ineffective for decontamination aspects.

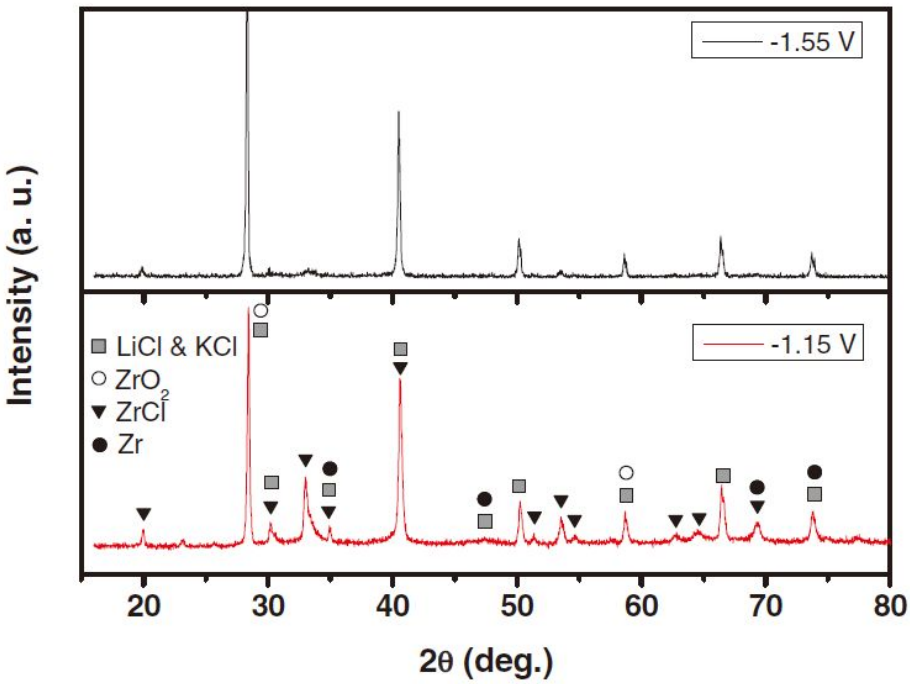

Figure 2.13 X-ray diffraction patterns of Zr compounds deposited at cathode potentials of (upper) -1.15 and (below) -1.55 V (vs. Ag/AgCl) in LiCl-KCl (Lee et al., 2012)

Chemical forms of zirconium deposits according to applied cathode potential were also investigated by Y. Sakamura. He conducted cathode deposition experiments in LiCl-KCl salts with $ZrCl_4$ of 0.0026 mole fraction. ZrCl was recovered at the case of cathode potential of -1.15~-1.04 V (vs. Ag/AgCl) as represented in Figure 2.14. When cathode potential was controlled between -1.42 and -1.35 V (vs. Ag/AgCl), Zr metal was produced with a little ZrCl.

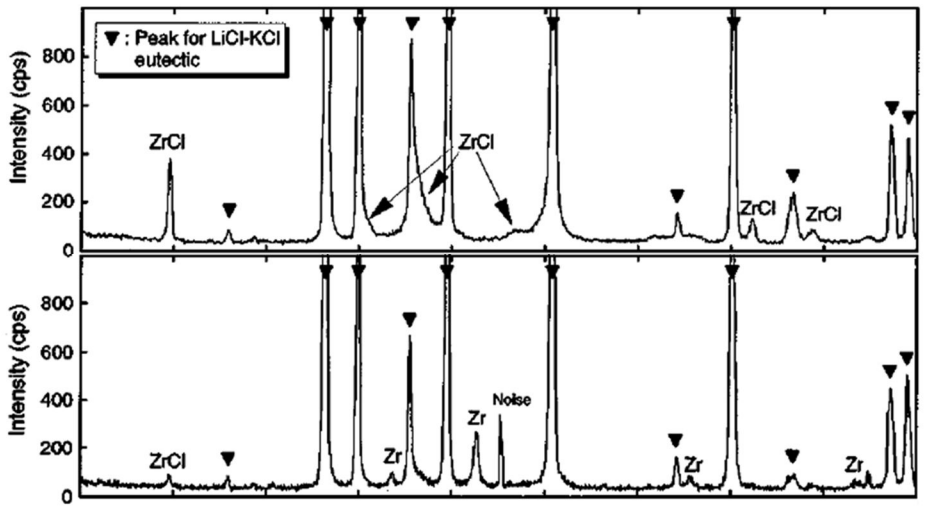

Figure 2.14 X-ray diffraction patterns of zirconium compound deposited at cathode potentials of (upper) -1.15~-1.04 and (below) -1.42~-1.35 V (vs. Ag/AgCl) (Sakamura, 2004)

Pros and cons according to molten salts are summarized in Table 2.1. LiCl-KCl salts have superior characteristics of low operating temperature about 500^{o}C and low corrosion risk. However, previous studies were not successful to recover Zr as metal without impurities since redox behavior of Zr in LiCl-KCl salts are very complicated with various oxidation states. If redox reactions of Zr would be controlled based on clarified redox mechanisms, high purity Zr metal would be prepared and a commercial scale electrorefiner for decontaminating irradiated spent nuclear fuel Zirclaoy-4 cladding would be developed.

Table 2.1 Comparison of decontamination processes for irradiated Zircaloy cladding

			Pros	**Cons**
Surface decontamination	hydrofluoric acid process		· Simple process	· U and TRU could not be decontaminated.
Volume decontamination	Iodination process		· High decontamination factor	· ZrI_4 is very hygroscopic · Decomposition process requires long reaction time
	Hydrochlorination process			· $ZrCl_4$ reduction process
	Electrorefining in fluoride salts		· One-step reduction of Zr(IV) into Zr metal · Metal deposition with high purity of 99.93% · Coarse metal recovery	· High operating temperature · Fluoride corrosion
	Electrorefining in fluoride-chloride salts	LiCl-KCl based	· Suppressed disproportionate reaction · Metal deposition with high purity of 99.9%	· High operating temperature · Fluoride corrosion · Complicated salt purification
		CsCl, $SrCl_2$ based	· More coarse metal recovery	· Fluoride corrosion · High operating temperature · Large amount of Cs and Sr waste
	Electrorefining in chloride salts	LiCl-KCl	· Low operating temperature · Low corrosion problem	· Complicated redox reactions · ZrCl codeposition

Chapter 3 Research Design

3.1 Research questions and approaches

The main objective is established as development of electrorefining process in LiCl-KCl salts for irradiated spent nuclear fuel Zircaloy-4 cladding. To achieve the objective, there would be several questions that should be settled in aspects of both zirconium redox mechanism clarification and large scale electrorefiner design. For the zirconium redox mechanism, following questions should be resolved:

> **Question 1**: What types of zirconium oxidation and reduction reactions could occur in LiCl-KCl?
>
> **Question 2**: How could all zirconium redox reactions which are not related to Zr metal recovery be suppressed?
>
> **Question 3**: How could zirconium metal be recovered without impurities?

Molten salt electrochemical experiments including cyclic voltammetry and electrorefining of Zirclaoy-4 specimen were conducted to settle these question and the results are described in the Chapter 4. In the Chapter 4, redox behaviors of Zr, Sn, Cr, Fe and Co in LiCl-KCl salts are suggested. In addition, lab-scale electorefining results are represented. The goal of the

Chapter 4 is to suggest some recommendations for Zircaloy-4 electrorefining based on the results of molten salts experiments.

Verification of the feasibility of large scale Zircaloy-4 electrorefining could be performed more efficiently by using computational model. However, to utilize a computational model for electrorefiner design and performance verification, following questions should be answered.

Question 1: How could cathodic deposition model and anodic dissolution model be validated separately?

Question 2: Where would the greatest modeling uncertainties be?

Question 3: Could the developed model be applied for zirconium multi-step electrochemical reactions?

In this dissertation, a 3-D computational electrochemo-hydrodynamic model is developed. Cathodic deposition model of the developed model was validated by benchmarking electrolysis experiment in aqueous system and validity of anodic dissolution model was investigated based on molten salt electrorefining experiment. In addition, multi-step electrochemical reaction model was validated by benchmarking lab-scale Zircaloy-4 electrorefining experiments. The results of the computational model development and validation are described in the Chapter 5. The goal of the Chapter 5 is to develop and validate a computational electrorefining model that could be utilized for electrorefiner design and performance verification.

Even though lab-scale electrorefining experiment was carried out successfully, performance of large scale electrorefining might be different. Therefore, to commercialize the developed electrorefining process, the feasibility of electrorefining process should be validated in at least pilot-scale. While the feasibility is being investigated, following questions should be checked.

Question 1: How high decontamination factor or purity of products could be obtained?

Question 2: How high throughput could be achieved?

Question 3: How would the electorefiner performance be changed according to operating condition?

In this dissertation, the pilot scale electrorefiner was designed based on the recommendation established from molten salt experiments and the performance of the electrorefiner was validated by using the developed computational model. The results are represented in the Chapter 6.

The relation among sections of this dissertation is summarized in Figure 3.1.

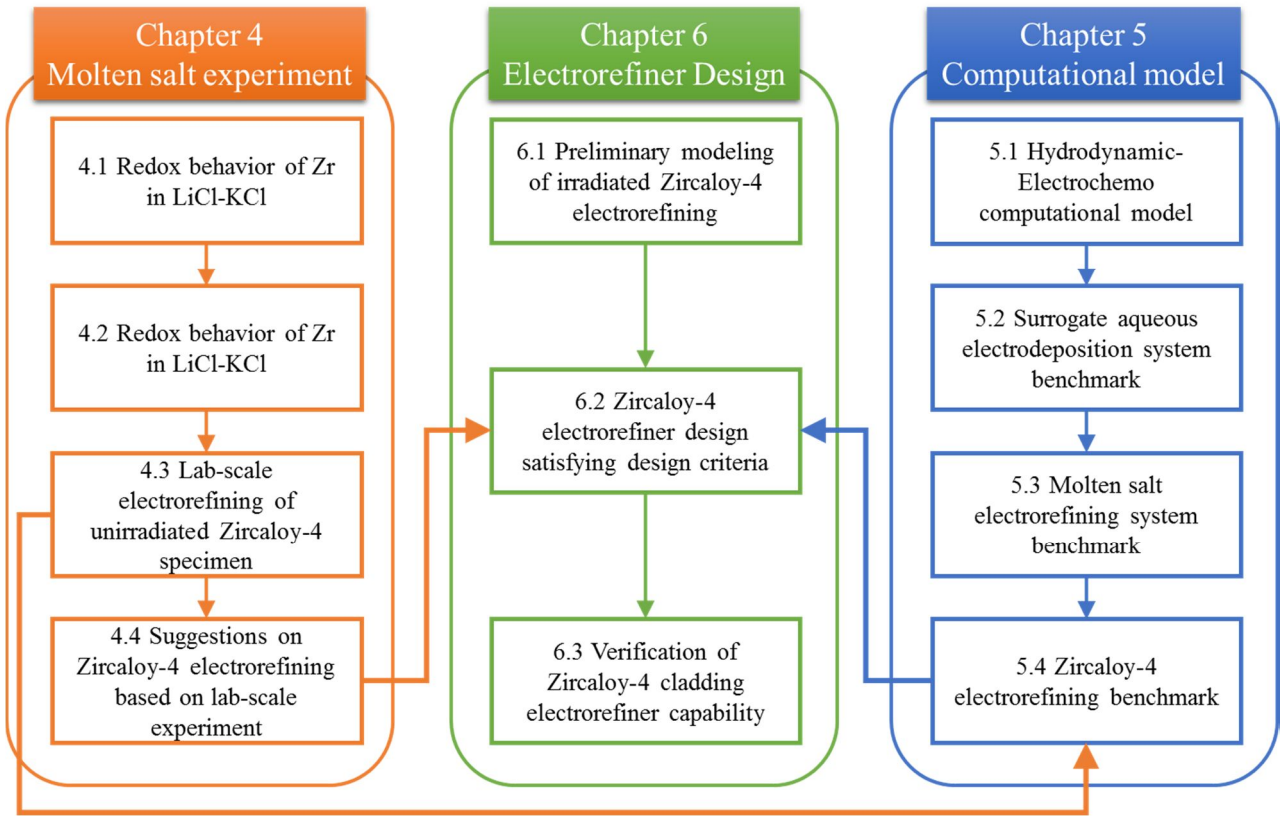

Figure 3.1 Correlation between each section of dissertation

3.2 Molten salt electrochemical experiment

There are various electrochemical and spectroscopic methods to investigate redox mechanism such as cyclic voltammetry, chronopotentiometry, laser absorption spectroscopy, Raman spectroscopy and so on. In LiCl-KCl salts, two insoluble states (Zr metal and ZrCl) and two soluble states (Zr(II) and Z(IV)) could exist. There could be more than six redox pair reactions between these oxidation states as represented in Figure 3.2 and reaction rates of these redox reactions might be dependent on various electrochemical conditions such as applied current density, electrode potential and initial concentration of $ZrCl_4$. Combining these electrochemical conditions, a huge number of experimental sets could be developed and it might be very hard to reveal the zirconium redox mechanism quantitatively in short time. Cyclic voltammetry is one of the most effective way to investigate redox mechanism for various electrochemical conditions with small amount of reagents and relatively short experiment time. For this reason, in this dissertation, cyclic voltammetry was utilized to investigate zirconium and other elements redox behaviors.

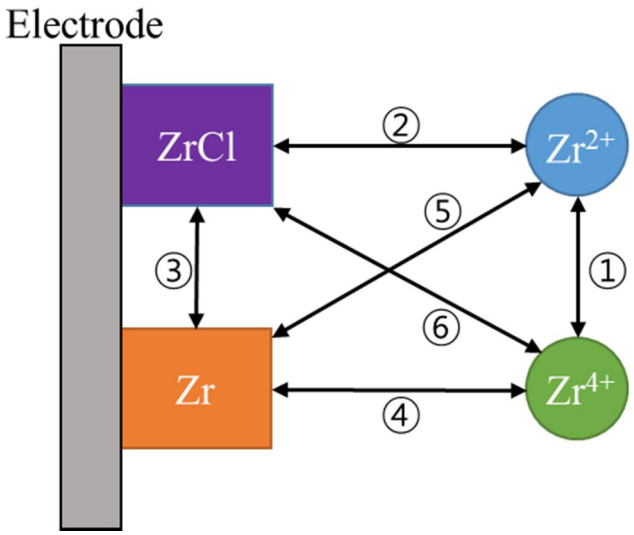

Figure 3.2 Potential redox reactions that could occur in LiCl-KCl salts

3.3 Computational electrorefining model development

The developed model was validated in three stages: cathodic deposition model validation, anodic dissolution validation and zirconium multi-step reaction model validation.

To validate cathodic deposition model of the developed computational model, benchmark studies using a Rotating Cylinder Hull (RCH) cell with a copper sulfate electrolyte solution were performed. The RCH cell with copper sulfate system was selected, because it has been widely utilized as a standard technique for quantitative electrodeposition studies and its high availability of reliable materials property data (Low et al., 2007).

To validate anode dissolution model of the developed 3-D computational model and to verify the developed computational electrorefining model in molten salt system, experimental data of Mark-IV electrorefiner located in Idaho National Laboratory (INL) is selected. Data from the electrorefining experiments was provided by the INL (Li et al., 2005; Hoover et al., 2010). This experiment was used to separate uranium from the other fuel materials.

To validate zirconium multi-step redox reaction model, lab-scale electrorefining experiment results according to concentration of $ZrCl_4$ are utilized.

3.4 Pilot-scale electrorefiner design

The pilot-scale electrorefiner for irradiated spent nuclear fuel Zircaloy-4 cladding was designed based on recommendations from lab-scale experiments by using the developed computational electrorefining model. The capability of designed electrorefiner was evaluated for various operating conditions including electrode rotating speed and applied current density.

Chapter 4 Molten Salt Electrochemical Experiment

4.1 Redox behavior of Zr in LiCl-KCl[3]

To investigate zirconium redox mechanisum, several CV experiments were conducted. Redox reactions that could occur in LiCl-KCl were determined based on electrolysis results and peak behaviors according to scan rate, scan range and concentration of $ZrCl_4$.

4.1.1 Experimental setup

All experiments using the LiCl-KCl based molten salt were conducted within an inert atmosphere glove box filled with Ar gas of 99.999% as represented in Figure 4.1. During the experiments, oxygen and moisture concentrations were maintained below 0.1 ppm. Inside the glove box, an electrochemical cell for CV was prepared as illustrated in Figure 4.2. Temperature of the molten salt was measured by k-type thermocouples, and it kept as 500^{o}C within ±1^{o}C by a proportional-integral-derivative (PID) heater controller as represented in Figure 4.3. Two identical quartz test tubes with an inner diameter of 11mm and a height

[3] This section has been written based on the following journal paper: Jaeyeong Park et. al., "Cyclic Voltammetry on Zirconium Redox Reactions in LiCl-KCl-$ZrCl_4$ at 500^{o}C for Electrorefining Contaminated Zircaloy-4 Cladding," Journal of The Electrochemical Society, 161, H97-H104, 2014.

of 380 mm were equipped at the same height in the cell for conducting CV and measuring molten salt temperature. A VersaStat3 potentiostat combined with a VersaStudio software applied potential and current on the electrochemical cell and provided necessary analysis packages as represented in Figure 4.3.

Figure 4.1 Glove box for maintaining inert atmosphere during molten salt experiment

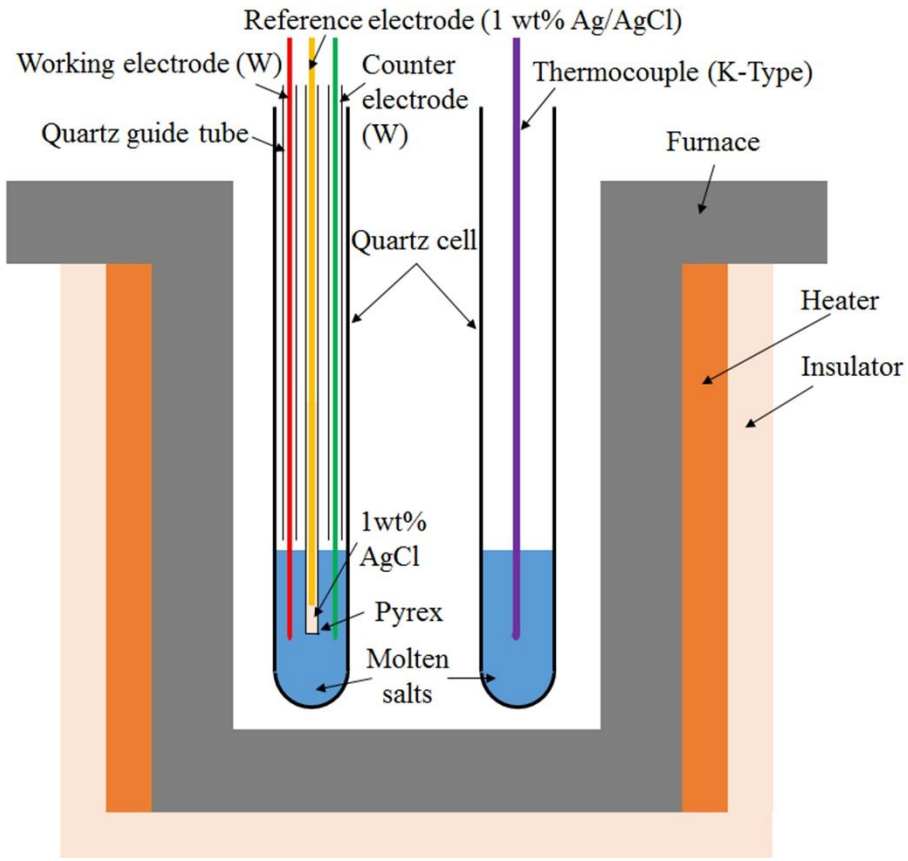

Figure 4.2 Electrochemical cell for CV with LiCl-KCl salts

Figure 4.3 Potentiostat and PID heater controller

An anhydrous LiCl-KCl eutectic mixture (i.e., solvent) with purity of 99.99% was obtained from the Sigma Aldrich, and an anhydrous $ZrCl_4$ (i.e., solute) with purity of 99.99% was also supplied from the same source. The working and counter electrodes were inserted and arranged along with a narrow quartz guide tube with an inner diameter of 2mm. These electrodes were made of 99.99% purity tungsten wires with a diameter of 1mm. These wires were also acquired from the Sigma Aldrich. The reference electrode was the Ag/AgCl electrode, a diameter of 1mm and purity of 99.99%, that was placed within the LiCl-KCl-AgCl(1wt. %) solution. The AgCl with purity of 99.999% again from the Sigma Aldrich was used for the reference electrode. The electrolyte mixture was contained in a Pyrex glass tube (an inner diameter of 2mm) whose ends were designed and manufactured as thin as possible for better ion diffusion.

The molten salt of LiCl-KCl-$ZrCl_4$(1 wt. %) was used for CV in the electrochemical cell. Prior to producing the solution for CV, a higher concentration salt, LiCl-KCl-$ZrCl_4$(10 wt. %), was first prepared in order to reduce the volume of reagent to be initially handled, and then the salt was diluted down to the concentration needed for CV. Since sublimation temperature of $ZrCl_4$ is 331^{o}C and melting temperature of LiCl-KCl eutectic is 353^{o}C, $ZrCl_4$ might be lost between 331 and 353^{o}C under the slow increase of temperature. However, once $ZrCl_4$ is dissolved into the LiCl-KCl salt, the amount of loss resulted from sublimation could be neglected (Sakamura, 2004; Lee et al., 2012). Therefore, a furnace was heated up to 600^{o}C before placing the quartz cell containing $ZrCl_4$ and the LiCl-KCl

mixture to raise molten salts temperature rapidly. Although a cold trap was set up to measure the amount of sublimated $ZrCl_4$, the collected amount was insignificant. The mass of molten salt contained in the quartz test tube for CV is 2.54g. Each area of counter electrode and working electrode was 0.628 cm^2.

Eight sets of experiments were conducted to investigate zirconium behavior in the LiCl-KCl-$ZrCl_4$ at 500^oC as represented in Table 4.1. We scanned, at first, a background cyclic voltammogram (#1 in Table 4.1) for the LiCl-KCl eutectic without $ZrCl_4$. Then, 11 different scan ranges (#2) within -2.0 to 0.0 V were tested with a fixed scan rate of 300 mV/s to identify comprehensive zirconium redox peaks. From a scan range between -1.0 to 0.0 V, the width of range is expanded by 0.1 V toward more negative potential. After that, we conducted four sets of experiments (#3-6) with various scan rates and scan ranges to determine possible redox reactions for each peak. Effects of $ZrCl_4$ concentration on each peak shape (#7 and #8) were also evaluated with five $ZrCl_4$ concentrations, 0.5, 1.0, 2.0, 4.0 and 8.0 wt. %, at a scan range of 0 ~ 1.3 V and a scan rate of 100 to 1,700 mV/s.

Table 4.1 Conditions and objectives of experiment sets conducted to investigate zirconium's electrochemical behavior in LiCl-KCl-$ZrCl_4$ at 500°C

	Concentration of ZrCl4 (wt. %)	Scan range (V)	Scan rate (mV/s)	Objective
#1	0.0	0.0 ~ -2.0	300	Measurement of background current density
#2	1.0	11 scan ranges from 0.0 ~ -1.0 to 0.0 ~ -2.0	300	Identification of zirconium redox peaks
#3	1.0	0.0 ~ -1.2	100~1500	Determination of redox reactions for identified peaks
#4	1.0	0.0 ~ -1.1	300~1500	
#5	1.0	0.0 ~ -1.6	100~1500	
#6	1.0	4 scan ranges from 0.0 ~ -1.0 to 0.0 ~ -1.3	500	
#7	0.5, 1.0, 2.0, 4.0 and 8.0	0.0 ~ -1.3	100~1700	Investigation of concentration effects on redox peaks
#8	1.0, 2.5, 5.0, 7.5	0.0 ~ -2.0	300	

CV on the LiCl-KCl-$ZrCl_4$ was carried out 1-2 days later after inserting electrodes into the cell for the equilibrium between the molten salt and the electrodes. While monitoring cathode potential for this period, it was determined that the equilibrium was sufficiently reached when the potential change rate became less than 0.5mV/hour. All the electrodes and the LiCl-KCl-$ZrCl_4$ solution were replaced after each experiment for preventing any disturbances from previous experiments. For example, after conducting CV with a scan range from -1.3 to 0 V (vs. Ag/AgCl), all the electrodes and the molten salt were changed to new ones before conducting the next CV with a scan range between -1.4 and 0 V (vs. Ag/AgCl).

4.1.2 Cyclic voltammetry results

This section presented the results of experiment sets in the order described in Table 1. The results of experiment set #1, 2 are first described in the next two sections, followed by the subsequent two sections containing the results of experiment set #3, 4, 5, 6. After that, the results of experiment #7 and the reversibility check of redox reactions are presented.

4.1.2.1 Background Cyclic Voltammogram

Before main experiments, CV on the LiCl-KCl eutectic without $ZrCl_4$ was conducted at 500^{o}C to obtain background data as represented in Figure 4.4. When the scan rate was 300 mV/s, current was smaller than 0.5 mA for

anodic reactions and larger than -5 mA for cathodic reactions. During the background scanning, no peaks were observed for the potential range between 0 and -2.0 V (vs. 1 wt. % Ag/AgCl). Moreover, peak currents measured in the LiCl-KCl-$ZrCl_4$(1 wt. %) solution were generally 20~200 times larger than those in the background scanning, up to over 100 mA for both oxidation and reduction reactions. For these reasons, it is revealed that the effects of background disturbances by the LiCl-KCl eutectic can be neglected in CV for the LiCl-KCl-$ZrCl_4$.

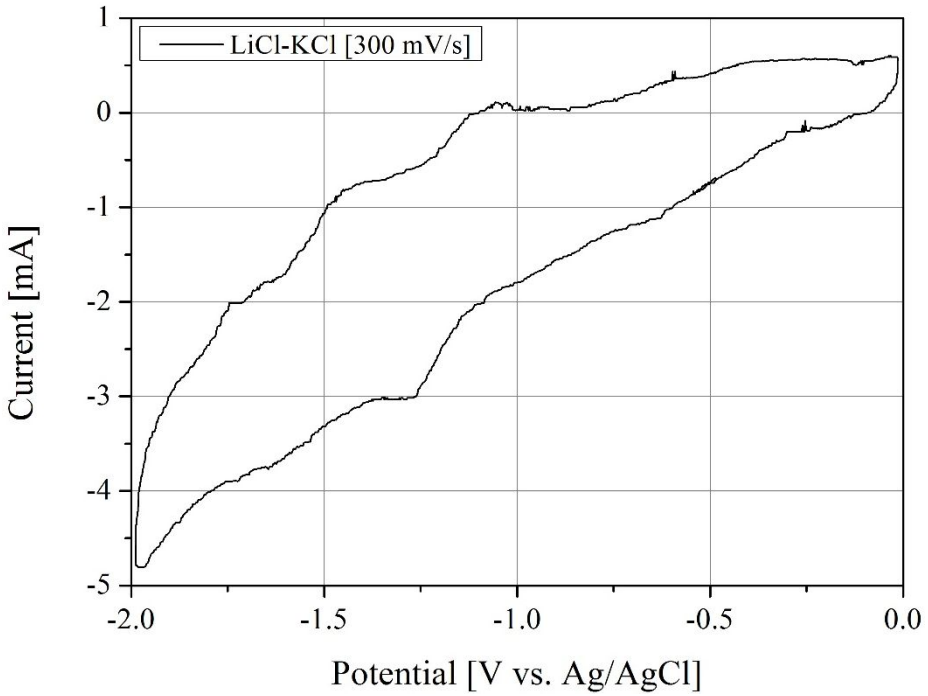

Figure 4.4 Background cyclic voltammogram on 500°C LiCl-KCl without any salts with scan rate of 300 mV/s: tungsten electrode (1Φ x 20 mm) for both working and counter electrodes, 1 wt. % Ag/AgCl for reference electrode

4.1.2.2 Identification of Zirconium Redox Peaks

As shown in Figure 4.5, a set of CV in the LiCl-KCl-$ZrCl_4$(1 wt. %) with a scan rate of 300 mV/s was carried out for 11 different scan ranges. In the cyclic voltammogram, major reactions which could mainly contribute to each peak are also represented. In this set of experiments, 3 peaks for reduction (R_1, R_2 and R_3) and 4 peaks for oxidation (O_1, O_2, O_3 and O_4) were observed. R_2, R_3, O_1 and O_2 peaks were relatively sharper and easier to be identified than R_1, O_3, and O_4 peaks for most of scan ranges. In particular, O_3 and R_1 peaks were difficult to determine peak potentials unless looking at them very closely because peak shapes did not appear. Their existence was only projected by the slope changes of cyclic voltammograms. The heights of reduction peaks proportionally increased as the scan range expanded without exceptions.

The height changes of oxidation peaks were more complicated behaviors than those of reduction peaks which only raised as the scan range expanded. For instance, peak O_1 begun to appear when the scan range was over -1.1 V, but it became unnoticeable after the scan range was over -1.5 V and totally disappeared after the scan range was over -1.7 V. In contrast, peak O_2 started to be identified when the scan range was over -1.2 V, and the peak became more defined as the expansion of scan range. The height of peak O_4 was about 3 mA in the scan range from 0 to -1.0 V where the peak was firstly observed. Since the peak has a relatively smaller height than other peaks, the peak is less conspicuous in Figure 4.5. In addition, the peak was getting

blurred as the scan range increased due to increasing the residual current of peak O_3.

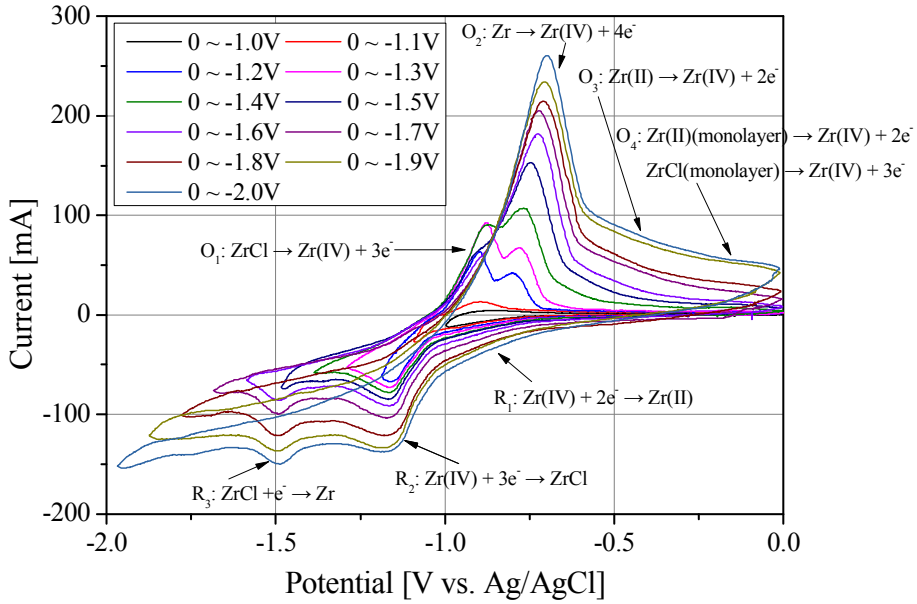

Figure 4.5 Cyclic voltammograms with the major reaction which could mainly contribute to each peak according to scan range for the scan rate of 300 mV/s in 500°C LiCl-KCl-$ZrCl_4$(1 wt. %): tungsten electrode (1Φ x 20 mm) for both working and counter electrodes, 1wt. % Ag/AgCl reference electrode

4.1.2.3 Peak behaviors with changing scan rates

Figure 4.6 shows voltammograms for a constant scan range from 0 to -1.2 V in the LiCl-KCl-$ZrCl_4$(1 wt. %) while changing scan rates from 100 to 1500 mV/s. In this range, peak O_1, O_2, and R_2 are well identified, whereas peak O_3, O_4, and R_1 are less conspicuous. Peak O_1 became distinct for scan rates from 100 to 300mV/s, and it was the most dominant oxidation peak. However, the peak current started to reduce after 300 mV/s, and it became hard to detect the peak at 1500 mV/s. Peak O_2, unlike peak O_1, was not found first at 100 mV/s, but it appeared and became dominant as the rise of scan rate. The potential of peak O_1 was shifted about 16 mV toward a positive direction when the scan rate changed from 100 to 1300 mV/s. The potential of peak O_2 moved about 44 mV upward while the scan rate changed from 500 to 1300 mV/s. The potential of peak R_2 was shifted to negative values as the scan rate increased, and the peak disappeared in the cases with wide potential range.

Peak O_4 was relatively well defined in the figure and the height of peak O_4 raised as the scan rate increased. The potential of peak O_4 moved about 30 mV as the scan rate increased from 300 to 1500 mV/s. Figure 4.6 shows that peak O_3 was minimal in magnitude. For the peak R_1, a peak shape did not appear but a slope change was observed from -0.7 to -1.0 V.

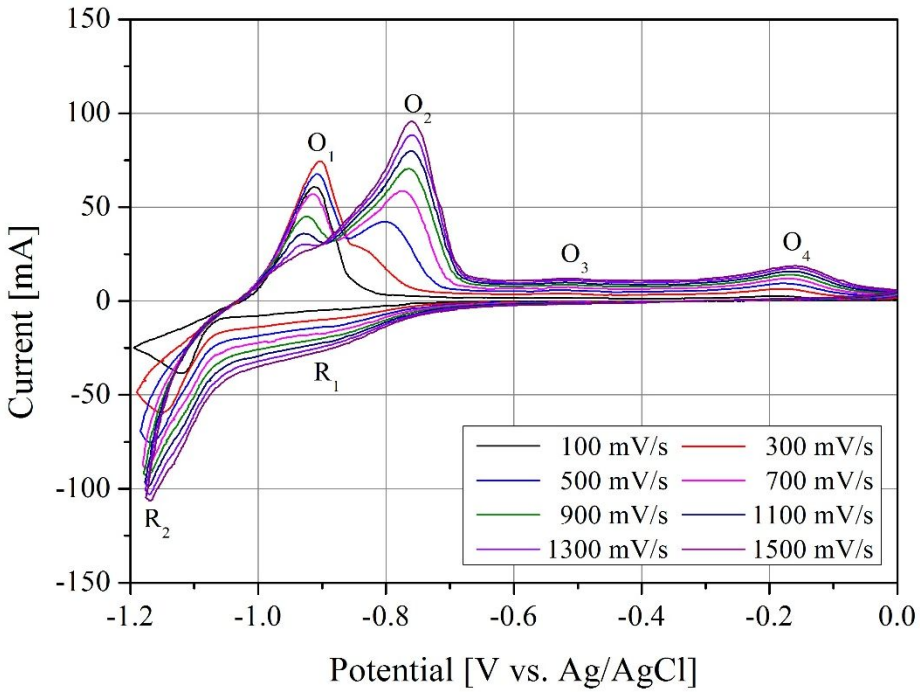

Figure 4.6 Cyclic voltammograms according to scan rate for the scan range from 0 to -1.2V (vs. 1 wt. % Ag/AgCl) in 500°C LiCl-KCl-$ZrCl_4$(1 wt. %): tungsten electrode (1Φ x 20 mm) for both working and counter electrodes, 1wt. % Ag/AgCl reference electrode

Figure 4.7 represents voltammograms in the LiCl-KCl-$ZrCl_4$(1 wt. %) for a scan range from 0 to -1.1 V. In this scan range, current densities are 3-5 times smaller than the scan range from 0 to -1.2 V. In this set of experiment, peak O_1 and O_4 were most noticeable. While the current densities of peak O_1 and O_2 are small, peak O_4 becomes much more distinct than the previous CV in Figure 4.6. The heights of peaks O_1 and O_4 increased with increasing scan rate. In addition, the potentials of these two peaks were almost consistent during the scan rate changed from 300 to 1500 mV/s; 23 mV for peak O1 and 13 mV for peak O_4. Peak O_3 was also developed with the increase of scan rate, but its peak height was relatively small. There was a slope change near -0.8 V, and this may be related to peak R_1. Other reduction peaks did not appear.

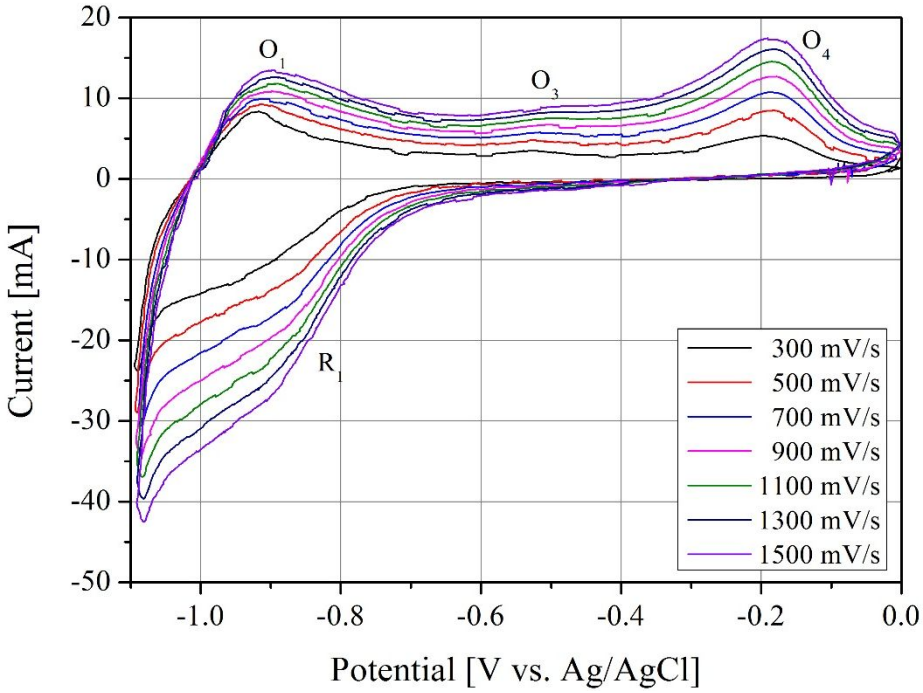

Figure 4.7 Cyclic voltammograms according to scan rate for the scan range from 0 to -1.1V (vs. 1 wt. % Ag/AgCl) in 500oC LiCl-KCl-$ZrCl_4$(1 wt. %): tungsten electrode (1Φ x 20 mm) for both working and counter electrodes, 1wt. % Ag/AgCl reference electrode

Figure 4.8 illustrates voltammograms for a scan range from 0 to -1.6 V in a constant concentration of $ZrCl_4$ in the LiCl-KCl. All reduction and oxidation peaks except O_1 were observed. Peak intensities tend to increase with the increase of scan rate. The potential of peak O_2 moved about 144 mV as the scan rate increased from 100 to 1500 mV/s. Peak R_2, R_3, and O_4 became unclear as the scan rate rose because of the height of other peaks located near these peaks intensified.

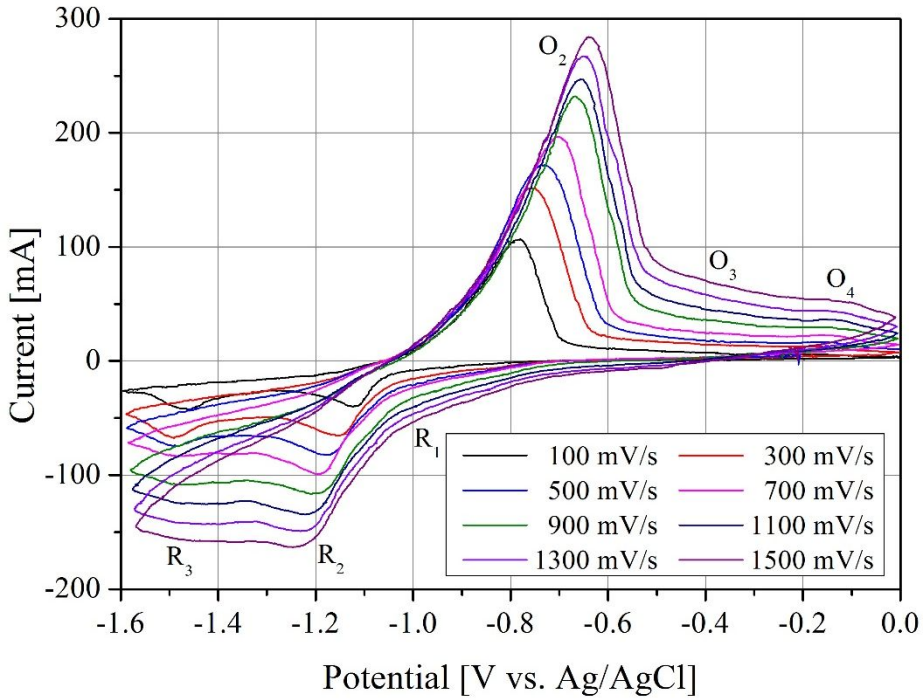

Figure 4.8 Cyclic voltammograms according to scan rate for the scan range from 0 to -1.6V (vs. 1 wt. % Ag/AgCl) in 500°C LiCl-KCl-$ZrCl_4$(1 wt. %): tungsten electrode (1Φ x 20 mm) for both working and counter electrodes, 1wt. % Ag/AgCl reference electrode

4.1.2.4 Peak O_4 behaviors with changing scan ranges

A set of CV at a scan rate of 500 mV/s was compared for 4 different scan ranges within 0 to -1.3 V in the LiCl-KCl-$ZrCl_4$(1 wt. %) as represented in Figure 4.9. Peak O_4 started to be noticeable at the scan range from 0 to -1.1V, and the height remained at almost constant, 9.5 mA, as the scan range became wider. Other peaks showed similar behavior to Figure 4.5.

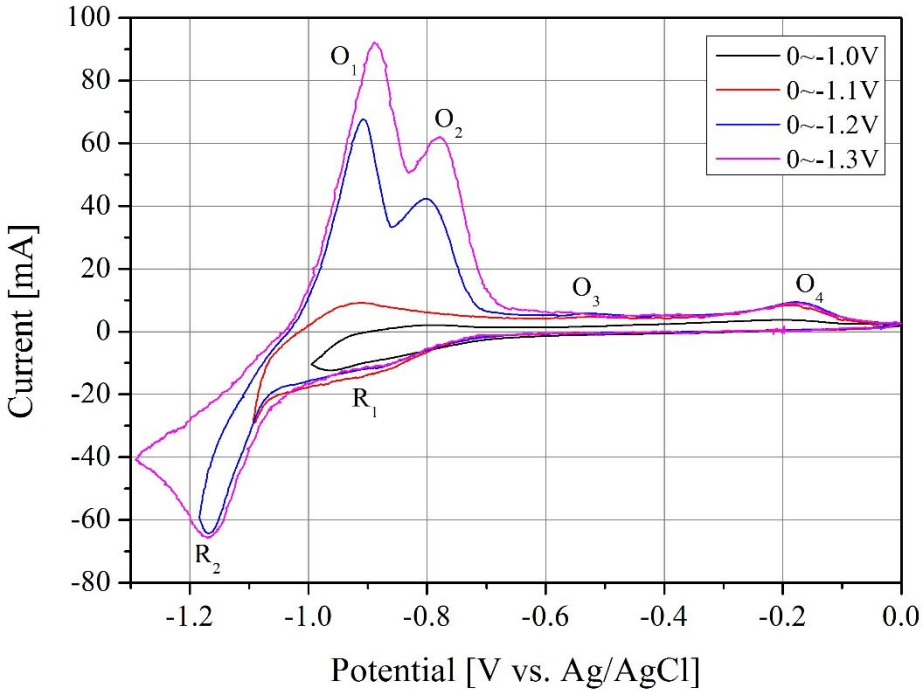

Figure 4.9 Cyclic voltammograms according to scan range for the scan rate of 500 mV/s in 500°C LiCl-KCl-$ZrCl_4$(1 wt. %): tungsten electrode (1Φ x 20 mm) for both working and counter electrodes, 1wt. % Ag/AgCl reference electrode

4.1.2.5 Concentration effects on redox peaks

From Figure 4.10 to Figure 4.14, it is represented CVs for a scan range from 0 to -1.3V in five different concentration of $ZrCl_4$ in LiCl-KCl. As $ZrCl_4$ concentration increases, peak height ratio of peak O_1 to O_2 decreases and peak O_3 becomes evident. It is also identified that peak height ratio of O_2 to O_1 tends to increase with the increase of scan rate for all $ZrCl_4$ concentration cases.

In addition, the effects of $ZrCl_4$ concentration in the LiCl-KCl on CV results were evaluated with a constant scan range from 0 to -2.0 V and a fixed scan rate of 300 mV/s as shown in Figure 4.15. The current densities of both reduction and oxidation peaks increased as the concentration of $ZrCl_4$ increased. All of reduction peaks became blurred as the concentration increased, whereas peak O_2 became clear. For the case of LiCl-KCl-$ZrCl_4$(7.5 wt. %), the reduction current increased almost proportional to potential although the actual reduction peaks were undistinguishable. Peak O_1 was not observed in this CV case and peak R_1, O_3 and O_4 did not show clear peak shape.

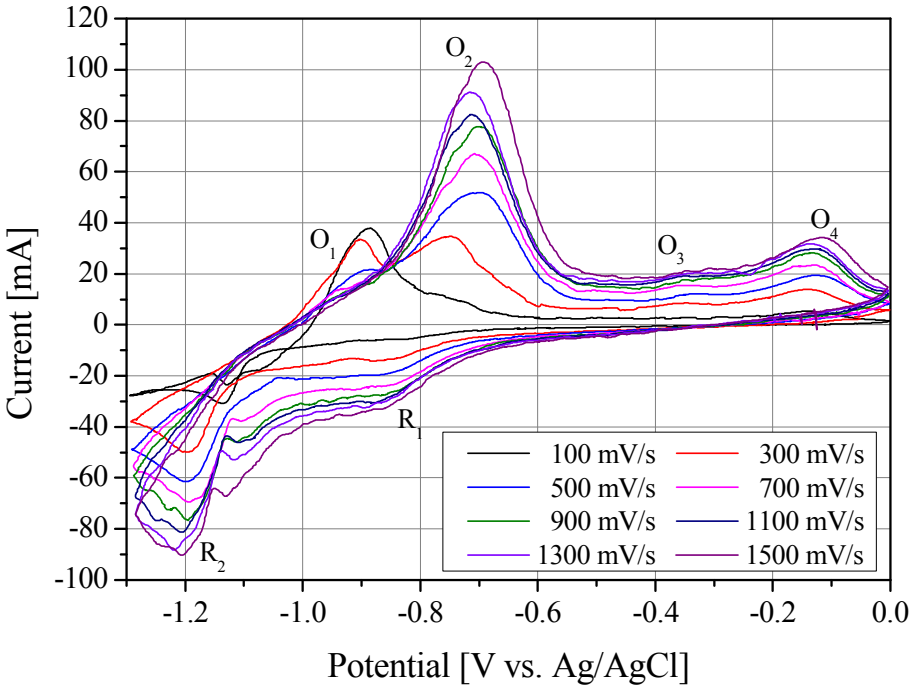

Figure 4.10 Cyclic voltammograms according to scan rate for the scan range from 0 to -1.3V (vs. 1 wt. % Ag/AgCl) in 500°C LiCl-KCl-$ZrCl_4$(0.5 wt. %): tungsten electrode (1Φ x 20 mm) for both working and counter electrodes, 1wt. % Ag/AgCl reference electrode

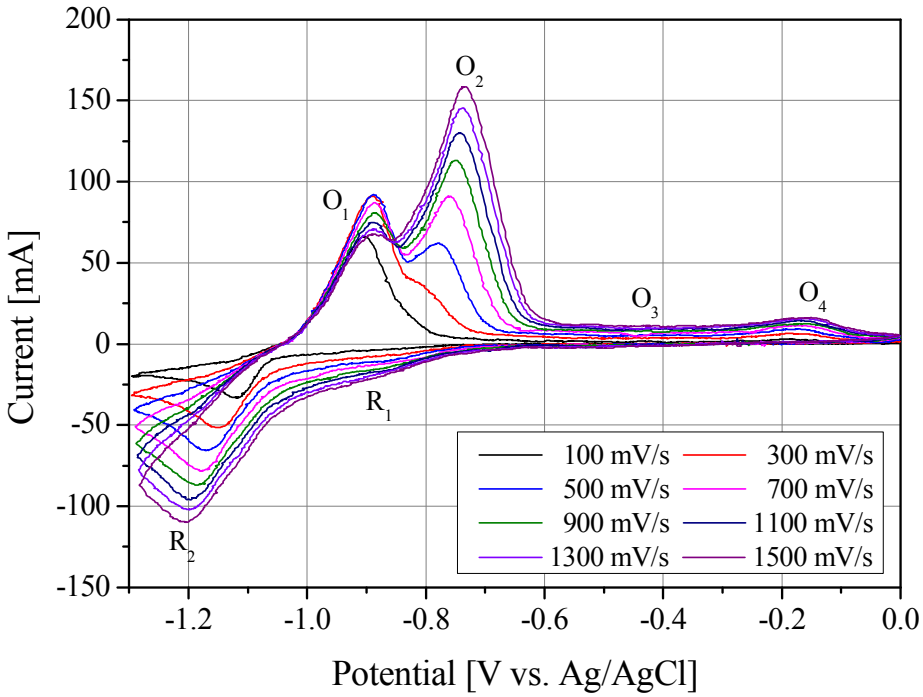

Figure 4.11 Cyclic voltammograms according to scan rate for the scan range from 0 to -1.3V (vs. 1 wt. % Ag/AgCl) in 500°C LiCl-KCl-$ZrCl_4$(1.0 wt. %): tungsten electrode (1Φ x 20 mm) for both working and counter electrodes, 1wt. % Ag/AgCl reference electrode

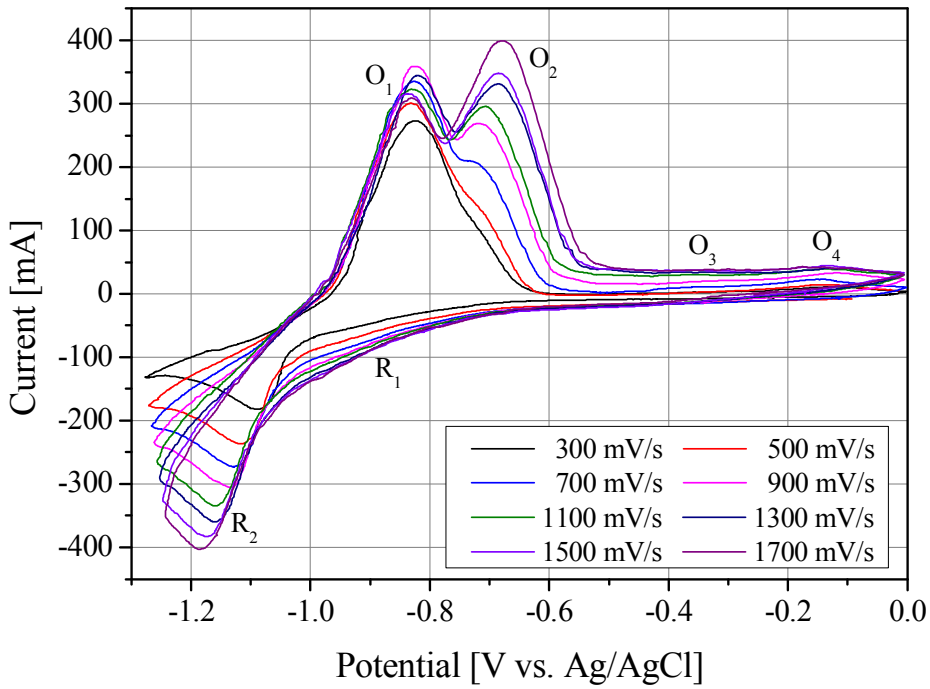

Figure 4.12 Cyclic voltammograms according to scan rate for the scan range from 0 to -1.3V (vs. 1 wt. % Ag/AgCl) in 500°C LiCl-KCl-$ZrCl_4$(2.0 wt. %): tungsten electrode (1Φ x 20 mm) for both working and counter electrodes, 1wt. % Ag/AgCl reference electrode

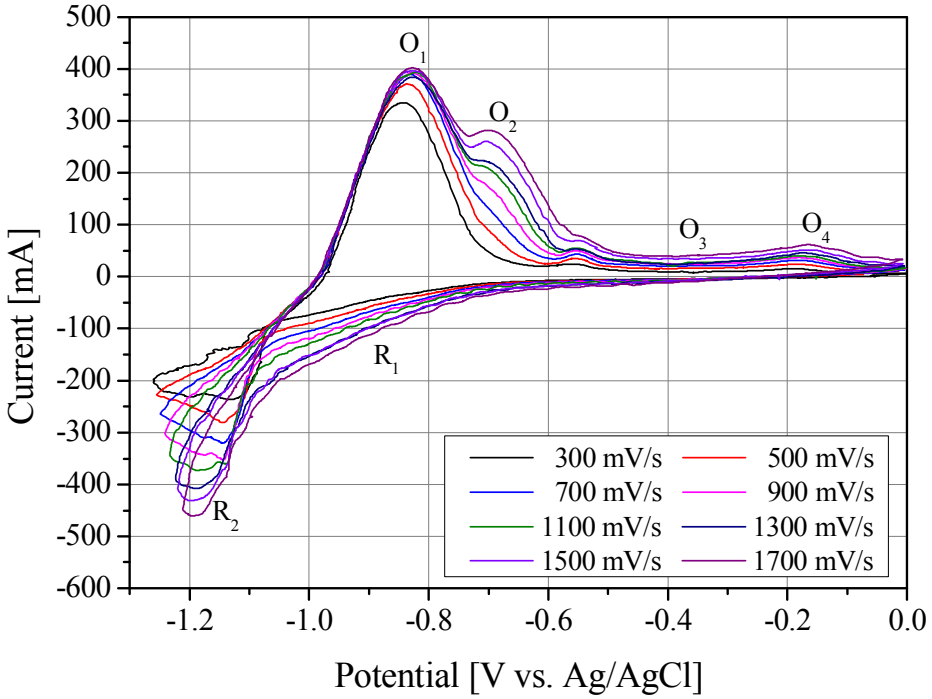

Figure 4.13 Cyclic voltammograms according to scan rate for the scan range from 0 to -1.3V (vs. 1 wt. % Ag/AgCl) in 500°C LiCl-KCl-$ZrCl_4$(4.0 wt. %): tungsten electrode (1Φ x 20 mm) for both working and counter electrodes, 1wt. % Ag/AgCl reference electrode

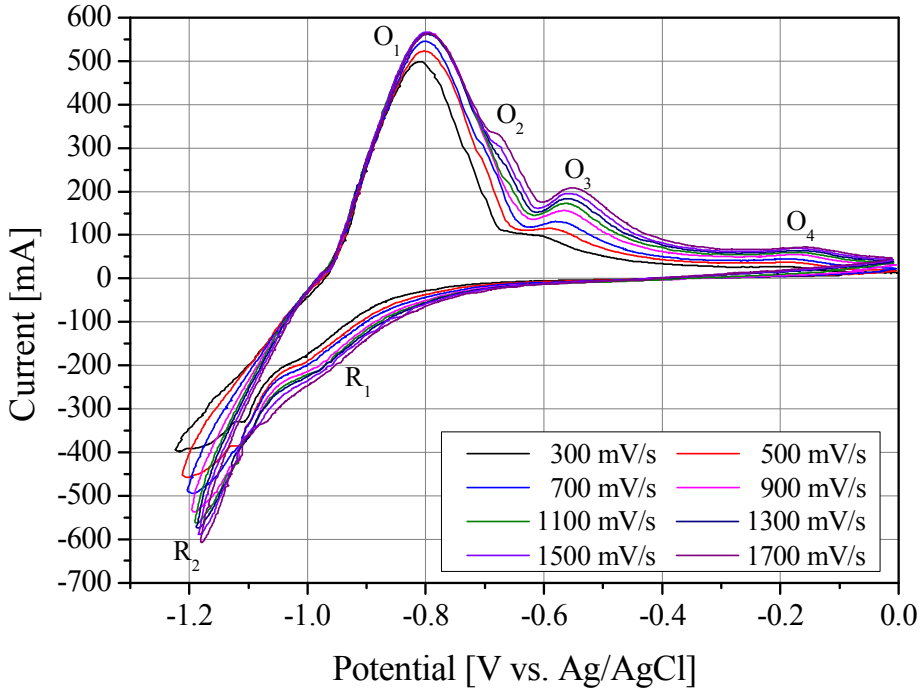

Figure 4.14 Cyclic voltammograms according to scan rate for the scan range from 0 to -1.3V (vs. 1 wt. % Ag/AgCl) in 500°C LiCl-KCl-$ZrCl_4$(8.0 wt. %): tungsten electrode (1Φ x 20 mm) for both working and counter electrodes, 1wt. % Ag/AgCl reference electrode

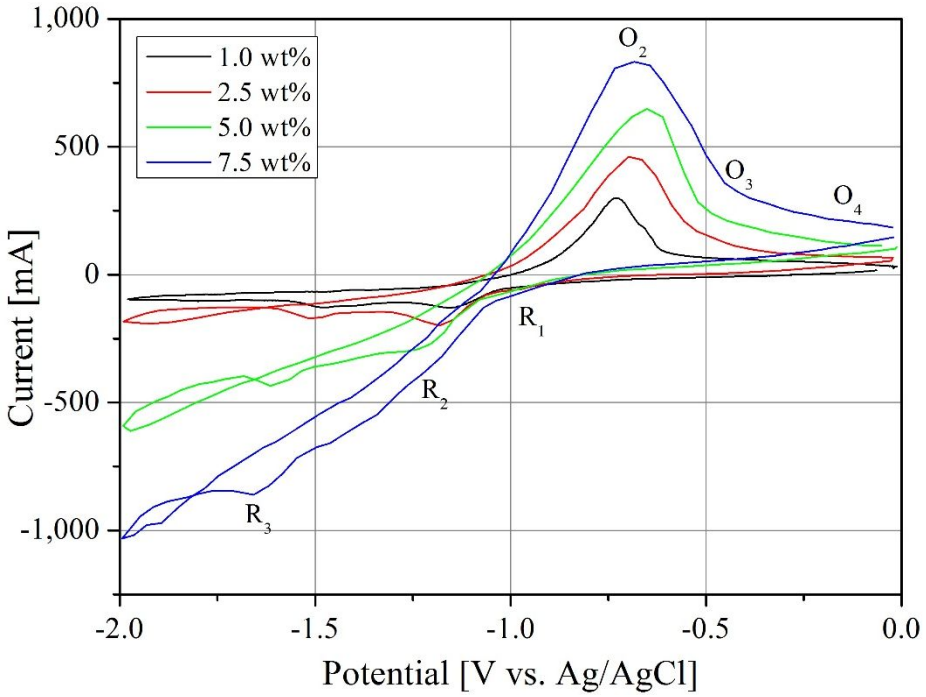

Figure 4.15 Cyclic voltammograms according to concentration of LiCl-KCl-$ZrCl_4$ for the scan rate of 300 mV/s: tungsten electrode (1Φ x 20 mm) for both working and counter electrodes, 1wt. % Ag/AgCl reference electrode

4.1.2.6 Reversibility of redox peaks

To check reversibility of each peak, the relationship between peak potential and square root of scan rate was plotted for several scan ranges as represented in Figure 9. Some peaks which were difficult to resolve were not analyzed. Peak potential depended on both scan rates and scan ranges. Peak O_1, O_4 and R_3 showed relatively small potential changes as about 19 mV (maximum 23 mV), 27 mV (maximum 38 mV) and 25 mV respectively. The potential of peak O_2 and R_2 was changed relatively large amount at about 76 mV (maximum 143 mV) and 88 mV (maximum 123 mV).

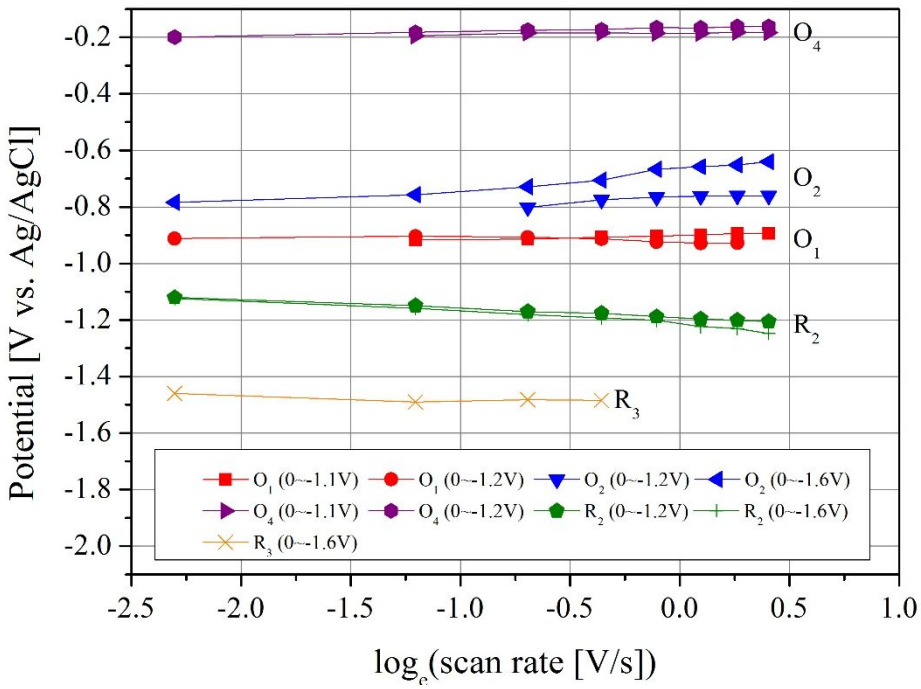

Figure 4.16 Peak potential changes according to scan rate and scan range (using cyclic voltammograms for scan range from 0.0 to -1.1, -1.2 and -1.6 V; see Figure 4.7, Figure 4.6 and Figure 4.8 respectively)

4.1.3 Discussion

Zirconium could have two soluble states, Zr(IV) and Zr(II), and two insoluble states, ZrCl and Zr metal, in the LiCl-KCl-$ZrCl_4$ at 500^oC (Sakamura, 2004; Lee et al., 2012). Since there are a lot of combinations of these states and the stabilities of these ions could be different as temperature, electrode materials, $ZrCl_4$ concentration, and other experimental variables, it is difficult to determine redox reactions for CV peaks based on only CV results without other experimental results. Therefore, in this study, previous electrolysis results in the literature are combined with the CV results to estimate zirconium redox reactions that could influence each CV peak. Major reaction for each peak is determined as represented in Figure 4.5 and Table 4.2. Reliability of cyclic voltammograms is evaluated by comparing the diffusion coefficient of Zr(IV) estimated in this study to other papers. Then, we suggested some Zircaloy-4 electrorefining conditions to recover high purity zirconium metal based on redox reactions in the LiCl-KCl-$ZrCl_4$.

Table 4.2 Comparison of reaction definitions for CV peaks in LiCl-KCl-ZrCl4 in the literature.

Peak	This study (500^oC, 1wt. % $ZrCl_4$, tungsten electrode)	Lee (500^oC, 4wt. % $ZrCl_4$, tungsten electrode) (Lee et al., 2012)	Ghosh (525^oC, 1.84E-4 mol/cm^3 $ZrCl_4$, tungsten electrode) (Ghosh et al., 2009)	Sakamura (500^oC, 0.00123 mole fraction $ZrCl_4$, tungsten electrode) (Sakamura, 2004)
O_1	$ZrCl \rightarrow Zr(IV) + 3e^-$ (major reaction) $ZrCl \rightarrow Zr(II) + e^-$	$ZrCl \rightarrow Zr(IV) + 3e^-$ $Zr \rightarrow Zr(II) + 2e^-$	$Zr \rightarrow Zr(I) + e^-$	$ZrCl \rightarrow Zr(IV) + 3e^-$
O_2	$Zr \rightarrow Zr(IV) + 4e^-$ (major reaction) $Zr \rightarrow Zr(II) + 2e^-$	$Zr \rightarrow Zr(IV) + 4e^-$	$Zr \rightarrow Zr(II) + 2e^-$ $Zr(I) \rightarrow Zr(II) + e^-$	$Zr \rightarrow Zr(IV) + 4e^-$
O_3	$Zr(II) \rightarrow Zr(IV) + 2e^-$	$Zr(II) \rightarrow Zr(IV) + 2e^-$	$Zr(II) \rightarrow Zr(IV) + 2e^-$	Not observed
O_4	$Zr(II)$ (monolayer) $\rightarrow Zr(IV) + 2e^-$ $ZrCl$ (monolayer) $\rightarrow Zr(IV) + 2e^-$	Not observed	Monolayer dissolution of Zr(II)	Not observed
R_1	$Zr(IV) + 2e^- \rightarrow Zr(II)$	$Zr(IV) + 2e^- \rightarrow Zr(II)$	$Zr(IV) + 2e^- \rightarrow Zr(II)$	$Zr(IV) + 2e^- \rightarrow Zr(II)$
R_2	$Zr(IV) + 3e^- \rightarrow ZrCl$ (major reaction) $Zr(II) + e^- \rightarrow ZrCl$ (Zr metal formation could influence this peak height but the major reaction might be ZrCl formation.)	$Zr(II) + 2e^- \rightarrow Zr$ $Zr(IV) + 3e^- \rightarrow ZrCl$	$Zr(II) + 2e^- \rightarrow Zr$ $Zr(II) + e^- \rightarrow Zr(I)$ *$Zr(I) + e^- \rightarrow Zr$ (*This reaction is located at slightly more negative potential than other reactions.)	$Zr(IV) + 4e^- \rightarrow Zr$ $Zr(IV) + 3e^- \rightarrow ZrCl$
R_3	$ZrCl + e^- \rightarrow Zr$ (major reaction) $Zr(II) + 2e^- \rightarrow Zr$ $Zr(IV) + 4e^- \rightarrow Zr$	$ZrCl + e^- \rightarrow Zr$ $Zr(IV) + 4e^- \rightarrow Zr$	Not observed	$ZrCl + e^- \rightarrow Zr$

4.1.3.1 Redox Reaction for Each Peak of Cyclic Voltammogram

We determine redox reactions of zirconium for each CV peak as following steps: 1) reviewing the literature on zirconium redox reactions to find the reactions that are consistently and widely observed, 2) determining possible reduction reactions related to ZrCl and Zr metal formation on cathode based on electrolysis results in the literature, 3) determining possible oxidation reactions based on the current CV results, and 4) matching major redox reactions to each CV peak by observing peak behaviors while changing scan rate and scan range (summarized in Table 4.2).

Overall, this study observed 4 oxidation peaks, peak O_1, O_2, O_3 and O_4, and 3 reduction peaks, R_1, R_2 and R_3. Among these peaks, reduction peak R_1 near -0.8 V (vs. 1 wt. % Ag/AgCl) and oxidation peak near -0.6 V are relatively well known as redox reactions between Zr(IV) and Zr(II) (Sakamura, 2004; Ghosh et al., 2009; Lee et al., 2012). Lee et al. has identified that peak R_1 may result from soluble-soluble reactions by electrolysis with LiCl-KCl-$ZrCl_4$(4 wt. %) at -1.0 V (vs. Ag/AgCl) cathode potential (Lee et al., 2012). Ghosh et al. and Lee at al. have estimated peak O_3 as oxidation of Zr(II) into Zr(IV) (Ghosh et al., 2009; Lee et al., 2012).

$$O_3: Zr(II) \rightarrow Zr(IV)+2e^-$$

$$R_1: Zr(IV) + 2e^- \rightarrow Zr(II)$$

Since these two peaks have much smaller peak currents than other reduction and oxidation peaks, it is expected that redox reactions between Zr(IV) and Zr(II) can be very slow. The slow reactions can be caused by small exchange current density in Butler-Volmer kinetics.

To determine reduction reactions for R_2 and R_3 peaks, XRD results on cathode deposits after electrolysis were utilized. Sakamura conducted electrolysis at cathode potential varying between -1.15 and -1.04 V as well as -1.42 and -1.35 V (vs. Ag/AgCl) (Sakamura, 2004). Mole fraction of $ZrCl_4$ in LiCl-KCl salts was 0.0026, equivalent to 1.08 wt. % similar to this study, 1.0 wt. %. Between -1.15 and -1.04 V, ZrCl was found in cathode deposits with LiCl-KCl, but Zr metal was not. Between -1.42 and -1.35 V, XRD peaks of Zr metal were found, while the peak height of ZrCl was much smaller than the previous case. Since peak R_2 was observed in the potential close to the Sakamura's first case (-1.15 and -1.04 V), peak R_2 may result from the reduction of Zr(IV) or Zr(II) into ZrCl. The dominant reaction of peak R_2 may be the reduction of Zr(IV) into ZrCl because the reduction of Zr(IV) into Zr(II), peak R_1, is slow.

$$R_2\text{: } Zr(IV) + 3e^- \rightarrow ZrCl \text{ (major reaction)}$$

$$Zr(II) + e^- \rightarrow ZrCl$$

In addition, since peak R_3 was observed in the Sakamura's second case (-1.42 and -1.35 V), peak R_3 can be caused by reaction forming Zr metal

from ZrCl, Zr(II) and Zr(IV).

$$R_3: ZrCl + e^- \rightarrow Zr \text{ (Major reaction)}$$
$$Zr(II) + 2e^- \rightarrow Zr$$
$$Zr(IV) + 4e^- \rightarrow Zr$$

In Figure 4.7, Figure 4.8, 3 oxidation peaks, O_1, O_3 and O_4, and 1 reduction peak R_1 appeared. Also, a slope change near -1.0 V might be related to peak R_2. Peak O_1 and O_4 might be related to the oxidations of Zr(II) and ZrCl. These two peak were not observed in in the scan range between 0 and -1.0 V (Figure 4.9), but became distinct in the scan range from 0 to -1.1 V or more negative value where Zr(II) and ZrCl could be produced (i.e., R_1, R_2). Since peak O_3 was defined as the oxidation reaction of Zr(II), peak O_1 might be related to the oxidation of ZrCl into Zr(IV) and Zr(II). Height of peak O_3 is relatively lower than other peaks and it could indicate that the oxidation of Zr(II) into Zr(IV) is a slow reaction. Therefore, peak O_1 might be mainly related to oxidation of ZrCl to Zr(IV).

$$O_1: ZrCl \rightarrow Zr(IV) + 3e^- \text{ (Major reaction)}$$
$$ZrCl \rightarrow Zr(II) + e^-$$

In the two oxidation peaks, peak O_4 may be related to monolayer oxidation of either ZrCl or Zr(II) or both since the height of peak was consistent with varying scan ranges from 0 ~ -1.1 V to 0 ~ -1.3 V. The

monolayer oxidation of Zr(II) can be explained because peak O_4 is still observed with the scan range between 0 and -1.6 V where most ZrCl, its competitor, could be reduced into Zr metal. On the other hand, the oxidation of monolayer ZrCl can be supported by that peak O_4 did not appear in the scan range from 0 to -1.0 V where Zr(II) can be produced. Also, the small amount of ZrCl might be remained in the scan range between 0 and -1.6 V, and involve in the reaction of peak O_4. To determine more plausible explanation on peak O_4, further electrochemical researches are required.

$$O_4\text{: } Zr(II)\ (monolayer) \rightarrow Zr(IV) + 2e^-$$

$$ZrCl\ (monolayer) \rightarrow Zr(IV) + 2e^-$$

Ghosh et al. observed a similar peak in slightly different conditions – tungsten electrodes with 1.84E-4 mol/cm^3 $ZrCl_4$ in the LiCl-KCl eutectic at 525^{o}C (Ghosh et al., 2009). That paper described that peak O_4 resulted from Zr^{2+} monolayer dissolution. Ghosh et al. added that the reason why the monolayer dissolution peak was not observed in Sakamura's results was low $ZrCl_4$ concentration. However, peak O_4 was identified in this study under the almost same $ZrCl_4$(1 wt. %) concentration with Sakamura's experiment. Therefore, the reason why peak O_4 was not observed in Sakamura's experiment is not low concentration, but it might be the difference in scan ranges. Sakamura scanned potential from -0.4 V while the potential of peak O_4 is estimated near -0.2 V.

In the case with the cathode potential scanned from 0 to -1.6 V,

peak O_1 disappeared, while O_2 became the most dominant oxidation peak as represented in Figure 6. Since peak R_3 could be caused by the formation of Zr metal from ZrCl, peak O_2 could be produced from the oxidation of Zr into Zr(II) or Zr(IV). As described above, the oxidation of Zr(II) into Zr(IV) might be slow and peak O_3 is relatively smaller than others. Peak O_2 might be mainly related to oxidation of Zr metal into Zr(IV).

$$O_2: Zr \rightarrow Zr(IV) + 4e^- \text{ (major reaction)}$$
$$Zr \rightarrow Zr(II) + 2e^-$$

In Figure 4.6, as the scan rate increased, peak O_1 decreased but peak O_2 increased. It means that the reduction of ZrCl into Zr metal could occur at the potential over -1.2 V. In addition, peak O_2 did not exist when the scan range was between 0 and -1.1 V. Thus, the equilibrium potential for the reduction of ZrCl to Zr metal in the LiCl-KCl-$ZrCl_4$(1 wt. %) might be between -1.1 and -1.2 V (vs. 1 wt. % Ag/AgCl). The exchange current density or transfer coefficient for the reaction might be very small since O_2 peak was not observed at low scan rate and there was large difference between peak R_3 potential and equilibrium potential of reduction of ZrCl. Since the equilibrium potential of the ZrCl reduction within the LiCl-KCl-$ZrCl_4$(1 wt. %)is between -1.1 and -1.2 V, Zr metal could be produced within the potential range. Lee et al. reported that they detected Zr metal on cathode deposits after electrolysis by maintaining cathode potential as -1.15 V (Lee et al., 2012). In the higher $ZrCl_4$ concentration (4 wt. %) of Lee et al.'s

experiment, the equilibrium potential for ZrCl reduction becomes more positive, so Zr metal is produced easier during electrolysis at -1.15 V.

Reversibility of each reaction was evaluated by plotting peak potential versus natural logarithm of scan rate as represented in Figure 4.16. Peak R_1 and O_3 were not analyzed because of their ambiguous peak shapes. Potential of peak O_2 and R_2 were changed by over 100 mV during the scan rate increased from 100 mV/s to 1500 mV/s. This large variation could represent that the reactions involved with these peaks are close to irreversible. Other peaks are nearly reversible because potential of other peaks were changed less than 40 mV.

Effects of $ZrCl_4$ concentration in the LiCl-KCl on the CV results is represented in from Figure 4.10 to Figure 4.14. Peak O_1 which is related to oxidation of ZrCl becomes dominant as $ZrCl_4$ concentration in LiCl-KCl increases. It could mean that high concentration of ZrCl4 makes it hard to recover zirconium as metal state without ZrCl on the cathode. In addition, in Figure 4.15, as increase of $ZrCl_4$ concentration, reduction peaks become blurred, while peak O_2 remains distinct. The reduction peak R_2 near -1.1 V is especially hard to resolve in the LiCl-KCl-$ZrCl_4$(7.5 wt. %). This may imply that ZrCl formation could still occur dominantly and compete with the reaction of ZrCl reduction into Zr metal near -1.5 V.

Identified redox reactions for each peak of cyclic voltammogram in the LiCl-KCl-$ZrCl_4$ are compared to other papers as represented in Table 4.2.

4.1.3.2 Material properties of zirconium in LiCl–KCl at

500℃

From cyclic voltammograms, diffusion coefficient and standard reduction potential could be identified. In this study, diffusion coefficient of Zr(IV) and standard reduction potentials for Zr(IV)/ZrCl and ZrCl/Zr reactions are estimated.

Peak R_2 was utilized to obtain diffusion coefficient of zirconium ion since the height of peak R_1 is hard to be identified and the reaction of peak R_3 is not the redox reaction involving zirconium ion. The reaction of peak R_2 is assumed as the reduction of Zr(IV) into ZrCl because, in a previous section, it is revealed that the reaction producing Zr(II) from Zr(IV) would be slow. In addition, in Figure 4.16, it is identified that the reaction of peak R_2 is close to irreversible. For this reason, the diffusion coefficient of Zr(IV) is obtained by Delahay equation (Bard and Faulkner, 2001),

$$\frac{i_p}{\sqrt{v}} = 0.4958nFAC\sqrt{\frac{n\alpha FD}{RT}} \tag{4.1}$$

where, i_p is the peak current, v is the scan rate, n is the number of electron participating in the reaction, F is the Faraday's constant (96,485 C/mol), A is the surface area of electrode, C is the ion concentration, α is the transfer coefficient, D is the diffusion coefficient, R is the universal gas constant (8.314 J/mol/K) and T is the absolute temperature.

Diffusion coefficients estimated from cyclic voltammograms in

Figure 4.6 and Figure 4.8 are represented in Table 4.3. The diffusion coefficient of Zr(IV) appears to be in the range of -1.28E-5 to 2.01E-5 cm^2/sec and the average is 1.63E-5 cm^2/sec when the transfer coefficient is assumed as 0.5. As scan rate increases, irreversibility of cyclic voltammetry could rise. In addition, if scan range become larger, effect of Zr(II) formation would increase. For this reason, the diffusion coefficient measured at high scan rate with the scan range from 0 to -1.2V might be more exact value. Therefore, the value of 1.28E-5 cm^2/sec would be the diffusion coefficient of Zr(IV). The estimated value is quite similar to diffusion coefficients in other papers. C. P. Fabian et al. determined the diffusion coefficient of Zr(IV) as 1.50E-5 cm^2/sec in LiCl-KCl at 500^oC by comparing computational simulations on cyclic voltammogram to experiments (Fabrian et al., 2013). In addition, D. Yamada et al. measured the diffusion coefficient of Zr(IV) as 1.13E-5 cm^2/sec in LiCl-KCl at 500^oC by a capillary method (Yamada et al., 2007a). Since the diffusion coefficient of Zr(IV) estimated in this study accords closely with diffusion coefficients obtained from other experimental and computational methods, it could be identified that cyclic voltammetries conducted in this study is reliable and the redox reactions for each peak of cyclic voltammogram are well defined.

Table 4.3 Comparison of diffusion coefficient of Zr(IV) in LiCl-KCl-$ZrCl_4$ at 500°C in the literature (using cyclic voltammograms for scan range from 0.0 to -1.2 and -1.6 V; see Figure 4, 6 respectively)

Scan rate [mV/sec]	Diffusion coefficient of Zr(IV) [cm^2/sec]				
	This study			Fabrian (determined from CV simulation) (Fabrian et al., 2013)	Yamada (measured by a capillary method) (Yamada et al., 2007a)
	Scan range		Average		
	0~-1.2V	0~-1.6V			
100	1.67E-5	1.81E-5	1.63E-5	1.50E-5	1.13E-5
300	1.33E-5	1.61E-5			
500	1.28E-5	1.53E-5			
700	1.28E-5	1.58E-5			
900	N/A	1.69E-5			
1100		1.86E-5			
1300		1.93E-5			
1500		2.01E-5			

For a peak of reversible insoluble products electrodeposition, peak potential could be defined as Eq. (4.2) (Schiffrin, 1986).

$$E_p = E^{0\prime} + \frac{RT}{nF} \ln C_{M^{n+}} + 0.8540 \frac{RT}{nF} \qquad (4.2)$$

where $E^{0'}$ is standard reduction potential and $C_{M^{n+}}$ is concentration of M^{n+} ion. From this equation, standard reduction potential could be obtained. In Figure 4.12, peak potentials of peak R_2 maintained nearly a constant at low scan rate: -1.0879 V (vs. Ag/AgCl) for the scan rate of 100 mV/sec and -1.0880 V (vs. Ag/AgCl) for the scan rate of 300 mV/sec. In this scan rate range, peak R_2 shows almost reversible behavior and Eq. (4.2) could be applied. Appling the equation, standard potential for the reaction between Zr^{4+} and ZrCl could be determined as -0.994 V (vs. Ag/AgCl). Since peak O_1 (oxidation of ZrCl into Zr(IV)) starts appearing when working electrode potential is scanned to -1.0 V, the equilibrium potential of ZrCl formation from Zr(IV) might be between -0.9 and -1.0 V (vs. Ag/AgCl). This observation agrees with the formal potential calculated from the Peak R_2 potential.

For the reduction of ZrCl into Zr metal, the standard potential would have the value between -1.1 and -1.2 V (vs. Ag/AgCl) according to the explanation in section of 4.1.3.1.

4.2 Redox behavior of Sn, Cr, Fe and Co in LiCl-KCl

4.2.1 Experimental setup

All redox behavior investigation on Sn, Cr, Fe and Co were conducted in the same experimental environment to experiments for Zr redox behavior study as represented in section of 4.1.1. An anhydrous LiCl-KCl eutectic mixture with purity of 99.99% was obtained from the Sigma Aldrich, and anhydrous $SnCl_2$, $CrCl_2$, $FeCl_2$ and $CoCl_2$ with purity of 99.99% were also supplied from the same source. Working, counter and reference electrodes were prepared as equivalent to that for experiments using $ZrCl_4$.

Molten salts of four different concentration for each chloride were utilized for CV in the electrochemical cell as represented in Table 4.4. Since concentration of $SnCl_2$, $CrCl_2$, $FeCl_2$ and $CoCl_2$ would be much smaller than that of $ZrCl_4$ during electrorefining of Zirclaoy-4 cladding, redox behaviors of these elements should be investigated in low concentration. To handle small amount of reagents, molten salt solutions of 10 wt. % were first prepared and they were diluted down to the concentration required for CVs. The mass of molten salt contained in the quartz test tube for CV is 2.54g. Each area of counter electrode and working electrode was 0.628 cm^2.

Table 4.4 Experiment sets for cyclic voltammogram of Sn, Cr, Fe and Co in LiCl-KCl salts at 500°C

	Chlorides	Concentration (wt. %)	Scan range [V vs Ag/AgCl]	Scan rate [mV/sec]
#1	$SnCl_2$	0.1 0.2 0.5 1.0	-1.0 ~ 0.5	100 ~ 1500
#2	$CrCl_2$	0.1 0.2 0.5 1.0	-1.3 ~ 0.6	100 ~ 1500
#3	$FeCl_2$	0.1 0.2 0.5 1.0	-1.0 ~ 0.6	100 ~ 1500
#4	$CoCl_2$	0.1 0.5 1.0 2.0	-0.5 ~ 0.5	100 ~ 1500

4.2.2 Cyclic voltammetry results

4.2.2.1 Cyclic voltammograms of Sn

CVs for 0.1, 0.2, 0.5 and 1.0 wt. % $SnCl_2$ salts are represented in Figure 4.17, Figure 4.18, Figure 4.19 and Figure 4.20 respectively. In CVs of low concentrations (0.1 and 0.2 wt. %), a oxidation peak and a reduction peak were identified and two oxidation peaks and a reduction peak were observed in CVs of high concentrations (0.5 and 1.0 wt. %). However, two oxidation peaks could not be clearly distinguished.

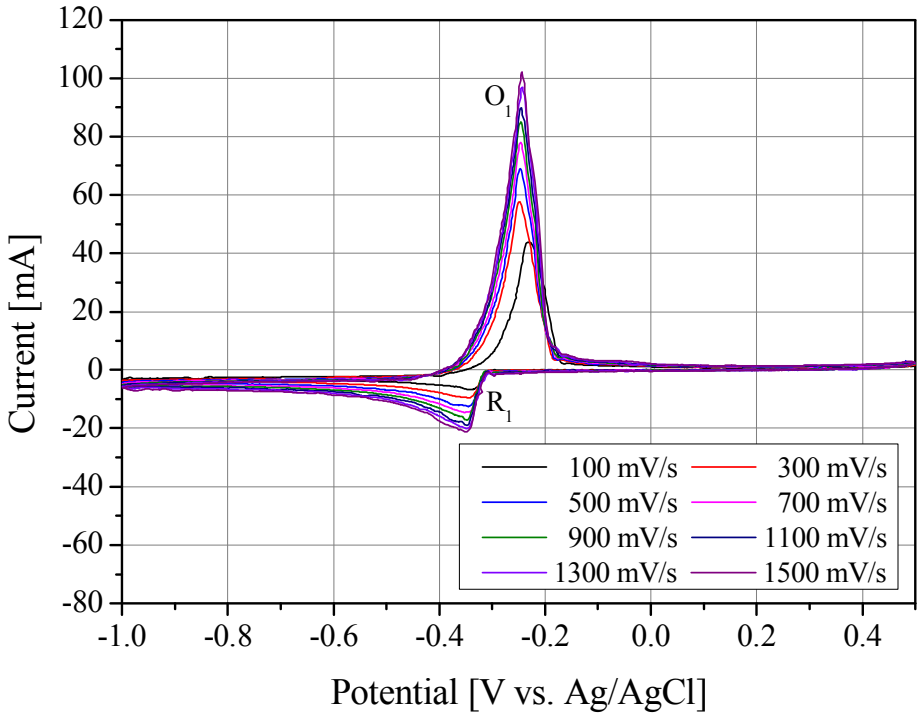

Figure 4.17 Cyclic voltammograms according to scan rate for the scan range from 0.5 to -1.0 V (vs. 1 wt. % Ag/AgCl) in 500°C LiCl-KCl-$SnCl_2$(0.1 wt. %): tungsten electrode (1Φ x 20 mm) for both working and counter electrodes, 1wt. % Ag/AgCl reference electrode

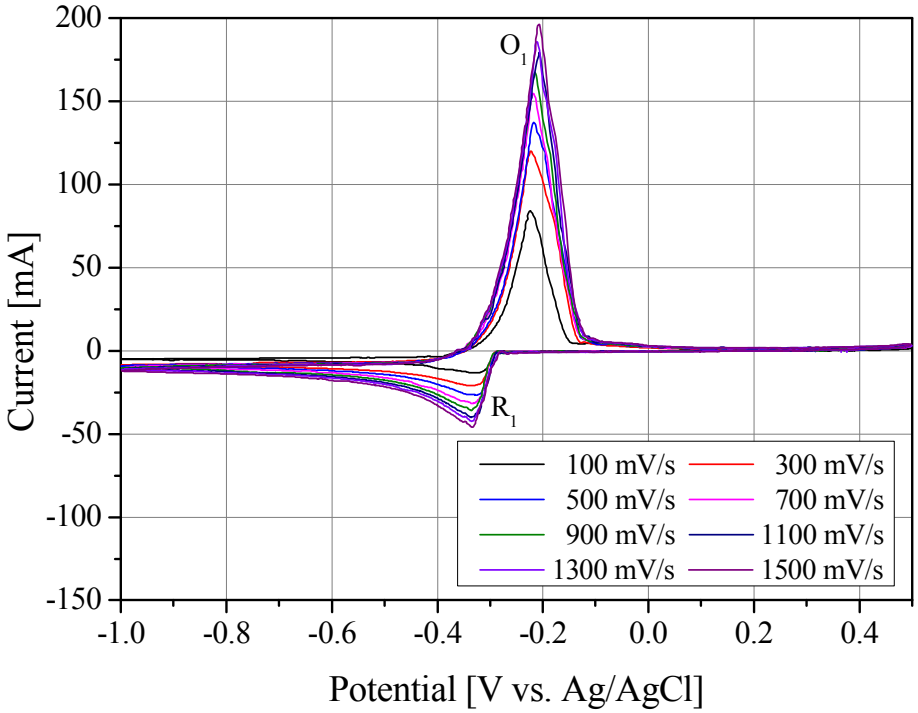

Figure 4.18 Cyclic voltammograms according to scan rate for the scan range from 0.5 to -1.0 V (vs. 1 wt. % Ag/AgCl) in 500°C LiCl-KCl-$SnCl_2$(0.2 wt. %): tungsten electrode (1Φ x 20 mm) for both working and counter electrodes, 1 wt. % Ag/AgCl reference electrode

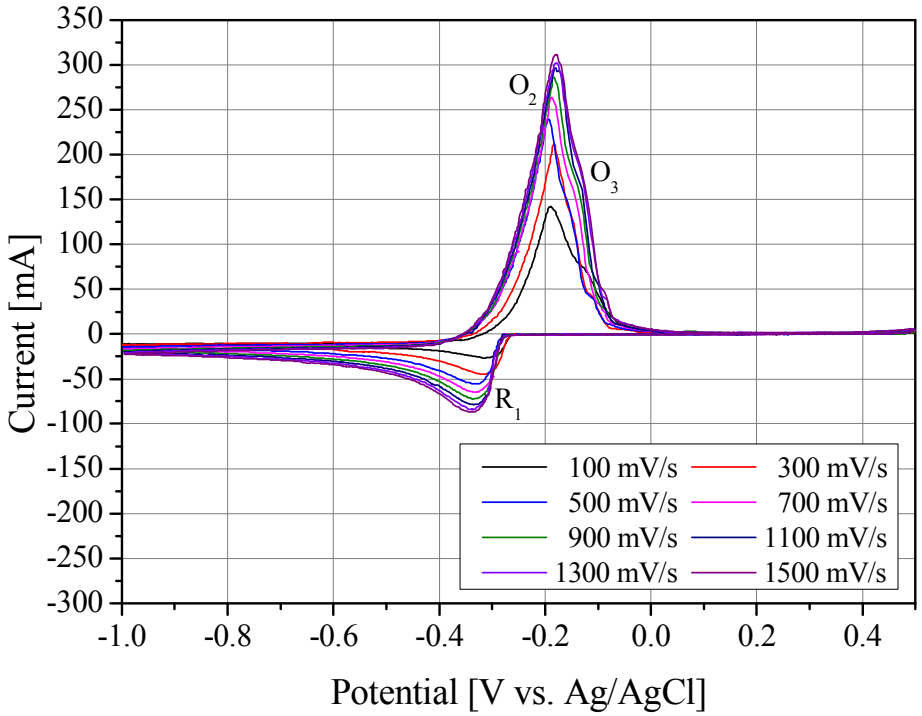

Figure 4.19 Cyclic voltammograms according to scan rate for the scan range from 0.5 to -1.0 V (vs. 1 wt. % Ag/AgCl) in 500°C LiCl-KCl-$SnCl_2$(0.5 wt. %): tungsten electrode (1Φ x 20 mm) for both working and counter electrodes, 1 wt. % Ag/AgCl reference electrode

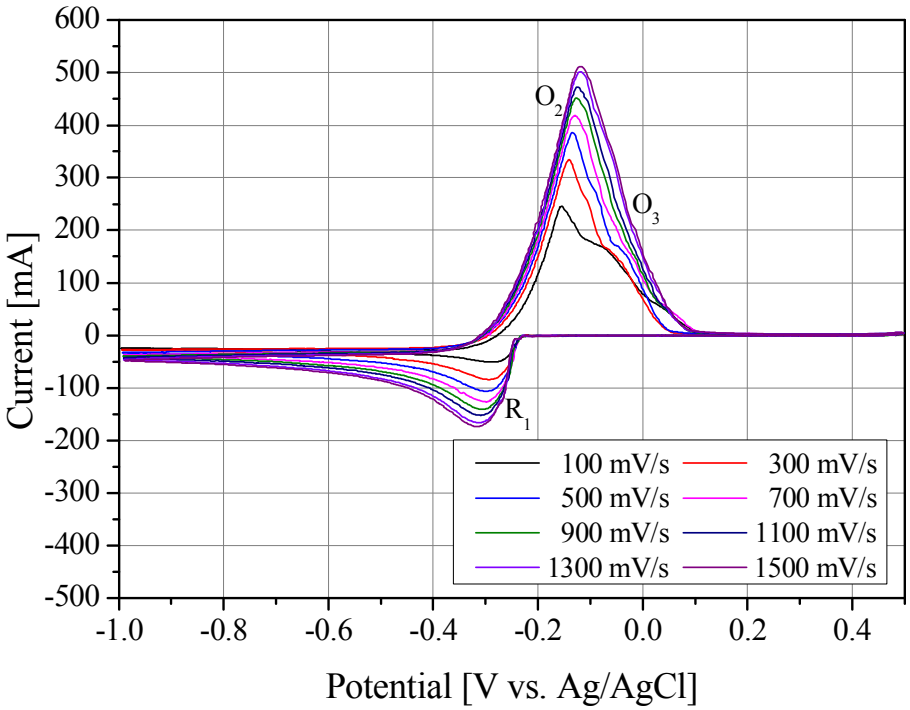

Figure 4.20 Cyclic voltammograms according to scan rate for the scan range from 0.5 to -1.0 V (vs. 1 wt. % Ag/AgCl) in 500°C LiCl-KCl-$SnCl_2$(1.0 wt. %): tungsten electrode (1Φ x 20 mm) for both working and counter electrodes, 1 wt. % Ag/AgCl reference electrode

4.2.2.2 Cyclic voltammograms of Cr

CVs for 0.1, 0.2, 0.5 and 1.0 $CrCl_2$ salts are represented in Figure 4.21, Figure 4.22, Figure 4.23 and Figure 4.24 respectively. For all concentration, two oxidation peaks and two reduction peaks were observed.

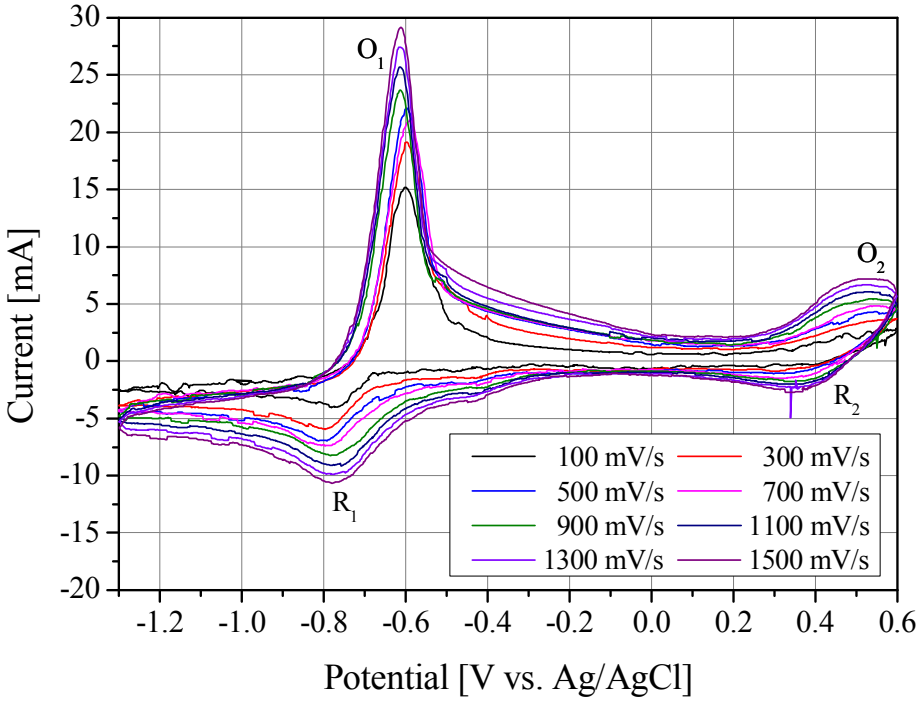

Figure 4.21 Cyclic voltammograms according to scan rate for the scan range from 0.6 to -1.3 V (vs. 1 wt. % Ag/AgCl) in 500°C LiCl-KCl-$CrCl_2$(0.1 wt. %): tungsten electrode (1Φ x 20 mm) for both working and counter electrodes, 1 wt. % Ag/AgCl reference electrode

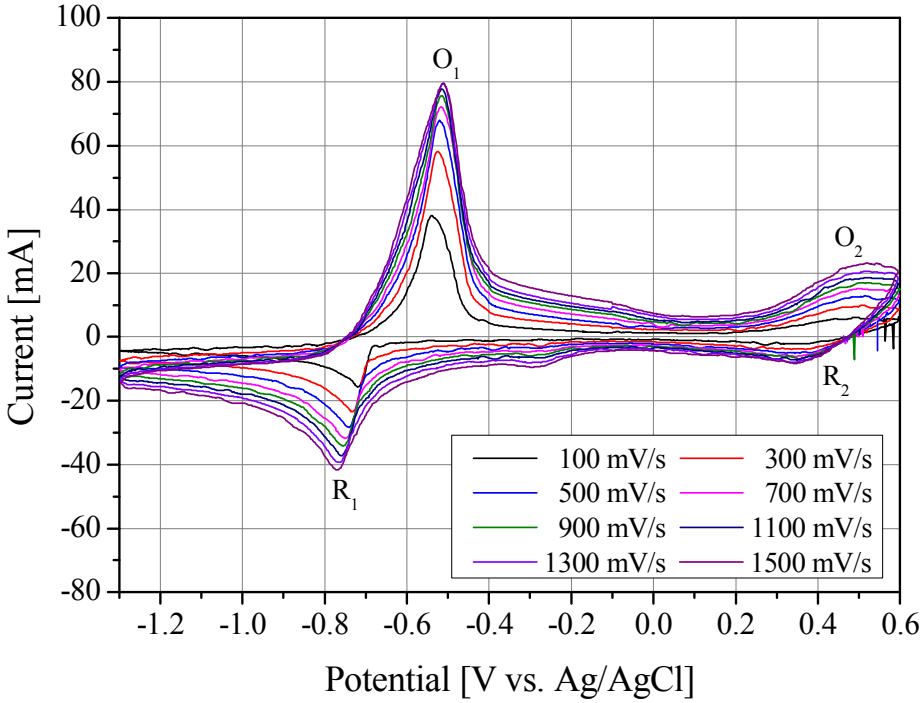

Figure 4.22 Cyclic voltammograms according to scan rate for the scan range from 0.6 to -1.3 V (vs. 1 wt. % Ag/AgCl) in 500°C LiCl-KCl-$CrCl_2$(0.2 wt. %): tungsten electrode (1Φ x 20 mm) for both working and counter electrodes, 1 wt. % Ag/AgCl reference electrode

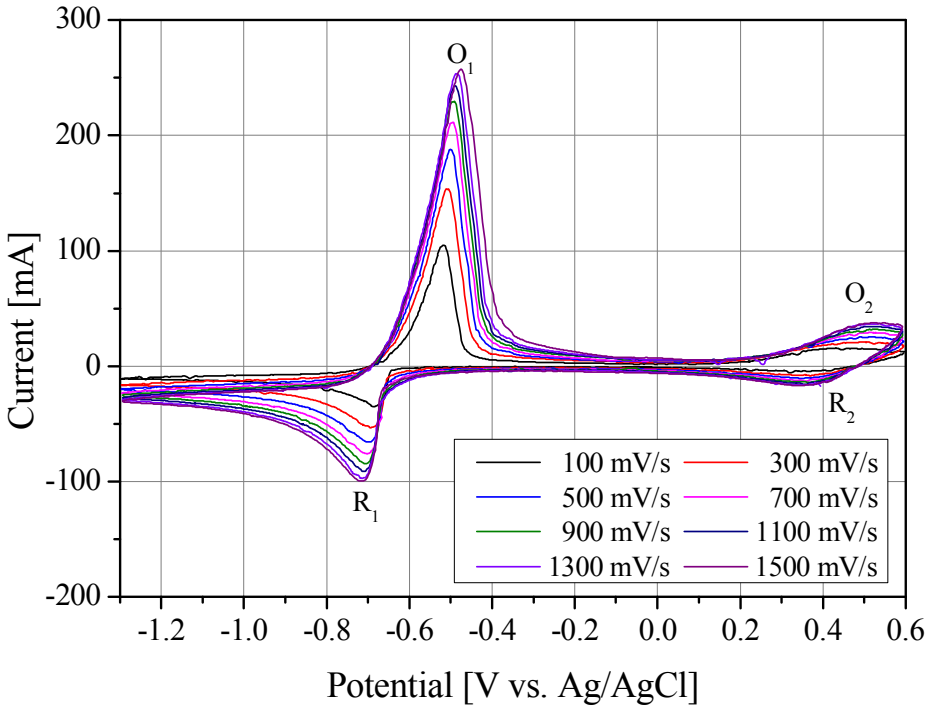

Figure 4.23 Cyclic voltammograms according to scan rate for the scan range from 0.6 to -1.3 V (vs. 1 wt. % Ag/AgCl) in 500°C LiCl-KCl-$CrCl_2$(0.5 wt. %): tungsten electrode (1Φ x 20 mm) for both working and counter electrodes, 1 wt. % Ag/AgCl reference electrode

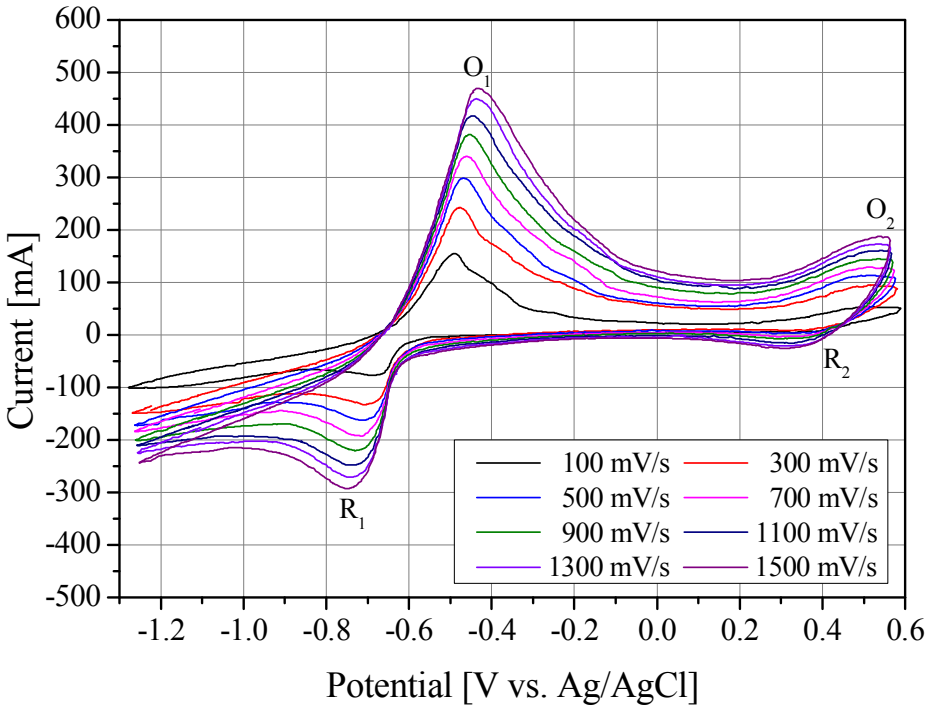

Figure 4.24 Cyclic voltammograms according to scan rate for the scan range from 0.6 to -1.3 V (vs. 1 wt. % Ag/AgCl) in 500°C LiCl-KCl-$CrCl_2$(1.0 wt. %): tungsten electrode (1Φ x 20 mm) for both working and counter electrodes, 1 wt. % Ag/AgCl reference electrode

4.2.2.3 Cyclic voltammograms of Fe

CVs for 0.1, 0.2, 0.5 and 1.0 wt. % $FeCl_2$ salts are represented in Figure 4.25, Figure 4.26, Figure 4.27 and Figure 4.28 respectively. For all concentration, single oxidation and reduction peaks were observed.

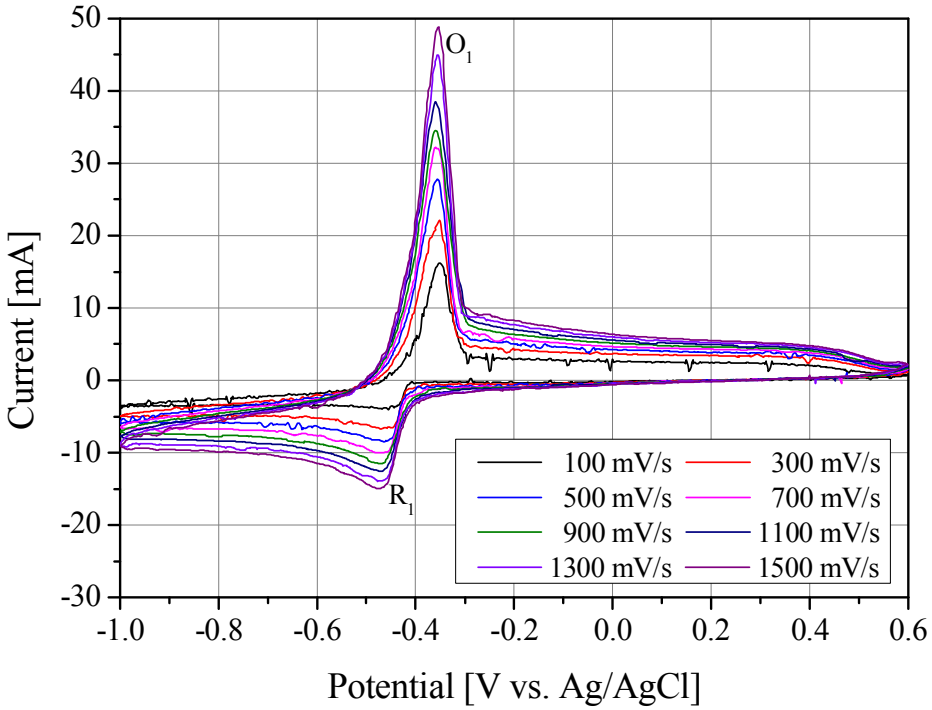

Figure 4.25 Cyclic voltammograms according to scan rate for the scan range from 0.6 to -1.0 V (vs. 1 wt. % Ag/AgCl) in 500°C LiCl-KCl-$FeCl_2$(0.1 wt. %): tungsten electrode (1Φ x 20 mm) for both working and counter electrodes, 1 wt. % Ag/AgCl reference electrode

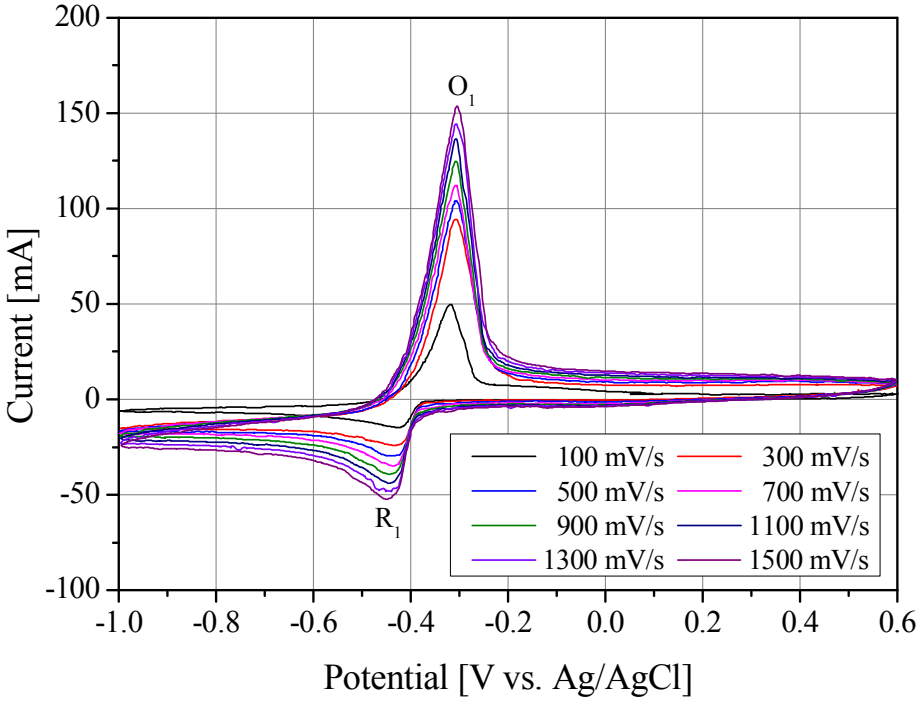

Figure 4.26 Cyclic voltammograms according to scan rate for the scan range from 0.6 to -1.0 V (vs. 1 wt. % Ag/AgCl) in 500°C LiCl-KCl-$FeCl_2$(0.2 wt. %): tungsten electrode (1Φ x 20 mm) for both working and counter electrodes, 1 wt. % Ag/AgCl reference electrode

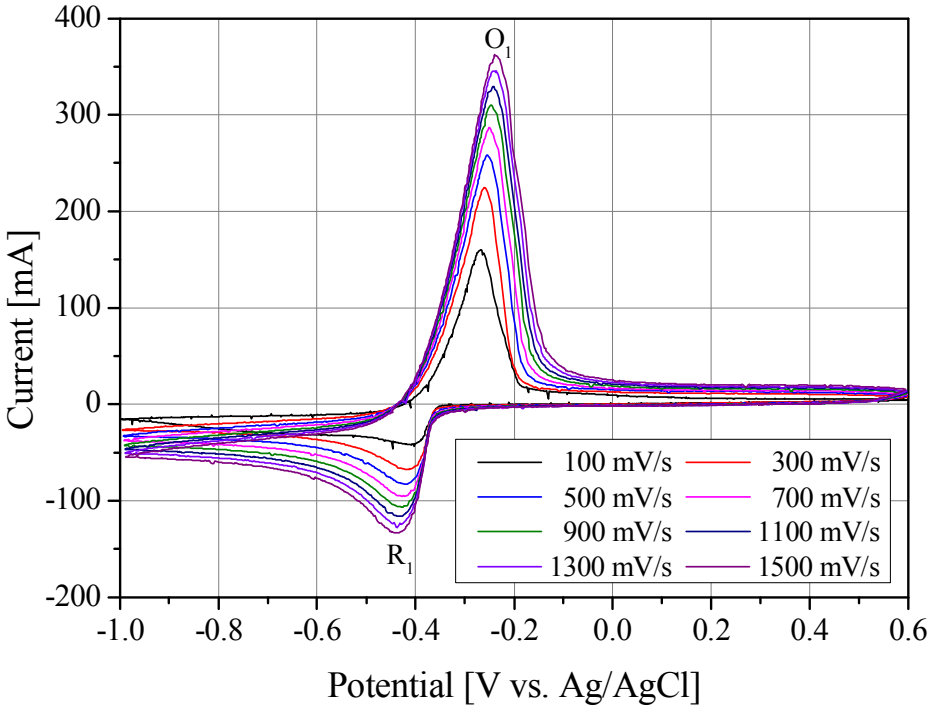

Figure 4.27 Cyclic voltammograms according to scan rate for the scan range from 0.6 to -1.0 V (vs. 1 wt. % Ag/AgCl) in 500°C LiCl-KCl-$FeCl_2$(0.5 wt. %): tungsten electrode (1Φ x 20 mm) for both working and counter electrodes, 1 wt. % Ag/AgCl reference electrode

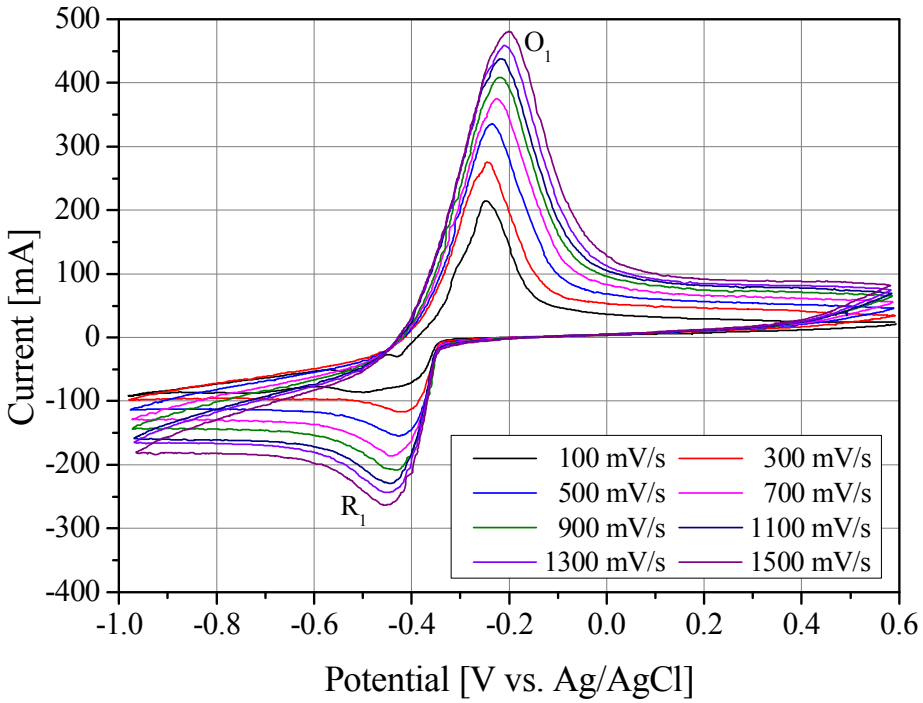

Figure 4.28 Cyclic voltammograms according to scan rate for the scan range from 0.6 to -1.0 V (vs. 1 wt. % Ag/AgCl) in 500°C LiCl-KCl-$FeCl_2$(1.0 wt. %): tungsten electrode (1Φ x 20 mm) for both working and counter electrodes, 1 wt. % Ag/AgCl reference electrode

4.2.2.4 Cyclic voltammograms of Co

CVs for 0.1, 0.2, 0.5 and 1.0 wt. % $FeCl_2$ salts are represented in Figure 4.29, Figure 4.30, Figure 4.31 and Figure 4.32 respectively. For all concentration, single oxidation and reduction peaks were observed.

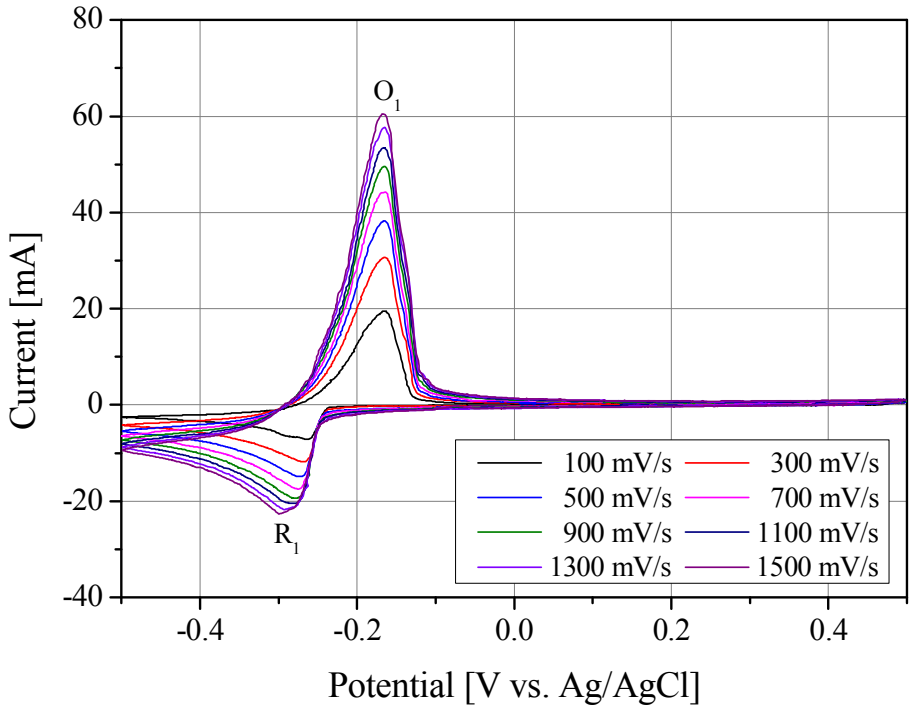

Figure 4.29 Cyclic voltammograms according to scan rate for the scan range from 0.5 to -0.5 V (vs. 1 wt. % Ag/AgCl) in 500°C LiCl-KCl-$CoCl_2$(0.1 wt. %): tungsten electrode (1Φ x 20 mm) for both working and counter electrodes, 1 wt. % Ag/AgCl reference electrode

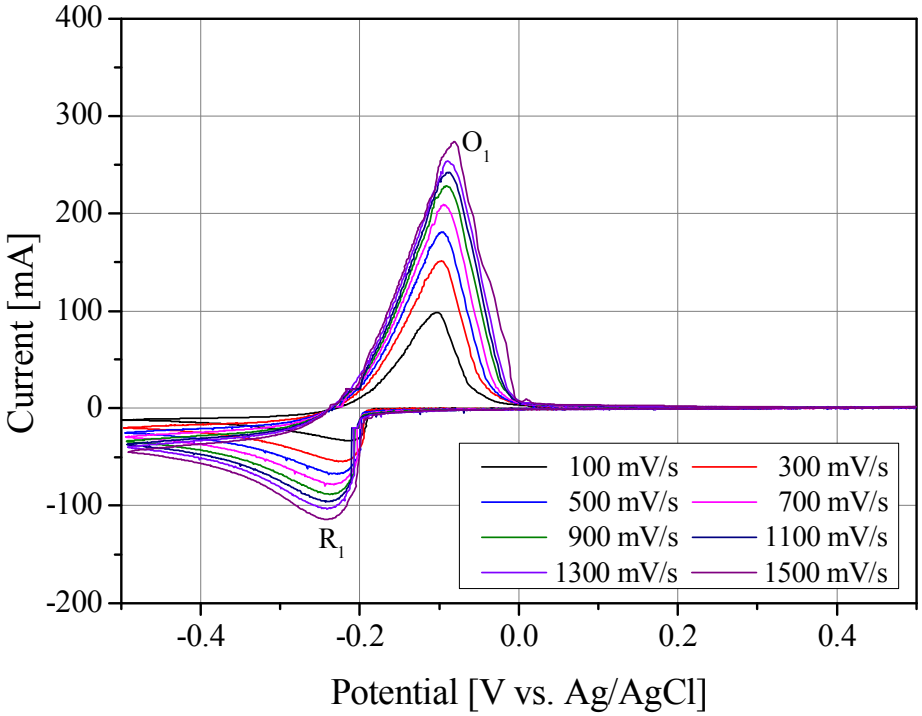

Figure 4.30 Cyclic voltammograms according to scan rate for the scan range from 0.5 to -0.5 V (vs. 1 wt. % Ag/AgCl) in 500°C LiCl-KCl-$CoCl_2$(0.5 wt. %): tungsten electrode (1Φ x 20 mm) for both working and counter electrodes, 1 wt. % Ag/AgCl reference electrode

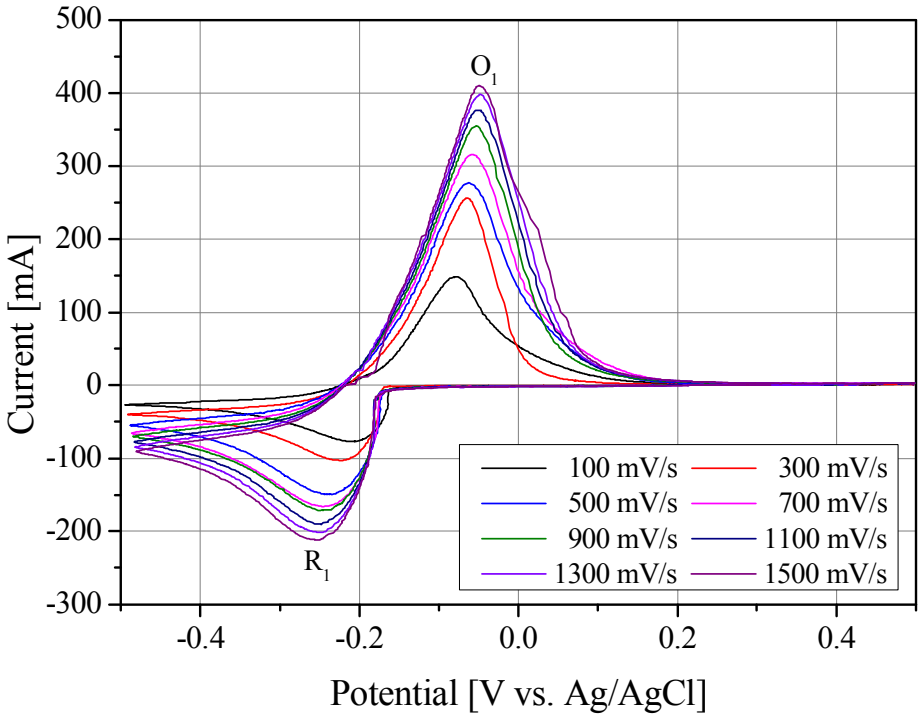

Figure 4.31 Cyclic voltammograms according to scan rate for the scan range from 0.5 to -0.5 V (vs. 1 wt. % Ag/AgCl) in 500°C LiCl-KCl-$CoCl_2$(1.0 wt%): tungsten electrode (1Φ x 20 mm) for both working and counter electrodes, 1 wt. % Ag/AgCl reference electrode

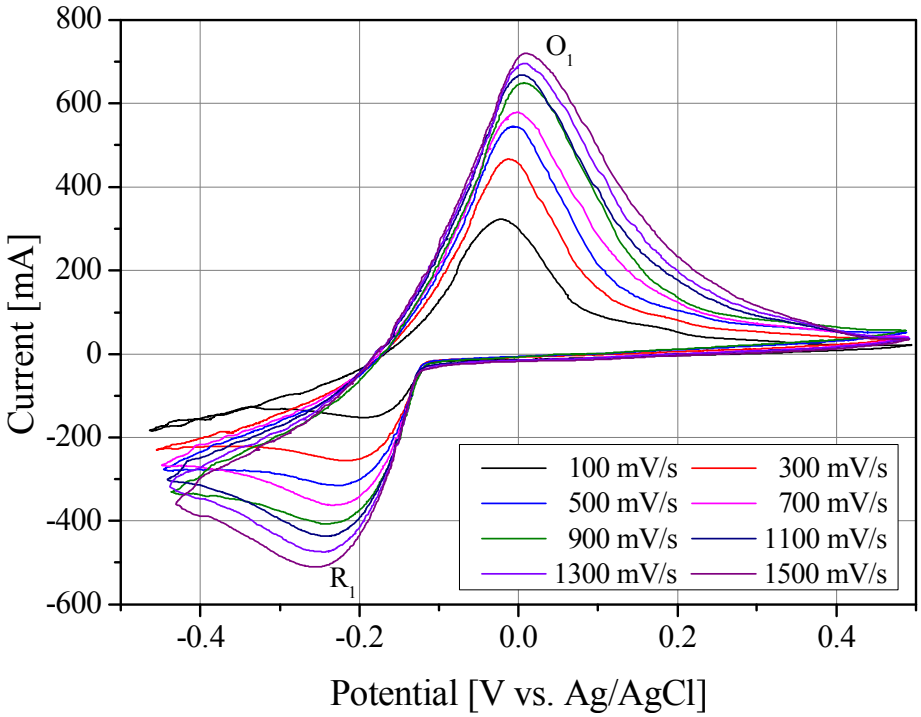

Figure 4.32 Cyclic voltammograms according to scan rate for the scan range from 0.5 to -0.5 V (vs. 1 wt. % Ag/AgCl) in 500°C LiCl-KCl-$CoCl_2$(2.0 wt. %): tungsten electrode (1Φ x 20 mm) for both working and counter electrodes, 1 wt. % Ag/AgCl reference electrode

4.2.3 Discussion

4.2.3.1 Redox reactions for each peak of cyclic voltammogram

Since there was only a pair of redox peak for $SnCl_2$ at low concentration (0.1 and 0.2 wt. %), redox reaction for Sn in LiCl-KCl could be determined as reactions between Sn and Sn(II):

$$R_1: Sn(II) + 2e^- \rightarrow Sn \text{ and}$$

$$O_1: Sn \rightarrow Sn(II) + 2e^-.$$

At high concentration of $SnCl_2$ (0.5 and 1.0 wt. %), oxidation peak looks like a superposed shape of two peaks (O_2 and O_3). Therefore, it would be expected that oxidation of Sn could occur in two steps:

$$O_2: Sn \rightarrow Sn(I) + e^- \text{ and}$$

$$O_3: Sn(I) \rightarrow Sn(II) + e^-.$$

However, since melting point of Sn is about 232^{o}C which is much lower than molten salt temperature of 500^{o}C, reduced Sn metal from Sn(II) could move away from electrode surface as a liquid metal state and this could result in changes of effective area of working electrode and distortion of oxidation peak shape. This phenomenon could become serious in high

concentration of $SnCl_2$ salts with low scan rate. While potential sweeps from positive side to negative side in high concentration salts, more amount of liquid Sn metal could be produced on working electrode and this could make electrode surface complicated. If scan rate is fast enough, most of reduced Sn would stay near working electrode and effective area of working electrode would not be changed severely.

For all concentration of $CrCl_2$ salts, two clear redox peak pairs were observed. Since peak O_1 of CVs for $CrCl_2$ shows almost symmetric shape with peak potential as the center without a diffusion tail which would be produced by ion mass transfer, peak O_1 might be related to an oxidation reaction of Cr metal and peak R_1 might be related to a reduction reaction producing Cr metal. Peak O_2 and R_2 has more fluent curves with diffusion tail and it would mean that they are related to redox reaction between soluble-soluble states. Since it has revealed that Cr(II) and Cr(III) are stable ion state in LiCl-KCl, redox reactions for redox peaks of $CrCl_2$ CV would be defined as follow (Inman et al., 1975; Levy and Reinhardt, 1975; Cotarta et al., 1997; Bonciocat and Cotarta, 2002):

$$R_1: Cr(II) + 2e^- \rightarrow Cr,$$

$$O_1: Cr \rightarrow Cr(II) + 2e^-,$$

$$R_2: Cr(III) + e^- \rightarrow Cr(II) \text{ and}$$

$$O_2: Cr(II) \rightarrow Cr(III) + e^-.$$

CVs for $FeCl_2$ and $CoCl_2$ have a single redox peak pair. Therefore,

redox reactions for these elements in LiCl-KCl could be determined relatively easily. Redox reaction of $FeCl_2$ for each peak would be determined as

$$R_1: Fe(II) + 2e^- \rightarrow Fe \text{ and}$$
$$O_1: Fe \rightarrow Fe(II) + 2e^-.$$

Redox reaction of $CoCl_2$ for each peak would be determined as

$$R_1: Co(II) + 2e^- \rightarrow Co \text{ and}$$
$$O_1: Co \rightarrow Co(II) + 2e^-.$$

4.2.3.2 Material properties of Sn, Cr, Fe and Co in LiCl–KCl at 500°C

In the same manner as CVs for $ZrCl_4$, diffusion coefficients and formal reduction potentials were calculated for Sn, Cr, Fe and Co. Since redox peak behaviors are close to reversible with small peak potential changes, a peak current equation for reversible reaction introduced by D. J. Schiffrin was utilized to estimate diffusion coefficient (Schiffrin, 1986):

$$i_p = 1.082nFAC\sqrt{\frac{nFDv}{RT\pi}} \quad (4.3)$$

Since reversible behavior is intensified at high concentration and low scan rate, the equation is applied at the highest concentration where peak could be defined clearly with the lowest scan rate. Diffusion coefficients obtained from CVs are represented in Table 4.5.

Diffusion coefficient of Sn(II) is estimated as 3.17E-9 m^2/s in molten salt of 0.5 wt. % with scan rate of 0.1 V/s. Measured diffusion coefficient of Sn(II) matches well with previous studies. H. El Ghallali measured diffusion coefficients of Sn(II) as from 2.86 to 3.94E-9 m^2/s using chronopotentiometry and as from 3.60 to 4.40E-9 m^2/s using cyclic voltammetry (El Ghallali et al., 2009). Diffusion coefficient of Cr(II) is calculated as 1.72E-9 m^2/s in 0.5 wt. % $CrCl_2$ salts with 0.1 V/s scan rate. The measured value is quiet similar to diffusion coefficients reported in previous study. D. Inman measured diffusion coefficient of Cr(II) as from 1.21E-9 to 1.86E-9 m2/s in different concentration of LiCl-KCl-$CrCl_2$ salts at 500^oC by chronopotentiometry (Inman et al., 1975). Diffusion coefficient of Fe(II) is obtained as 2.61E-9 in 0.5 wt. % $FeCl_2$ salts with 0.1 V/s scan rate. The measured value is also quiet similar to diffusion coefficients reported in previous study. D. Inman reported the diffusion coefficient of Fe(II) as from 2.08E-9 to 2.26E-9 by conducting chronopotentiometry in different concentration at 500^oC (Inman et al., 1978). Diffusion coefficient of Co(II) is measured as 3.24E-9 m^2/s in 0.5 wt. % $CoCl_2$ with 0.1 V/s scan rate. The measured value is almost equivalent to diffusion coefficients reported in previous study. H. Groult reported the diffusion coefficient of Co(II) as 3.74E-9 m^2/s by conducting chronopotentiometry in 0.02 mol/l $CoCl_2$ salts at

500^{o}C (Groult et al., 2010).

Formal potentials for Sn, Cr, Fe and Co are calculated by Eq. (4.2) and they are represented in Table 4.6 and they are compared to values from previous study of M. Iizuka. Since standard potentials of M.Iizuka are reported based on a reference electrode of Cl^{-}/Cl_2, if differences to values from previous study are equivalent regardless of elements, it could be clarified that measured values are reliable. The differences are almost consistent as 1.1 V. Therefore, it could be identified that CVs are conducted reliably.

Table 4.5 Diffusion coefficients of Sn(II), Cr(II), Fe(II) and Co(II) in LiCl-KCl at 500°C

Ion	This study [m^2/s]	Other literatures [m^2/s]
Sn^{2+}	3.17E-9	2.86~3.94[a] 3.60~4.40[a]
Cr^{2+}	1.72E-9	1.21~1.86E-9[b]
Fe^{2+}	2.61E-9	2.08~2.26E-9[c]
Co^{2+}	3.24E-9	3.74E-9[d]

[a](El Ghallali et al., 2009)

[b](Inman et al., 1975)

[b](Inman et al., 1978)

[d](Groult et al., 2010)

Table 4.6 Formal potential of Sn(II), Cr(II), Fe(II) and Co(II) in LiCl-KCl at 500°C

Reaction	This study [V vs. Ag/AgCl]	M. Iizuka[a] [V vs. Cl^-/Cl_2] (Iizuka et al., 2001)	Difference between this study and previous study [V]
Sn^{2+}/Sn	-0.156	-1.298	1.142
Cr^{2+}/Cr	-0.601	-1.641	1.040
Fe^{2+}/Fe	-0.288	-1.388	1.100
Co^{2+}/Co	-0.089	-1.207	1.118

[a]standard redox potential

4.3 Lab-scale electrorefining of unirradiated Zircaloy-4 specimen

4.3.1 Experimental setup

Lab-scale Electrorefining of Zirclaoy-4 experiments were conducted using equivalent equipment for CV experiments. Electrochemical cell was prepared as represented in Figure 4.33. Quartz tube with an inner diameter of 27 mm, an outer diameter of 30 mm and a height of 380 mm was utilized for a molten salt container. Tungsten rod with a diameter of 3.175 mm and purity of 99.95% obtained from Alfa Aessa was used for a cathode. Anode basket made of 316 stainless steel with each side of 10 mm and height of 30 mm was utilized. The reference electrode was a 1 wt. % Ag/AgCl electrode. Since prepared quartz cell is large enough to place thermocouple, temperature of molten salts was measured directly in the electrorefining cell using a k-type thermocouple. Mixture of anhydrous LiCl-KCl salts with purity of 99.99% from Sigma Aldrich and anhydrous $ZrCl_4$ with purity of 99.99% from the same source was used as electrolyte. Six Zircaloy-4 cuts having size of about 5 x 10 x 2mm were loaded into the anode basket as represented in Figure 4.34.

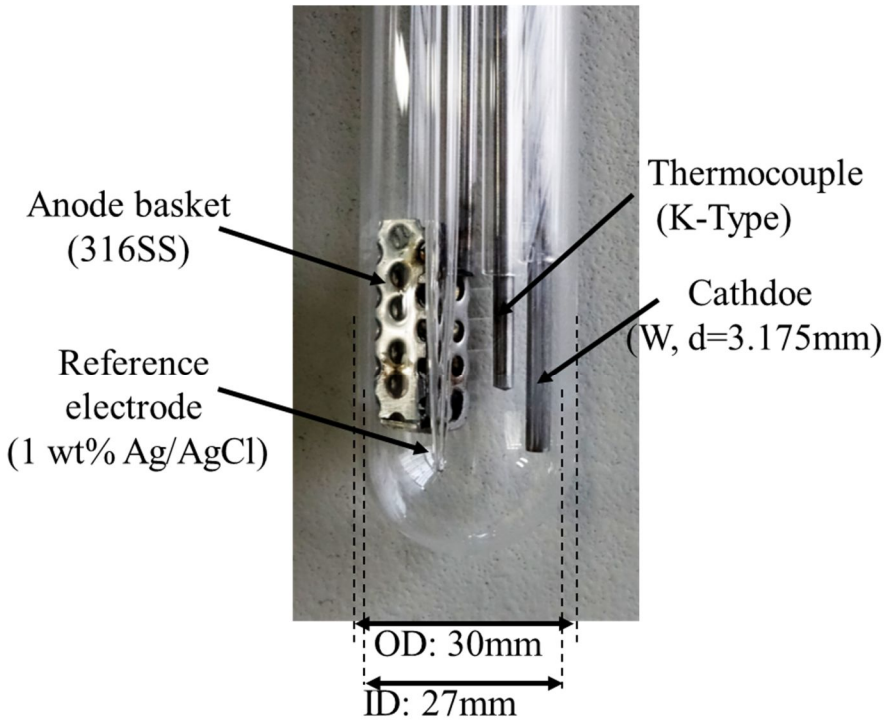

Figure 4.33 Configuration of lab-scale Zircaloy-4 electrorefining cell

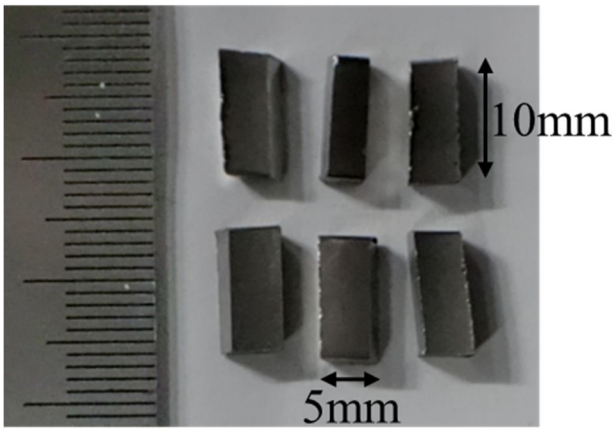

Figure 4.34 Zircaloy-4 cuts for lab-scale electrorefining experiment

To recover high purity zirconium without other elements such as Sn, Cr, Fe and Co by suppressing dissolution of these elements, all electrorefining experiments were conducted by controlling anode potential. Since these elements have much positive formal reduction potential as represented in Table 4.7, these elements would be deposited on cathode and contaminate cathode deposits if these elements are dissolved from anode basket. Among these elements, Cr is the most oxidative element and it means that contamination from Cr likely occur. LiCl-KCl regent used in electrorefining experiments contains Cr of 10 ppm as impurity and the equilibrium potential of Cr in this salt is about -0.899 V (vs. Ag/AgCl). Therefore, to minimize the dissolution of Cr, anode potential is maintained as -0.9 V (vs. Ag/AgCl) for all electrorefining experiments.

Total five electrorefining experiments with different concentrations of $ZrCl_4$ (0.1, 0.5, 1.0, 2.0 and 4.0 wt. % $ZrCl_4$) were conducted for about 5 hours to investigate the effect of $ZrCl_4$ concentration to chemical form of cathode deposits. Since ZrCl oxidation peak diminishes as $ZrCl_4$ concentration decreases as revealed in section 4.1, it is expected that cathode deposit will be Zr metal in low concentration of $ZrCl_4$ and ZrCl in high concentration of $ZrCl_4$. Composition of cathode deposits was investigated by Inductively coupled plasma mass spectrometry (ICP-MS) and chemical form was identified by X-ray diffraction (XRD).

Table 4.7 Formal reduction potentials on major reactions which could occur during Zircaloy-4 electrorefining

Reaction	Formal reduction potential[a] [V vs. Ag/AgCl]
Zr^{4+}/ZrCl	-0.994
ZrCl/Zr	-1.1 ~ -1.2
Sn^{2+}/Sn	-0.156
Cr^{2+}/Cr	-0.601
Fe^{2+}/Fe	-2.88
Co^{2+}/Co	-0.089

[a] these values are measured by CVs in section of 4.1 and 4.2.

4.3.2 Electrorefining Results

Composition of Zircaloy-4 specimen was investigated by ICP-MS as represented in Table 4.8. The zircaloy-4 specimen was mainly composed of Zr of 98.6 wt. % and there were also some amount of Sn, Cr and Fe as major elements and Co as an impurity. Other elements could also exist in Zircaloy-4 specimen but they were not analyzed because amount of these elements might be very small. For all electrorefining experiments, high purity zirconium of almost 100% was recovered from the cathode deposits as represented in Table 4.8. Concentrations of Sn, Cr, Fe and Co were below detection limits of ICP-MS.

Table 4.8 Comparison of compositions of cathode deposits after Zircaloy-4 electrorefining to previous study

		This study						Lee (Lee et al., 2012)	
$ZrCl_4$ concentration [wt. %]		Zircaloy-4 specimen	0.1	0.5	1.0	2.0	4.0	4.0	4.0
Operating condition			Anode potential is maintained as -0.9 V to prevent dissolution of all elements except Zr.					Cathode potential was maintained at -1.15 V	Cathode potential was maintained at -1.55V
Composition of cathode deposits [wt. %]	Zr	98.6	Over 99.999	Over 99.999	Over 99.999	Over 99.999	Over 99.999	99.44	98.95
	Sn	1.104	N/D	N/D	N/D	N/D	N/D	0.56	0.87
	Cr	0.0830	N/D	N/D	N/D	N/D	N/D	N/D	0.14
	Fe	0.1595	N/D	N/D	N/D	N/D	N/D	N/D	0.04
	Co	0.0016	N/D	N/D	N/D	N/D	N/D	Not analyzed	
Chemical form of zirconium deposits			Zr	Zr	Zr and ZrCl	ZrCl	ZrCl	ZrCl and Zr	

For all electrorefining experiments, zirconium was recovered as powder on the cathode but chemical forms of cathode deposits were different in different concentration of $ZrCl_4$. When concentrations of $ZrCl_4$ in LiCl-KCl salts were low as 0.1 and 0.5 wt. %, zirconium was recovered as a metal state without ZrCl. On the other hand, when concentration of $ZrCl_4$ in LiCl-KCl salts were relatively high as 2.0 and 4.0 wt. %, zirconium was recovered as ZrCl without Zr metal. After the electrorefining in LiCl-KCl-$ZrCl_4$ (1.0 wt. %), both Zr metal and ZrCl were observed at cathode deposits. For all experiments, some amount of LiCl-KCl-$ZrCl_4$ salts trapped in cathode deposits were observed with Zr metal in XRD patterns of cathode deposits.

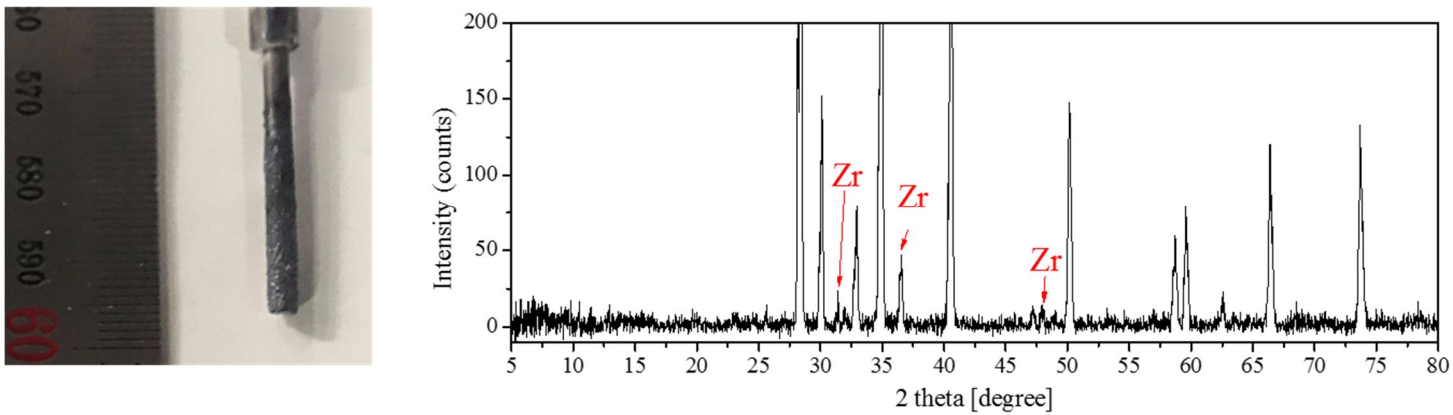

Figure 4.35 Picture (left) and XRD results (right) of cathode deposits after electrorefining in LiCl-KCl-$ZrCl_4$(0.1 wt. %): unnamed XRD peaks are resulting from LiCl-KCl-$ZrCl_4$

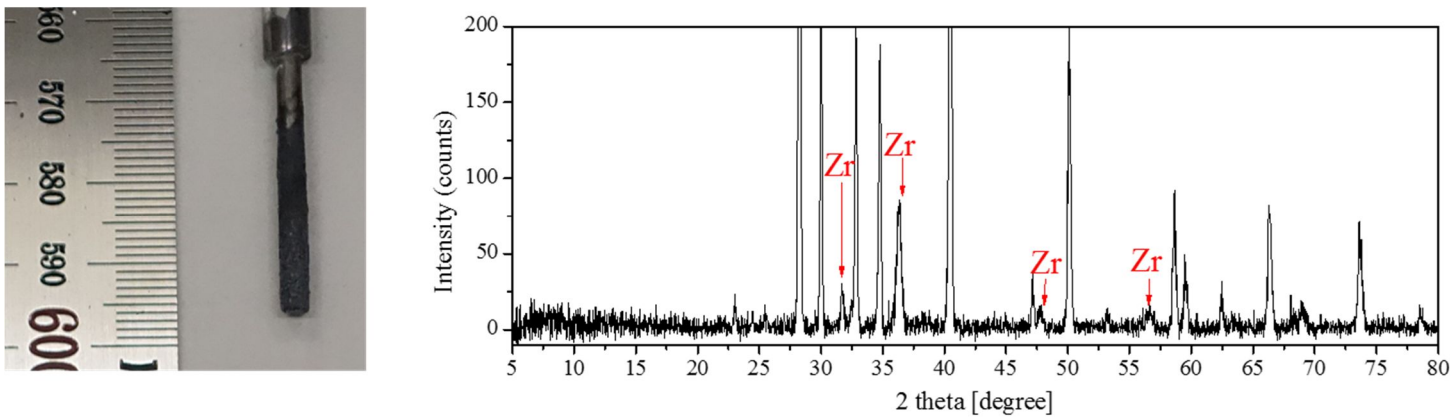

Figure 4.36 Picture (left) and XRD results (right) of cathode deposits after electrorefining in LiCl-KCl-$ZrCl_4$(0.5 wt. %): unnamed XRD peaks are resulting from LiCl-KCl-$ZrCl_4$

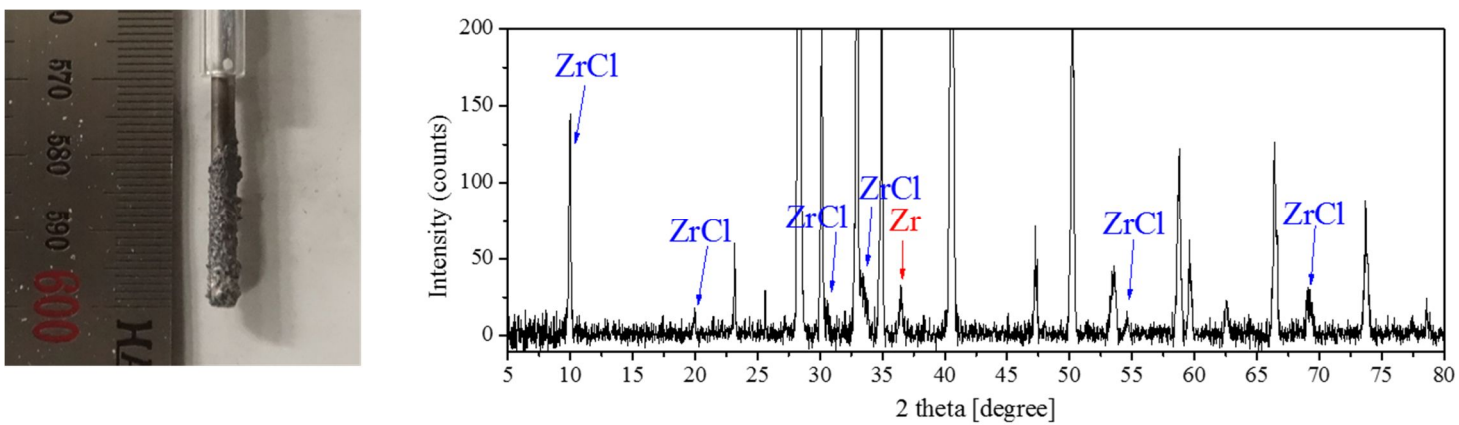

Figure 4.37 Picture (left) and XRD results (right) of cathode deposits after electrorefining in LiCl-KCl-$ZrCl_4$(1.0 wt. %): unnamed XRD peaks are resulting from LiCl-KCl-$ZrCl_4$

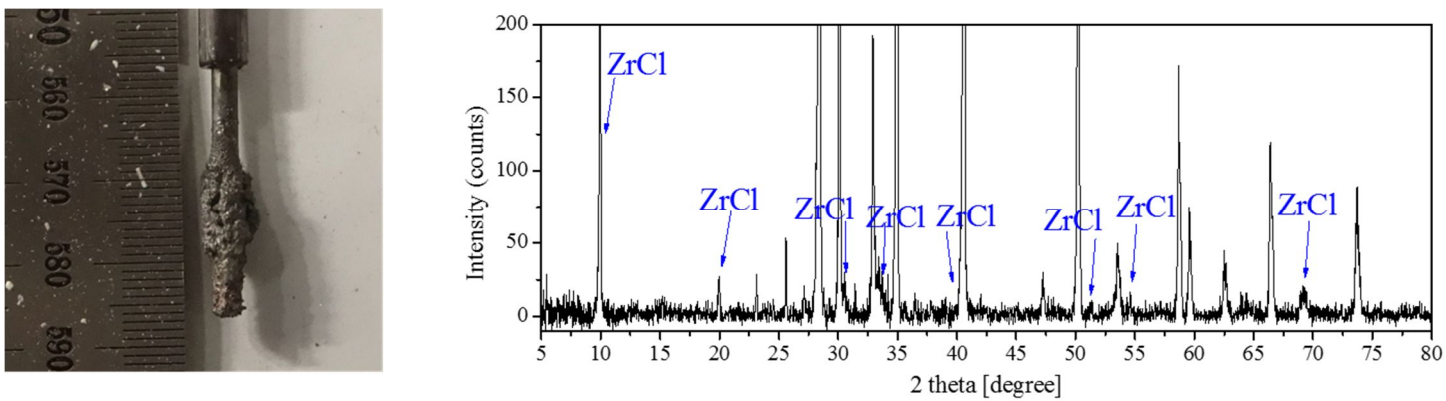

Figure 4.38 Picture (left) and XRD results (right) of cathode deposits after electrorefining in LiCl-KCl-$ZrCl_4$(2.0 wt. %): unnamed XRD peaks are resulting from LiCl-KCl-$ZrCl_4$

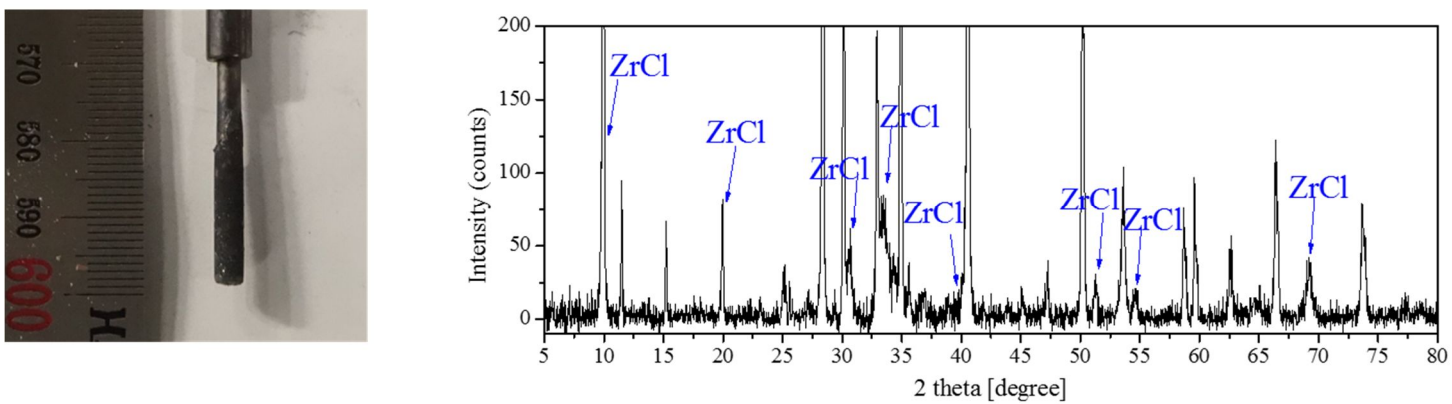

Figure 4.39 Picture (left) and XRD results (right) of cathode deposits after electrorefining in LiCl-KCl-$ZrCl_4$(4.0 wt. %): unnamed XRD peaks are resulting from LiCl-KCl-$ZrCl_4$

After electrorefining in molten salts containing $ZrCl_4$ of 0.1, 0.5 and 1.0 wt. %, black powders were observed in the bottom of molten salts as represented in Figure.4.40, Figure 4.41 and Figure 4.42. These powders were investigated by XRD and it was revealed that chemical forms of these powders are equivalent to those of cathode deposits for each concentration. It means that black powders were Zr metal for 0.1 and 0.5 wt. % molten salts while the black powders were the mixture of Zr metal and ZrCl for 1.0 wt. % molten salts. After electrorefining in molten salts including $ZrCl_4$ of 2.0 and 4.0 wt. %, black powders were not shown at the bottom of the salts as represented in Figure 4.43. Color of molten salts after electrorefining became darker – light brown to dark brown – as $ZrCl_4$ concentration increases.

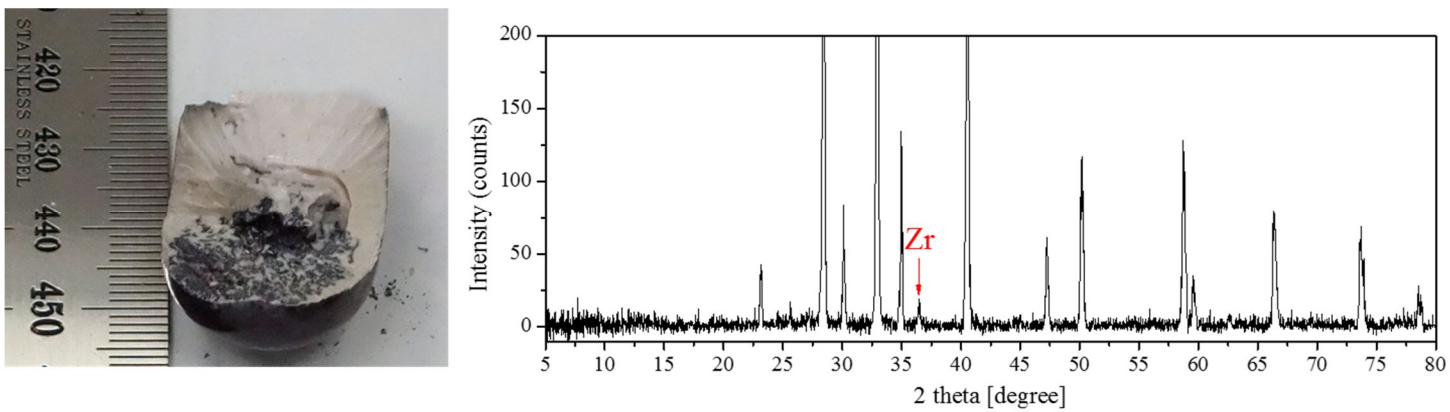

Figure.4.40 Picture (left) and XRD results (right) of molten salts after electrorefining in LiCl-KCl-$ZrCl_4$(0.1 wt. %): XRD was conducted for the bottom of molten salts including black powders and unnamed XRD peaks are resulting from LiCl-KCl-$ZrCl_4$

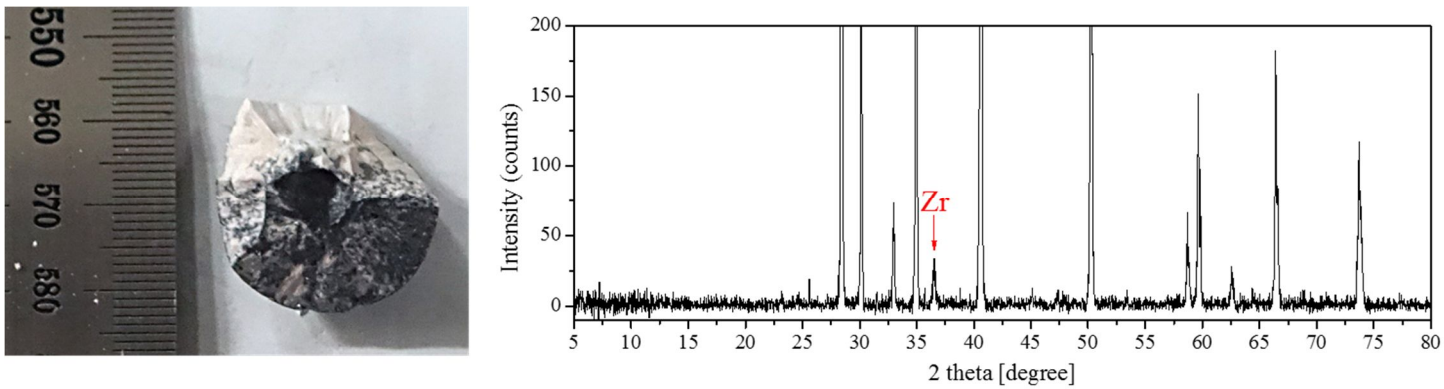

Figure 4.41 Picture (left) and XRD results (right) of molten salts after electrorefining in LiCl-KCl-$ZrCl_4$(0.1 wt. %): XRD was conducted for the bottom of molten salts including black powders and unnamed XRD peaks are resulting from LiCl-KCl-$ZrCl_4$

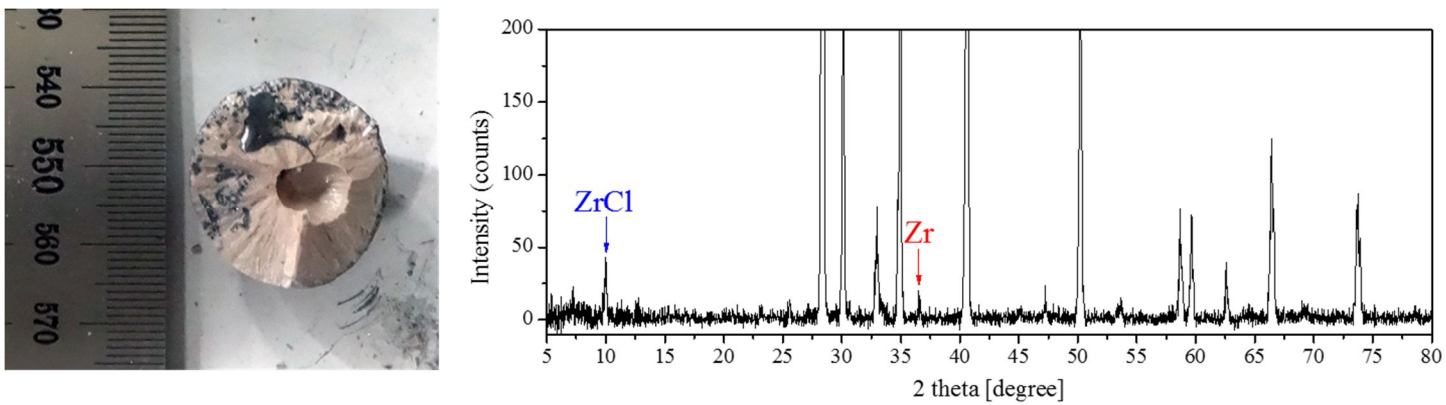

Figure 4.42 Picture (left) and XRD results (right) of molten salts after electrorefining in LiCl-KCl-$ZrCl_4$(0.1 wt. %): XRD was conducted for the bottom of molten salts including black powders and unnamed XRD peaks are resulting from LiCl-KCl-$ZrCl_4$

Figure 4.43 Pictures of molten salts after electrorefining in (left) LiCl-KCl-$ZrCl_4$(2.0 wt. %) and (right) LiCl-KCl-ZrCl4 (1.0 wt. %)

4.3.3 Discussion

4.3.3.1 Composition of cathode deposits

Since anode potential was controlled as -0.9 V (vs. Ag/AgCl) which is almost equivalent to the equilibrium potential of Cr in molten salts containing Cr of 10 ppm, only zirconium was dissolved from Zircaloy-4 specimen in the anode basket and other elements were not deposited on the cathode. This results would imply that electrorefining would be an effective decontamination process for irradiated Zircaloy-4 cladding if anode potential is maintained properly during electrorefining. The value of anode potential that should be maintained during electrorefining would be determined by investigating the most oxidative elements among elements which are more reductive than zirconium. If the electrorefiner is operated galvanostatically, the termination time of electrorefining would be determined by monitoring whether anode potential is more positive than the value determined in the same manner of the above.

In this study, Sn was not observed for all electrorefining experiments because of relatively short operating time but there would be some concerns related to melting of Sn from Zircaloy-4 specimen at the end of stage of electrorefining if this electrorefining is operated until most of Zr in Zircaloy-4 specimen is depleted. The melting point of Sn is about 232^{o}C which is much lower than the electrorefiner operating temperature of 500^{o}C. At the initial stage of electrorefining, because composition of Sn in

Zircalaoy-4 is about 1 wt. %, Zr-Sn solid solution is formed and Sn would not melt out from Zircaloy-4 specimen. However, as electrorefining progresses, local Sn concentration in Zircaloy-4 specimen would increase above about 99 atomic percent and Sn would melt out (Abriata et al., 1983; Okamoto, 2010). If Sn melts out from the anode as liquid states, liquid Sn could be trapped with LiCl-KCl salts inside the cathode deposits and the purity of recovered zirconium would be lowered. Therefore, operating conditions to minimize Sn melting would be need to be developed to recover zirconium without Sn.

4.3.3.2 Powdery deposits and powders in the bottom of molten salts

Zirconium recovered from both cathode deposits and the bottom of molten salts had a powdery morphology. Powdery shape would have some concerns in post-process of recovered metal after electrorefining because powdery zirconium might be easy to be oxidized. If oxygen content in zirconium compounds is over 0.7%, zirconium would become unworkable (Kipouros and Flengas, 1985). For this reason, reactor-grade zirconium requires oxygen content lower than 1,000 ppm. Therefore, melting and casting processes such as arc melting should be applied as soon as possible after recovering zirconium from electrorefining.

Black powders were observed in the bottom of molten salts after electrorefining in 0.1, 0.5 and 1.0 wt. % $ZrCl_4$ molten salts and it was

revealed that chemical forms of black powders were equivalent to cathode deposits. From this results, it could be deduced that disproportionate reactions forming ZrCl would be greatly slow. G. J. Kipouros reported that ZrCl could be produced by a disproportionate reaction in chloride salts such as KCl-NaCl-CsCl as follow:

$$3Zr + ZrCl_4 \rightarrow 4ZrCl$$

If the disproportionate reaction occurred and the reaction rate was fast enough in this study, ZrCl should have been detected at powders recovered in the bottom of both 0.1 and 0.5 wt. % $ZrCl_4$ molten salts. However, ZrCl was not detected from powders in the bottom of both 0.1 and 0.5 wt. % $ZrCl_4$ salts and it could means that decline of Zr recovery efficiency resulting from ZrCl forming disproportionate reaction would be negligible.

4.3.3.3 Chemical form of zirconium deposits according to $ZrCl_4$ concentration

As concentration of $ZrCl_4$ increases, more amount of ZrCl was recovered with Zr metal. Therefore, low concentration of $ZrCl_4$ would be preferred to recover zirconium as metal state without ZrCl. This phenomena could be explained by the reduction mechanism of zirconium as follow:

$$Zr(IV) + 3e^- + Cl^- \rightarrow ZrCl \text{ and}$$

$$ZrCl + e^- \rightarrow Zr + Cl^- .$$

In this reduction mechanism, Zr metal is prepared from ZrCl reduction reaction. Therefore, if ZrCl mole production rate of the first reaction is faster than Zr mole consumption rate of the second reaction, ZrCl would be remained in the cathode deposits. On the contrary, if ZrCl mole production rate of the first reaction is slower than Zr mole consumption rate of the second reaction, ZrCl would not be remained in the cathode deposits because all of produced ZrCl would be reduced into Zr metal.

The electrochemical reaction rates are greatly depend on applied current density and concentrations of reactants and products. The mole production rate of ZrCl from the first reaction, $\dot{m}_{ZrCl}$, could be determined as

$$\begin{aligned} \dot{m}_{ZrCl} &= -\frac{i_{ZrCl}}{n_{ZrCl}F} \\ &= -k_{0,ZrCl}[-C_{Zr(IV)}(0,t)\exp(-\alpha_{ZrCl}\frac{n_{ZrCl}F}{RT}(E - E^{0'}_{ZrCl})) \\ &\quad + \exp((1-\alpha_{ZrCl})\frac{n_{ZrCl}F}{RT}(E - E^{0'}_{ZrCl}))] \end{aligned} \qquad (4.4)$$

where i_{ZrCl} is the current density resulting from the ZrCl formation reaction, n_{ZrCl} is the number of electron participating in the ZrCl formation reaction, F

is the faraday constant, $k_{0,ZrCl}$ is the rate constant for the reaction of ZrCl formation, $C_{Zr(IV)}(0,t)$ is the surface concentration of Zr(IV), α_{ZrCl} is the transference coefficient for the ZrCl formation, E is the electrode potential and $E^{0'}_{ZrCl}$ is the formal potential of the ZrCl formation. The mole consumption rate of ZrCl from the second reaction, $\dot{m}_{Zr}$, would be determined as

$$\begin{aligned}\dot{m}_{Zr} &= \frac{i_{Zr}}{n_{Zr}F} \\ &= k_{0,Zr}[-\exp(-\alpha_{Zr}\frac{n_{Zr}F}{RT}(E-E^{0'}_{Zr})) \\ &\quad +\exp((1-\alpha_{Zr})\frac{n_{Zr}F}{RT}(E-E^{0'}_{Zr}))]\end{aligned} \tag{4.5}$$

where i_{Zr} is the current density resulting from the Zr formation reaction, n_{Zr} is the number of electron participating in the Zr formation, $k_{0,Zr}$ is the rate constant for the Zr formation reaction, α_{Zr} is the transference coefficient for the Zr metal formation and $E^{0'}_{Zr}$ is the formal potential of the Zr metal formation.

As represented in Eq.(4.4), the current density for ZrCl formation from Zr(IV) is proportionate to the surface concentration of Zr(IV). However, the current density for Zr metal formation from ZrCl does not have Zr(IV) concentration dependency. It means that if concentration of $ZrCl_4$ increases

at the given electrode potential, the reaction rate of ZrCl formation would increases but that of Zr metal formation would not be changed. Therefore, more negative potential is required for a high $ZrCl_4$ concentration case to completely reduce ZrCl to Zr metal than that for a low $ZrCl_4$ concentration case.

4.4 Suggestions on Zircaloy-4 electrorefining based on lab-scale experiment[4]

In LiCl-KCl salts, zirconium metal will be oxidized into mainly Zr(IV) with the small amount of Zr(II) and the produced Zr(II) would be eventually oxidized into Zr(IV) on anode surface. For catholic deposition, ZrCl and Zr metal are insoluble chemical forms that could be recovered as cathode deposits. ZrCl is produced from the reduction of Zr(IV). For recycling zirconium, Zr metal is more preferable than ZrCl. To selectively recover Zr metal without ZrCl, cathodic potential has to increase over -1.5 V (vs. Ag/AgCl) where ZrCl is reduced into Zr metal thoroughly. However, ZrCl start to be reduced into Zr metal at over -1.2 V (vs. Ag/AgCl), the potential for recovering high purity Zr metal without ZrCl could be changed according

[4] This section has been written based on the following journal paper: Jaeyeong Park et. al., "Cyclic Voltammetry on Zirconium Redox Reactions in LiCl-KCl-$ZrCl_4$ at 500^{o}C for Electrorefining Contaminated Zircaloy-4 Cladding," Journal of The Electrochemical Society, 161, H97-H104, 2014.

to operating condition of electrorefining.

If high current density is applied on anode, other elements in the irradiated Zircaloy-4 will be dissolved. Since most of these elements such as Sn, Cr, Fe and Co are more reductive than Zr, these elements can be deposited on cathode before Zr. The deposition of other elements will contaminate cathode deposits and greatly reduce efficiency of Zr recycling.

Therefore, we need to achieve high cathodic current density for recovering zirconium as a metal state while simultaneously small anodic current density for preventing the dissolution of other elements. This requires large anode area and small cathode area during electrorefining. It is noted that the upper limit of cathode current density is decided by the reduction of U or TRU which are more oxidative than zirconium. Similar to Sn, Cr, Fe and Co, the co-deposition of U and TRU with zirconium is undesirable contamination.

There are both pros and cons in high concentration of $ZrCl_4$ for irradiated Zircaloy-4 cladding electrorefining. The high $ZrCl_4$ concentration will enhance limiting current density, and this will eventually secure high throughput. However, if $ZrCl_4$ concentration is too high, ZrCl will be largely co-deposited on cathode with Zr metal even if high voltage is applied on cathode because the reaction of Zr(IV) to ZrCl competes to the reaction of ZrCl to Zr metal. In this case, an additional process may be required to reduce ZrCl into Zr metal. On the other hand, low $ZrCl_4$ concentration, favorable to more pure Zr metal deposits, would be in unfavorable to achieving high throughput.

Chapter 5 Computational Electrorefining Model Development

5.1 Hydrodynamic-electrochemical computational model

Three-dimensional computational electrorefining model has been developed based on a commercial fluid dynamics software package, ANSYS-CFX by combining an electrochemical model developed by author as represented in Figure 5.1. The commercial software is utilized to calculate diffusion boundary layer thickness by solving Navier-Stokes equation, mass transport equation, continuity equation and so on at the given operating condition of electrorefiner. After fluid dynamic modeling, electrochemical reaction model was used to electrochemical information such as current density for each element and overpotential distribution over cathode. Since there could be a lot of electrochemical reactions according to electrochemical systems, electrochemical model has been developed for that users can select electrochemical reaction equations including multi-element and multi-step reactions depending on modeling condition.

The developed model has two iteration options to combine fluid dynamic code and electrochemical model. In the first iteration option, fluid dynamic simulation is conducted repeatedly after calculating electrochemical model if convergence criteria on electrostatics is not satisfied. During

calculating electrochemical equations, local current densities on electrode could be changed and it could have influence on diffusion boundary layer thickness. In the first model, diffusion boundary layer thickness is re-estimated by simulating fluid dynamic equations with updated local current density distribution. This iteration option might generate more exact results than another option but it requires lots of computational time and resources and convergence problem of computational code might become worse since fluid dynamic calculation should be conducted in bulk medium with a lot of nodes. In the second iteration option, only electrochemical model is re-calculated when convergence criteria on electrostatics is not satisfied. This option is based on the assumption that local current density distribution which is directly converted to mass sink and source distribution could not greatly affect diffusion boundary layer thickness and the diffusion boundary layer thickness could be dominantly determined by convection of bulk electrolyte. This option might produce less exact result but it requires less computational time and resources because calculations are conducted on the surface not in bulk electrolyte. For this reason, if the number of nodes in bulk electrolyte are small, the first iteration option could be adopted and the second iteration option could be utilized when convergence problem is worried.

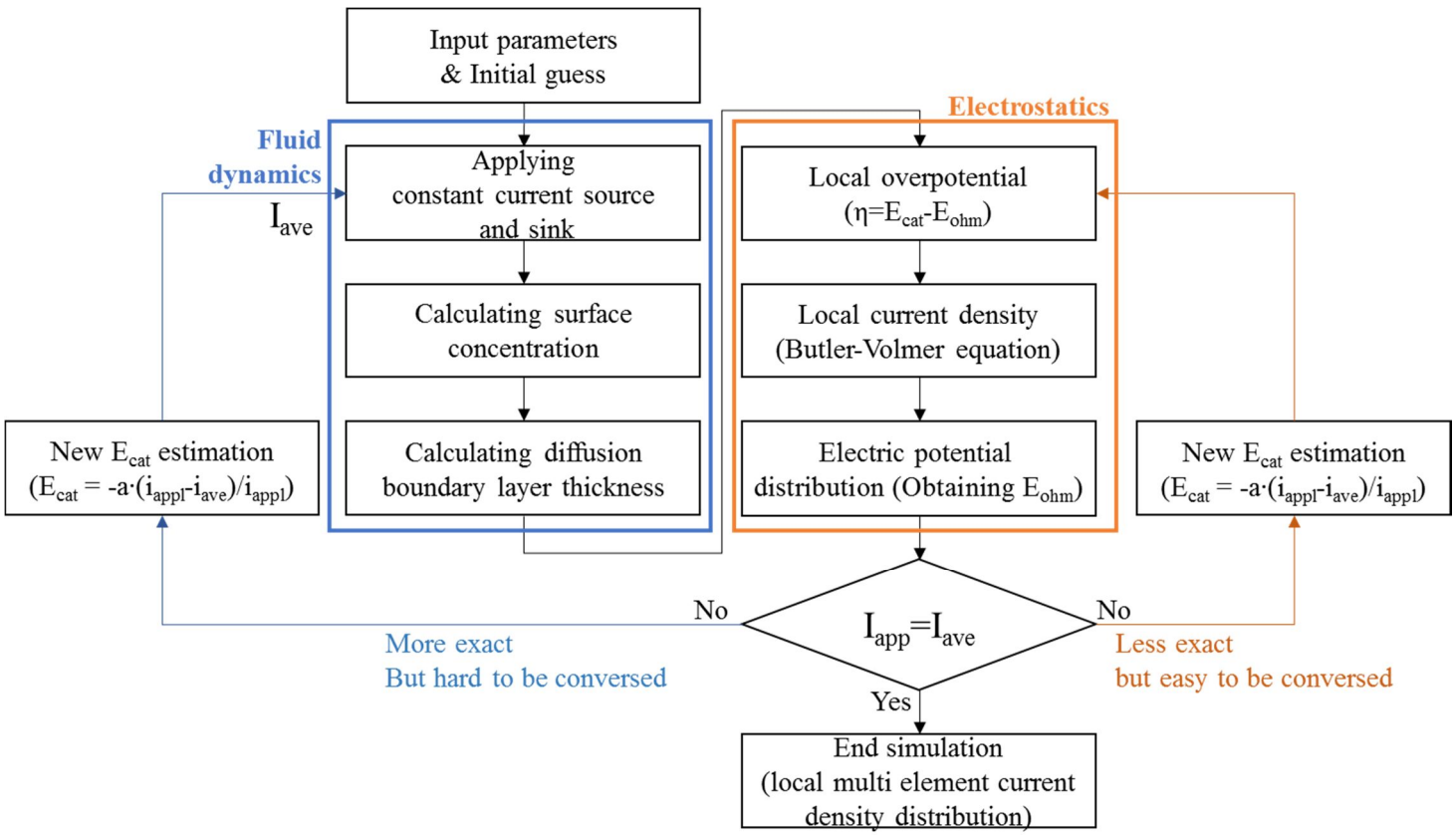

Figure 5.1 Flow chart of Hydrodynamic-electrochemical simulation algorithm

5.2 Surrogate aqueous electrodeposition system benchmark

To validate cathode deposition model of the developed computational model, benchmark studies using a RCH cell with a copper sulfate electrolyte solution were performed. The RCH cell with copper sulfate system was selected, because it has been widely utilized as a standard technique for quantitative electrodeposition studies and its high availability of reliable materials property data (Low et al., 2007).

5.2.1 Rotating Cylindrical Hull cell description

The geometry of the RCH cell used for this study is represented in Figure 5.2. The RCH cell is designed based on the RotaHull® cell and the geometry presented by Low et al. (Low et al., 2007). The height and diameter of the electrolyte container, which is made of acrylic glass, are 18 cm and 16 cm, respectively. The rotating cylindrical working electrode made of type 316 stainless steel is placed at the center of the cell. The total length and diameter of the electrode are 17.5 cm and 0.6 cm, respectively, while the length immersed in the electrolyte is 8 cm, with the remaining length of the working electrode insulated by polytetrafluoroethylene (PTFE). The Pt-Ti mesh counter electrode with a height of 2.5 cm is located outside of an acrylic glass concentric insulator with 4.5 cm inner diameter, 5.5 cm outer diameter and 14.5 cm height. Both the electric current and electrolyte can flow

through the open bottom of the concentric insulator from anode to cathode. To experimentally measure overpotential distribution along the working electrode with the minimum ohmic drop, eight Luggin probes made of PTFE are placed about 1 mm from the rotating working electrode surface and a vertical separation from each other of 1 cm. The probes are not considered when generating the geometry of the RCH cell for the modeling because fluid dynamics are not directly simulated in this study. The other insulated parts of the cell are constructed of PTFE.

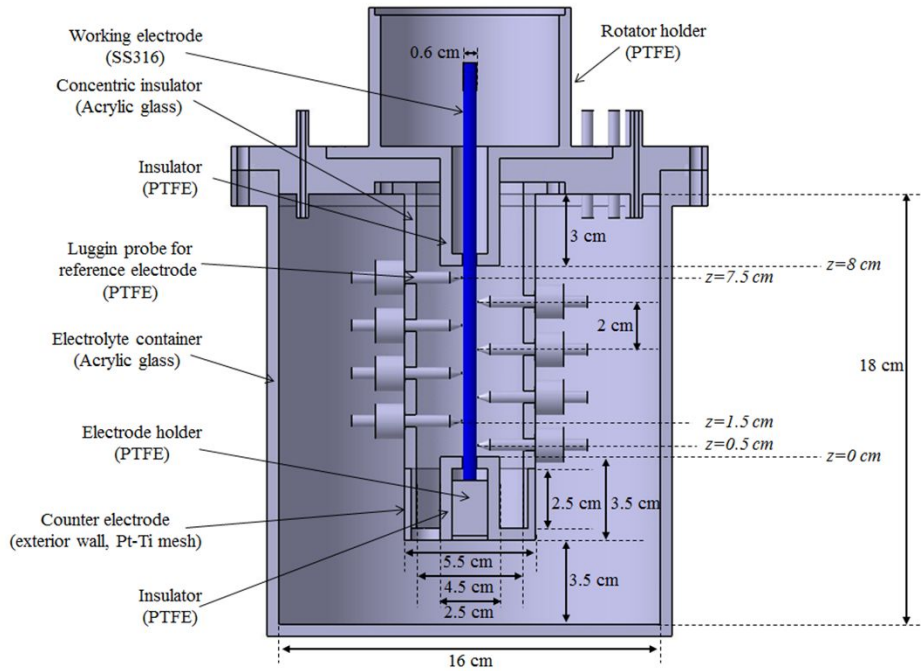

Figure 5.2 Sectional view of the rotating cylinder Hull cell design

5.2.2 Mathematical model

The modified Butler-Volmer equation is a widely utilized current-overpotential equation for general electrochemical reactions:

$$i = -i_0[\frac{C_{O,surface}}{C_{O,bulk}}\exp(-\alpha\frac{nF}{RT}\eta) - \frac{C_{R,surface}}{C_{R,bulk}}\exp((1-\alpha)\frac{nF}{RT}\eta)] \quad (5.1)$$

where i is the current density, i_0 is the exchange current density, $C_{O,surface}$ is the surface concentration of the oxidized species, $C_{O,bulk}$ is the bulk concentration of the oxidized species, α is the transfer coefficient, n is the number of electrons participating in the reaction, F is the Faraday constant (96,485 C/mol), R is the universal constant (8.314 J/(K·mol)), T is the absolute temperature, η is the overpotential, $C_{R,surface}$ is the surface concentration of the reduced species and $C_{R,bulk}$ is the bulk concentration of the reduced species. This equation was utilized for copper ion reduction on the cathode. The overpotential could be determined as the difference between the electrode potential, E and the equilibrium potential, Eq:

$$\eta = E - E_{eq} \quad (5.2)$$

The equilibrium potential could be expressed by Nernst equation:

$$E_{eq} = E^0 + \frac{RT}{nF} \ln\left(\frac{a_O}{a_R}\right) \tag{5.3}$$

where E^0 is the standard reduction potential, a_o is the activity of the oxidized species and a_R is the activity of the reduced species.

The surface concentration of the oxidized species could be calculated from the mass balance between the reduction reaction on the cathode and the mass transfer in the diffusion boundary layer near the cathode:

$$\frac{i}{nF} = J_{O,surface} = -D_O \frac{C_{O,bulk} - C_{O,surface}}{\delta} \tag{5.4}$$

where $J_{0,surface}$ is the mass flux of the oxidized species on cathode surface, D_O is the diffusion coefficient of the oxidized species and δ is the diffusion boundary layer thickness near cathode. In Eq. (5.16), one-dimensional diffusion and a Nernst diffusion layer are assumed to describe the mass transfer rate near the cathode. The diffusion boundary layer thickness could be obtained by solving the continuity equation, the Navier-Stokes equation and the mass transport equation. However, for rotating concentric geometries including the RCH cell, Taylor-Couette flow could be developed and this could make it difficult to calculate the bulk electrolyte behavior and the ion concentration profile (Taylor, 1923). Therefore, in this study, the Eisenberg correlation which was derived from experiments with concentric cylindrical

geometry is used in place of solving fluid dynamic equations to estimate diffusion boundary layer thickness (Eisenberg et al., 1954; Low et al., 2007),

$$\delta = 12.64 d^{0.3} v^{0.344} D_O^{0.356} U^{-0.7} \tag{5.5}$$

where d is the diameter of the cathode, v is the kinematic viscosity of the electrolyte and U is the tangential speed of the cathode.

Electric potential distribution in the RCH cell could be simulated by solving the Laplace equation,

$$\nabla^2 \phi = 0 \tag{5.6}$$

where ϕ is the electric potential. At the electrically insulated wall, a zero current condition is applied as a Neumann boundary condition,

$$\nabla \phi = 0 \tag{5.7}$$

The boundary condition for the anode is fixed as ground, while the boundary condition for the cathode is dependent on the type of current density distribution. The primary current distribution applies when the activation and concentration overpotentials are negligible (Newman and Thomas-Alyea, 2012). Therefore, to simulate the primary current distribution, equipotential is applied for the boundary condition at the cathode:

$$\phi = E \tag{5.8}$$

The tertiary current distribution takes account of both activation and concentration overpotentials. Therefore, the relationship between current density and overpotential should be applied for the boundary condition at the cathode:

$$-\sigma\nabla\phi = i = -i_0[\frac{C_{O,surface}}{C_{O,bulk}}\exp(-\alpha\frac{nF}{RT}\eta) - \frac{C_{R,surface}}{C_{R,bulk}}\exp((1-\alpha)\frac{nF}{RT}\eta)] \tag{5.9}$$

where σ is the conductivity of the solution.

In this study, because the fluid dynamics are not simulated directly, geometry of one 6 degree segment of the RCH cell is generated and unstructured mesh with 240,456 tetrahedral elements and 129,173 nodes is generated as represented in Figure 5.3.

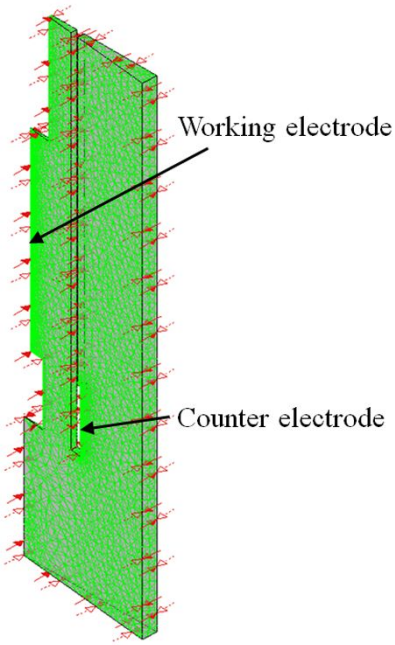

Figure 5.3 Unstructured mesh configurations

5.2.3 RCH cell experiment

The RCH cell used in this study is based on the RotaHull® cell as represented in Figure 3. To obtain the overpotential distribution along the working electrode, eight Luggin probes located approximately 1 mm away from the working electrode are connected to Ag/AgCl reference electrodes. The potential differences between the working electrode and each reference electrode are measured by a multi-channel recorder (e-corder ED1621, eDAQ). The experiment was conducted galvanostatically. A constant negative reduction current is applied to the working electrode for copper deposition.

An electrolyte of 50 mM $CuSO_4$ with 0.5 M Na_2SO_4 is used in the current work, which is similar to that used in Ref. (Low et al., 2007), which included sulfuric acid. Therefore, the conductivity and pH of the electrolyte is 11 S/m and 4, respectively, while the solution of Ref. (Low et al., 2007) had a conductivity of 35 S/m and a pH of 2. In addition, the transfer coefficient experimentally measured by a polarization curve in the electrolyte is 0.13.

A total 5 RCH experiments with 5 different average applied current densities on the working electrode (-20, -40, -60, -80, -100 A/m^2) were performed. If the applied current density is higher than the limiting current density, subsidiary reactions that are not of primary interest could take place, resulting in data representing the behavior of both the desired primary and undesired secondary reactions. Therefore, only cathodic current densities

smaller than the cathodic limiting current density at a given rotational speed are applied to the working electrode.

Figure 5.4 The RotaHull® cell (left) and the modified RCH cell used in the experimental work (right)

5.2.4 Results

5.2.4.1 Primary current density distribution

Primary current density distributions along the working electrode are numerically predicted by solving the Laplace equation in the developed computational model. The ratio between local and average current density on the working electrode in a RCH cell is independent of the average applied current density in the primary distribution; therefore, the ratio distributions along the working electrodes can be compared as represented in Figure 4. In addition, the ratio distributions obtained from the two computational models are compared to an empirical equation on the ratio in a similar RCH cell reported by Madore et al. (Madore et al., 1992a):

$$\frac{i_{local}}{i_{average}} = \frac{0.535 - 0.458 \times (z/h)}{[0.0233 + (z/h)^2]^{0.5}} + 8.52 \times 10^{-5} \exp(7.17 \times \frac{z}{h}) \quad (5.10)$$

where i_{local} is the local current density on the working electrode, $i_{average}$ is the average current density on working electrode, z is the vertical distance from the bottom of the working electrode and h is the total length of the working electrode. Because there are relatively large discrepancies between Madore's empirical equation and the computational model, five coefficients of Madore's equation are re-estimated based on five-parameter curve fitting of

the current density distribution of the three-dimensional computational model:

$$\frac{i_{local}}{i_{average}} = \frac{0.698 - 0.9664 \times (z/h)}{[0.03634 + (z/h)^2]^{0.5}} + 0.03455 \exp(2.428 \times \frac{z}{h}) \quad (5.11)$$

This modified Madore empirical equation is also compared to the computational models.

The root-mean-square deviation (RMSD) could be utilized for a measure of the discrepancies between two vectors:

$$\text{RMSD} = \sqrt{\frac{\sum_{j=1}^{n} (x_{1,j} - x_{2,j})^2}{n}} \quad (5.12)$$

where $x_{1,j}$ is the jth element of vector 1, $x_{2,j}$ is the jth element of value set 2 and n is the dimension of the vectors. The RMSDs between the computational model and two empirical equations are calculated. Madore's empirical equation does not correspond well with the computational model with RMSD of 0.0959. The modified Madore empirical equation is better matched to the computational model with 0.0120 RMSD. The vertical distance from the bottom of the working electrode where local current density is equivalent to the average current density is identical at 0.275 cm for all cases.

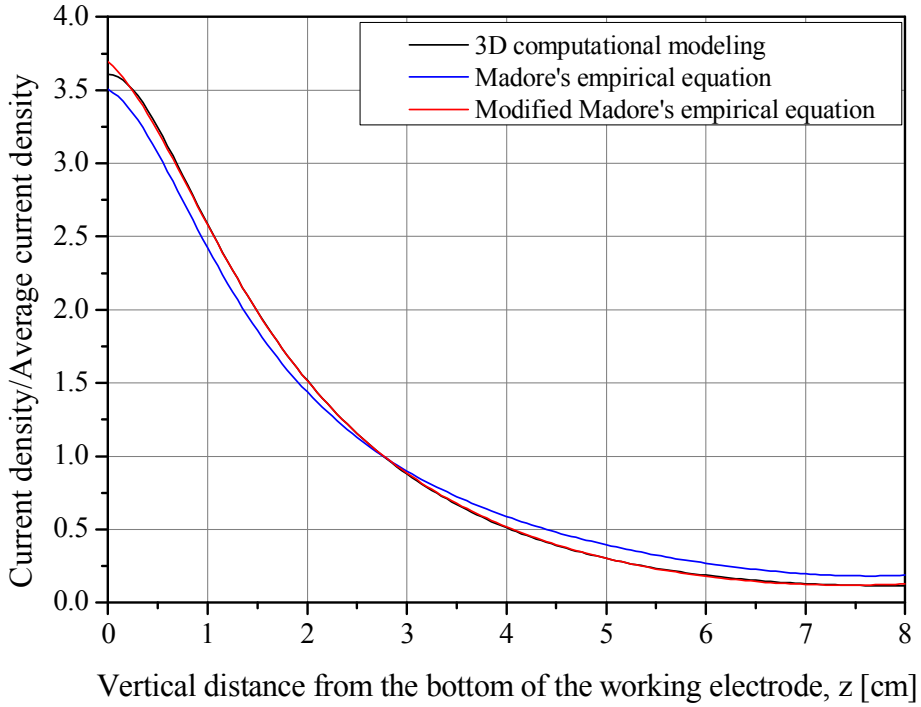

Figure 5.5 Comparison of calculated primary current distributions along the working electrode among the 3D computational model, Madore's empirical equation and a Modified Madore empirical equation

5.2.4.2 Tertiary current density distribution

For all applied current densities, calculated overpotential distribution is almost equivalent to measured overpotential distribution with RMSD of 0.02642 as represented in Figure 5.6. Since the measured overpotentials had a noise level of about ± 25 mV as represented in Figure 5.7, the discrepancies are within estimated error.

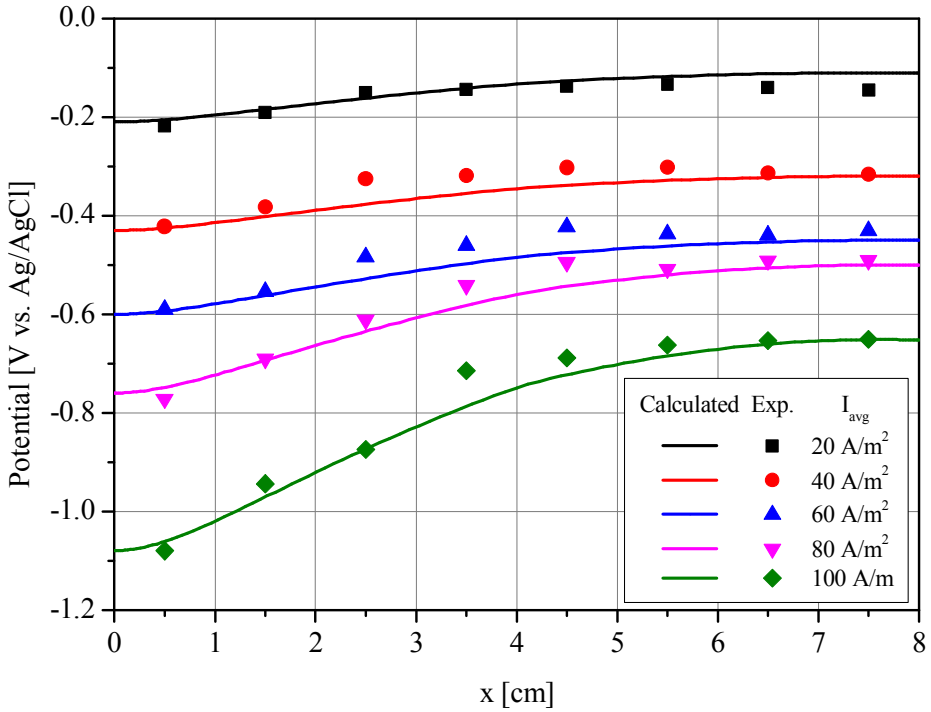

Figure 5.6 Comparison of calculated primary current distributions along the working electrode between experiment and computational model

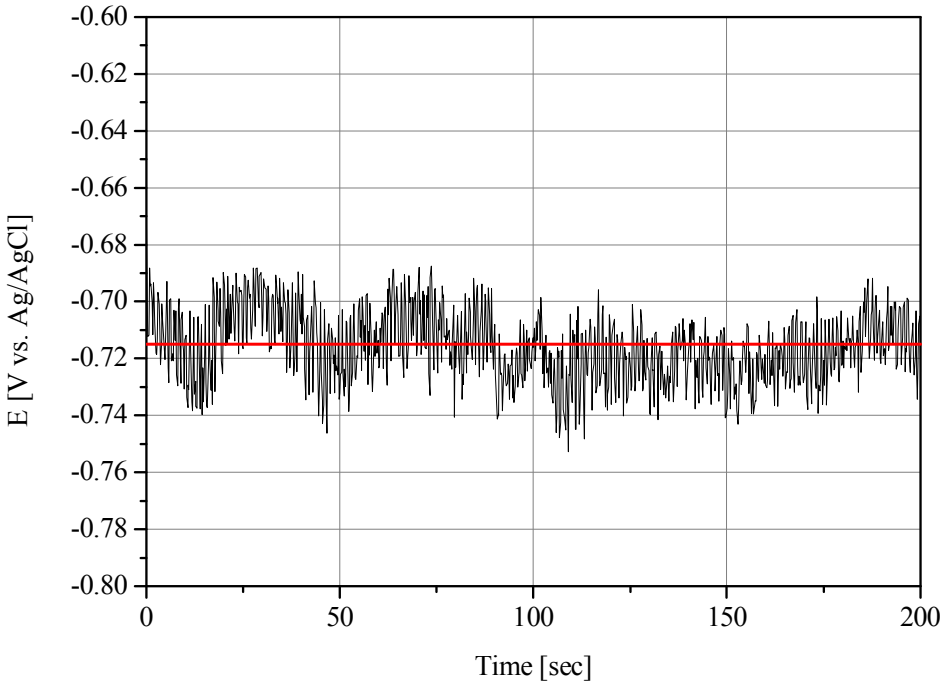

Figure 5.7 Experimentally measured potential at x=3.5 cm with applied current density of 100 A/m^2

5.2.5 Discussion

The primary current density distribution estimated by Madore's empirical equation is more uniformly distributed than the computational model. Since Madore's equation was generated by a theoretical analysis on recessed electrodes of specific geometries, discrepancy could result from the fact that the RCH geometry used in this study is not exactly identical to the one utilized for generating the empirical equation (Madore et al., 1992a; Madore et al., 1992b). In addition, since Madore's equation is developed based on experiment, the equation would not represent a perfect primary current density distribution. It is estimated activation overpotential had influenced the empirical equation. The modified Madore equation, which was generated by reestimating five coefficients of Madore's empirical equation, is almost identical to the computational model when vertical distance from the bottom of the working electrode is over 0.2 cm. Therefore, the modified Madore equation could be utilized to estimate the primary current density distribution along the working electrode in a RCH cell designed based on the RotaHull® cell.

Tertiary overpotential distribution obtained from the computational model agrees well with experimentally measured overpotential distribution and discrepancies are less than noise level. Therefore, the electrodeposition model of the developed computational model could be utilized for electrorefiner cathode design.

5.3 Molten salt electrorefining system benchmark[5]

To verify the developed computational electrorefining model in molten salt system and to verify anode dissolution model of the developed 3-D computational model, experimental data of Mark-IV electrorefiner located in INL is selected. Data from the electrorefining experiments was provided by the INL (Li et al., 2005; Hoover et al., 2010). This experiment was used to separate uranium from the other fuel materials.

5.3.1 Selected experiment for simulation

The configuration of the Mark-IV electrorefiner is illustrated in Figure 5.8. The vessel is composed of a steel (2.25%Cr – 1%Mo, ASME SA-387 steel) with both an inside diameter and height of 100cm. This ER has a liquid cadmium layer with about a 10 cm height below the salt. The LiCl-KCl molten salt layer is approximately 35 cm in height (See the reference, (Li et al., 2005), for a more detailed schematic and pictures).

[5] This section has been written based on the following journal paper: Sungyeo l Choi, Jaeyeong Park et. al., "Uncertainty studies of real anode surface area in computati onal analysis for molten salt electrorefining," Journal of Nuclear Materials, 416, 318-326, 2011.

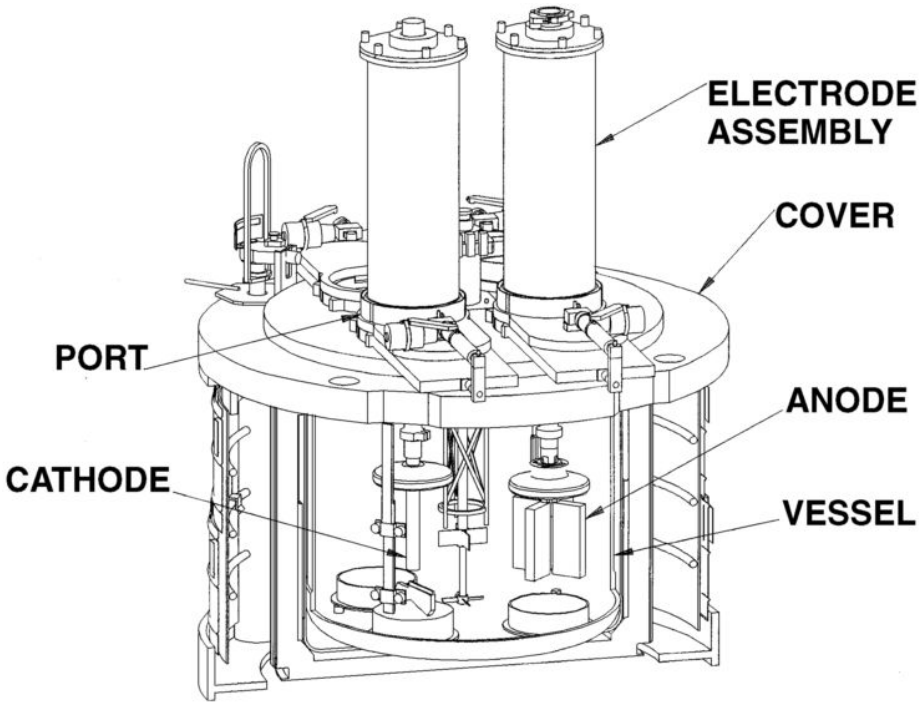

Figure 5.8 Schematic view of the Mark-IV electrorefiner (two anodes were used for this study).

For the experiment considered, the ER used two cruciform anodes and one cylindrical cathode. The cathode was a cylindrical mandrel made of mild steel. Within the two anode ports, there were eight stainless steel anode baskets containing chopped EBR-II metallic spent nuclear fuel with stainless steel cladding and sodium bond metal. The initial loading in the anode baskets was about 19 kg of fuel and 6 kg of cladding. The spent fuel contained 84.4 wt. % U, 11.4 wt. % Zr, 0.4 wt. % Pu, 3.5 wt. % Na, 0.3 wt. % fission products, and small amounts of minor actinides. An Ag/AgCl reference electrode was used to monitor the potential changes of both the anode and cathode. The anode and cathode potentials for the same experimental data set are reported by Hoover et al. (Hoover et al., 2010; Hoover et al., 2011).

As shown in Figure 5.9, the experiment was run galvanostatically (i.e., a controlled current mode) with several total current levels during operation for about 80 hours with 20 million coulombs of charge passed. Maximum applied current was 100 A; applied current decreased step by step down to 40 A. The cathode mandrel was replaced after 39 hours of operation when 12 million coulombs of charge were transferred and the cathode radius reached its maximum allowable diameter. A steel scraper installed on the inner sidewall of the vessel limited the cathode diameter (Ahluwalia et al., 2001). A sudden drop of the measured cell potential between 40-45 hours operation is unexplainable, but there might be an electrical short circuit or other malfunction of the ER equipment. The ER was operated slowly with a relatively low applied current density. Theoretically, 20 million coulombs

should dissolve 16.4 kg uranium. Because recent electrorefining runs have a current efficiency ranging from 65 to 76%, about 10.6-12.4 kg uranium may be deposited with a small amount of salt and zirconium during the process (Choi et al., 2010).

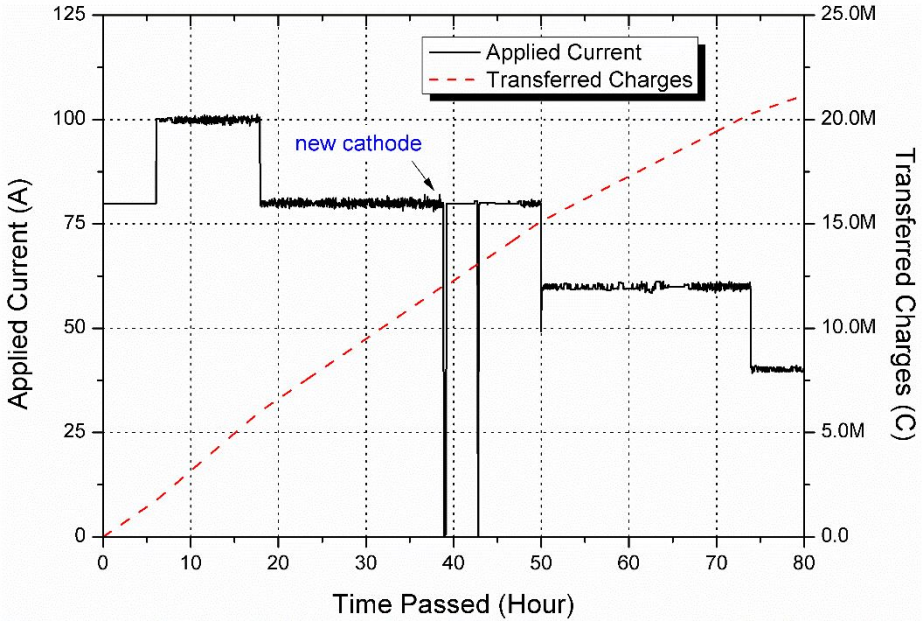

Figure 5.9 Applied current and transferred charges during 80 hours electrorefining with cathode change after 39 hours operation

5.3.2 Modeling strategy

During electrorefining process, uranium, TRU, and other elements are dissolved from an anode basket into LiCl-KCl electrolyte as ions. Among them, uranium is selectively reduced and deposited in metallic form on a cathode surface. During dissolution, the fuel in the anode shrinks and develops a rough and porous structure, while a dendritic uranium metal deposit forms on the cathode. Those dissolution and deposition processes constitute macro- and micro-scale complex electrode surface shapes. Consequently, it is important to decide real electrode surface area that is defined as the area that really participates in electrochemical reactions, because most kinetic parameters of the electrode reaction as well as electrical double layer parameters have to be given per unit area (Jarzabek and Borkowska, 1997).

Electrode surfaces where ion species involve electrochemical reactions may differ considerably from visible surfaces with the naked eye. In conventional smooth solid electrodes, a real electrode surface area is expressed by the roughness factor, R_f , which is $R_f=A_{real}/A_{geom}$ where A_{real} is the real electrode surface area and A_{geom} is the geometric electrode surface area (Jarzabek and Borkowska, 1997); however, electrodes in electrorefining produce significant shape changes which result in a serious difficulty to even decide geometrical area. According to the report of the International Union of Pure and Applied Chemistry (Trasatti and Petrii, 1991), the real surface area for a solid electrode is determined by considering several aspects: 1)

surface topography (macro- and micro-roughness), 2) homogeneity/heterogeneity, 3) dispersion of active material, and 4) distribution law of the dispersed active material. Porosity also could increase roughness factor. These factors have been considered for electrochemical reactions without significant dissolution and deposition behaviors in mostly aqueous cells (Jarzabek and Borkowska, 1997; Kulkarni et al., 2007; Watt-Smith et al., 2008) but may still be applicable to complex electrorefining processes in molten salt.

For the ideal smooth cylindrical anode without any roughness, porosity, and dispersion of active materials, the real anode surface area is determined by Eq. (5.13), but there are still several factors that have to be considered in a computational analysis; that is,

$$A_a(t) = n_a n_d n_s \left(\frac{2\pi D_a(t)^2}{4} + \pi D_a(t) H_a(t) \right) \qquad (5.13)$$

where A_a is the real anode surface area, n_a is the number of anodes, n_d is the number of fuel dissolution baskets per each anode, n_s is the number of fuel segments per each dissolution basket, D_a is the diameter of a fuel segment, H_a is the height of a fuel segment, and t is the time passed.

Five anode surface area models were generated to investigate how much cell potential (see section 2.3 for the definition) could be influenced by different assumptions regarding the real anode surface area over an ER operating period of 80 hours. Figure 5.10 shows cathode surface area as well

as five cases of total real surface area for two anodes with a zero initial roughness factor.

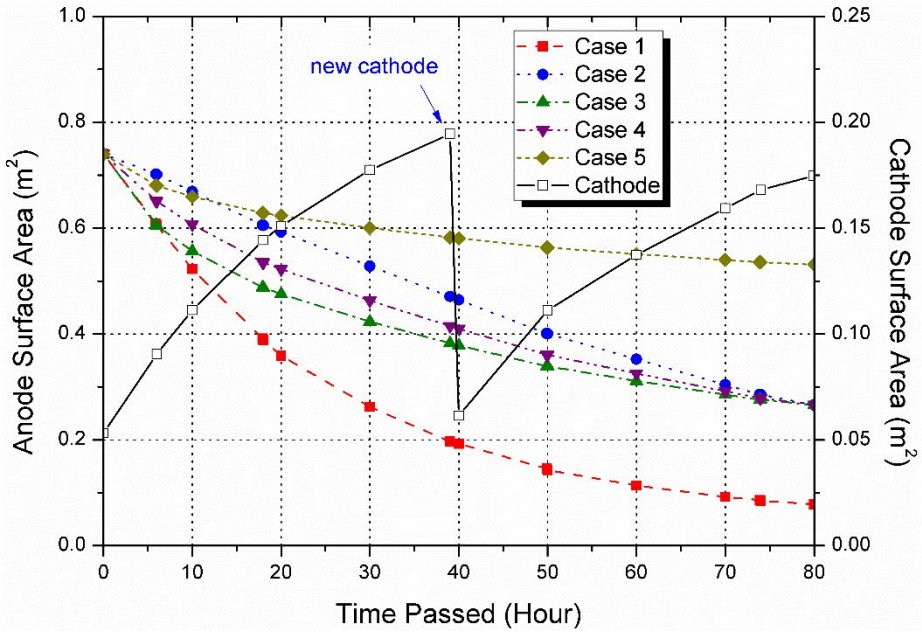

Figure 5.10 Five anode surface area cases and cathode surface area for comparative modeling of the Mark-IV electrorefiner

All cases have the same initial surface area, while there are three different final stages. Initial total anode area was calculated by multiplying the average exposure area of each cylindrical fuel pin segment by the total number of segments that were loaded into the 8 fuel dissolution baskets. It was assumed that the only exposed area was the two ends of the chopped fuel segment at the initial stage and another area was shielded from dissolution by the sodium bonding and the stainless steel cladding. Here, the initial anode surface area of 0.74 m^2 is calculated by

$$A_{ai} = n_a n_d n_s \frac{2\pi D_{ai}^{\ 2}}{4} \tag{5.14}$$

where A_{ai} is the initial real anode surface area and D_{ai} is the initial diameter of a fuel segment. Here, each real anode surface area case is described below:

Case 1—This case assumed that only the two ends of the fuel segments were exposed to the molten salt during the whole experiment, while other surfaces were protected from dissolution. In a given cell potential, fuel segments near an anode dissolution basket were presumed to be first dissolved because of lower Ohmic drop than that of fuel segments further inside. As a prediction, nearly 90% of anode materials were dissolved into the molten salt. Final anode surface area was determined by about 10% of initial area. The slope was assumed to follow an exponential curve as shown in $A_a = 0.74 \times e^{-1.075\times10^{-7} Q}$, where Q is the amount of transferred charge during electrorefining.

Case 2—The final real anode surface area would be larger than that of Case 1 because the side area of the cylindrical fuel segments could be partly exposure to the molten salt after active liquid sodium was dissolved in this low burn-up case. Moreover, the real anode area could further increase due to roughness and porosity. For these reasons, final anode surface area of this case is increased three times larger than that of Case 1. Side area of the cylindrical fuel segments was two times larger than the area of two ends. In Case 2, anode area has a direct proportion to the electrical charge transferred, $A_a = 0.74 - 2.23 \times 10^{-8} Q$. This relation reflects an anode area variation in which the first term of Eq. (5.13) dominates over the second.

Case 3—As illustrated in Figure 5.10, the relation of anode surface area variation was changed from that of Case 2, while retaining the same final area. The anode surface area shrinks faster than Case 2 and can be described by $A_a = 0.74 - 1.03 \times 10^{-4} Q^{1/2}$. As a result, this relation reflects an anode area variation where the second term of Eq. (1) dominates over the first.

Case 4—This two-third proportionality of anode surface area to transferred charge is equivalent to an anode area variation between Cases 2 and 3. The anode surface area in this case shrinks faster than Case 2 and slower than Case 3. The final anode area of this case is the same as Case 2. The equation is $A_a = 0.74 - 6.17 \times 10^{-6} Q^{2/3}$.

Case 5—As illustrated in Figure 5.10, the final anode area of this

profile, $A_a = 0.74 - 2.70 \times 10^{-6} Q^{2/3}$, is twice as much as those of Cases 2, 3, and 4, while the relation of the anode area and the transferred charge is the same as that of Case 4. This case considers the further significant rise of real anode area caused by porosity and roughness of the anode surface area.

The different anode area models can be used to compare how much the calculated cell potential agrees with the experimental result. Case 1 assumed only axial dissolution while the other cases assumed both axial and radial dissolution. Case 1 had a large deviation from the other four cases because it is assumed there is no radial exposure of fuel segments to molten salt. Comparison among Cases 2, 3, and 4 may demonstrate the proportionality effect of anode surface area with transferred charge on cell potential calculation. Case 5 allows an examination of the influence of final area to calculated cell potential via comparison with Case 4. These calculated cell potential results were compared with experimental data, and possible descriptions were offered to explain any disagreement between the simulations and the experiment.

As illustrated in Figure 5.11, cathode current density continuously decreased until the first cathode mandrel was replaced with a new one, and then a similar trend with time was observed for the second one. Maximum cathode current density was slightly over 1500 A/m^2 at the initiation of electrorefining. Anode current density for Case 1 continuously increased due to the rapid reduction of anode surface area. Cases 2-4 showed only a slightly surface area deviation for the duration of the operation. The applied

anode current density ranged from 100 to 200A/m^2. For Case 5, the final current density was less than the initial because the applied current was reduced up to 40A and the surface area was not decreased enough to increase applied current density.

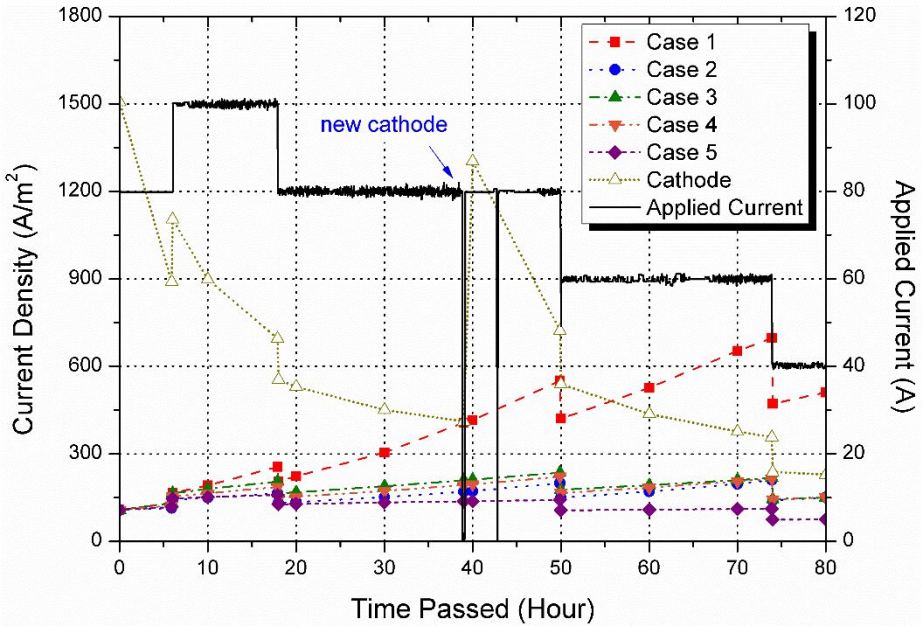

Figure 5.11 Current density variation of five anode surface area cases and cathode for comparative modeling of the Mark-IV electrorefiner.

To simplify the calculations, the cathode electrode was assumed to maintain a cylindrical structure with no change in height. It achieves increasing surface area via an increase in diameter. Because of sparse dendrite growth of uranium metal on the cathode surface, the density of deposited uranium metal is reduced down to about 5% of the normal density of uranium metal fuel considering porosity and roughness. The maximum cathode area is assumed to be reached after 39 hours of electrorefining and is replaced once as noted in Figure 5.10.

5.3.3 Mathematical model

To calculate the cell potential, constant current source and sink were respectively applied to the anode and cathode. While Ohmic drop was calculated with these conditions, anode and cathode overpotentials were obtained by concentration distribution of electro-active species. Table 5.1 contains operating conditions and thermodynamic data for this electrorefining simulation. A single-component uranium metal phase was assumed in all simulations, because uranium was the most prevalent reactant and product except during the initial transient period in which sodium and active metal fission products are oxidized and partition into the salt phase. Hoover et al. reported a similar observation showing the same trend in their 2-D computational studies on the interface between the fuel basket/anode and the eutectic salt mixture of the Mark-IV electrorefiner (Hoover et al., 2010). The electrically disconnected cadmium layer below the salt layer was

neglected, because a two-phase based (i.e. molten salt and liquid metal) geometry could bring with it significant convergence problems. Nevertheless, rotational motion of Cd stirrer's vertical rod submerged in the molten salt was considered in simulating fluidic behavior of the molten salt.

Table 5.1 Operating condition and thermodynamic data.

Molten-salt composition	LiCl(59mol%)-KCl(41mol%)
Molten-salt molar mass [kg/mol]	0.055832
Molten-salt density [kg/m^3]	1620
Molten-salt dynamic viscosity [$N \cdot s/m^2$]	0.00244
Molten-salt electrical conductivity [S/m]	157 (at 700-750K)
Operating temperature [K]	750-800
Transfer coefficient	0.5 (assumed)
Diffusion coefficient of uranium [m^2/s]	1.03×10^{-9}
Exchange current density [A/m^2]	5 (assumed)

All five calculation cases assumed an identical smooth cylindrical cathode that grew only in the radial direction with increasing total coulombs transferred; that is, the cathode radius can be expressed as:

$$R_c^2(t) = R_{ci}^2 + \frac{1}{\pi H_{ci}} \frac{mQ(t)}{\rho_c zF} \tag{5.15}$$

where R_c is the cathode radius, R_{ci} is the initial cathode radius, H_{ci} is the cathode height, m is the molar mass of an element, ρ_c is the average density of deposited metal phase on the cathode, z is the number of electrons involved in a reaction, and F is the Faraday's constant.

When oxidation potential and oxidizing current are considered as positive for the anode side and reduction potential and reducing current are considered as positive for the cathode side, a cell potential (E_{cell}) is generally defined using the following expression:

$$E_{cell} = E_{anode} + \eta_a + IR_{Ohmic} + \eta_c + E_{cathode} \tag{5.16}$$

where E_{anode} is the anode potential, $E_{cathode}$ is the cathode potential, IR_{Ohmic} is the Ohmic drop, η_a is the anode overpotential, and η_c is the cathode overpotential. However, anode potential offsets cathode potential because of the single element assumption. Therefore, cell potential can be simplified to:

$$E_{cell} = \eta_a + IR_{Ohmic} + \eta_c \tag{5.17}$$

Here, the mass flux, N, for each species includes terms for electro-migration, diffusion, and convection and is expressed by:

$$N = -zuFC\nabla\Phi - D\frac{C_b - C_s}{\delta} + Cv \tag{5.18}$$

where u is the ion mobility, C is the concentration as a function of location and time, C_b is the bulk ion concentration, C_s is the ion concentration at the electrode surface, Φ is the electrical potential, D is the ion diffusion coefficient, δ is the Nernst diffusion boundary layer thickness, and v is the flow velocity. The electro-migration effect could be negligible compared to convection and diffusion in most electrorefining with sufficient supporting electrolytes (Choi et al., 2010). In the bulk region, convection is a dominant ion transport mechanism. If mass transfer is dominated by diffusion within the diffusion boundary layer, mass flux to the electrode surface is reduced to:

$$I = -zFAD\frac{C_b - C_s}{\delta} \tag{5.19}$$

Where I is the applied current and A is the electrode area.

At high temperatures, electron transfer rates are generally rapid, and reaction at the electrodes is controlled by mass transfer in the diffusion

boundary layer near the electrode surface. A recent cyclic voltammetry measurement showed mass transport resistance is approximately ten times larger than the summation of Ohmic resistance and charge transfer resistance within the double layer and diffusion boundary layer (Lee et al., 2010).

The local reaction rate on the electrode surface is governed by a modified Butler-Volmer equation with concentration-dependent terms:

$$i = i_o \left[\frac{C_s}{C_b} \exp\left(-\frac{\alpha F}{RT} \eta \right) - \frac{C_s}{C_b} \exp\left(\frac{(1-\alpha) F}{RT} \eta \right) \right] \qquad (5.20)$$

where i is the current density, i_0 is the exchange current density, α is the symmetric constant (also known as the transference number), R is the ideal gas constant, T is the operating temperature, and η is the overpotential. Local overpotential is obtained by solving ion concentration distribution via fluid dynamics analysis if the applied current is known.

Due to lack of measured data, transference number and exchange current density are assumed to be 0.5 and 0.0005 A/cm^2, respectively. These values have inconclusively been applied to other similar studies [21, 35-36]. Ion transport behavior is determined by the combination of the continuity equation (Eq. (5.21)), the Navier-Stokes equation (Eq. (5.22)), and the mass transport equation (Eq. (5.23)).

$$\rho_m (\nabla \cdot v) = 0 \qquad (5.21)$$

$$\rho_m \frac{\partial v}{\partial t} + \rho_m v \nabla v = -\nabla P + \mu \nabla^2 v + S_u \tag{5.22}$$

$$\rho_m \frac{\partial C}{\partial t} + \rho_m \nabla \cdot (vC) = \rho_m \nabla \cdot (D \nabla C) + S_c \tag{5.23}$$

where ρ_m is the density of molten salt containing multispecies ions, P is the pressure, μ is the dynamic viscosity, S_u is the momentum source for forced convection such as electrolyte stirring, and S_c is the ion mass source. The k-ω turbulence model is used in this calculation for its strong simulation capability of close-to-wall behavior (Choi et al., 2010). The k-ω model is found to have better capability of close-to-wall behavior simulation in cases of high Sc number than that of k-ε model.

Ohmic drop across the bulk of the electrolyte is calculated by solving the Laplace equation:

$$\nabla^2 \Phi = 0 \tag{5.24}$$

Boundary conditions for the mass source and sink are derived from applied current density by Faraday's law:

$$\dot{M} = \pm \frac{i_{app} m}{zF} \tag{5.25}$$

where $\dot{M}$ is the mass flux at electrode surface and i_{app} is the applied current density.

The outer shell of the electrorefiner, the baffles, and the central stir rod are assumed to have no slip and insulating conditions, that is (Hoover et al., 2010)

$$\frac{\partial C}{\partial n} = \frac{\partial \Phi}{\partial n} = 0 \tag{5.26}$$

where *n* is the normal direction to a surface. In spite of the vessel being made of steel, this assumption may be valid; that is, because electrical resistance between the anode and cathode through molten salt electrolytes with high electric conductivity should be much smaller than that of a subordinate circuit through the vessel. Free slip condition is applied to the top surface contacting a gas phase.

Root Mean Square Deviation (RMSD) is used to assess deviation between the experimental results and the model predictions, which is:

$$RMSD(\theta_1, \theta_2) = \sqrt{\frac{\sum_{i=1}^{n} (x_{1,i} - x_{2,i})^2}{n_l}} \tag{5.27}$$

where θ_1 and θ_2 are respectively vectors of experimental data and modeling

data, $x_{1,i}$ and $x_{2,i}$ are respectively the i^{th} element of θ_1 and θ_2, and n_l is the length of the vectors. Generally, lower RMSD indicates smaller deviation of the model from experimental data.

Exceptionally expensive computational resources would be required to simulate continuous electrorefining with the 3-D transient analysis. With continuous analysis it is difficult to incorporate geometrical changes of the cathode and anode into the computational modeling (Choi et al., 2010). Hence, this benchmark modeling was conducted at 13 selected discrete points when applied current was changed or a new solid cathode was loaded. The experimental data was obtained at every 0.03 hours for about 80 hours of electrorefining. Computational modeling results were compared with average experimental data from 0.1 hours before to 0.1 hours after the selected point to minimize the influence of random signal errors in the measured cell potential.

5.3.4 Results

A one-dimensional (1-D) analysis was preliminarily conducted to investigate material dissolution behaviors without cathode change after 39 hours operation. All elements were assumed to be located at the anode surface. Figure 5.12 shows that TRU and fission products dominate applied current density until 5 hours into the electrorefining. Na initially showed large material dissolution rate while this reaction caused uranium deposition to the anodes, because it was thermodynamically more reactive than uranium

chloride in the molten salt electrolyte. After that, uranium became the dominating element of anodic dissolution. Concentrations of uranium and other elements in molten salt were almost constant after 5 hours operation because the amount of dissolved uranium was equal to the amount of deposited uranium without current loss. In this preliminary computational analysis, dissolution of zirconium from the anode may be underestimated at the latter part of operation. For Figure 5.12, it has been shown that zirconium oxidation/dissolution from the anode tends to occur at a higher rate than is predicted thermodynamics (Ahluwalia et al., 1999), which has yet to be fully accounted for in the models. In preliminary 1-D analysis, uranium may still be enough to satisfy applied current because the amount of uranium increased for the initial Na dissolution, which reduced the amount of uranium in the molten salt.

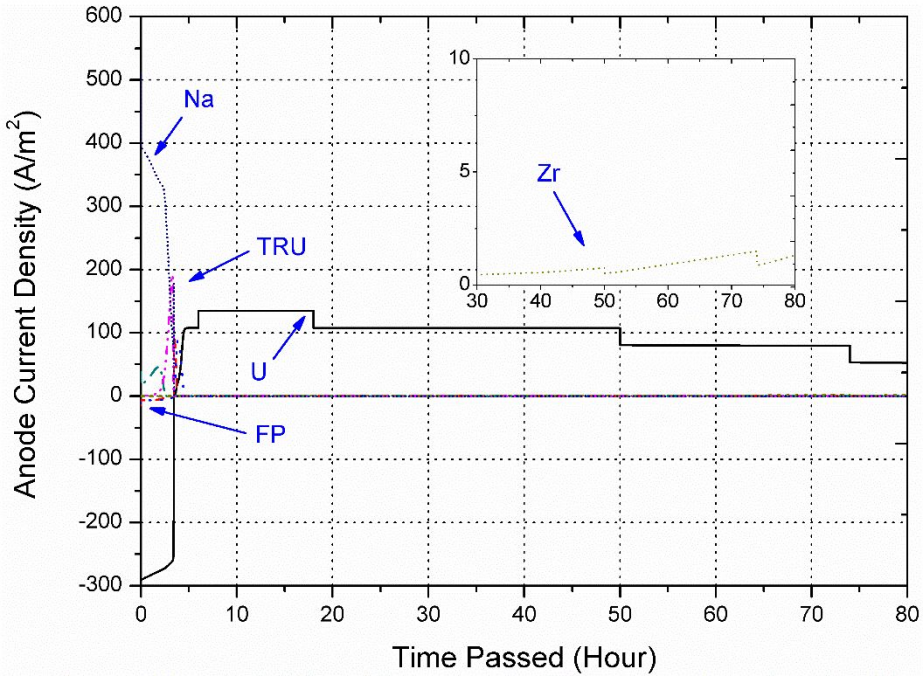

Figure 5.12 Calculated anodic current density in proportional to material dissolution from fuel segments into molten salt electrolyte during 80 hours electrorefining (at the initial stage, Na was dissolved from and uranium was deposited to anode thermodynamically)

Figure 5.13 presents the initial concentration of uranium distributed in the molten salt electrolyte from anode to cathode based on a 3-D fluid dynamic result. The concentration profile was fully developed both near the electrode and in the bulk electrolyte. Uranium concentration decreased near the cathode from the bulk, whereas it increased near the anode. Because of smaller initial cathode area than that of anode, the concentration more rapidly changed around the cathode. Within the near electrode surface region, diffusion was the more dominant material transport mechanism. Convection became pronounced in the bulk electrolyte where the uranium concentration distribution was relatively flat (that is, dominance of Ohmic resistance). The fluid dynamics calculation results demonstrated that no limiting current condition was achieved over the whole electrorefining operation (i.e., no material concentration reached zero on cathode surface).

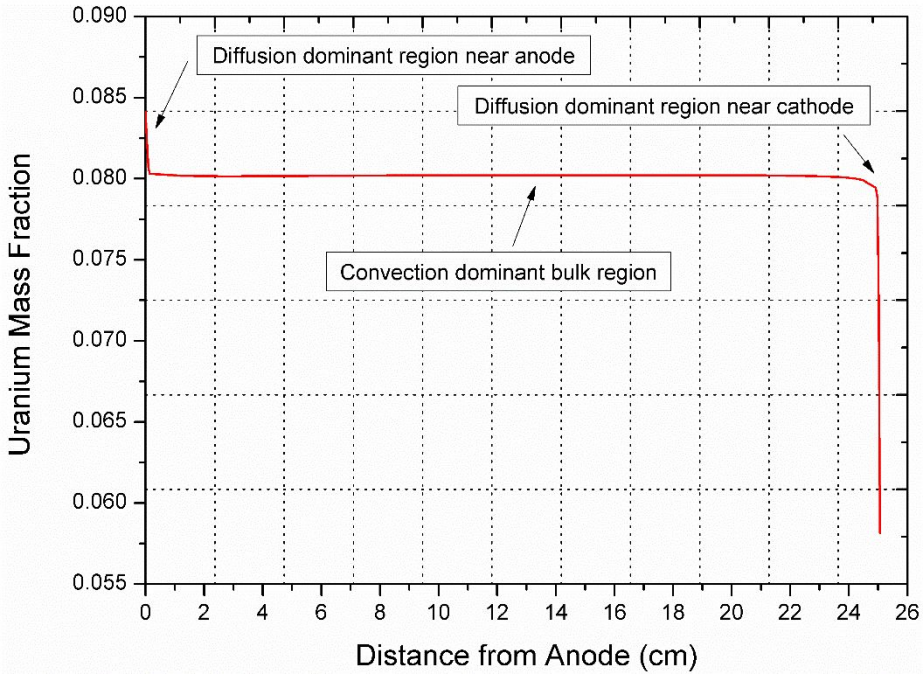

Figure 5.13 Early stage distribution of uranium concentration along with straight line from anode to cathode at middle height.

Figure 5.14 compares the calculated cell potentials for the five anode area cases with the experimental result. It was readily apparent that the real anode surface area model has a significant effect on the calculated cell potentials. With the exception of Case 1, the calculated cell potentials were initially well matched with the measured cell potential. Deviation between model and experiment increased at the end of electrorefining. It was noted that replacement of the cathode resulted in rapid potential change in both the experiment and the simulation. As shown in Figure 5.15, Case 1 with the assumption of materials dissolution only from two ends of fuel segments showed the largest RMSD from the experimental result, approximately seven times larger than that of Case 3. It may be that real anode surface area increases for roughness, porosity, and partly exposed radial area. Case 3 with dissolution from both axial and radial directions had the lowest RMSD value. The benchmark results suggested that anode materials would be dissolved from both axial and radial directions at least for low burn-up metallic fuels after active liquid sodium bonding was dissolved. This conclusion is different from the study reported by Hoover et al. (Hoover et al., 2010) who found axial dissolution with increasing porosity was sufficient to follow the overall trend of the experimental result.

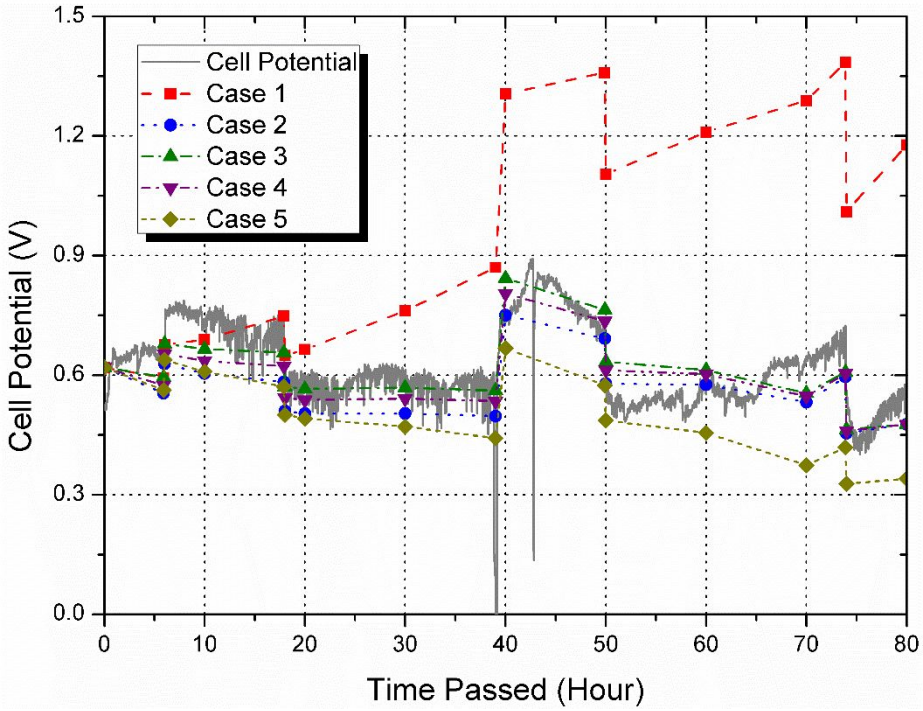

Figure 5.14 Comparison of cell potential between the experimental result and the calculated potentials based on five anode area cases

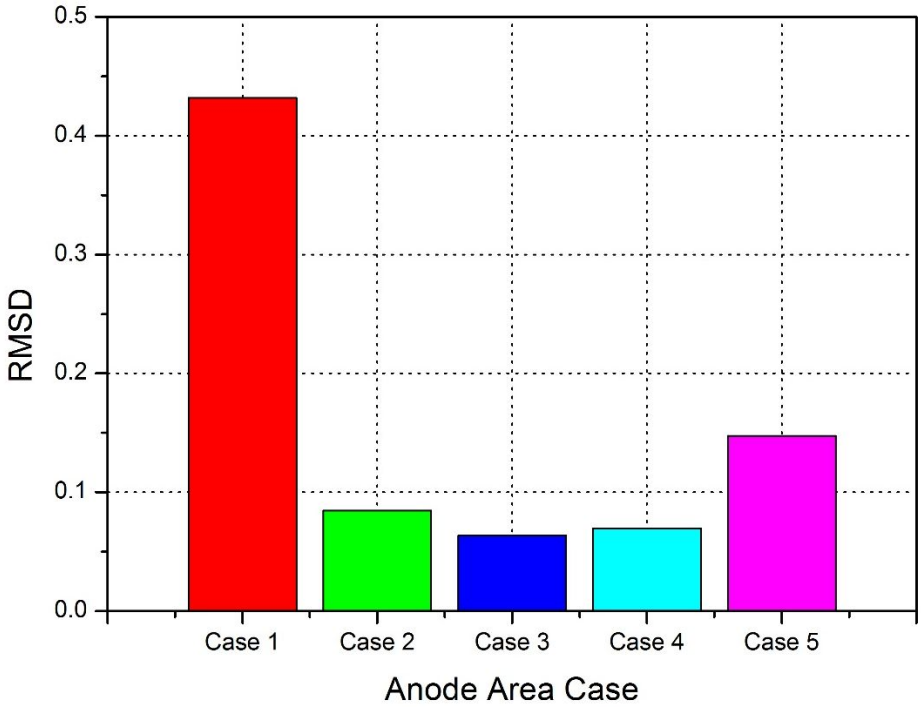

Figure 5.15 Root mean square deviation for 3-D analysis results from experimental molten-salt electrorefining data

The model calculations based on Cases 2, 3, and 4 in which the final area was the same produced similar cell potential trends and smaller RMSD compared to Cases 1 and 5. Due to its relatively large final area, Case 5 underestimated cell potential at the end of operation. By comparing Cases 2, 3, and 4 in which the final state was the same but the curves were different, it was deduced that the final anode surface area had a larger effect than slope of the curve. Based on the RMSD values shown in Figure 5.15, slight improvement was achieved by assuming the anode area is proportional to the square root of transferred charge. However, Cases 2 and 4 had relatively better agreement with the experimental data than Case 3 after the cathode change.

5.3.5 Discussion

The comparative study showed a growing difference in calculated cell potentials with time among five anode area cases. Because initial anode surface area was identical for the five cases, all calculations resulted in comparable cell potentials at the beginning of electrorefining as represented in Figure 5.14. Moreover, the calculated initial cell potentials closely matched the measured initial cell potential. However, modeled growth of a complicated electrode shape and a rough surface steadily increased inconsistencies between the model and experimental results. Although Case 3 with the lowest RMSD value agreed well with the overall trend of the measured cell potential, no case could follow the detailed local variation.

Among uncertainty factors that are not reflected in this computational analysis, anodic dissolution behavior is one of the most significant factors. Assumed exchange current density in Table 5.1 could also produce disagreement between modeling and observation (Hoover et al., 2009). In the following discussion, several anode uncertainty factors along with a few cathode uncertainty factors are presented to explain possible causes for disagreement between simulation and experiment.

Right after the initiation of electrorefining a batch of spent fuel, all calculated cell potentials were larger than that of the experimental data; a measured cell potential showed an initial jump due to increasing anode potential and decreasing cathode potential as shown in Figure 5.14. One reasonable explanation for the discrepancy may be found in the assumption of constant diffusion coefficient, which is actually a function of concentration of ion species and temperature. M. Iizuka et al. suggested that higher concentrations of an ion species may lead lower diffusivity of that ion species (Iizuka et al., 2005). Increasing concentration of an ion near the anode leads to a decreasing diffusion coefficient of the ion, causing a reduction of surface concentration as well as a rise of anode overpotential. The reverse process occurs near the cathode. As a result, the measured cell potential, defined as potential difference between the anode and the cathode, rapidly increased in the initial hour as illustrated in Figure 5.14.

For all cases except Case 1, the calculated cell potentials decreased for the first 5 hours of electrorefining. Meanwhile, the measured cell potential remained higher than that predicted via simulations. A conceivable

explanation is overestimation of initial cathode growth in the model. In the initial uranium deposition on the cathode, a thin layer of Fe-U alloy on the mild steel cathode surface forms before the deposition of adhering uranium on the thin layer. Forming the thin Fe-U alloy layer would require additional overpotential from the direct uranium deposition (Gao et al., 2009). From 5 to 18 hours of operation, both calculation and experiment had decreasing cell potentials because of cathode growth. After that time period, both calculated and measured potentials remained relatively constant.

The disagreement could be a consequence of a heterogeneous material distribution in the fuel segments in the anode baskets—nominally consisting of 75 wt. % spent fuel and 25 wt. % cladding. The nominal spent fuel composition was 84.4 wt. % U, 11.4 wt. % Zr, 0.4 wt. % Pu, 3.5 wt. % Na, 0.3 wt. % fission products, and a small amount of minor actinides. Because the 1-D model assumed that all elements existed on the anode surface, most elements with lower oxidation potential than that of uranium were predicted to be oxidized and partition into molten salt within the initial 5 hours as shown in Figure 5.12. The 3-D analysis presumed single uranium species based on this 1-D result; however, some fission products and actinides remained in the fuel segments for a while.

Surface porosity is believed to have contributed to the disagreement between experiment and simulation. Even geometrical area was difficult to be determined due to complex anodic dissolution. Due to porosity growth, roughness factors were expected to be quite higher than the usual smooth electrode. It is not known whether the anode surface formed periodic fractal

structures that could be treated as a theoretical prediction, but roughness was believed to increase as materials were dissolved from the anode via formation of porosity (Hoover et al., 2009). The rough surface would enlarge the real anode surface area as the electrorefining proceeded. An increasing surface roughness factor might also intensify any irregularity of surface reactions on the electrodes (Keiser Jr and Mariani, 1999).

Initial uranium amounts could be slightly different from original loaded fuels, because sodium bond inside the fuels thermodynamically oxidized into the molten salt by reducing uranium as presented in the Results section and Figure 5.12. After liquid sodium bond between the metallic fuel slug and cladding was dissolved at the low burn-up case, it may be possible that oxidation occurred in the radial direction, or from the side of the cylindrical fuel segments. Both increasing surface roughness factor and radial exposure of fuel segments would increase final anode surface area three times larger than that of Case 1.

As the electrorefining progressed, the effect of Zr on the disagreement between calculation and experiment could have increased. Despite there being no zirconium chloride within molten salt initially, to achieve high uranium dissolution, a large amount of Zr had to be dissolved into the molten salt. Zr is the second most prevalent species in EBR-II spent nuclear fuels. In addition, Zr is the most active noble metal whose oxidation follows right after uranium (Sakamura, 2004; Phongikaroon and Yoo, 2007). It has been shown that to recover over 98.5 wt. % and 99.7 wt. % of U, 50 wt. % and 88 wt. % of Zr respectively had to be oxidized (Ahluwalia et al.,

2001; Li et al., 2005). During later stages of electrorefining a batch of fuel, zirconium may become one of the dominant dissolving elements after the remaining uranium has been significantly depleted.

The Zr^{4+} ion is the most stable ion in the LiCl-KCl electrolyte among Zr oxidation states. A very small amount of Zr^{4+} ion could react with Zr metal and produce Zr^{2+} ion at 773K via disproportionation (Baboian et al., 1965; Sakamura, 2004; Fujita et al., 2005a). The Zr metal could come from reduction and deposition at the cathode (Ahluwalia et al., 2001; Li et al., 2005). Alternatively and perhaps more importantly, Zr from the salt-phase is reduced and partitions into the Cd phase while simultaneously oxidizing dissolved U from the Cd phase into the molten salt. This reaction is a source of uncertainty regarding uranium content in the molten salt phase. In one experiment involving a U-Pu-Zr alloy in the anode basket (Iizuka et al., 2005), a viscous Zr-salt diffusion layer was observed between the anode alloy and the outer molten salt diffusion layer during electrorefining. Small diffusion coefficients in the viscous diffusion layer may increase anode overpotential; however, it is unclear whether this Zr-salt layer also occurred in the Mark-IV epxeriment because the U-Pu-Zr anode alloy experiment had a low initial uranium concentration in the molten salt (Ahluwalia and Hua, 2002; Iizuka et al., 2005).

Non-ideal current efficiency during experiments is a possible source of error/uncertainty. In the simulation, it was assumed that there was no loss of current. In the experiments, current efficiency of actual electrorefining ranged from 65% to 76%. With no consideration of current efficiency, the

calculation overestimated material dissolution and deposition as much as current loss. In the experiment, deposited uranium metal could be dropped to Cd phase due to the rotational motion of cathode, limiting the radial growth of cathode surface. Although Cd phase is not directly connected with voltage and current sources, uranium or other materials could be transported from anode to cathode through Cd phase that interfaces with molten salt electrolyte. If this bypass mass transport is as fast as ionic transport inside molten salt due to stirring effect, the assumption which neglects the electrochemical reactions at the Cd/molten salt interface is approximately valid; however, it still requires further investigation in both experiment and simulation. In addition, larger chopped fuel segments tend to cause higher electrical resistance, increasing potential difference within anode baskets. This effect has not been considered in the computational model (Li and Simpson, 2002). The calculated cell potential deviation from the experiment was intensified near the end of electrorefining a batch because of a rapid increase and irregular behavior of the measured anodic potential.

Sine there are uncertainties that could greatly influence on current-potential calculation during electrorefining transient simulation, it is recommendable to utilize the computational model for the initial stage of electrorefining when anode surface area could be defined relatively easily. To simulate transient or mid-time of electrorefining, anode surface area change and anodic dissolution model should be improved.

5.4 Zircaloy-4 electrorefining benchmark

To verify multi-step electrochemical reaction model of the developed computational model and to estimate material properties of various electrochemical reactions of Zr in LiCl-KCl, benchmark on lab-scale Zircaloy-4 specimen electrorefining experiments which were conducted with five different $ZrCl_4$ concentration as represented in the section 4.3 were conducted by using the developed 3-D computational model.

5.4.1 Modeling strategy

Lab-scale Zircaloy-4 electrorefining experiments were conducted in five different $ZrCl_4$ concentration with fixed anode potential as -0.9 V (vs. Ag/AgCl) and three different chemical forms of cathode deposits were obtained: Zr metal only, Zr metal-ZrCl compound and ZrCl only. These different chemical form in different concentration of $ZrCl_4$ was explained as following multi-step reduction of Zr(IV) ion in the section 4.3:

$$Zr(IV) + 3e^- + Cl^- \rightarrow ZrCl \quad \text{and}$$

$$ZrCl + e^- \rightarrow Zr + Cl^- .$$

Therefore, by benchmarking different chemical forms of cathode deposits in different $ZrCl_4$ concentration by using this multi-step reaction, the multi-step

reduction model of the developed computational model would be verified.

To benchmark electrorefining experiments more strictly, computational modeling should be conducting by fixing anode potential like lab-scale experiments. In this modeling method, chemical from should be calculated by considering not only cathodic multi-step reaction but also anodic dissolution reaction. However, as revealed in the section 5.3, because there would be large uncertainties on anodic dissolution modeling, conducting computational electrorefining modeling including anodic dissolution modeling would not be proper for verifying multi-step reduction model of the developed computational model. For this reason, steady state modeling was carried out using the current of the initial stage of electrorefining rather than using fixed anode potential. In this approach, since anodic dissolution model would not greatly influence on total applied current, multi-step cathodic deposition benchmark could be focused.

To simulate electrochemical reactions, various thermodynamic and kinetic properties are required such as diffusion coefficient, formal redox potential, rate constant and transference coefficient. Among these properties, it is relatively easy to obtain diffusion coefficient and formal potential from electrochemical methods including cyclic voltammetry and chronopotentiometry. However, transference numbers and rate constants are hard to obtain experimentally and they have been rarely reported when they are compared to diffusion coefficient and formal redox potential. In this study, multi-step Zr(IV) reduction reaction was benchmarked by using thermodynamic and kinetic properties as represented in Table 5.2.

For the first reduction reaction, formal potential of -0.994 V (vs. Ag/AgCl) obtained from cyclic voltammograms in this dissertation was utilized and transference coefficient was assumed as 0.5. The reaction rate constant of this reaction, $k_{0,ZrCl}$, was assumed as 1.69E-4 m/s which is the rate constant for the reaction between U(III) and U in LiCl-KCl at 500°C since the rate constant for the reaction between Zr(IV) and ZrCl has not been reported and the numbers of electrons participating in both reactions are equivalent as 3 (Kim et al., 2012). For the second reduction reaction, formal potential of -1.15 V (vs. Ag/AgCl) which is the medium value of potential range for the second reduction reaction estimated by cyclic voltammogram in this dissertation was utilized. The transference coefficient was assumed as 0.5. Various reaction rate constants from 1E-6 to 1E-1 were tested to investigate which reaction rate constant is the most suitable for Zr multi-step reduction reaction. From this approach, a reaction rate constant for the second reduction reaction which could explain cathode deposits chemical form changes according to $ZrCl_4$ concentration was selected for pilot-scale electrorefiner design and modeling.

Table 5.2 Material properties used in the computational Zr multi-step reduction modeling

Property	Values for the first reduction reaction ($Zr(IV) + 3e^- + Cl^- \rightarrow ZrCl$)	Property	Values for the second reduction reaction ($ZrCl + e^- \rightarrow Zr + Cl^-$)
[a] n_{ZrCl}	3	[a] n_{Zr}	1
[b] $E^{0'}_{ZrCl}$	-0.994 [V vs. Ag/AgCl] (experimentally measured in the section 4.1)	[b] $E^{0'}_{Zr}$	-1.15 [V vs. Ag/AgCl] (experimentally measured in the section 4.1)
[c] α_{ZrCl}	0.5 (assumed)	[c] α_{Zr}	0.5 (assumed)
[d] $k_{0,ZrCl}$	1.69E-4 [m/s] (assumed as the value of U(III)/U rate constant) (Kim et al., 2012)	[d] $k_{0,Zr}$	1E-6 ~ 1E-1 [m/s]

[a]: the number of electrons participating in the redox reaction

[b]: formal reduction potential

[c]: transference number

[d]: reaction rate constant

5.4.2 Mathematical model

Basic mathematical models such as fluid dynamics model and boundary conditions for mass sink and source are almost equivalent to the model explained in the section 5.3 and . Therefore, in this section, the mathematical model explanation is focused on Zr multi-step reduction model. The mole production rate of ZrCl from Zr(IV), $\dot{m}_{ZrCl}$, and the current density resulting from the first reduction reaction, i_{ZrCl}, can be determined as

$$\begin{aligned}\dot{m}_{ZrCl} &= -\frac{i_{ZrCl}}{n_{ZrCl}F} \\ &= -k_{0,ZrCl}[-C_{Zr(IV)}(0,t)\exp(-\alpha_{ZrCl}\frac{n_{ZrCl}F}{RT}(E-E^{0'}_{ZrCl})) \\ &\quad +\exp((1-\alpha_{ZrCl})\frac{n_{ZrCl}F}{RT}(E-E^{0'}_{ZrCl}))]\end{aligned} \tag{5.28}$$

where n_{ZrCl} is the number of electron participating in the ZrCl formation reaction, F is the faraday constant, $k_{0,ZrCl}$ is the rate constant for the reaction of ZrCl formation, $C_{Zr(IV)}(0,t)$ is the surface concentration of Zr(IV), α_{ZrCl} is the transference coefficient for the ZrCl formation, E is the electrode potential and $E^{0'}_{ZrCl}$ is the formal potential of the ZrCl formation. As the first reaction progresses, Zr(IV) would be consumed on the cathode surface. To meet mass balance, consumption rate of Zr(IV) resulting from the first

Zr(IV) reduction reaction, $-\dot{m}_{Zr(IV)}$, should be equivalent to mass transfer rate of Zr(IV) from bulk to the cathode surface, $J_{Zr(IV)}$, that could be defined by the Fick's first law:

$$J_{Zr(IV)} = D_{Zr(IV)} \frac{C_{b,Zr(IV)} - C_{Zr(IV)}(0,t)}{\delta} = -\dot{m}_{Zr(IV)} = \dot{m}_{ZrCl} \qquad (5.29)$$

where $C_{b,Zr(IV)}$ is the bulk concentration of Zr(IV) and δ is the diffusion boundary layer near the cathode. By combining Eq. (5.28) and Eq. (5.29), a new current-voltage relation for the first reduction reaction can be driven as

$$i_{ZrCl} = \frac{n_{ZrCl} F k_{0,ZrCl} [-C_{Zr(IV)}(0,t) \exp(-\alpha_{ZrCl} \frac{n_{ZrCl} F}{RT}(E - E^{0'}_{ZrCl})) + \exp((1-\alpha_{ZrCl}) \frac{n_{ZrCl} F}{RT}(E - E^{0'}_{ZrCl}))]}{1 + \frac{\delta k_{0,ZrCl}}{D_{Zr(IV)}} \exp(-\alpha_{ZrCl} \frac{n_{ZrCl} F}{RT}(E - E^{0'}_{ZrCl}))} \qquad (5.30)$$

The black solid line in Figure 5.16 represents the Eq. (5.30) with an arbitrary diffusion boundary layer thickness. As shown in the figure, the current density resulting from the first reduction reaction could not increases infinitely in negative direction at a given diffusion boundary layer thickness because of depletion of Zr(IV) on the cathode surface.

The mole consumption rate of ZrCl from the second reaction, $\dot{m}_{Zr}$, and the current density resulting from the second reduction reaction, i_{Zr}, can be represented as

$$\begin{aligned}\dot{m}_{Zr} &= \frac{i_{Zr}}{n_{Zr}F} \\ &= k_{0,Zr}[-\exp(-\alpha_{Zr}\frac{n_{Zr}F}{RT}(E-E_{Zr}^{0'})) \\ &\quad +\exp((1-\alpha_{Zr})\frac{n_{Zr}F}{RT}(E-E_{Zr}^{0'}))]\end{aligned} \tag{5.31}$$

where i_{Zr} is the current density resulting from the Zr formation reaction, n_{Zr} is the number of electron participating in the Zr formation, $k_{0,Zr}$ is the rate constant for the Zr formation reaction, α_{Zr} is the transference coefficient for the Zr metal formation and $E_{Zr}^{0'}$ is the formal potential of the Zr metal formation. As represented in Eq. (5.31), the current density for the second reduction reaction does not have Zr(IV) concentration dependency. Therefore, the current would increases infinitely in negative direction as applied potential become more negative unless any restriction is applied to Eq. (5.31) as the red dashed line in Figure 5.16. If so, below a certain electrode potential, ZrCl consumption rate resulting from the second reduction reaction could be larger than ZrCl production rate resulting from the first reduction reaction. This phenomenon could not occur in steady state modeling.

Therefore, a restriction for Eq. (5.31) was established as follow. If a

molar consumption rate of ZrCl calculated by Eq. (5.31) is higher than a molar production rate of ZrCl calculated by Eq. (5.30), it is assumed that molar consumption rate of ZrCl is equivalent to molar production rate of ZrCl. It means that if electrode potential is more negative than the potential where the restriction is effective, produced ZrCl from the first reduction reaction is reduced into Zr metal completely. The current-voltage curve with the restriction is represented as the red solid line in Figure 5.16.

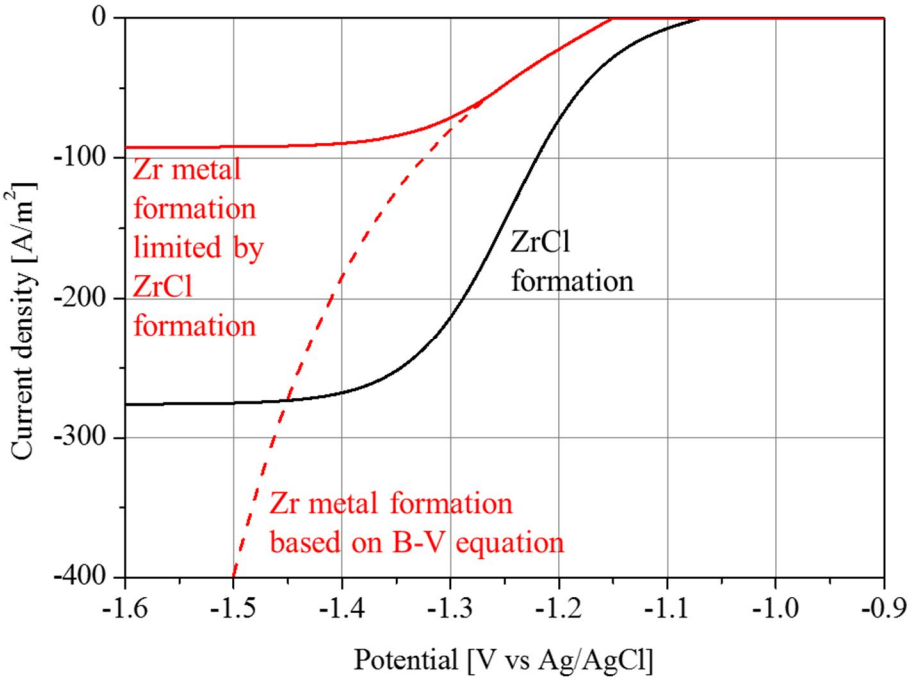

Figure 5.16 Current densities resulting from Zr metal and ZrCl formation according to applied potential with arbitrary diffusion boundary layer

The geometry and mesh for benchmarking lab-scale Zircaloy-4 electrorefining experiments were generated as represented in Figure 5.17. Configuration inside anode basket including Zircaloy-4 specimens is not considered in this computational modeling to increase mesh quality and improve convergence problem. In addition, because anodic dissolution model of the developed computational model is not strict, it might be hard to obtain precise computational modeling results for anode side even if the configuration inside anode is considered. For the similar reason, geometry of the reference electrode was assumed as cylindrical shape rather than actual geometry having corn shape. The high resolution tetrahedral mesh with the minimum size of 1 μm was generated to investigate sharp concentration profiles near electrodes. Total number of elements and nodes were 314,783 and 84,725 respectively.

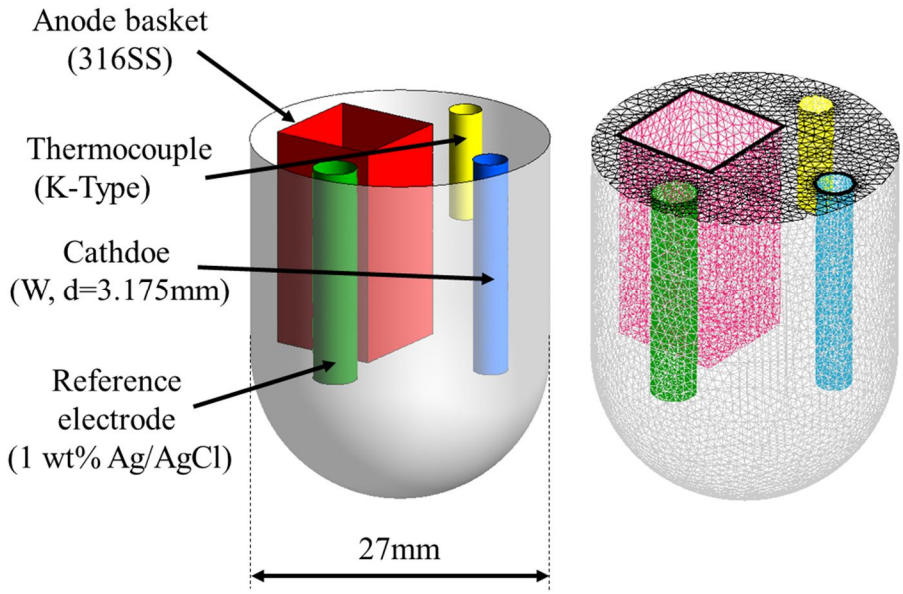

Figure 5.17 Lab-scale Zircaloy-4 electrorefining cell (left) geometry and (right) mesh grid generated for Zr multi-step reaction modeling

5.4.3 Results

Eight reaction rate constants for Zr metal formation reaction from ZrCl were utilized and chemical form of cathode deposits were estimated by 3-D computational electrorefining modeling for each case as represented in Table 5.3. For all reaction rate constants, calculated chemical forms of cathode deposits in 0.1 and 0.5 wt. % $ZrCl_4$ salts were Zr metal without ZrCl and the chemical form in 4.0 wt. % was ZrCl without Zr metal. This results are identical to lab-scale Zriclaoy-4 electrorefining in the section 4.3. In cases of 1.0 and 2.0 wt. % $ZrCl_4$ salts, chemical forms of zirconium compounds were dependent on reaction rate constant. As rate constant for the second reduction reaction producing Zr metal from ZrCl increases, weight fraction of Zr metal in cathode deposits increases. The rate constant range was from 1.0E-3 to 1.5E-3 m/s to reflect lab-scale electrorefining results that chemical form of cathode deposit for 1.0 wt. % $ZrCl_4$ concentration is a mixture of Zr metal and ZrCl while that for 2.0 wt. % $ZrCl_4$ concentration is ZrCl without Zr metal.

Table 5.3 Computational modeling results on weight percent of Zr metal in cathode deposits according to rate constant of Zr formation reaction

Rate constants [m/s]		Weight percent of Zr metal in cathode deposits				
$k_{0,Zr}$ (ZrCl/Zr)	$k_{0,ZrCl}$ (Zr(IV)/ZrCl)	0.1 wt. %	0.5 wt. %	1 wt. %	2 wt. %	4 wt. %
1.00E-06	1.69E-4	100	100	0	0	0
1.00E-05		100	100	0	0	0
1.00E-04		100	100	0	0	0
1.00E-03		100	100	45	0	0
1.50E-03		100	100	50.554	0	0
2.00E-03		100	100	57	10.037	0
1.00E-02		100	100	90	62.18	0
1.00E-01		100	100	100	72.01	0
Experimental results		100	100	>0	0	0

As represented in Figure 5.18, Figure 5.19 and Figure 5.20, computational modeling results on local mass production rates of ZrCl and Zr metal are compared to XRD patterns of cathode deposits from lab-scale Zircaloy-4 electrorefining in molten salts containing 0.5, 1.0 and 2.0 wt. % $ZrCl_4$. In these figures, mass production rates were calculated with reaction rate constant of 1.5E-3 m/s for the second reduction reaction. Since XRD patterns were obtained by scrapping all deposits on the cathode, calculated local mass production rates of Zr and ZrCl were not compared to experimental results directly.

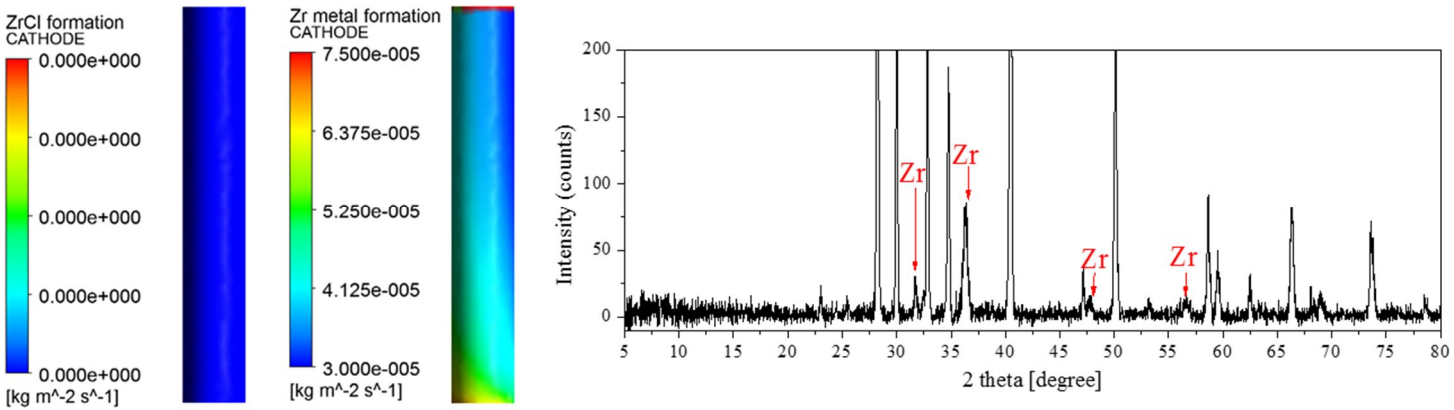

Figure 5.18 Computational results on mass production rate of (left) ZrCl and (middle) Zr on the cathode in LiCl-KCl-$ZrCl_4$ (0.5 wt. %) and (right) XRD patterns of cathode deposits after electrorefining in the same salts

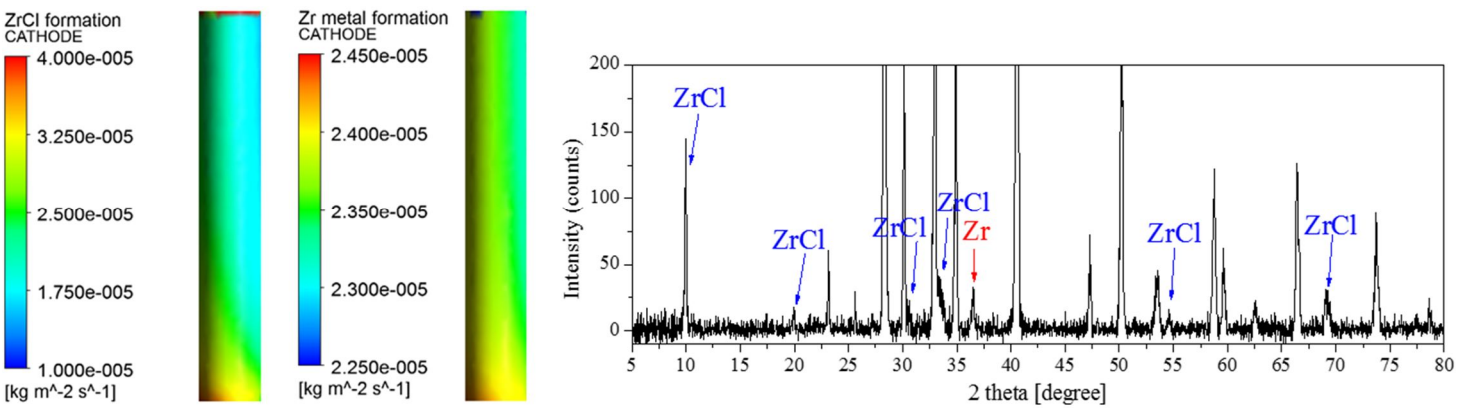

Figure 5.19 Computational results on mass production rate of (left) ZrCl and (middle) Zr on the cathode in LiCl-KCl-$ZrCl_4$ (1.0 wt. %) and (right) XRD patterns of cathode deposits after electrorefining in the same salts

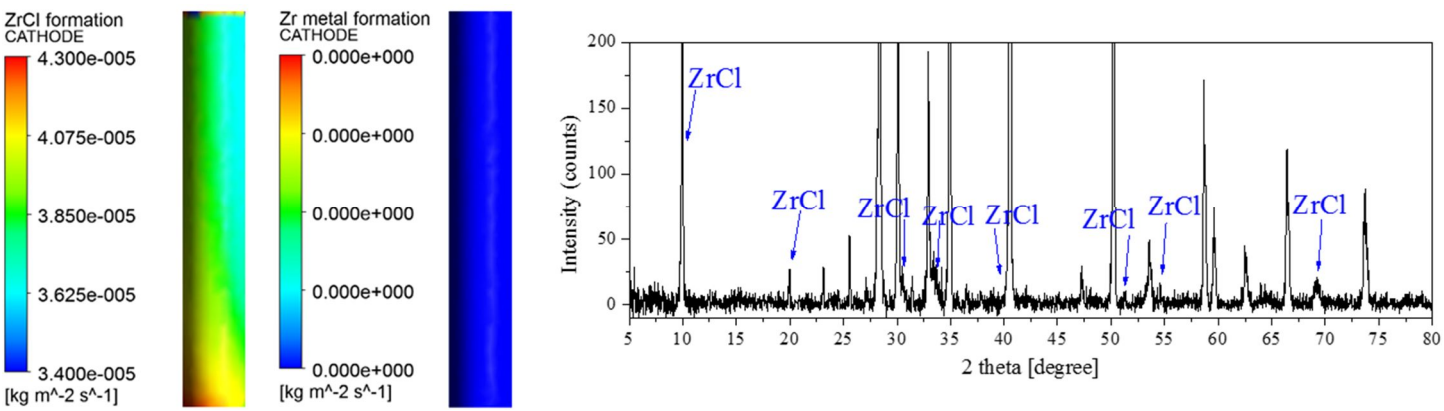

Figure 5.20 Computational results on mass production rate of (left) ZrCl and (middle) Zr on the cathode in LiCl-KCl-$ZrCl_4$ (2.0 wt. %) and (right) XRD patterns of cathode deposits after electrorefining in the same salts

5.4.4 Discussion

Conducting computational simulation on chemical form of Zr cathode deposits in five different $ZrCl_4$ concentration, it is identified that reaction rate constants from 1E-3 to 1.5E-3 for the second reduction reaction producing Zr metal form ZrCl would be preferred for reconciling computational modeling results with experimental results. The reaction rate constant for the first reduction reaction was assumes as 1.69E-4 m/s. Thus, the deduced reaction rate constant range is six to nine times higher than the first reduction reaction and it would mean that the second reduction reaction would be much faster than the first reduction reaction.

It would be electrochemically reasonable because the second reduction reaction is a metal/insoluble salt reaction. Since ZrCl is insoluble material, ZrCl could be located much closer to the electrode than ion species such as Zr(IV). Thus, electrons could be passed much easier and faster to ZrCl than to Zr(IV). In other words, current density resulting from the reaction between ZrCl and Zr metal would increase rapidly as electrode potential increases. In this reason, metal/insoluble salt reactions such as Ag/AgCl and $Hg/HgCl_2$ have used for reference electrode because electrode potential of a reference electrode using these reactions is maintained as almost constant even if current is applied (Bard and Faulkner, 2001; Patra et al., 2010; Newman and Thomas-Alyea, 2012).

Using the reaction rate constants from 1E-3 to 1.5E-3 for the second reduction reaction and material properties represented in Table 5.2, chemical

form changes of cathode deposits according to $ZrCl_4$ concentration were well estimated. Therefore, material properties might be utilized for pilot-scale irradiated spent nuclear fuel Zircaloy-4 cladding electrorefiner design and verification. However, transfer coefficient was just assumed as 0.5 and reaction rate constants for the first reduction reaction was assumed as the value of the reaction between U(III) and U metal in LiCl-KCl at 500^{o}C. To carry out more accurate computational electrorefining modeling, precise material properties related to electrochemical reaction such as transfer coefficient and rate constant are required. Both transfer coefficient and rate constant could greatly influence tendency of redox reaction and uncertain material properties could make the computational modeling results unreliable. Therefore, more experimental work and atomic scale modeling to produce material properties in molten salts would be needed to improve computational modeling accuracy.

Chapter 6 Pilot-scale Electrorefiner Design

6.1 Preliminary Zircaloy-4 electrorefining modeling[6]

Before conducting 3-D design of electrorefiner for irradiated spent nuclear fuel Zircaloy-4 cladding, preliminary 1-D simulation was conducted for various operating conditions including stirring effects, initial molten-salt composition and pre-set termination conditions. For the simulation, a 1-D time-dependent code for electrochemical reactions named as REFIN was utilized (Park, 1999; Choi et al., 2010).

6.1.1 Mathematical model

REFIN can calculate potential and current density distributions for each element in multispecies molten salt electrorefining. Also, this code can estimate surface concentration of each element and the amount of materials dissolved into molten salt or deposited on cathode. These variables are predicted as a function of time (Park, 1999). The key software has been

[6] This section has been written based on the following journal paper: Jaeyeong Park et. al., "Effect of operating conditions on molten-salt electrorefining for zirconium re covery from irradiated Zircaloy-4 cladding of pressurized water reactor," Nuclear Enginee ring and Design 275, 44-52, 2014.

developed as a proprietary code with full source programs maintained in FORTRAN language at Seoul National University.

In general electrorefining, elements at the anode are electrochemically dissolved into molten salts and metals are produced by reduction reactions on the cathode. The reversible or equilibrium potential for redox reaction could be expressed by Nernst equation;

$$E_{eq} = E_i^0 + \frac{RT}{z_i F} \ln\left(\frac{a_{i,salt}}{a_{i,metal}}\right) \tag{6.1}$$

where E_{eq} is the equilibrium potential, E_i^0 is the standard reduction potential, R is the universal constant (8.314 J/K/mol), T is the absolute temperature, z_i is the number of electrons participating in the reaction, F is the Faraday constant (96,485 C/mol) and $a_{i,j}$ is the activity of species i in the medium j.

Butler-Volmer equation is widely utilized as a governing equation for electrochemical reaction;

$$i_j = i_{0,j}\left[\exp\left(\frac{\alpha_j z_j F}{RT}\eta_j\right) - \exp\left(-\frac{(1-\alpha_j) z_j F}{RT}\eta_j\right)\right] \tag{6.2}$$

where, i_j is the current density of species j, $i_{0,j}$ is the exchange current density of species j, α_j is the transfer coefficient of species j, η_j is the overpotential of species j. The overpotential can be expressed as the

difference between the electrode potential, E and the equilibrium potential of species j, $E_{eq,j}$;

$$\eta_j = E - E_{eq,j} \tag{6.3}$$

In REFIN, to utilize Butler-Volmer equation, one-step reaction is assumed for all of electrochemical redox reactions. It is also supposed that thermodynamic and transport properties for ions and electrolytes such as diffusion coefficients and exchange current densities are maintained at a constant during electrorefining. In addition, because REFIN is a one-dimensional model, uniform reactions over electrodes are presumed.

Various multi-species electrochemical reactions could occur in actual electrorefining. To consider both multi-species reactions and mass transfer effect through Butler-Volmer equation, overpotential can be redefined by introducing the assumption of the reference state.

$$\eta_j = E - E_{eq,j,ref} \tag{6.4}$$

$E_{eq,i,ref}$ is the equilibrium potential for any reference states as represented in Eq. (6.5);

$$E_{eq,j,ref} = E^0_{eq,j} + \frac{RT}{n_j F}\sum_i s_{i,j} \ln a_{i,ref} \tag{6.5}$$

where $s_{i,j}$ is the stoichiometric coefficient of species i for reaction j. Finally, Butler-Volmer equation could be expressed as described in Eq. (6.6);

$$i_j = i_{0,j}^0 \prod_i a_{i,ref}^{(1-\alpha_j)p_{i,j}+\alpha_j q_{i,j}} \left[\prod_i \left(\frac{a_i}{a_{i,ref}} \right)^{p_{i,j}} \exp\left(\frac{\alpha_j n_j F}{RT} \eta_j \right) - \prod_i \left(\frac{a_i}{a_{i,ref}} \right)^{q_{i,j}} \exp\left(-\frac{(1-\alpha_j) n_j F}{RT} \eta_j \right) \right] \tag{6.6}$$

where $p_{i,j}$ and $q_{i,j}$ are defined as Eq. (6.7) and (6.8).

$$p_{i,j} = s_{i,j},\ q_{i,j} = 0 \text{ if } s_{i,j} > 0 \tag{6.7}$$

$$q_{i,j} = -s_{i,j},\ \mathrm{p}_{i,j} = 0 \text{ if } s_{i,j} < 0 \tag{6.8}$$

Total anodic and cathodic current density for multi-species redox reactions are described by the summation of current densities for each reaction;

$$I_a = \sum_j^n i_{j,a} \tag{6.9}$$

$$I_c = \sum_j^n i_{j,c} \tag{6.10}$$

where I_a is the total anodic current, I_c is the total cathodic current density, $i_{j,a}$ is the anodic current density for the reaction j and $i_{j,c}$ is the cathodic current density for the reaction j.

Mass transport in electrolyte could be described by the equation combining electromigration, diffusion and convection. Since the electrolyte beyond diffusion boundary layer is not considered in REFIN by assuming that there are not concentration differences in bulk electrolyte, mass transport could be calculated by the combination of electromigration and diffusion as represented in Eq. (6.11);

$$\vec{J_i} = -D_i \Gamma_i \vec{\nabla} C_i - \frac{z_i F D_i}{RT} C_i \vec{\nabla} \varphi \qquad (6.11)$$

where $\vec{J_i}$ is the flux density of species i, D_i is the diffusion coefficient of species i, Γ_i is the correction of diffusion coefficient by the change of activity, C_i is the concentration of species I and ϕ is the electrical potential. The effect of convection can be considered by modifying diffusion boundary layer thickness which is an input parameter of REFIN.

6.1.2 Modeling conditions and electrorefiner geometry

For computational efficiency, we have selectively considered important elements for electrochemical and fluid-dynamic behavior. Four major elements of Zircaloy-4 cladding are simulated: Zr, Sn, Fe, and Cr. Among activations products from impurities, cobalt is chosen because Co-60 is the highest contributor for irradiated cladding to exceed the IAEA clearance

level after 10 years cooling as represented in Figure 1.1. Moreover, uranium, as the most substantial actinide, represents all other actinide elements within spent zirconium cladding. Thus, the material composition of spent PWR cladding is decided as shown in Table 6.1 for the initial stage of multi-stage Zr electrorefining. Ion properties in molten salt used in Zircaloy-4 electrorefining simulation such as standard potential and diffusion coefficient are represented in Table 6.2.

Table 6.1 Simplified weight fraction of irradiated PWR Zircaloy-4 cladding for electrochemical simulation; it is used as the composition of anode in electrorefining simulation

Elements	Weight fraction
Zr	0.980748
Sn	0.015
Fe	0.0021
Cr	0.001
Co	0.00002
U	0.001132

Table 6.2 Ion properties used in electrorefining simulation

Redox pair	Standard potential [V vs. Cl_2/Cl^-]	Diffusion coefficient of ion [cm^2/s]	Exchange current density [A/cm^2]	Transfer coefficient
Zr^{4+}/Zr	-2.186[a]	1.12 $x10^{-5}$ [b]		
Sn^{2+}/Sn	-1.298[a]	$2.5x10^{-5}$ (assumed)		
Fe^{2+}/Fe	-1.388[a]	2.5 $x10^{-5}$ (assumed)	1 $x10^{-6}$ (assumed)	0.5 (assumed)
Cr^{2+}/Cr	-1.641[a]	2.5 $x10^{-5}$ (assumed)		
Co^{2+}/Co	-1.207[a]	3.7 $x10^{-5}$ [c]		
U^{3+}/U	-2.5[a]	2.7 $x10^{-5}$ [d]		

[a](Iizuka et al., 2001)

[b](Yamada et al., 2007b)

[c](Groult et al., 2010)

[d](Serp et al., 2006)

Various values for U^{3+} diffusivity in LiCl-KCl molten salts have been reported (Serp et al., 2006; Yamada et al., 2007b). The diffusivity from Serp et al. is about twice as high as the value from Yamada et al. where the diffusivity of Zr^{4+} used in this study is described. Although it is more desirable to use material properties from the same reference, the diffusivity from Serp et al. is utilized in this study to obtain conservative results for U deposition. If diffusivity is high, relatively small overpotential would be required at a given applied current density or relatively large current density could be secured at the given electrode potential. Therefore, if U is not deposited in the case of high U diffusivity, U would not be deposited in the case of low diffusivity.

For irradiated Zircaloy-4 electrorefiing simulation using REFIN, it is assumed that Zr^{4+} is reduced to Zr metal through one-step reaction because one-step reaction is a basic assumption of REFIN. Previous studies reported that Zr^{4+} could be directly reduced into Zr in LiCl-KCl molten salts at high negative potential near -1.5 V (vs. Ag/AgCl) (Lee et al., 2012; Park et al., 2014). However, Zr metal could be formed on the cathode at more positive potential near -1.2 V (vs. Ag/AgCl) through two-step reaction (Park et al., 2014):

$$Zr^{4+} + 3e^{-} \rightarrow ZrCl$$
$$ZrCl + e^{-} \rightarrow Zr$$

Since two-step reaction is more dominant reaction on Zr metal formation, the

one-step redox of Zr assumed in this study represents the simplified two-step reaction rather than one-step reaction at high negative potential.

Total 240 cases are simulated and presented here to analyze the effects of operating conditions in zirconium electrorefining. Three important conditions are selected: initial concentration of chlorides in molten salts except $ZrCl_4$, diffusion boundary layer thickness and termination condition of electrorefining. Initial concentration concentration is a significant parameter for electrorefining because equilibrium potential which could determine whether redox reaction could occur at the given electrochemical condition is a function of concentration. As ion concentration in molten salts raises, equilibrium potential increases logarithmically. Previous study on U electrorefining in Mark-IV electrorefiner located at Idaho National Laboratory revealed that current resulting from Zr redox reaction could rises as initial U concentration in the molten salts increases (Hoover et al., 2009). As represented in Table 6.3, ten different values for the sum of initial chloride concentrations ($SnCl_2$, $FeCl_2$, $CrCl_2$, $CoCl_2$ and UCl_3) are chosen from $1x10^{-11}$ to $1x10^{-2}$ wt. %. The concentration ratio between metals in chlorides except $ZrCl_4$ corresponds with the concentration ratio of anode. The concentration of $ZrCl_4$ is fixed as 1wt. % because $ZrCl_4$ is added as initiator of electrorefining.

Table 6.3 Molten salts composition used in spent Zircaloy-4 cladding electrorefining simulation

	$ZrCl_4$	Other Chlorides					Molten salt	
		$SnCl_2$	$FeCl_2$	$CrCl_2$	$CoCl_2$	UCl_3	LiCl	KCl
Concentration	1 wt. %	$1x10^{-11}$, $1 x10^{-10}$, $1 x10^{-9}$, $1 x10^{-8}$, $1 x10^{-7}$, $1 x10^{-6}$, $1 x10^{-5}$, $1 x10^{-4}$, $1 x10^{-3}$, $1 x10^{-2}$ wt. %					Remainder	
Chloride concentration ratio in group	1	0.73111	0.14544	0.07213	0.00134	0.04998	0.425	0.575

Diffusion boundary layer thickness is also an important operation condition because this is related to concentration overpotential and ion transfer from/to electrode. If diffusion boundary layer thickness is large, relatively large overpotential is required at a given applied current density and it could result in impurities deposition on a cathode (Choi et al., 2010). Diffusion boundary layer thickness is closely related to stirring conditions such as rotational speeds of electrodes. For diffusion boundary layer, its thickness includes eight different values – 0.25, 0.1, 0.05, 0.025, 0.001, 0.005, 0.0025 and 0.001mm.

Electrorefining termination condition could influence impurity dissolution from an anode (Hoover et al., 2011). At the final stage of electrorefining, target element could be depleted at the anode and this could result in rapid increase of anode potential. Oxidative elements could be dissolved from the anode and cause contamination on the cathode. Therefore, it is very significant to monitor anode potential for preventing impurity dissolution. In this study, for the electrorefining termination condition, three values of anode potential – -2.1, -1.8 and -1.5V (vs. Cl_2/Cl^-) are adopted.

As shown in Figure 6.1, this study used a simple geometry of electrorefiner. The areas of cathode and anode are 6.4795 cm^2 and 13.352 cm^2, respectively. The volume of LiCl-KCl molten-salt is 98.175 cm^3 and the weight is 159.04 g. The weight of Zircaloy-4 on the anode is 20.609 g. Applied current density on the cathode is assumed as 0.1 A/cm^2.

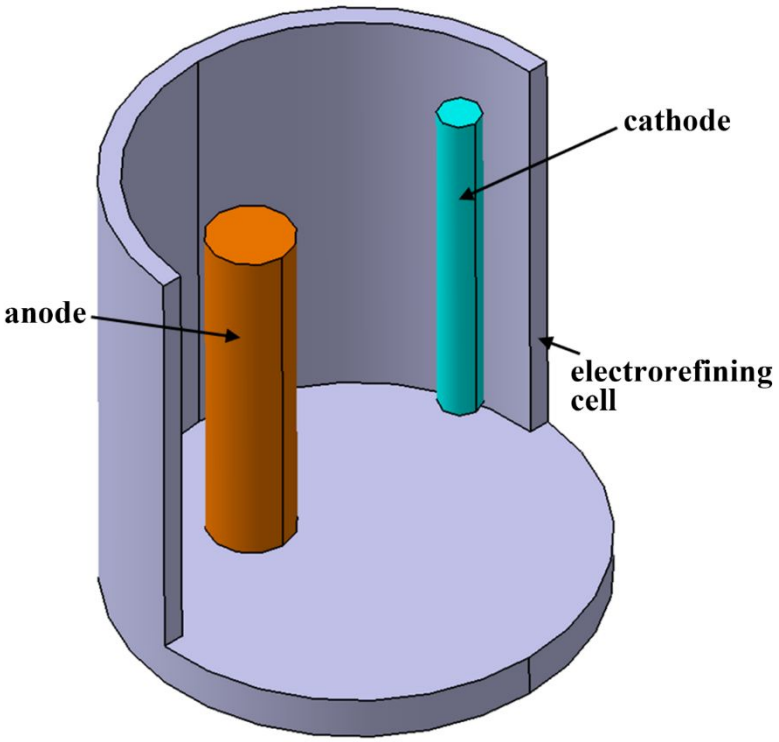

Figure 6.1 Schematic geometry utilized for the zirconium electrorefining simulation: the anode has 1 cm diameter and 4 cm height and the cathode has 0.5 cm diameter and 4 cm height

Several important assumptions are made for avoiding unnecessary calculation difficulties. First, all electrochemical reactions are considered as one step reaction since it is hard to reflect a multi-step electrochemical reaction in REFIN. In actual zirconium electrorefining in LiCl-KCl molten salt, Zr(IV) ion could react with zirconium metal to form Zr(II) ion (Fujita et al., 2005a) and Zr(IV) ion could be reduced into Zr(I) or Zr(II) on cathode (Lee et al., 2012). Second, Zr(II) ion is ignored in molten-salt since Sakamura (Sakamura, 2004) reported that Zr(II)/Zr(IV) ratio is very low in 500^{o}C LiCl-KCl. The dominant oxidation state is Zr(IV) that is considered for this simulation. Third, radial distribution of elements is ignored with the assumption that all elements exist on the cathode surface.

It is assumed that there is no radioactive decay reaction during the electrorefining because half-life of Co-60 is long enough compared to decontamination time. All Co materials in anode, cathode and molten-salt have the same isotope composition of irradiated Zircaloy cladding after 5 years post cooling. Only 1.06wt. % of Co is Co-60.

6.1.3 Results

6.1.3.1 General behavior of Zircaloy-4 electrorefining

Figure 6.2 shows time-dependent electrodeposition results on cathode during electrorefining of irradiated PWR Zircaloy-4 cladding. In this calculation, the simulation was finished when all elements in anode were dissolved as a

preset condition. Total operation time was 36.9 hours. At the initial stage of electrorefining, Sn^{2+}, Cr^{2+} and Co^{2+} were reduced into metallic form on cathode since these ions were more reductive than Zr^{4+}. These ions were quickly depleted in molten-salt and their reduction potentials largely decrease. These ions were initially in molten-salt, not yet coming from anode. As represented in Figure 6.3 and Figure 6.4, there are no significant concentration change of these ions in molten salt and no significant dissolution from anode until the end stage of electrorefining. Meanwhile, zirconium was continuously dissolved into molten-salt as ionic form.

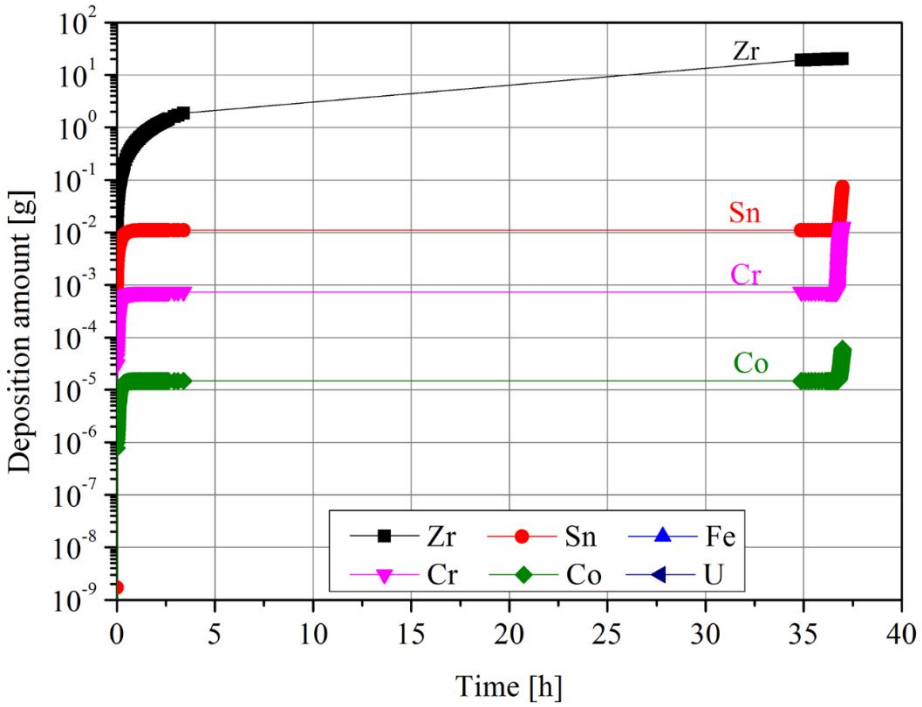

Figure 6.2 Deposition behavior on cathode during electrorefining of irradiated PWR Zircaloy-4 cladding: diffusion boundary layer thickness of 0.1 cm and impurity fraction of 1 x10^{-4} in molten salt

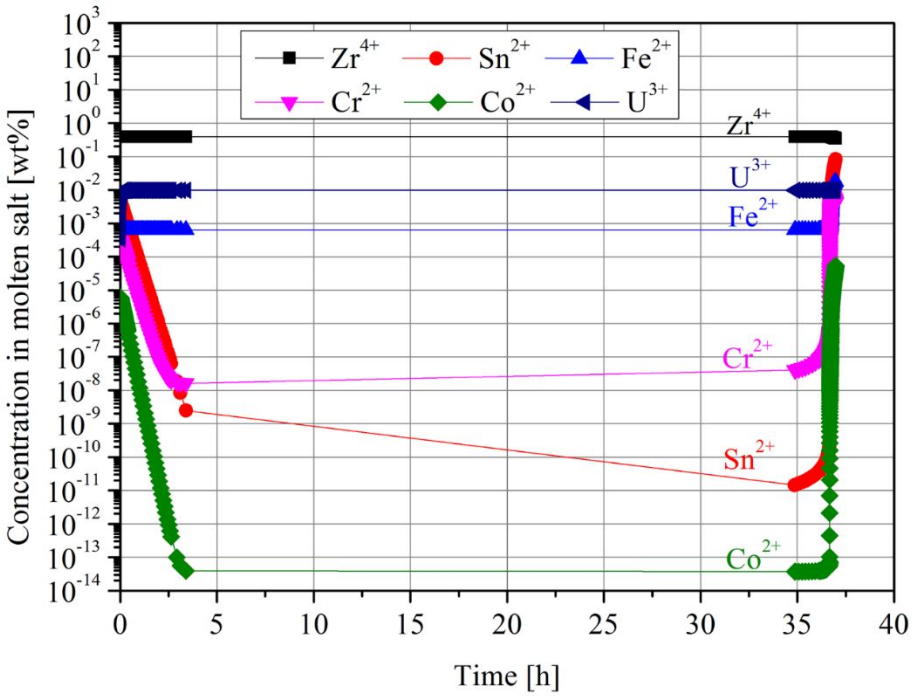

Figure 6.3 Ion concentration change in molten salt during electrorefining of irradiated PWR Zircaloy-4 cladding: diffusion boundary layer thickness of 0.1 cm and impurity fraction of 1 x10^{-4} in molten salt

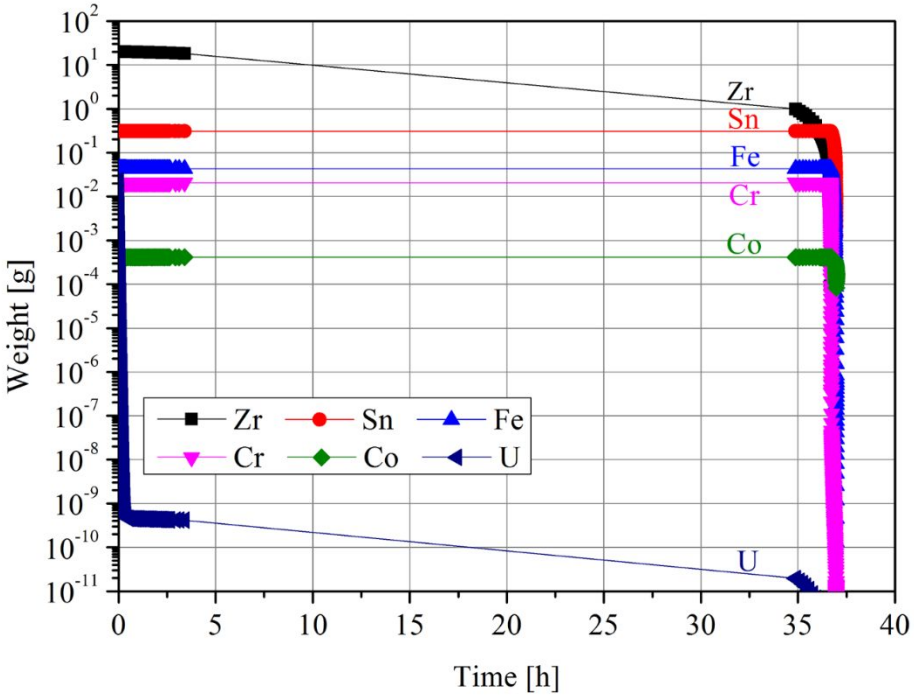

Figure 6.4 Dissolution behavior on anode during electrorefining of irradiated PWR Zircaloy-4 cladding: diffusion boundary layer thickness of 0.1 cm and impurity fraction of 1 x10^{-4} in molten salt

After about an hour operation of electrorefining, only zirconium ion began to be deposited on cathode until 36.5 hours. On the other hand, U and Fe are not theoretically deposited because they are less reductive than other ions. Only after most zirconium was dissolved from anode to molten-salt, other noble elements such as Sn, Cr, Co and Fe in anode started to be oxidized. Uranium began to be dissolved from anode earlier than other elements including zirconium because its standard potential is more oxidative. Since U is not deposited on the cathode although U is dissolved from anode, U is accumulated during electrorefining. However, since most of uranium, about 0.02333 g, is dissolved for an hour and U of $1x10^{-9}$ g is dissolved during remaining time, U concentration in the molten salts seems like maintaining a constant during electrorefining as represented in Figure 6.3. After 36.5 hours, Zr depletion in molten-salt results in decrease of reduction potential of Zr, causing co-deposition on Sn, Cr and Co with Zr again.

If a termination condition of Zr electrorefining is appropriately presumed, most contamination of deposited zirconium would depend on the initial concentration of Sn^{2+}, Cr^{2+} and Co^{2+} in molten-salt. As long as initial molten-salt maintains clean enough without significant contamination by these ions, the contamination on deposited zirconium by these ions would be greatly reduced. The termination condition may be determined by monitoring anode potential change because anode potential would increase to find other reactive elements if zirconium in anode is depleted as represented in Figure 6.5. Potential of all elements suddenly increase at 36.67 hours after

electrorefining and Zr potential becomes more positive than other elements. This time agrees the time when Zr starts being depleted at the anode and other elements starts being dissolved from the anode. This approach might leave a small amount of zirconium still in anode, but it could keep salt clean enough while the purity of deposited zirconium could be also enhanced. To investigate the effect of electrorefining termination condition on decontamination factor, three termination conditions (-2.1, -1.8 and -1.5 V (vs. Cl_2/Cl^-)) are selected as represented in Figure 6.5.

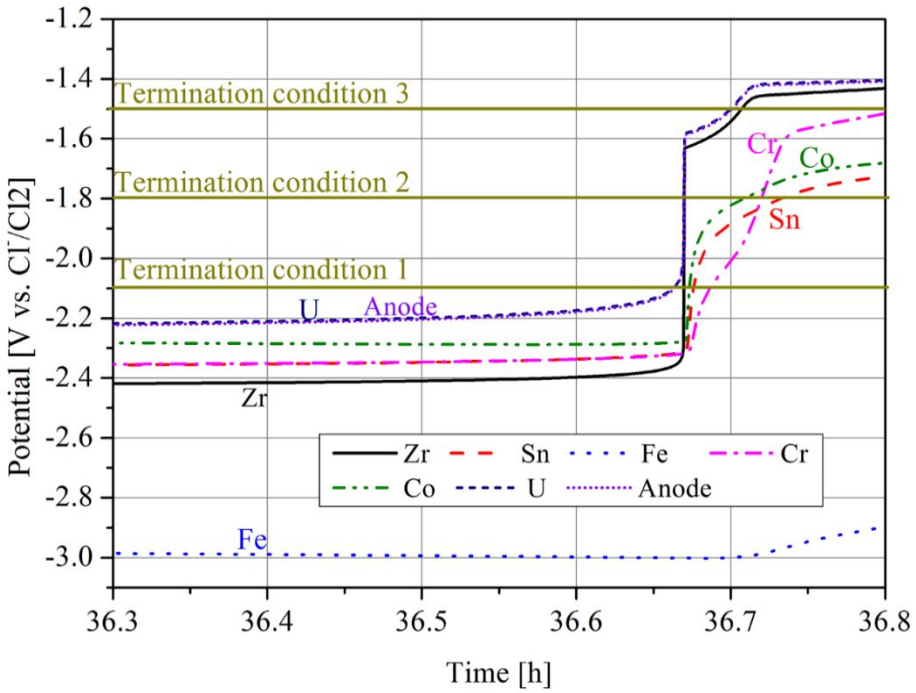

Figure 6.5 Anode potential behavior at the end stage of electrorefining of irradiated PWR Zircaloy-4 cladding: diffusion boundary layer thickness of 0.1 cm and impurity fraction of 1 x10^{-4} in molten salt

6.1.3.2 Decontamination factors for operating condition

A decontamination factor (DF) of an element is defined as:

$$DF = \frac{\text{Initial amount loaded at anode}}{\text{Deposition amount at cathode}} \qquad (6.12)$$

Thus, the decontamination factor determines the purity of deposited zirconium. Low DF for zirconium and high DF for other elements increase the purity of zirconium. Since the radioactivities of Sn and Cr do not exceed the clearance level from the beginning and Co is a major radioactive impurity, the radioactivity of Co in the deposited zirconium or the decontamination factor of Co determines the purity of recovered zirconium.

Overall 240 different cases were calculated, analyzed, and compared for finding the effects of diffusion boundary layer thickness, initial contamination of molten-salt and electrorefining termination condition on the decontamination factors of Co in recovered zirconium. As shown in Figure 6.7 and Figure 6.8, for termination conditions of -2.1 and -1.8 V (vs. Cl_2/Cl^-) anode potential, decontamination factor for Co and initial contamination in molten salt has linear inverse proportional relation in log scale. For the termination condition of -1.5 V (vs. Cl_2/Cl^-) anode potential, decontamination factor for Co is in linear inverse proportion to the initial contamination of molten salt from 1 $x10^{-5}$ to 1 $x10^{-2}$ weight fraction but there are no marked changes when initial contamination in molten salt is lower

than 1 $x10^{-7}$ weight fraction as represented in Figure 6.8. The decontamination factors of Co for the -1.5 V (vs. Cl_2/Cl^-) anode potential are much lower than others because of Co deposition on cathode at the end stage of electrorefining. The differences among termination conditions could result from deposition of Co at the end stage of electrorefining as represented in Figure 6.9.

In most of cases, thicker boundary layer results in lower decontamination factor. This tendency becomes reverse in low initial concentration of Co. For most cases, Co-60 is decontaminated in deposited zirconium over decontamination factor of 10. Only a few extreme cases using dirty molten-salt (i.e. high initial concentration of Co) failed to decontaminate Co-60 and produced more contaminated zirconium than the beginning.

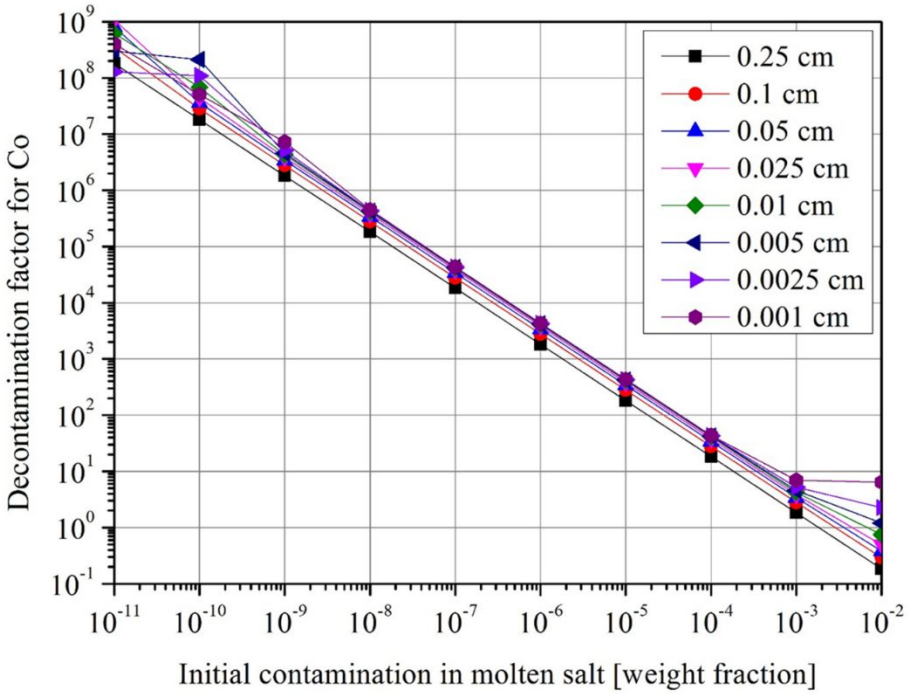

Figure 6.6 Decontamination factors for Co according to diffusion boundary layer thickness and initial contamination in molten salt; the electrorefining is terminated at -2.1 V (vs. Cl_2/Cl^-) of anode potential

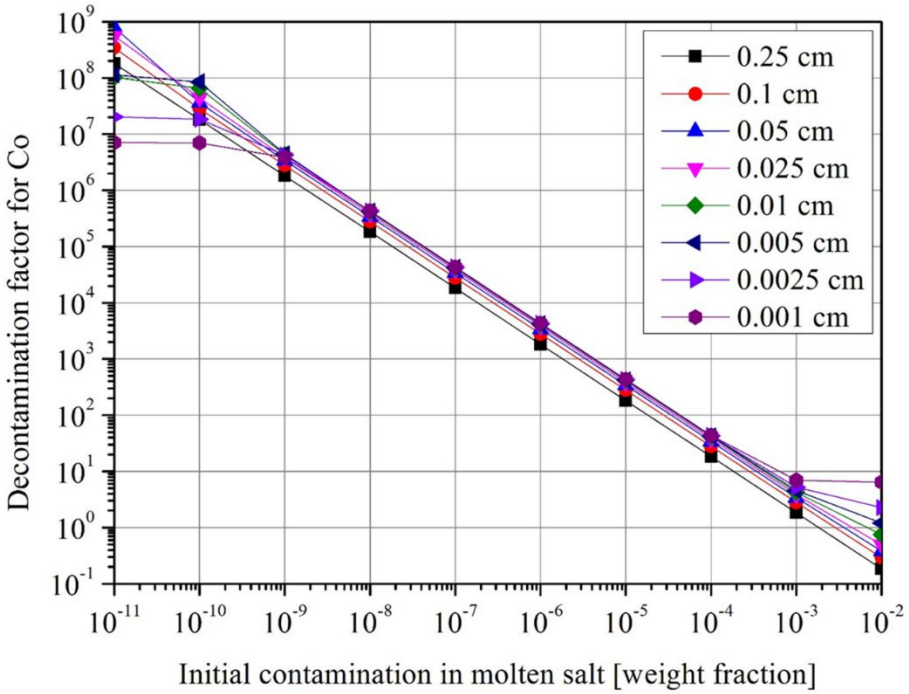

Figure 6.7 Decontamination factors for Co according to diffusion boundary layer thickness and initial contamination in molten salt; the electrorefining is terminated at -1.8 V (vs. Cl_2/Cl^-) of anode potential.

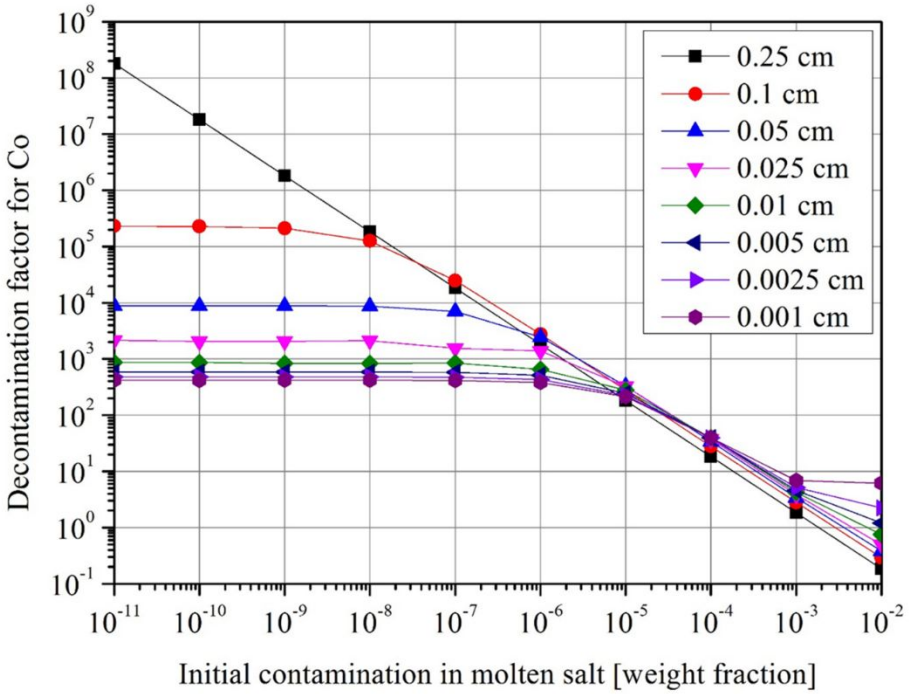

Figure 6.8 Decontamination factors for Co according to diffusion boundary layer thickness and initial contamination in molten salt; the electrorefining is terminated at -1.5 V (vs. Cl_2/Cl^-) of anode potential.

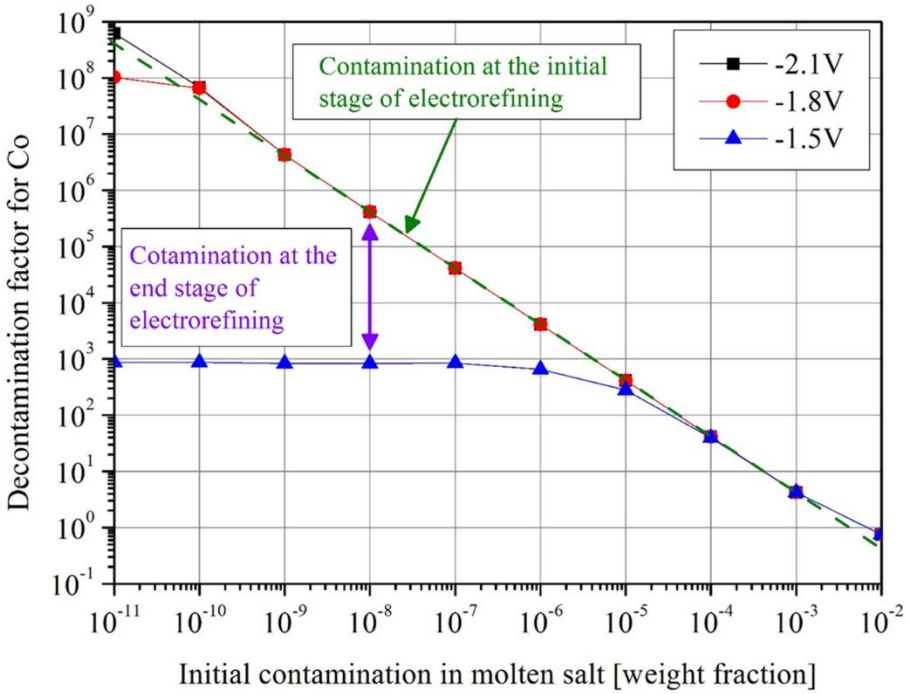

Figure 6.9 Comparison of decontamination factors according to electrorefining termination condition; the diffusion boundary layer thickness is 0.01 cm

6.1.4 Discussion

6.1.4.1 Diffusion boundary layer effect

Because Co is more reductive than Zr, the Co^{2+} ion which existed in initial molten-salt could be thermodynamically reduced on anode at the initial stage of electrorefining while other metals are oxidized. More Co^{2+} ion might be transported to anode with thinner boundary layer thickness; as a result, less amount of cobalt could be deposited on the cathode. In addition, large concentration overpotential is required for the applied current density when boundary layer is thick and this could cause codeposition of Co. For the termination condition of -1.5 V (vs. Cl_2/Cl^-) anode potential, thicker diffusion boundary layer cases cause lower cobalt contamination in cases of low concentration contamination. This trend could be because thinner diffusion boundary layer increases ion transfer from anode to cathode. Co might be dissolved when zirconium at anode is exhausted at the last stage. If mass transfer is fast near the electrode, Co^{2+} which is dissolved at the end of electrorefining could reach cathode faster than small diffusion boundary layer case. Therefore, at the initial stage of electrorefining, thinner diffusion boundary layer would be preferable and thicker diffusion boundary layer would be better for preventing contamination on cathode.

When cylindrical cathode is located in the cylindrical cell, the diffusion boundary layer thickness (δ) near electrode could be expressed as the rotation speed of cathode by Eisenberg equation as following (Low et al.,

2007):

$$\delta_N = 12.64 U^{-0.7} d^{0.3} \nu^{0.34} D^{0.356} \quad (6.13)$$

where U is the tangential speed of cathode, d is the diameter of cathode, ν is the kinematic viscosity of molten salt and D is the diffusion coefficient of Zr(IV) ion in molten salt. The rotating speeds equivalent to the diffusion boundary layer thicknesses utilized in the simulation are represented in Table 6.4. For the calculation, diffusion coefficient of Zr(IV) ion is 1.12 x10^{-5} cm^2/s and kinematic viscosity of molten salt is 0.00793 cm^2/s (Bae et al., 2010; Choi et al., 2010). In the simulated electrorefining system which is close to the lab scale, the diffusion boundary layer thicknesses of 1 x10^{-3} and 2.5 x10^{-3} cm would be hard to be secured by rotation of the cathode since about 5,950 and 1,610 rpm are required respectively. In addition, diffusion boundary layer thicknesses of 5 x10^{-3} and 1 x10^{-2} cm might be difficult to be achieved in the geometry used in this study because they requires high rotational speeds and it might results in turbulence. If turbulence becomes serious, Eisenberg equation might be hard to be applied because the geometry used in this study is not perfectly concentric. However, by adopting additional stirrer or increasing cathode size, small diffusion boundary layer thickness could be obtained.

Table 6.4 Rotating speed of cathode equivalent to diffusion boundary layer thickness used in the simulation: Eisenberg equation is used for the relationship between diffusion boundary layer thickness and rotating speed

Diffusion boundary layer thickness [cm]	Rotating speed of cathode [rpm]
0.25	2.23
0.1	8.25
0.05	22.2
0.025	60.0
0.01	221
0.005	597
0.0025	1610
0.001	5950

6.1.4.2 Initial molten salt contamination effect

If chlorides like $SnCl_2$, $CrCl_2$ and $CoCl_2$ except $ZrCl_4$ exist in molten salt which is prepared for zirconium electrorefining, the purity of recovered zirconium could be lowered because elements such as Sn, Cr and Co which is more reductive than Zr would be deposited on cathode at the initial stage of electrorefining. Therefore, if the molten salt is planned to be reused for the next electrorefining, the contamination level of used molten salt should be considered. In case that most of zirconium loaded at anode is recovered with almost 100% purity at the simulated system, chlorides except $ZrCl_4$ would have 4.25 $x10^{-3}$ weight fraction in molten salt. If the molten salt is reutilized for the next electrorefining, decontamination factor for Co greater than 10 would be hard to be achieved due to severe contamination on cathode at the initial stage of electrorefining.

Zircaloy-4 cladding irradiated in pressurized water reactor has Co-60 whose radioactivity is about 6.10 $x10^7$ Bq/g. Since it is 6.10 $x10^8$ times greater than IAEA clearance level, decontamination factor for Co should be larger than 6.10 $x10^8$ so that radioactivity of Co-60 in recovered zirconium satisfies IAEA clearance level. To achieve this, the initial concentration of chlorides except $ZrCl_4$ should be prepared lower than 1 $x10^{-11}$ weight fraction. Because of the radioactivity of Zr-93 in the recovered zirconium, radioactivity of recovered zirconium could not be lower than 358.6 Bq/g which is higher than the IAEA clearance level of Zr-93, 10 Bq/g. For this reason, if the radioactivity of Co-60 in recovered zirconium is

targeted as the level of ratio between Zr-93 radioactivity and IAEA clearance level, the decontamination factor for Co greater than 1.7E7 should be secured. To reach this, the initial concentration of chlorides except $ZrCl_4$ should be prepared lower than 1 $x10^{-10}$ weight fraction. High purity molten salts based on LiCl-KCl could be prepared by various salt purification processes such as reductive extraction and selective oxidation which have been developed for pyroprocessing of used nuclear fuel (Kinoshita et al., 1999; Kwon et al., 2009; Cho, 2013). In addition, composition of prepared salt could be measured by various methods including ICP methods and spectroscopies.

6.1.4.3 Electrorefining termination condition effect

Electrorefining termination condition could influence on recovery ratio of zirconium and decontamination factor of Co. In this study, three anode potentials are selected as termination conditions and compared. Since anode potential starts to be rapidly changed when zirconium is depleted at anode, there are no significant differences for recovery ratios of zirconium. For all termination conditions, it was possible to recover over 96% zirconium for $1x10^{-3}$ weight fraction contamination in initial molten salt, over 99.5% zirconium for 1 $x10^{-3}$ weight fraction contamination and over 99.9% zirconium for 1 $x10^{-4}$ weight fraction. When the contamination weight fraction is lower than 1 $x10^{-4}$, the recovery ratio of zirconium is greater than 100% and it means some amount of $ZrCl_4$ which is added to molten salt as

an initiator of electrorefining is reduced to zirconium metal on cathode. Decontamination factors for Co are similar between electrorefining termination conditions of -2.1 V (vs. Cl_2/Cl^-) anode potential and -1.8 V (vs. Cl_2/Cl^-) anode potential. However, decontamination factors for Co of -1.5 V (vs. Cl_2/Cl^-) anode potential termination condition differ widely from that of other cases. As a result of this, it could be identified that most deposition of Co could occur during anode potential changes from -1.8 to -1.5 V (vs. Cl_2/Cl^-) and depositions before -1.8V (vs. Cl_2/Cl^-) are performed at the initial stage of electrorefining.

6.2 3-D Zircaloy-4 cladding electrorefiner design

Pilot-scale electrorefiner to decontaminate irradiated spent nuclear fuel Zircaloy-4 cladding was designed based on the developed 3-D computational electrorefining model and suggestions developed from lab-scale molten salt experiments. Final electrorefiner design is described in Table 6.5. The detailed reasons for the design are explained in following sections.

Table 6.5 Final design of the pilot-scale electrorefiner for irradiated spent nuclear fuel Zircaloy-4 cladding

Configuration of the electrorefiner	**1. Reactor vessel**	
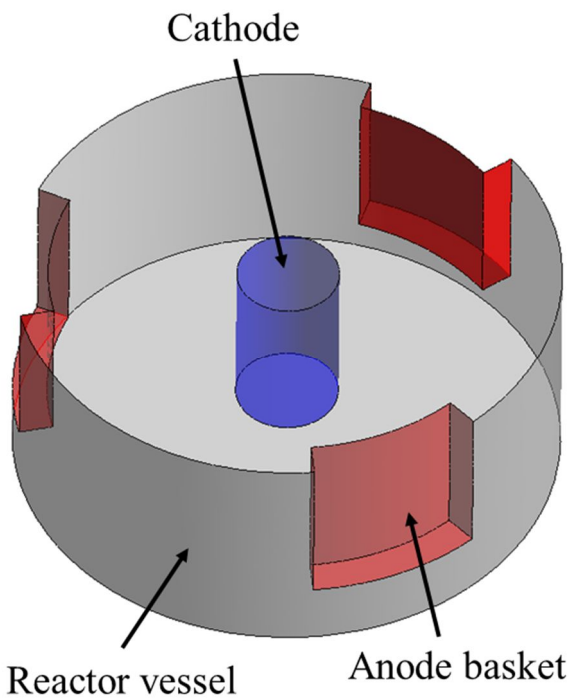	1.1 Height	35 cm
	1.2 Diameter	80 cm
	1.3 Volume (including anode basket)	175,929 cm^3
	2. Anode basket	
	2.1 Height	25 cm
	2.2 Inner diameter of anode basket	75 cm
	2.3 Angle of anode basket	37^o
	2.4 The number of anode basket	3
	2.5 Total volume of anode baskets	9081 cm^3
	2.6 Weight of Zircaloy-4 claddings	10 kg
	2.7 Volume of Zircaloy-4 cladding including hollow	6799 cm^3
	2.8 Area of Zircaloy-4 loaded into anode basket	53,820 cm^2
	2.9 Zircaloy-4 cladding loading efficiency	75%
	3. Cathode	
	3.1 Height	25 cm
	3.2 Diameter	15 cm
	3.3 Area	1,355 cm^2

6.2.1 Design concept and assumptions

The amount of irradiated Zircaloy-4 claddings loaded into the anode basket was determined as 10 kg which is similar amount of Mark-IV electrorefiner which is a pilot-scale LiCl-KCl salt based electrorefiner used for reprocessing metallic fuels of EBR-II. If the irradiated cladding geometry is assumed as an inner diameter of 0.836 cm and an outer diameter of 0.950 cm, the total surface area of fuel claddings loaded into anode basket is about 53,820 cm^2 (Ronen and Raitses, 2002). If claddings are loaded into the anode basket with cylindrical shape, the volume of Zircaloy-4 cladding including hollow of the cladding would be 6799 cm^3. Anode basket volume is determined as 9081 cm^3 with the assumption that cladding loading efficiency is about 75%. LiCl-KCl-$ZrCl_4$ (0.5 wt. %) salts were used as the initial electrolyte to obtain Zr metal without ZrCl. The cylindrical shape is introduced for molten salt container of electrorefiner as represented in Table 6.5.

Rotating anode basket could make cross flows near the cathode and this could result in complicated local mass transfer over the cathode (Labraga and Berkah, 2004; Choi et al., 2010). This could cause local depletion of Zr(IV) and local uranium deposition on cathode. In addition, rotating anode could intensify global mass transfer over the cathode. It means that Zr(IV) could be well transferred to the cathode. As revealed in the section 4.3, high surface concentration of Zr(IV) on the cathode could enhance the reduction reaction producing ZrCl from Zr(IV) but this could

not influence on the reaction rate of Zr metal formation from ZrCl. For this reason, to suppress ZrCl formation and recover Zr metal without ZrCl and U, fan-shaped anode baskets are fixed at the electrorefiner wall as represented in Table 6.5. A cylindrical cathode is placed into the center of the electrorefiner to secure circumferential electric field symmetry near the cathode. To secure small enough anodic current density during electrorefining, the cathode area is determined as 1,355 cm^2 with the height of 25 cm and diameter of 15 cm which is much smaller than the area of Zircaloy-4 claddings loaded into anode baskets.

Since it is identified that dissolution of elements which are more reductive than Zr such as Sn, Cr, Fe, Co and some fission products could be prevented by anode potential control and anodic dissolution model of the developed computational electrorefining model does not entirely work, these elements are not considered for pilot-scale electrorefiner design. However, U is considered with Zr as a representative of actinide penetrating into Zircaloy-4 cladding. For the conservative design on U decontamination, it is assumed that all uranium elements in irradiated Zirclaoy-4 cladding are dissolved into molten salts immediately and uniform UCl_3 salts solution is prepared at the very initial stage of electrorefining. Although Cs-137 and Sr-90 are one of radioisotopes that should be decontaminated from irradiated spent nuclear fuel Zircaloy-4 cladding, Cs and Sr are not considered because these elements are more oxidative than U. If U is not deposited on the cathode, Cs and Sr would not be also deposited.

6.2.2 Potential window for obtaining high purity Zr metal

The relations among current density, electrode potential and mole production rate at an arbitrary diffusion boundary layer thickness for ZrCl formation and Zr metal formation were derived in the section 5.4 as follow:

$$\dot{m}_{ZrCl} = -\frac{i_{ZrCl}}{n_{ZrCl}F} = -\frac{\begin{array}{c} n_{ZrCl}Fk_{0,ZrCl}[-C_{Zr(IV)}(0,t)\exp(-\alpha_{ZrCl}\frac{n_{ZrCl}F}{RT}(E-E^{0'}_{ZrCl})) \\ +\exp((1-\alpha_{ZrCl})\frac{n_{ZrCl}F}{RT}(E-E^{0'}_{ZrCl}))] \end{array}}{1+\frac{\delta k_{0,ZrCl}}{D_{Zr(IV)}}\exp(-\alpha_{ZrCl}\frac{n_{ZrCl}F}{RT}(E-E^{0'}_{ZrCl}))} \quad (6.14)$$

$$\dot{m}_{Zr} = \frac{i_{Zr}}{n_{Zr}F} = k_{0,Zr}[-\exp(-\alpha_{Zr}\frac{n_{Zr}F}{RT}(E-E^{0'}_{Zr})) + \exp((1-\alpha_{Zr})\frac{n_{Zr}F}{RT}(E-E^{0'}_{Zr}))] \quad (6.15)$$

For the same reason in the section of 5.4, a restriction could be applied to Eq. (6.15) as follow:

If a molar consumption rate of ZrCl calculated by Eq.(6.15)

is higher than a molar production rate of ZrCl calculated by Eq.(6.14), it is assumed that molar consumption rate of ZrCl is equivalent to molar production rate of ZrCl.

ZrCl produced from Zr(IV) could be consumed by the reduction reaction producing Zr metal from ZrCl. Since the mole consumption rate of ZrCl by the Zr metal formation reaction is equivalent to the mole production rate of Zr metal, actual mole production rate of ZrCl during electrorefining, $\dot{m}_{ZrCl,actual}$,could be defined as

$$\dot{m}_{ZrCl,acutal} = \dot{m}_{ZrCl} - \dot{m}_{Zr} \tag{6.16}$$

For the uranium deposition, the relations among current density, electrode potential and mole production rate at an arbitrary diffusion boundary layer thickness could be derived in the same manner of ZrCl formation from Zr(IV):

$$\dot{m}_U = -\frac{i_U}{n_U F}$$

$$= -\frac{\begin{array}{c} n_U F k_{0,U}[-C_{U(III)}(0,t)\exp(-\alpha_U \frac{n_U F}{RT}(E - E_U^{0'})) \\ + \exp((1-\alpha_U)\frac{n_U F}{RT}(E - E_U^{0'}))] \end{array}}{1 + \frac{\delta k_{0,U}}{D_{U(III)}}\exp(-\alpha_U \frac{n_U F}{RT}(E - E_U^{0'}))} \quad (6.17)$$

where $\dot{m}_U$ is the mole production rate of U, i_U is the current density resulting from the U formation, n_U is the number of electron participating in the U formation, F is the faraday constant, $k_{0,U}$ is the rate constant for the reaction of U formation, $C_{U(III)}(0,t)$ is the surface concentration of U(III), α_U is the transference coefficient for the U formation, E is the electrode potential and $E_U^{0'}$ is the formal potential of the ZrCl formation.

In Figure 6.10, mass production rates of ZrCl, Zr metal and U metal at an arbitrary diffusion boundary layer thickness are represented based on the Eq. (6.15), (6.16) and (6.17) respectively. This calculation is conducted using material properties for Zr as represented in Table 5.2. For uranium, standard reduction potential of -1.287 V (vs. Ag/AgCl), diffusion coefficient of 2.7E-5 m^2/s and reaction rate constant of 1.69E-4 m/s are utilized (Bechtel and Storvick, 1999; Serp et al., 2006; Kim et al., 2012). There are a potential window to recover Zr metal without ZrCl and U. The potential window would be changed according to diffusion boundary layer thickness,

concentration of $ZrCl_4$ and UCl_3 and other electrorefiner operating conditions. Since the objective of this dissertation is to recover Zr metal without other impurities, it would be desirable to secure the potential window as wide as possible.

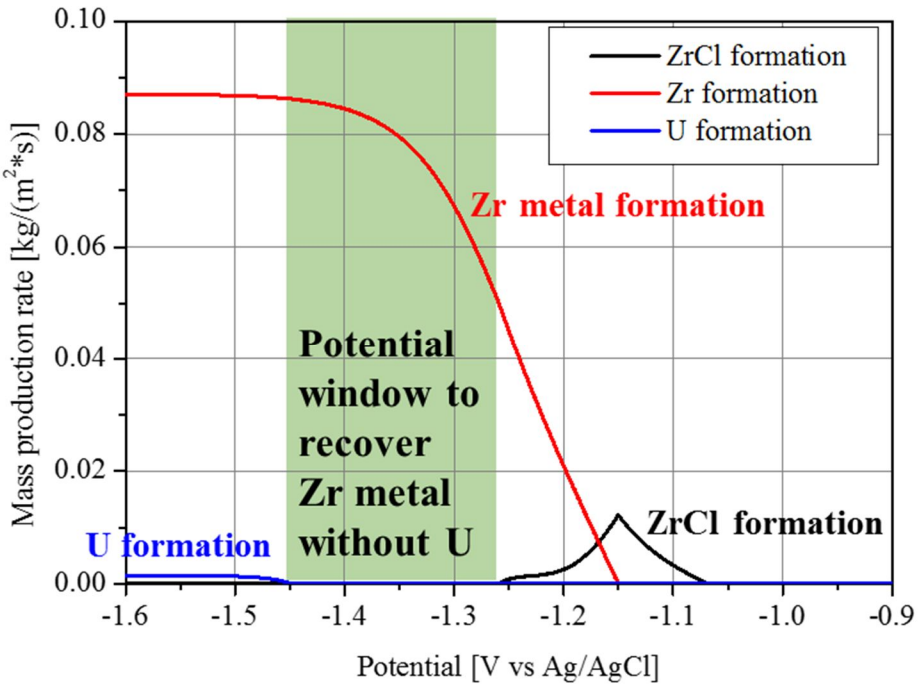

Figure 6.10 Mass production rates of Zr metal, ZrCl and U according to applied potential at an arbitrary diffusion boundary layer thickness

6.2.3 Weights of molten salts

Since it is assumed that all uranium in irradiated Zircaloy-4 cladding is immediately dissolved into molten, weight of molten salts in the electrorefiner could greatly influence on potential window to obtain Zr metal without ZrCl and U. The initial concentration of UCl_3 in the electrorefiner is inversely proportionate to the weight of molten salts. High concentration of UCl_3 could increase the potential where the uranium deposition starts to occur and this could result in diminishing the potential window.

The effect of weight of molten salts on potential window is evaluated with several diffusion boundary layer thickness near the cathode as represented in Figure 6.11. As expected, potential windows becomes wider as weight of molten slats increases while the potential window becomes narrower as diffusion boundary layer thickness decreases.

The target of potential windows width is determined based on Mark-IV electrorefiner experimental data as represented in Figure 5.9 and Figure 5.14. Cell potential of the electrorefiner oscillated in the range of 0.1 V when constant current was applied. In this study, the target of potential window width is established as 0.15 V to secure 50% margin compared to Mark-IV electrorefiner.

Diffusion boundary layer thickness near the cathode in molten salt electrorefining system would be from several micro meters to several hundred micrometers depending on configuration of electrorefiner and rotating speed of the cathode (Kobayashi and Tokiwai, 1993; Choi et al.,

2010). Since small diffusion boundary layer thickness might not be desirable for recovering Zr metal without ZrCl, the minimum diffusion boundary layer thickness for the irradiated Zircaloy-4 cladding electrorefiner is assumed as 50 μm. Therefore, the molten salt volume is determined about 250 kg from the Figure 6.11. To contain the amount of molten salts, reactor vessel for the electrorefiner is determined as the diameter of 80 cm and the height of 25 cm.

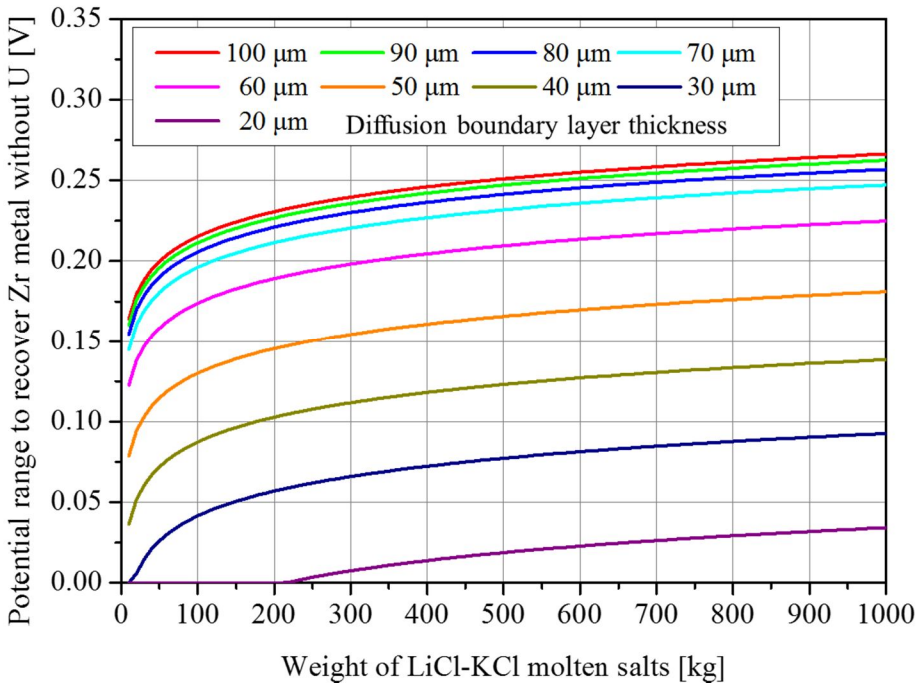

Figure 6.11 Changes of potential range to recover Zr metal without U according to weight of LiCl-KCl molten salts and diffusion boundary layer thickness

6.2.4 The number of anode basket

A small number of fan-shaped anode baskets could decrease circumferential symmetry electric field near the cathode while a large number of anode baskets would be hard to be managed in actual electrorefiner operation. Therefore, the optimized number of anode baskets are determined by conducting several computational electrorefining simulation. Four different simulations with applied current of 50A and cathode rotating speed of 100 rpm were conducted to investigate the effect of the number of anode basket on circumferential cathode potential distributions as represented in Figure 6.13. In the case of one anode basket, circumferential cathode potential variance at the mid height of the cathode is about 117.6 mV. The variance decreases as the number of anode basket increases: 12.2 mV for 2 anode baskets, 1.8 mV for 3 anode baskets and 0.29 mV for 4 anode baskets. Since vertical cathode potential variance is about 30 mV, more than two anode baskets are required to secure circumferential cathode potential symmetry.

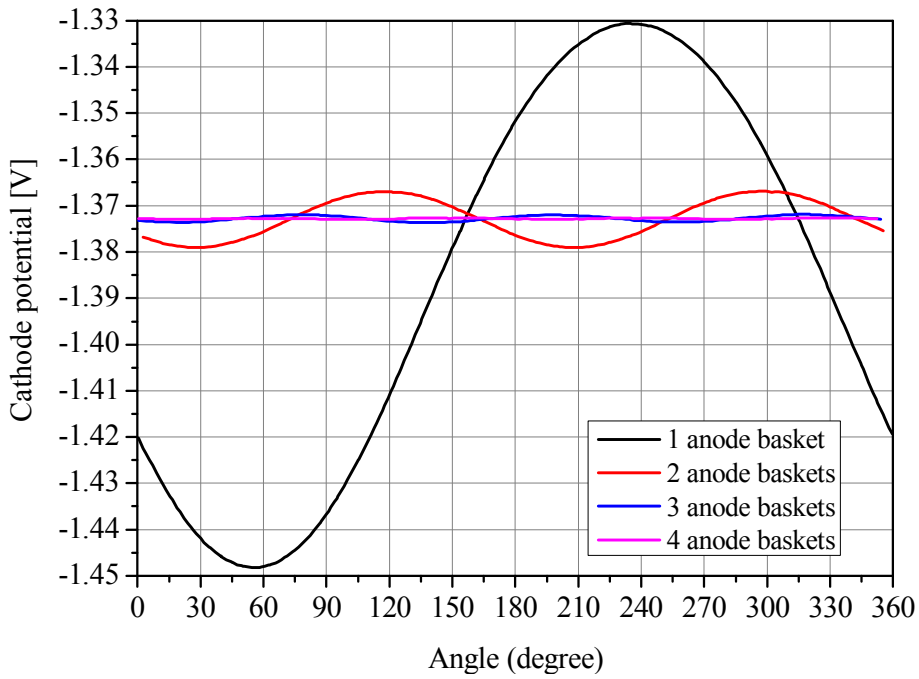

Figure 6.12 Local cathode potential distributions in the circumferential direction at the mid height of the cathode according to the number of anode baskets; applied current of 50 A and rotating speed of cathode of 100 rpm

Local mass production rates of Zr metal deposition and U metal are compared at the applied current of 52 A and cathode rotating speed of 100 rpm as represented in Figure 6.13. Although equivalent current is applied to the electrorefiner, U is deposited on the cathode for only the case of one anode basket. In addition, Zr metal production rate distribution over the cathode for one anode basket is not uniform in both circumferential and vertical directions. For this reason, in this dissertation, three anode baskets are selected for the pilot-scale electrorefiner. Final geometry of anode basket is determined as inner diameter of 75 cm, outer diameter of 80 cm, height of 25 cm and angle of a fan-shaped basket of 37^{o}.

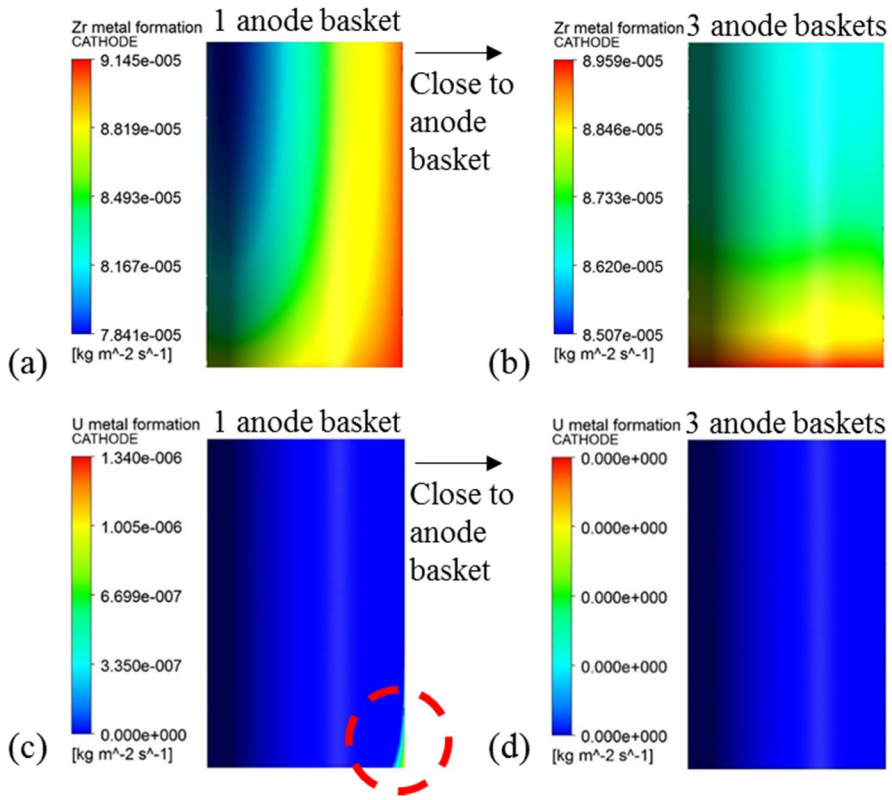

Figure 6.13 Local mass production rate distributions over cathode of Zr for cases of (a) one anode basket and (b) three anode baskets and those of U for cases of (c) one anode basket and (d) three anode baskets; applied current of 52 A and rotating speed of cathode of 100 rpm

6.3 Verification of Zircaloy-4 cladding electrorefiner capability

Capabilities of the designed pilot-scale electrorefiner for irradiated spent nuclear fuel Zircaloy-4 cladding are verified by 3-D computational electrorefining modeling. In general, electrorefining processes have been operated in galvanostatically to estimate the amount of deposition and dissolution (Sharma and Mukherjee, 1986; Zuca and Ene, 1991; Kato et al., 2006; Kongstein et al., 2007; Choi et al., 2011). Therefore, to estimate throughput of the electrorefiner, capabilities of the electrorefiner are investigated with current control method.

6.3.1 Effect of applied current and cathode rotating speed

To evaluate the effect of applied current and cathode rotating speed on depositions of Zr metal, ZrCl and U metal, various applied currents with four different cathode rotating speeds (100, 75, 50 and 25 rpm) are simulated. For all cases of cathodes rotating speeds, current ranges where could recover Zr metal without ZrCl and U are developed as represented in Figure 6.14, Figure 6.15, Figure 6.16 and Figure 6.17. When the applied current is lower than the current range for each cathode rotating speed, ZrCl is deposited with Zr metal on the cathode while U is deposited with Zr metal if the applied current is higher than the current range.

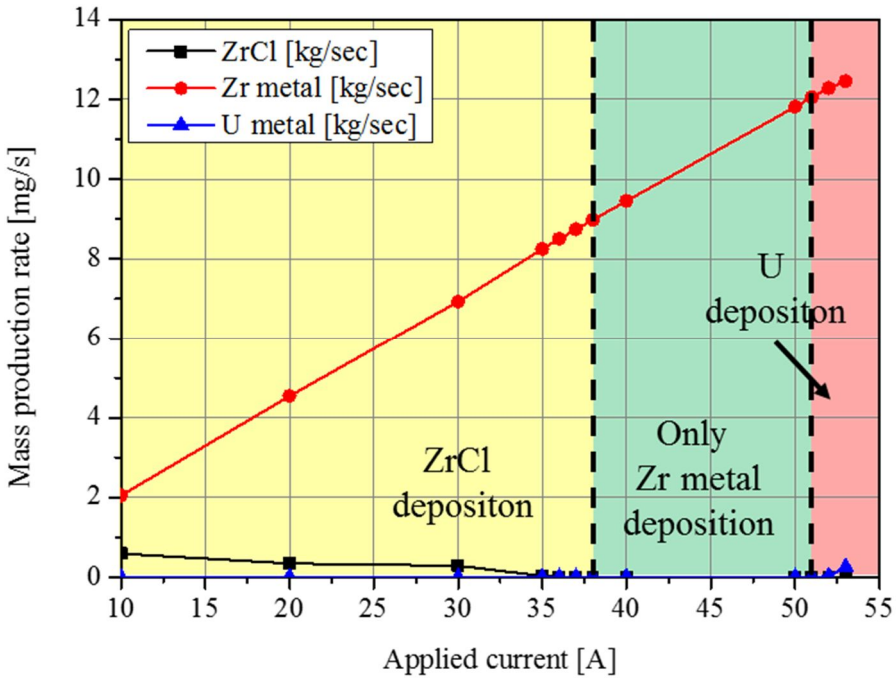

Figure 6.14 Mass production rate of ZrCl, Zr and U according to applied current: rotating speed of cathode is 100 rpm

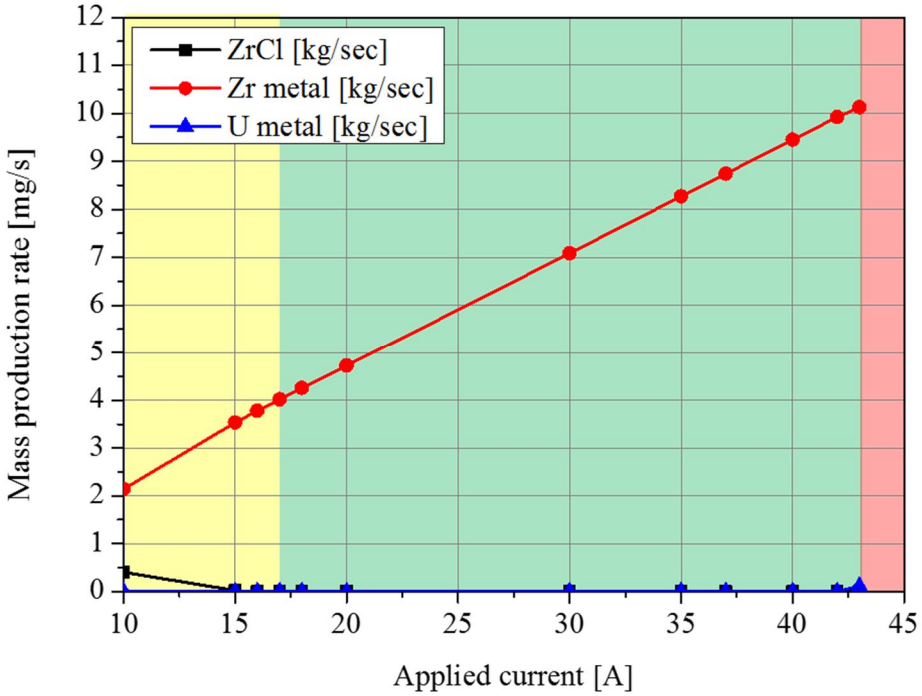

Figure 6.15 Mass production rate of ZrCl, Zr and U according to applied current: rotating speed of cathode is 75 rpm

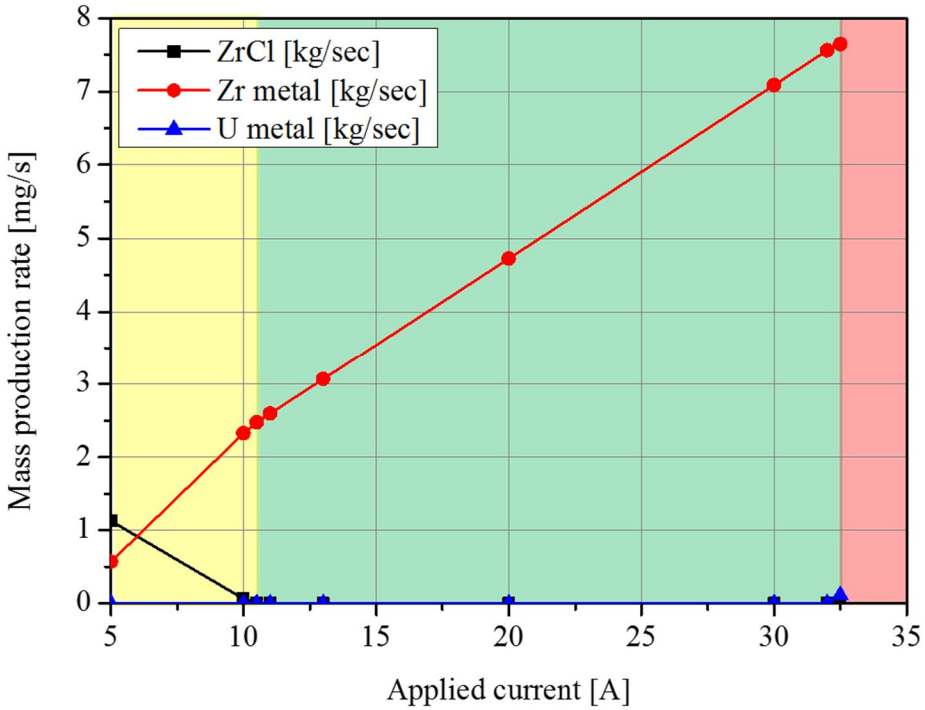

Figure 6.16 Mass production rate of ZrCl, Zr and U according to applied current: rotating speed of cathode is 50 rpm

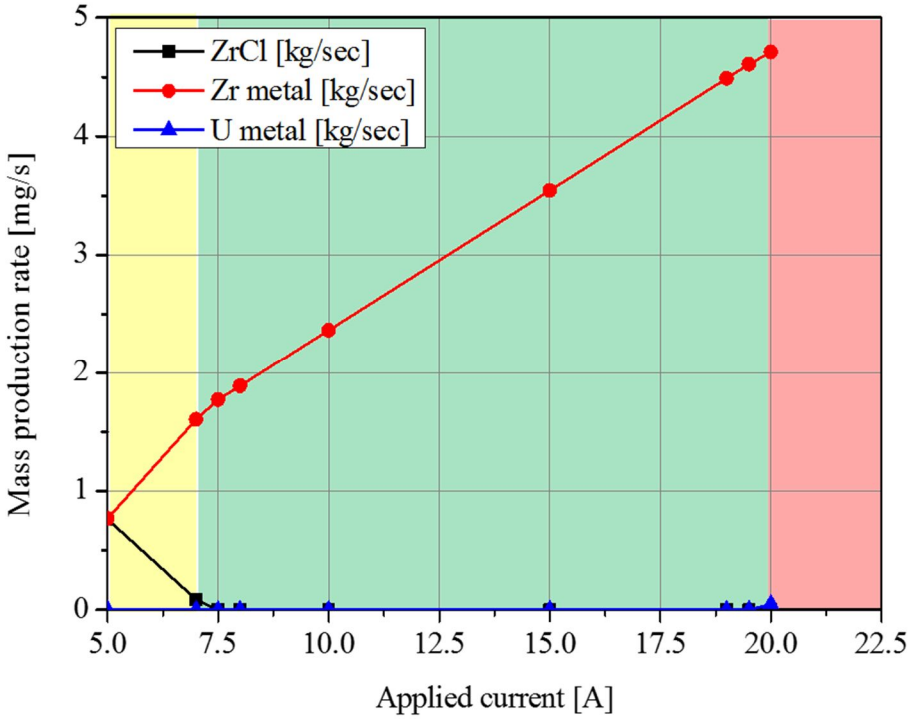

Figure 6.17 Mass production rate of ZrCl, Zr and U according to applied current: rotating speed of cathode is 25 rpm

Since the limiting current density is inversely proportionate to diffusion boundary layer thickness, the current range moves to a higher region when the rotational speed is faster. For example, if the cathode rotates with 100 rpm, the current range is developed from 38 to 51 A but when the cathode rotating speed is 25 rpm, the current range is formed between 7.5 and 19.5 A. Therefore, to secure high throughput, fast cathode rotating speed would be preferred.

However, as revealed in the section 6.2.3, potential window for recovering Zr metal without ZrCl and U metal would be shrunk as diffusion boundary layer thickness decreases. This is because if diffusion boundary layer thickness is small, surface concentration of Zr(IV) could be maintained high although highly negative electrode potential is applied and this results in enhancing ZrCl formation from Zr(IV). Therefore, the current range for recovering Zr metal without ZrCl and U metal would be diminished if the diffusion boundary layer thickness decreases. For instance, if the cathode rotates with 100 rpm, the width of the current range is 13 A but the width of the current range is 25 A when the cathode rotating speed is 75 rpm. If the width of the current range become smaller, concerns on deposition of ZrCl and U metal would grow. For the above reasons, since thin diffusion boundary layer thickness has pros and cons, the cathode rotating speed should be determined properly.

In the Figure 6.18, local mass production rate distributions of ZrCl, Zr metal and U metal. There are little changes in the circumferential direction but the distribution varies seriously in the vertical direction.

Because of the edge effect of electric fields near the cathode, current density is concentrated near the bottom of the cathode. For this reason, Zr metal and U metal starts to be deposited on the cathode as applied current density increases. Therefore, ZrCl deposits are likely to be found near the top of the cathode but U metal deposits are likely to be observed neat the bottom of the cathode.

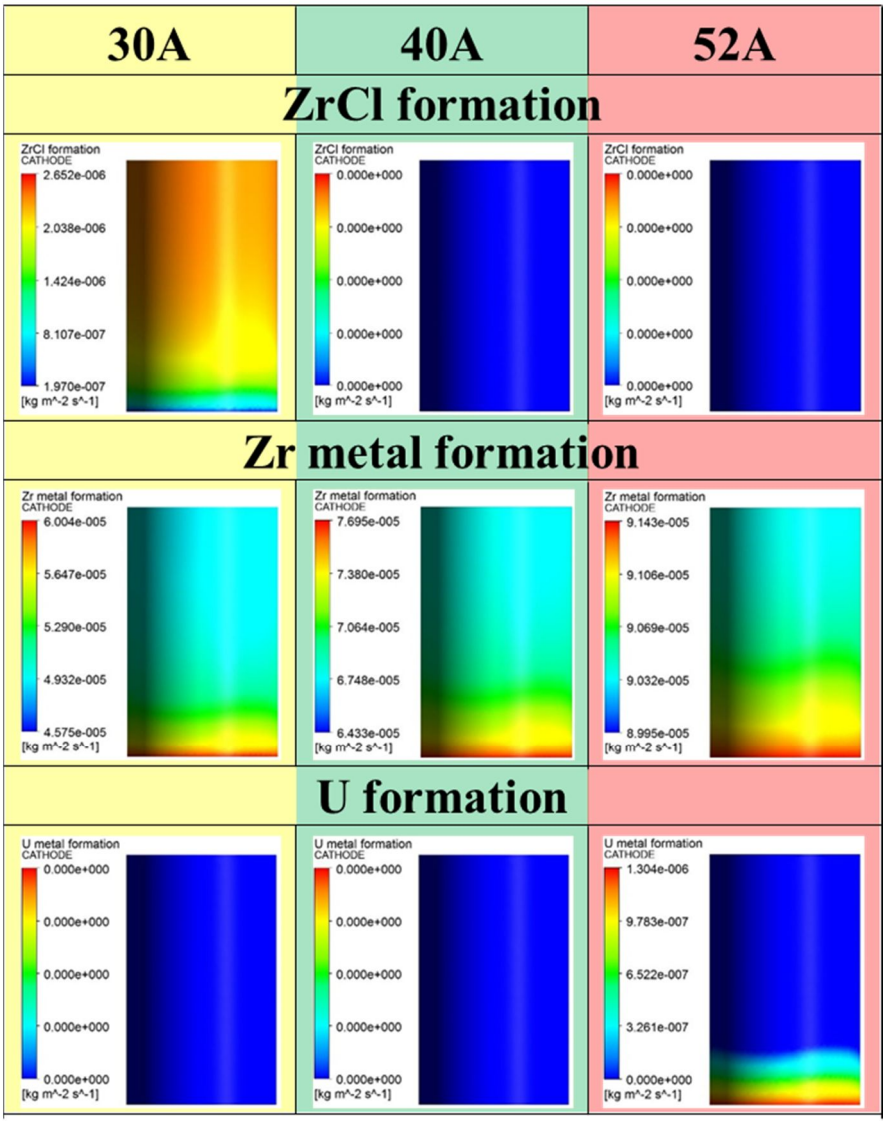

Figure 6.18 Local mass production rate distributions of ZrCl, Zr and U according to applied current density at cathode rotating speed of 100 rpm

6.3.2 Verified capabilities of electrorefiner

Two different operating conditions with cathode rotating speeds of 50 and 75 rpm are established as represented in Table 6.6. Diffusion boundary layer thicknesses are 76.75 and 57.79 μm respectively and these values satisfy diffusion boundary layer criteria of over 50 μm which was derived when weight of molten salts was determined. For the first operating condition, currents from 11 to 32 A could be applied and throughput of 0.06~0.16 ton/year could be achieved. For the second operating condition, currents from 17 to 42 A could be applied and throughput of 0.09~0.21 ton/year could be obtained. Throughputs for each operating condition are estimated as with assumption of 24 hours/day operating hours and 250 days/year operating days. Elements more reductive than Zr such as Sn, Cr, Fe and some activation products and fission products would be remained as metallic powders in anode baskets. On the other hands, elements more oxidative than Zr such as U, Cs, Sr and most of TRUs would exist in the molten salts as ionic states and their deposition would be prevented by managing the cathode potential.

Table 6.6 Two operating conditions of the designed electrorefiner for irradiated spent nuclear fuel Zircaloy-4 cladding

	Operting condition 1	Operating condition 2
Throughput [ton/year]	0.06~0.16	0.09~0.21
Operating hours [hours/day]	24	24
Operating days [days/year]	250	250
Applied current [A]	11~32	17~42
Number of anode basket	3	3
Zircaloy-4 cladding loaded into anode baskets [kg]	10	10
Rotating speed of cathode [rpm]	50	75
Diffusion boundary layer thickness [μm]	76.75	57.79
U and TRU decontamination	These elements would not be deposited on the cathode if applied potential is properly controlled.	
Activation products decontamination	These elements would not be dissolved from anode if anode potential is properly managed.	

Throughput of the designed pilot-scale electrorefiner could be improved by increasing the area ratio of cathode to anode. In this chapter, the pilot-scale electrorefiner with throughput 0.1~0.2 ton/year was designed. Electrorefiner throughput would be proportionate to cathode area at the given cathode potential if cathodic reaction is rate determining step. Since the cathode area of the designed electrorefiner is much smaller than anode area, throughput of the designed electrorefiner could be raised by enlarging cathode area. However, if cathode area is raised too much, reductive elements could be dissolved from anode because of anodic current density increase as increase of total applied current. Therefore, experimental work might be required to secure the optimized area ratio for high throughput with high decontamination factor.

Chapter 7 Conclusions and Future Work

7.1 Conclusions

The main objective of this dissertation to develop an electrorefining process to decontaminate and recycle the irradiated spent nuclear fuel Zircaloy-4 cladding by using LiCl-KCl salts has been achieved by combining lab-scale experiments for clarifying Zr redox mechanism and computational electrorefining model development. The developed electrorefining process controls anode potential, cathode potential and $ZrCl_4$ concentration in LiCl-KCl salts.

Issues with ZrCl deposition and disproportionate reaction between Zr metal and Zr(IV) in LiCl-KCl salts have been overcome by examining reduction and oxidation behaviors as a function of cathodic potential and $ZrCl_4$ concentration in LiCl-KCl salts. From lab-scale experiments, redox behaviors of Zr in LiCl-KCl has been revealed as follow:

1. Zr metal can be produced by reducing ZrCl which is formed by Zr(IV) reduction processes.
2. Zr(II) can be produced from Zr(IV) but the reaction rate is much lower than that of ZrCl production from Zr(IV).
3. The production of both ZrCl and Zr(II) can be suppressed at low concentrations of $ZrCl_4$.

Redox behaviors of significant elements in irradiated Zicaloy-4 cladding (Sn, Cr, Fe and Co) have been also investigated and it is confirmed that these elements are much reductive than Zr and redox mechanisms are much simpler than Zr.

Lab-scale electrorefining was conducted using unirradiated Zircaloy-4 specimen on the basis of investigated redox behaviors of Zr and other elements. Electrorefining experiments were conducted in five different concentration of $ZrCl_4$ (0.1, 0.5, 1.0, 2.0, 4.0 wt. %) with the anode potential of -0.9 V (vs. Ag/AgCl). As identified in cyclic voltammetry, at low $ZrCl_4$ concentrations, 0.1 and 0.5 wt. %, Zr metal was recovered on cathode without ZrCl while ZrCl was recovered at high $ZrCl_4$ concentration, 2.0 and 4.0 wt. %. At the concentration of 1.0 wt. %, both Zr metal and ZrCl were recovered. For all cases of electrorefining, only zirconium without other elements was detected in cathode deposits. Because, high concentration is preferred to secure high throughput of electrorefiner, $ZrCl_4$ concentration of 0.5 wt. % would be recommendable to recover Zr metal with high throughput.

In this dissertation, a three-dimensional computational electrorefining model has been developed for a cylindrical electrorefiner design based on a commercial package named as ANSYS-CFX©. Cathode deposition model in the developed computational model was verified by measuring overpotential distribution for copper deposition in a rotating cylindrical Hull (RCH) cell with aqueous cupric sulfate solution. Utility of

anode dissolution model was evaluated by benchmarking potential versus current experimental data of Mark-IV electrorefiner. At the initial stage of electrorefining, computational modeling results accorded with experimental results but, as electrorefining progressed, calculated potential became very dependent on assumed effective anode surface area profiles. Therefore, the developed computational model needs to be improved to take into accout the anode evolution for modeling of late stages of electrorefining.

Based on lab-scale experiments and by applying the developed computational model, a pilot-scale electrorefiner for irradiated spent nuclear fuel Zircaloy-4 cladding has been designed. The designed electrorefiner with the diameter of 80 cm and the height of 35 cm has three fan-shaped anode and one cylindrical cathode. The optimum concentration of $ZrCl_4$ was set as 0.5 wt. %. The throughput of a pilot-scale electrorefiner for spent nuclear fuel Zircaloy-4 cladding designed by applying computer models is predicted to be about 0.1~0.2 ton/year at the $ZrCl_4$ concentration of 0.5 wt. %. It is expected that the throughput can be further increased by optimizing design parameters.

7.2 Future Work

Electrorefinig of irradiated spent nuclear fuel Zircaloy-4 cladding in LiCl-KCl has been developed and it has been identified that high purity Zr metal could be prepared without ZrCl and other impurities in both lab-scale and pilot-scale. However, there are some issues to be resolved for

commercializing the developed electrorefining process and recycling the recovered zirconium.

In all lab-scale electrorefining experiments, zirconium was recovered as powder and some amount of powdery zirconium was detached from cathode and sank to the bottom of molten salts. To increase recovery rate of zirconium, some equipment collecting detached powdery zirconium might be need to be introduced. In addition, powdery zirconium might be easy to be oxidized. If oxygen content in zirconium compounds is over 0.7%, zirconium would become unworkable (Kipouros and Flengas, 1985). For this reason, reactor-grade zirconium requires oxygen content lower than 1,000 ppm. Therefore, melting and casting processes such as arc melting should be applied as soon as possible after recovering zirconium from electrorefining.

Area ratio of cathode to anode would be required to be optimized to improve electrorefiner throughput. In the Chapter 6, the pilot-scale electrorefiner with throughput 0.1~0.2 ton/year was designed. Electrorefiner throughput would be proportionate to cathode area at the given cathode potential if cathodic reaction is rate determining step. Since the cathode area of the designed electrorefiner is much smaller than anode area, throughput of the designed electrorefiner could be raised by enlarging cathode area. However, if cathode area is raised too much, reductive elements could be dissolved from anode because of anodic current density increase as increase of total applied current. The optimized area ratio between cathode and anode could not be determined by the computational model because of incomplete anodic dissolution model. Therefore, experimental electrorefining work

might be required to secure the optimized area ratio for high throughput with high decontamination factor.

In the aspect of computational modeling, anodic dissolution computational model is need to be improved. In the section of 5.3, it is revealed that cell potential modeling results are greatly dependent on anode area change profile. If a correlation on effective anode area changes as a function of operating conditions are available, utility of the computational model would be extremely raised and it might be utilized for transient electrorefining modeling.

To carry out more accurate computational electrorefining modeling, precise material properties related to electrochemical reaction such as transfer coefficient and rate constant are required. Until now, a lot of electrochemical researches have used transfer coefficient of 0.5 indiscriminately when analyzing cyclic voltammogram peak and conducting electrochemical modeling. Even at this dissertation, the transfer coefficient of 0.5 was also utilized for all of electrochemical reactions because transfer coefficients for Zr, Sn, Cr, Fe and Co have rarely reported. In addition, because rate constants of electrochemical reaction in molten salts have been rarely investigated, various values have been utilized for the same electrochemical reaction. However, both transfer coefficient and rate constant could greatly influence tendency of redox reaction and uncertain material properties could make the computational modeling results unreliable. Therefore, more experimental work and atomic scale modeling to produce material properties in molten salts would be needed to improve

computational modeling accuracy.

Bibliography

Abriata, J., Bolcich, J., Arias, D., 1983. The Sn− Zn (Tin-Zirconium) system. Journal of Phase Equilibria 4, 147-154.

Ahluwalia, R., Hua, T.Q., Geyer, H.K., 1999. Behavior of uranium and zirconium in direct transport tests with irradiated EBR-II fuel. Nuclear technology 126, 289-302.

Ahluwalia, R.K., Hua, T.Q., 2002. Electrotransport of uranium from a liquid cadmium anode to a solid cathode. Nuclear technology 140, 41-50.

Ahluwalia, R.K., Hua, T.Q., Geyer, H.K., 2001. Removal of zirconium in electrometallurgical treatment of experimental breeder reactor II spent fuel. Nuclear technology 133, 103-118.

Ahmad, M., Akhter, J., Shaikh, M., Iqbal, M., Ahmad, W., 2003. Role of solute segregation on microstructure and mechanical properties of zircaloy-4. Journal of materials engineering and performance 12, 179-182.

Baboian, R., Hill, D., Bailey, R., 1965. Electrochemical Studies on Zirconium and Hafnium in Molten LiCl-KCl Eutectic. Journal of The Electrochemical Society 112, 1221-1224.

Bae, J., Nam, H.O., Yi, K.W., Park, B.G., Hwang, I.S., 2010. Numerical assessment of pyrochemical process performance for PEACER system. Nuclear Engineering and Design 240, 1679-1687.

Bard, A., Faulkner, L., 2001. Electrochemical methods: principles and applications. Electrochemical Methods: Principles and Applications.

Bechtel, T.B., Storvick, T.S., 1999. Activity coefficients of actinide and rare-earth chlorides in molten LiCl/KCl eutectic salt. Industrial & engineering chemistry research 38, 1723-1728.

Bonciocat, N., Cotarta, A., 2002. The electrodeposition of chromium from molten alkali chlorides. The effect of the direct voltammetry on the quality of an initial deposit of metallic chromium. High Temperature Material Processes (An International Quarterly of High-Technology Plasma Processes) 6.

Cho, I.-J., 2013. Current Status of Pyroprocessing Development at KAERI. Science and Technology of Nuclear Installations 2013.

Choi, S., Park, J., Hoover, R.O., Phongikaroon, S., Simpson, M.F., Kim, K.-R., Hwang, I.S., 2011. Uncertainty studies of real anode surface area in computational analysis for molten salt electrorefining. Journal of Nuclear Materials 416, 318-326.

Choi, S., Park, J., Kim, K.-R., Jung, H., Hwang, I., Park, B., Yi, K., Lee, H.-S., Ahn, D., Paek, S., 2010. Three-dimensional multispecies current density simulation of molten-salt electrorefining. Journal of Alloys and Compounds 503, 177-185.

Collins, E.D., DelCul, G.D., Spencer, B.B., Brunson, R.R., Johnson, J.A., Terekhov, D., Emmanuel, N., 2012. Process Development Studies for Zirconium Recovery/Recycle from used Nuclear Fuel Cladding. Procedia Chemistry 7, 72-76.

Collins, E.D., DelCul, G.D., Terekhov, D., Emmanuel, N., 2011. Recycle of Zirconium from Used Nuclear Fuel Cladding: A Major Element of Waste Reduction. Oak Ridge National Laboratory (ORNL).

Cotarta, A., Bouteillon, J., Poignet, J., 1997. Electrochemistry of molten LiCl–KCl–CrCl3 and LiCl–KCl–CrCl2 mixtures. Journal of applied electrochemistry 27, 651-658.

Del Cul, G.D., Collins, E.D., Terekhov, D., Emmanuel, N., 2011. Recycle of Zirconium from Used Nuclear Fuel Cladding: A Progress Report. Transactions of the American Nuclear Society 104, 141.

Del Cul, G.D., Hunt, R.D., Spencer, B.B., Collins, E.D., Bateman, K., Howden, K., Westphal, B., 2004. Advanced head-end processing of spent fuel: A progress report. Trans. Am. Nucl. Soc 91, 507-508.

Eisenberg, M., Tobias, C., Wilke, C., 1954. Ionic mass transfer and concentration polarization at rotating electrodes. Journal of the Electrochemical Society 101, 306-320.

El Ghallali, H., Groult, H., Barhoun, A., Draoui, K., Krulic, D., Lantelme, F., 2009. Electrochemical synthesis of Ni–Sn alloys in molten LiCl–KCl. Electrochimica Acta 54, 3152-3160.

Fabrian, C.P., Luca, V., Le, T., Bond, A.M., Chamelot, P., Massot, L., Caravaca, C., Hanley, T.L., Lumpkin, G.R., 2013. Cyclic Voltammetric Experiment-Simulation Comparisons of the Complex Mechanism Associated with Electrochemical Reduction of Zr4+ in LiCl-KCl Eutectic Molten Salt. Journal of The Electrochemical Society 160, H81-H86.

Fujita, R., Nakamura, H., Haruguchi, Y., Takahashi, R., Sato, M., Shibano, T., Ito, Y., Goto, T., Terai, T., Ogawa, S., 2005a. Development of zirconium recovery process for zircaloy claddings and channel boxes from boiling water reactors by electroreˆning in molten salts, ICAPP '05, Seoul, Korea.

Fujita, R., Nakamura, H., Haruguchi, Y., Takahashi, R., Utsunomiya, K., Sato, M., Ito, Y., Goto, T., Terai, t., Ogawa, S., 2007. Development of a

Zirconium Recycle Process from Zircaloy Waste of a Boiling Water Reactor (BWR). Transactions of the Atomic Energy Society of Japan 6, 343-357.

Fujita, R., Nakamura, H., Mizuguchi, K., Sato, M., Shibano, T., Ito, Y., Goto, T., Terai, T., Ogawa, S., 2005b. Zirconium recovery process for spent Zircaloy components from Light Water Reactor (LWR) by electrorefining in molten salts. ELECTROCHEMISTRY-TOKYO- 73, 751.

Gao, F., Wang, C., Liu, L., Guo, J., Chang, S., Chang, L., Li, R., Ouyang, Y., 2009. Electrode processes of uranium ions and electrodeposition of uranium in molten LiCl-KCl. Journal of radioanalytical and nuclear chemistry 280, 207-218.

Ghosh, S., Vandarkuzhali, S., Venkatesh, P., Seenivasan, G., Subramanian, T., Prabhakara Reddy, B., Nagarajan, K., 2009. Electrochemical studies on the redox behaviour of zirconium in molten LiCl–KCl eutectic. Journal of Electroanalytical Chemistry 627, 15-27.

Groult, H., El Ghallali, H., Barhoun, A., Briot, E., Perrigaud, L., Hernandorena, S., Lantelme, F., 2010. Preparation of Co–Sn alloys by electroreduction of Co (II) and Sn (II) in molten LiCl–KCl. Electrochimica Acta 55, 1926-1932.

Hofman, G.L., Walters, L.C., Bauer, T., 1997. Metallic fast reactor fuels. Progress in Nuclear Energy 31, 83-110.

Hoover, R., Li, S., Simpson, M., Phongikaroon, S., Yoo, T.-S., 2009. A Computational Model of the Mark-IV Electrorefiner: Phase I—Fuel Basket/Salt Interface. Journal of Engineering for Gas Turbines and Power 131, 054503.

Hoover, R.O., Phongikaroon, S., Simpson, M.F., Li, S.X., Yoo, T.-S., 2010. Development of computational models for the mark-IV electrorefiner—

effect of uranium, plutonium, and zirconium dissolution at the fuel basket-salt interface. Nuclear technology 171, 276-284.

Hoover, R.O., Phongikaroon, S., Simpson, M.F., Yoo, T.-S., Li, S.X., 2011. Computational Model of the Mark-IV Electrorefiner: Two-Dimensional Potential and Current Distributions. Nuclear Technology 173, 176-182.

IAEA, 1996. Clearance levels for radionuclides in solid materials: Application of exemption principles, Interim Report for comment. International Atomic Energy Agency, Vienna.

IAEA, 2009. Classification of Radioactive Waste.

Ibrahim, E., Cheadle, B., 1985. Development of zirconium alloys for pressure tubes in CANDU reactors. Canadian Metallurgical Quarterly 24, 273-281.

Iizuka, M., Inoue, T., Shirai, O., Iwai, T., Arai, Y., 2001. Application of normal pulse voltammetry to on-line monitoring of actinide concentrations in molten salt electrolyte. Journal of nuclear materials 297, 43-51.

Iizuka, M., Kinoshita, K., Koyama, T., 2005. Modeling of anodic dissolution of U–Pu–Zr ternary alloy in the molten LiCl–KCl electrolyte. Journal of Physics and Chemistry of Solids 66, 427-432.

Inman, D., Legey, J., Spencer, R., 1975. The electrochemistry of chromium in molten LiCl+ KCl. Journal of Electroanalytical Chemistry and Interfacial Electrochemistry 61, 289-301.

Inman, D., Legey, J., Spencer, R., 1978. I. A chronopotentiometric study of iron in LiCl-KCl. Journal of Applied Electrochemistry 8, 269-272.

Jarzabek, G.y., Borkowska, Z., 1997. On the real surface area of smooth solid electrodes. Electrochimica acta 42, 2915-2918.

Jeong, Y.H., Park, S.-Y., Lee, M.-H., Choi, B.-K., Baek, J.-H., Park, J.-Y., Kim, J.-H., Kim, H.-G., 2006. Out-of-pile and in-pile perfomance of advanded zirconium alloys (HANA) for high burn-up fuel. Journal of Nuclear Science and Technology 43, 977-983.

Jung, I.H., Shin, J.M., Lee, H.H., Park, J.J., Yang, M.S., 2006. Investigation of PWR Hull with a View to Downgrade. Separation science and technology 41, 2097-2109.

Kato, T., Inoue, T., Iwai, T., Arai, Y., 2006. Separation behaviors of actinides from rare-earths in molten salt electrorefining using saturated liquid cadmium cathode. Journal of nuclear materials 357, 105-114.

Keiser Jr, D.D., Mariani, R.D., 1999. Zr-rich layers electrodeposited onto stainless steel cladding during the electrorefining of EBR-II fuel. Journal of nuclear materials 270, 279-289.

Kim, G.-Y., Yoon, D., Paek, S., Kim, S.-H., Kim, T.-J., Ahn, D.-H., 2012. A study on the electrochemical deposition behavior of uranium ion in a LiCl–KCl molten salt on solid and liquid electrode. Journal of Electroanalytical Chemistry 682, 128-135.

Kim, Y.S., Hayes, S., Hofman, G., Yacout, A., 2006. Modeling of constituent redistribution in U–Pu–Zr metallic fuel. Journal of nuclear materials 359, 17-28.

Kinoshita, K., Inoue, T., Fusselman, S., Grimmett, D., Roy, J., Gay, R., Krueger, C., Nabelek, C., Storvick, T., 1999. Separation of uranium and transuranic elements from rare earth elements by means of multistage

extraction in LiCl-KCl/Bi system. Journal of Nuclear Science and Technology 36, 189-197.

Kipouros, G.J., Flengas, S.N., 1985. Electrorefining of zirconium metal in alkali chloride and alkali fluoride fused electrolytes. Journal of The Electrochemical Society 132, 1087-1098.

Kobayashi, T., Tokiwai, M., 1993. Development of TRAIL, a simulation code for the molten salt electrorefining of spent nuclear fuel. Journal of alloys and compounds 197, 7-16.

Kongstein, O.E., Wollan, C., Sultana, S., Haarberg, G.M., 2007. Electrorefining of Silicon in molten calcium chloride. ECS Transactions 3, 357-361.

Kroll, W., 1937. The formation of titanium and zirconium. Z Anorg Chem 234, 42-50.

Kroll, W., Schlechten, A., Carmody, W., Yerkes, L., Holmes, H., Gilbert, H., 1947. Recent progress in the metallurgy of malleable zirconium. Transactions of The Electrochemical Society 92, 99-113.

Kroll, W., Schlechten, A., Yerkes, L., 1946. Ductile zirconium from zircon sand. Transactions of The Electrochemical Society 89, 263-276.

Kulkarni, M., Baker, M., Greisen, D., Ng, D., Griffin, R., Liang, H., 2007. Effects of electrochemistry on surface roughness during chemical-mechanical polishing of copper. Tribology Letters 25, 33-41.

Kwon, S.W., Ahn, D.H., Kim, E.H., Ahn, H.G., 2009. A study on the recovery of actinide elements from molten LiCl–KCl eutectic salt by an electrochemical separation. Journal of Industrial and Engineering Chemistry 15, 86-91.

Labraga, L., Berkah, T., 2004. Mass transfer from a rotating cylinder with and without crossflow. International journal of heat and mass transfer 47, 2493-2499.

Lee, C.H., Kang, K.H., Jeon, M.K., Heo, C.M., Lee, Y.L., 2012. Electrorefining of Zirconium from Zircaloy-4 Cladding Hulls in LiCl-KCl Molten Salts. Journal of The Electrochemical Society 159, D463-D468.

Lee, S.-J., Kang, Y.-H., Park, S.-B., Hwang, S.-C., Kim, J.-G., 2010. Study on electrorefining of uranium focusing on anodic dissolution, the 11th OECD-NEA Information Exchange Meeting on Actinide and Fission Product Partitioning and Transmutation, San Francisco, California, p. 157.

Levy, S.C., Reinhardt, F.W., 1975. Electrochemical Reduction of Cr (III) in Molten LiCl-KCl Eutectic. Journal of The Electrochemical Society 122, 200-204.

Li, S., Simpson, M., 2002. Anodic Process of Electrorefining Spent Nuclear Fuel in Molten LiCl-KCl-UCl3/Cd System, Proceedings of the 201st meeting of the Electrochemical Society, 13th International Symposium on Molten Salts, Philadelphia.

Li, S.X., Johnson, T.A., Westphal, B.R., Goff, K.M., Benedict, R.W., 2005. Experience for Pyrochemical Processing of Spent EBR-II Driver Fuel, Global 2005.

Low, C., Roberts, E., Walsh, F., 2007. Numerical simulation of the current, potential and concentration distributions along the cathode of a rotating cylinder Hull cell. Electrochimica acta 52, 3831-3840.

Madore, C., Matlosz, M., Landolt, D., 1992a. Experimental investigation of the primary and secondary current distribution in a rotating cylinder Hull cell. Journal of applied electrochemistry 22, 1155-1160.

Madore, C., West, A., Matlosz, M., Landolt, D., 1992b. Design Considerations for a cylindrical hull cell with forced convection. Electrochimica acta 37, 69-74.

Newman, J., Thomas-Alyea, K.E., 2012. Electrochemical systems. John Wiley & Sons.

Okamoto, H., 2010. Sn-Zr (Tin-Zirconium). Journal of phase equilibria and diffusion 31, 411-412.

Pahl, R., Porter, D., Lahm, C., Hofman, G., 1990. Experimental studies of U-Pu-Zr fast reactor fuel pins in the experimental breeder reactor-ll. Metallurgical Transactions A 21, 1863-1870.

Park, B., 1999. A time-dependent simulation of molten salt electrolysis for nuclear wastes transmutation, Nuclear Engineering. Seoul National University, Seoul, p. 169.

Park, J., Choi, S., Sohn, S., Kim, K.-R., Hwang, I.S., 2014. Cyclic Voltammetry on Zirconium Redox Reactions in LiCl-KCl-ZrCl4 at 500° C for Electrorefining Contaminated Zircaloy-4 Cladding. Journal of The Electrochemical Society 161, H97-H104.

Park, K.T., 2013. Metalization and Purification Behavior of Zirconium by Combustion Synthesis and Molten Salt Electrorefining for Nuclear Applications. Chungnam National University, Daejeon.

Park, K.T., Lee, T.H., Jo, N.C., Nersisyan, H.H., Chun, B.S., Lee, H.H., Lee, J.H., 2013. Purification of nuclear grade Zr scrap as the high purity dense Zr deposits from Zirlo scrap by electrorefining in LiF–KF–ZrF4 molten fluorides. Journal of Nuclear Materials 436, 130-138.

Patra, B., Samantray, B., Patra, B., 2010. Engineering Chemistry I (for BPUT). Pearson Education India.

Phongikaroon, S., Yoo, T.-S., 2007. Identification of statistical invariance for anodic signals of Mk-IV electrorefiner, Proceedings of GLOBAL.

Restani, R., Aerne, E., Bart, G., Linder, H., Muller, A., Petrik, F., 1992. Characterisation of PWR Cladding Hulls from Commercial Reprocessing. NAGRA.

Ronen, Y., Raitses, G., 2002. Spectral Shift Control for Pressurized Water Reactors.

Rudisill, T.S., 2009. Decontamination of Zircaloy cladding hulls from spent nuclear fuel. Journal of Nuclear Materials 385, 193-195.

Sabol, G.P., Bradley, E., 1996. Zirconium in the nuclear industry: eleventh international symposium. ASTM International.

Sabol, G.P., Moan, G.D., 2000. Zirconium in the Nuclear Industry: Twelfth International Symposium.[12th ASTM International Symposium on Zirconium in the Nuclear Industry, Held in Toronto, 15-18 June 1998]. ASTM International.

Sakamura, Y., 2004. Zirconium behavior in molten LiCl-KCl eutectic. Journal of The Electrochemical Society 151, C187-C193.

Schiffrin, D., 1986. Theory of cyclic voltammetry for reversible electrodeposition of insoluble products. Journal of electroanalytical chemistry and interfacial electrochemistry 201, 199-203.

Serp, J., Chamelot, P., Fourcaudot, S., Konings, R.J., Malmbeck, R., Pernel, C., Poignet, J.-C., Rebizant, J., Glatz, J.-P., 2006. Electrochemical behaviour

of americium ions in LiCl–KCl eutectic melt. Electrochimica acta 51, 4024-4032.

Sharma, I., Mukherjee, T., 1986. A study on purification of metallurgical grade silicon by molten salt electrorefining. Metallurgical and Materials Transactions B 17, 395-397.

Song, K.W., Jeong, Y.H., Kim, K.S., Bang, J.G., Chun, T.H., Kim, H.K., Song, K.N., 2008. High burnup fuel technology in Korea. Nuclear Engineering and Technology 40, 21.

Taylor, G.I., 1923. Stability of a viscous liquid contained between two rotating cylinders. Philosophical Transactions of the Royal Society of London. Series A, Containing Papers of a Mathematical or Physical Character 223, 289-343.

Trasatti, S., Petrii, O., 1991. Real surface area measurements in electrochemistry. Pure and applied chemistry 63, 711-734.

Vesterlund, G., Johansson, A., Andersson, I., Asberg, G., 1980. Corrosion-resistant BWR zircaloy-4 channels. Trans. Am. Nucl. Soc.;(United States) 34.

Watt-Smith, M., Friedrich, J., Rigby, S., Ralph, T., Walsh, F., 2008. Determination of the electrochemically active surface area of Pt/C PEM fuel cell electrodes using different adsorbates. Journal of Physics D: Applied Physics 41, 174004.

Yamada, D., Murai, T., Moritani, K., Sasaki, T., Takagi, I., Moriyama, H., Kinoshita, K., Yamana, H., 2007a. Diffusion behavior of actinide and lanthanide elements in molten salt for reductive extraction. Journal of Alloys and Compounds 444, 557-560.

Yamada, D., Murai, T., Moritani, K., Sasaki, T., Takagi, I., Moriyama, H., Kinoshita, K., Yamana, H., 2007b. Diffusion behavior of actinide and lanthanide elements in molten salt for reductive extraction. Journal of Alloys and Compounds 444–445, 557-560.

Zuca, S., Ene, N., 1991. Electrorefining of Titanium Metal in Molten Alkali Halide Mixtures, Materials Science Forum. Trans Tech Publ, pp. 643-652.

초 록

지르코늄 합금은 낮은 열중성자 흡수단면적과 우수한 내부식성 및 기계적 성질을 가지고 있어, 원자로의 고온·고압·고방사선과 같은 가혹한 환경에 적합해 원자력 발전소의 주요 구조재로 활용되어 왔다. 우리나라는 가압경수로와 중수로에서 핵연료피복관, 압력관, 칼란드리아관 등의 용도로 지르코늄 합금을 사용해오고 있다. 따라서 원전의 운영 중, 운영 후에 많은 양의 방사성 지르코늄 폐기물의 발생은 필연적이다. 방사성 지르코늄 합금 폐기물 중 사용후핵연료 피복관은 사용후핵연료 집합체 질량의 약 16%를 차지하여 발생량이 가장 많다. 또한 핵연료와 직접 맞닿아 있어 원전 운영 중 악티나이드 원소와 핵분열생성물이 침투하여 IAEA 방사성폐기물 신분류 체계의 중준위폐기물로 분류된다. 그러나 피복관의 대부분은 방사화되지 않은 지르코늄으로 이루어져 있다. 따라서 사용후핵연료 피복관 내 지르코늄을 방사성 원소 및 기타 불순물로부터 분리해낼 수 있다면, 사용후핵연료 집합체로부터 발생하는 방사성폐기물 처분량을 크게 감소시킬 수 있을 것으로 예상되며, 회수된 지르코늄을 원자력 산업에서 다시 재활용될 수 있을 것으로 기대된다.

이러한 이유로 사용후핵연료 피복관을 제염하기 위한 다양한 공정이 연구되어왔다. 2009년 발표된 논문에서는 HF를 사용한 사용후핵연료 피복관 표면제염을 통해 악티나이드 원소 및 핵분열생성물을 제거하고자 하였다. 그러나 이들 원소의 침투깊이가 깊어 180μm 이상 제염이후에도 방사선 준위가 GTCC (Greater Than Class C) 폐기물 분류기준을 상회하였다. 따라서 표면제염만으로는 사용후핵연료 피복관의 방사선 준위를 낮추기에는 부족하다. 사용후핵연료 피복관의 충분한 제염을 위해서는 체적제염이 이루어져야 하며 체적제염 방법에는 염

소나 아이오딘 기체와 피복관을 반응시키는 기체반응법과 전해정련 방법 등이 있다. 기체반응법은 높은 순도의 지르코늄을 분리할 수 있다는 장점이 있으나, 아이오다인 기체반응법은 ZrI_4의 흡습성이 높고, ZrI_4에서 Zr을 분리하는 공정의 속도가 느리다는 단점이 있으며, 염소 기체반응법은 $ZrCl_4$에서 Zr을 Kroll 공정으로 분리하는 과정에서 많은 양의 Mg 폐기물이 발생할 수 있다.

전해정련을 통한 사용후핵연료 피복관의 제염은 염화물이나 불화물과 같은 용융염을 전해질로 사용하는 공정이 연구되어 왔다. 불화물 LiF-KF를 전해질로 사용하는 전해정련 공정은 높은 순도의 지르코늄을 큰 입자형태로 회수할 수 있다는 장점이 있으나 불화물의 녹는점이 높아 전해정련 운전온도가 높으며 불화물로 인한 구조재 부식의 우려가 있다. 염화물과 불화물을 함께 사용하는 공정의 경우에는 운전온도를 낮출 수는 있으나 염화물을 사용하는 경우보다는 높고, 불화물로 인한 부식의 가능성이 여전히 존재한다. 염화물을 전해질로 사용하는 전해정련은 비교적 낮은 온도에서 작업이 가능하며 상대적으로 부식문제도 적어 상용 공정에 적합한 특성을 지니고 있다. 그러나 염화염 내 지르코늄의 산화환원 거동이 복잡하여 ZrCl가 지르코늄 금속과 함께 음극에 전착될 가능성이 있으며, 음극에서 지르코늄 이온의 환원 반응 이외에 Zr(IV) 이온이 지르코늄 금속과 반응하여 Zr(II)을 형성하는 불균등화 반응이 함께 일어날 수 있다. 염화물 내 지르코늄의 산화환원 거동 대한 연구를 바탕으로 ZrCl 형성 및 불균등화 반응을 억제할 수 있다면, 염화염 기반 전해정련을 사용후핵연료 피복관 제염을 위한 주요 공정으로 활용할 수 있을 것으로 기대된다.

본 논문에서는 염화염을 기반으로한 전해정련 공정을 개발하는 것을 목표로 한다. 방사화 피복관 내부에는 Cs-137, Sr-90과 같은 고방사성 동위원소가 존재하여 염화염 CsCl 및 SrCl2를 기반으로 하는 용융염은 이들 동위원소를 희석시켜 자칫 최종 처분되는 폐기물의 양을

증가시킬 우려가 있어 본 논문에서는 염화염 중 LiCl-KCl을 전해질로 채택하였다. 또한 제염대상 피복관은 국내에서 가장 먼저 사용되어 사용후핵연료 재활용 공정 적용 시 가장 먼저 폐기물로 발생할 가능성이 높은 Zircaloy-4 피복관으로 한정하였다. 본 논문에서는 실험실 규모 실험을 바탕으로 한 용융염 내 지르코늄 및 기타 주요 원소 산화·환원 거동 연구 수행과 함께 실험실에서 다루기 어려운 악티나이드 원소에 대한 영향을 평가하고 실험을 통해서는 파악하기 어려운 전해정련로 내 국부적 이온 거동을 확인하기 위한 3차원 전기화학 반응 전산 모델을 개발·검증하고 이를 활용하여 파일럿 규모의 전해정련로를 설계하는 것을 최종목표로 하였다.

용융염 내 지르코늄의 산화환원 거동에 대한 연구는 LiCl-KCl-$ZrCl_4$ 용융염에서 순환전위법을 통해 이루어졌다. 순환전위법을 통해 LiCl-KCl-$ZrCl_4$ 용융염에서 4개의 산화 피크와 3개의 환원 피크가 나타나는 것을 확인하였으며 각 피크에 해당하는 산화환원 반응은 전기분해 반응 후 음극전착물의 화학적 형태 분석과 주사속도 및 주사범위에 따른 피크 높이의 변화를 통해 정의되었다. 이를 바탕으로 Zr(IV) 이온은 −1.5 V (vs. Ag/AgCl) 보다 높은 전압 영역에서는 ZrCl를 거쳐 Zr 금속으로 환원되는 것이 확인되었으며, 이보다 충분히 낮은 전압영역에서는 Zr(IV)에서 Zr 금속으로 바로 환원될 가능성이 있음이 확인되었다. -1.0 V (vs. Ag/AgCl) 근처에서는 Zr(IV)가 Zr(II)로 환원될 수 있으나 ZrCl4의 농도가 낮은 경우에는 반응속도가 느려 Zr(II)의 양이 매우 적을 것으로 예상된다. Zr 금속의 산화 과정은 환원과정과는 달리 ZrCl를 거치지 않고 Zr(IV) 또는 Zr(II) 이온으로 바로 산화되는 것으로 조사되었으며, ZrCl4의 농도가 낮은 경우에는 환원반응과 마찬가지로 Zr(II)는 거의 형성되지 않고 대부분 Zr(IV)로 바로 환원되는 것으로 나타났다. 피복관 전해정련 과정에서 중요한 문제 중 하나인 ZrCl의 전착은 Zr(IV)가 ZrCl을 거쳐 Zr 금속으로 환원되므로 낮은 농도의

ZrCl4을 사용하는 경우, Zr(IV)로부터 ZrCl가 형성되는 속도가 ZrCl이 Zr 금속으로 변하는 속도보다 느려져 음극에서 ZrCl이 함께 회수되는 것을 방지할 수 있음을 확인하였다. 사용후핵연료 Zircaloy-4 피복관 내 주요 원소인 Sn, Cr, Fe과 함께 주요 방사성 동위원소인 Co에 대해서도 순환전위법을 통해 LiCl-KCl 용융염 내 산화환원 거동을 파악하였다. 이들 원소는 지르코늄과는 달리 부차적인 단계 없이 금속으로 바로 환원되었으며, 지르코늄보다 환원경향성이 큰 것으로 확인되었다.

사용후핵연료 Zircaloy-4 피복관 내 주요 원소들의 산화환원 거동에 대한 정보를 바탕으로 연구실 규모의 비방사화 Zircaloy-4 시편에 대한 전해정련을 수행하였다. Zr을 제외한 Zircaloy-4 내 주요원소들이 Zr보다 환원경향성이 크므로 양극에서 용해될 시 음극에 지르코늄보다 우선 전착된다. 따라서 양극의 전위를 −0.9 V (vs. Ag/AgCl) 이하로 유지하며 전해정련을 진행하여 양극에서 지르코늄만 용해되도록 하였다. 5가지의 ZrCl4 농도 (0.1, 0.5, 1.0, 2.0, 4.0 wt. %)에서 전해정련을 수행하고 XRD로 전착물의 화학적 형태를 분석함으로써 $ZrCl_4$ 농도가 지르코늄 전착물 형태에 미치는 영향을 파악하였으며 전착물의 조성은 ICP-MS로 분석하였다. 모든 전해정련 경우에 대해서 지르코늄을 제외한 원소가 검출되지 않았으며 순환전위법을 통해 예측한 바와 같이 상대적으로 $ZrCl_4$의 농도가 낮은 경우 (0.1, 0.5 wt. %)에는 음극에 ZrCl 없이 Zr 금속만 전착되었으며, 농도가 높은 경우 (2.0, 4.0 wt. %)에는 음극에 ZrCl만 전착되었다. ZrCl4의 농도가 1.0 wt. %인 경우에는 ZrCl와 Zr 금속이 함께 검출되었다. 일반적으로 용융염 내에 회수하고자 하는 원소의 농도가 높을 때, 높은 생산량을 확보하는 것이 가능하므로 ZrCl의 전착 없이 Zr 금속 회수가 가능한 $ZrCl_4$ 농도 중 가장 큰 0.5 wt. %가 피복관 전해정련을 위해 가장 적합하다.

3차원 전기화학 반응 전산 모델은 상용 전산유체 코드인 ANSYS-

CFX를 바탕으로 전해질의 유체역학적 거동과 전기장 해석 및 전기화학 반응 해석을 결합하여 개발되었다. 개발된 모델 중 음극전착 모델은 rotating cylindrical Hull cell에서 구리전착 반응 시 음극 위치에 따른 과전압 분포를 벤치마크함으로써 검증하였다. 양극 용해 및 파일럿 스케일 전해정련로에 대한 전산 모델 검증은 미국 아이다호 국립연구소에서 EBR-II 원자로의 사용후핵연료의 처리를 위해 운용하고 있는 Mark-IV 전해정련로의 인가 전류에 따른 셀 전위를 벤치마크함으로써 수행하였다. 양극 면적의 변화가 적은 전해정련 초기에 대해서는 실험적으로 측정된 셀전위와 전산 모델링을 통해 얻은 값이 잘 일치하였으나, 전해정련이 진행됨에 따라 양극 면적이 복잡하게 변화하여 가정한 양극면적 변화 곡선에 따라 계산된 셀전위의 차이가 비교적 크게 나타났다. 따라서 개발된 전산모델은 음극 전착 거동을 모사하는데 사용하거나 전해정련 초기단계 모델링에 활용하는 것이 좋을 것으로 판단된다.

지르코늄 환원 반응은 앞서 벤치마크한 수용액 시스템에서의 구리 전착이나 용융염 시스템에서 악티나이드 원소의 전착거동과는 달리, Zr(IV) 이온이 ZrCl을 거쳐 Zr 금속으로 전착되는 다단계 환원과정을 거친다. 따라서 Zircaloy-4 피복관 전해정련에 대한 모델링을 위해서는 전산모델의 다단계 환원반응에 대한 검증이 필요하다. 이를 위해 앞서 다양한 농도에서 수행된 비방사화 Zircaloy-4 전해정련 데이터를 활용하였다. 전산모델을 통해 실험 결과와 동일하게 용융염 내 ZrCl4의 농도가 0.1, 0.5 wt. %인 경우에는 음극에 ZrCl 전착 없이 Zr 금속만 회수되는 것을 확인하였으며, 1 wt. %인 경우에는 ZrCl와 Zr 금속이 함께 회수됨을, 그 이상의 농도에서는 ZrCl만 전착되는 것을 확인하였다.

용융염 실험을 통해 파악한 지르코늄의 산화·환원 거동 특성과 개발된 3차원 전산모델을 바탕으로 파일럿 규모의 사용후핵연료

Zircaloy-4 피복관 전해정련로를 설계하였다. 3차원 모델링을 통한 설계에 앞서 1차원 시간종속 전기화학 반응 전산 모델 코드인 REFIN을 사용하여 방사화 피복관 전해정련에 대한 예비해석을 수행하였다. 이를 통해 양극 전위 조절을 통해 Sn, Cr, Fe, Co와 같은 환원경향성이 큰 원소의 용해를 막아 음극 오염을 최소화 할 수 있음을 재차 확인하였다. 우라늄을 포함한 악티나이드 원소의 경우 지르코늄 보다 산화경향성이 커 전해정련이 진행되는 동안 용융염 내로 용해되나 음극에는 전착되지 않음을 확인하였다.

파일럿 규모의 사용후핵연료 Zircaloy-4 피복관 전해정련로 설계는 연간 0.1~0.2톤의 피복관을 처리할 수 있는 전해정련로를 설계하는 것을 목표로 진행하였다. 피복관 내에 존재하는 우라늄 및 악티나이드 원소는 지르코늄보다 산화경향성이 크기 때문에 양극 바스켓에 한 번에 투입되는 피복관의 양이 많으면 용융염 내 악티나이드의 농도가 증가하여 악티나이드 원소가 음극에 가능성이 증가한다. 이러한 이유로 전해정련로에 투입되는 피복관의 양은 10 kg으로 제한하였으며, 전체 셀의 크기는 피복관 내의 악티나이드가 모두 용해되어도 용융염 내 악티나이드 농도가 충분히 낮게 유지되어 악티나이드 전착 없이 높은 순도의 지르코늄을 회수할 수 있도록 충분히 크게 설계하였다. 음극 주변 확산경계층이 너무 작은 경우, 음극 표면으로 Zr(IV) 이온의 음극으로의 공급이 빨라져, ZrCl의 형성 속도가 증가하여 ZrCl이 Zr 금속과 함께 음극에서 회수될 수 있어 양극바스켓은 고정시키고 음극만을 회전시켜 적당한 수준의 확산경계층을 유지할 수 있도록 하였다. 양극 바스켓은 전해정련로 가운데 있는 음극을 중심으로 등간격으로 배치하여 국부적 전류의 집중을 최소화 하였다. 본 논문을 통해 개발된 3차원 전산 모델을 통해 설계된 전해정련로의 다양한 운전조건에 대해 모델링을 진행함으로써 성능을 검증하였다. 양극 바스켓을 3개 이상 사용하는 경우, 원주방향의 전위 편차가 충분히 감소함을 확인

하였다. 또한 설계된 전해정련로에서 우라늄에 의한 오염과 ZrCl의 공전착 없이 Zr 금속을 회수하는 것이 가능함을 확인하였으며 목표로 하는 0.1~0.2 톤 규모의 연간처리량의 달성이 가능함을 확인하였다.

주요어: 지르코늄 재활용, LiCl-KCl, 지르코늄 산화환원 거동, 양극 전위 조절, 3차원 전산 모델, 전해정련로 설계
학 번: 2010-21032